Advances in semiconducting-superconducting nanowire devices

Borsoi, F.

DOI
10.4233/uuid:10522213-d19e-4b33-98a1-e5f87bf64f79

Publication date
2021

Document Version
Final published version

Citation (APA)
Borsoi, F. (2021). *Advances in semiconducting-superconducting nanowire devices*. [Dissertation (TU Delft), Delft University of Technology]. Delft University of Technology. https://doi.org/10.4233/uuid:10522213-d19e-4b33-98a1-e5f87bf64f79

ADVANCES IN SEMICONDUCTING-SUPERCONDUCTING NANOWIRE DEVICES

ADVANCES IN SEMICONDUCTING-SUPERCONDUCTING NANOWIRE DEVICES

Dissertation

for the purpose of obtaining the degree of doctor
at Delft University of Technology
by the authority of the Rector Magnificus, Prof.dr.ir. T.H.J.J. van der Hagen,
chair of the Board for Doctorates
to be defended publicly on Wednesday 14 April 2021 at 10:00 o'clock

by

Francesco BORSOI

Master of Science in Physics,
Università di Pisa, Pisa, Italy,
born in Pordenone, Italy.

This dissertation has been approved by the promotors.

Composition of the doctoral committee:

Rector Magnificus,	chairperson
Prof.dr.ir. L.P. Kouwenhoven,	Delft University of Technology, promotor
Dr. M.T. Wimmer,	Delft University of Technology, copromotor
Independent members:	
Prof.dr. G.A. Steele,	Delft University of Technology
Dr.ir. M. Veldhorst,	Delft University of Technology
Prof.dr. Y. Oreg,	Weizmann Institute of Science, Israel
Prof.dr. A. Tredicucci,	Università di Pisa, Italy
Prof.dr. Y.V. Nazarov,	Delft University of Technology, reserve member
Other member:	
Dr. M. Quintero-Pérez,	Microsoft Quantum Lab Delft

Keywords: hybrid devices, semiconducting nanowires, superconductivity, interfaces, Josephson junctions, Aharonov-Bohm interferometers
Printed by: Ipskamp Printing, Enschede
Front & Back: Design by Bregje Jaspers, ProefschriftOntwerp.nl, Nijmegen

Casimir PhD Series, Delft-Leiden 2021-04

ISBN 978-90-8593-470-7

An electronic version of this dissertation is available at
http://repository.tudelft.nl/.

CONTENTS

SUMMARY

After a century from the quantum description of nature, the scientific community has laid the basis for using nature's properties to our advantage. The quantum technology vision stems from the idea of capitalizing these principles in various sectors, such as computation and communication. However, in contrast to classical processors, encoding and processing quantum information suffer from the quantum states' fragility to environmental disturbances. To mitigate their susceptibility, disruptive proposals suggested encoding information in non-local degrees of freedom such as in pairs of delocalized Majorana modes in topological superconductors. Although these materials remain elusive in nature, it is possible to engineer solid-state devices with the same properties such as semiconducting-superconducting nanowires.
Starting from this idea, experimental signatures of zero-energy Majorana modes have been accompanied in recent years by continuous theoretical validations and rejections. The refinement in the theoretical understanding aligns with the swift advances on the experimental side, and this thesis finds its place in this phase of advancement, focusing on the intricate physics of the building blocks of Majorana qubits and proposing solutions to various nanofabrication challenges. In particular, we consider with attention the challenge of reading out the Majoranas information by detecting changes in their transmission phase. To this purpose, the minimal circuit requires a phase-coherent interferometer embedding a semiconducting-superconducting segment. Despite the apparent simplicity of this experiment, the Majoranas fingerprint in the transmission phase remains mostly unexplored due to the complexity of the circuit building blocks. Motivated by this challenge, our quest begins by considering each piece of the puzzle separately.

We start by exploiting recent breakthroughs in the growth of nanowire-based interferometers to study the transmission phase of a large quantum dot, a setup similar to the one required for the Majoranas read-out. The conductance of this Aharonov-Bohm loop manifests gate- and magnetic field-tunable Fano resonances, that arise from the interference between electrons that travel through the reference arm and undergo resonant tunnelling in the dot. This experiment serves to point out the limitations of the currently available nanowire networks and provide critical insights for future topological interferometers' design.
Thereafter, we explore the intricate physics of Coulomb semiconducting-superconducting wires, commonly known as hybrid island devices. Here, we demonstrate for the first time that InSb nanowires coupled to superconducting Al films manifest charging mediated by Cooper pairs of electrons. This observation implies that the low-energy spectrum of the semiconductor is fully proximitized by the superconductor, a fundamental requirement for achieving parity control in topological circuits. Starting from a Cooper pair condensate with an even electron parity, we can tune the nature of the island ground state with

experimental knobs such as magnetic field and gate voltages. In particular, when a spin-resolved subgap state moves from the edge of the induced gap down to zero energy, single electrons can charge the island leading to conductance oscillations with a gate-voltage periodicity halved than for Cooper pairs. By mapping out such a 2e-to-1e transition in large ranges of gate voltage and magnetic field, we identify potential topological regions where the 1e oscillations are caused by discrete subgap states oscillating around zero energy.

Part of the challenges concerning the realization of scalable hybrid devices lies in the complexity of their nanofabrication and the open questions in the material science involved. Stimulated by these interrogatives, the second part of this thesis introduces significant advances in the arena of hybrid nanowire devices.
Having so far dealt with InSb nanowires with a maximum length of $\sim 3\,\mu m$, we turn our attention to the synthesis and the characterization of much longer InSb nanowires with a higher chemical purity than their predecessors and electron mobility exceeding $40000\,cm^2/Vs$. Having quantified their pronounced spin-orbit interaction, adding a superconductor in the game is the logical next step.
At the time of these experiments, hybrid nanowire devices were obtained by interfacing the two materials *in situ*, directly after the growth of the semiconductor. Despite ensuring a barrier-free semiconducting-superconducting interface, this approach has significant drawbacks in creating gate-tunable junctions due to the challenges in controlling the selectivity and the accuracy of the superconductor etching step. Considering that the semiconducting-superconducting interface is unstable even at room temperature, the devices quality, turnaround, and reproducibility become severely affected by extensive and low-yield fabrication processes.
To circumvent these roadblocks, we have established a new fabrication paradigm based on on-chip shadow walls and shadow evaporations that offers substantial advances in device quality and reproducibility. Our approach results in devices with a hard induced superconducting gap and ballistic hybrid junctions. In Josephson junctions, we observe large gate-tunable supercurrents and high-order multiple Andreev reflections indicating the resulting junctions' exceptional coherence. Crucially, our approach enables the realization of three-terminal devices, where zero-bias conductance peaks emerge in a magnetic field concurrently at both boundaries of the one-dimensional hybrids. In the near future, correlating such Majoranas' signatures with the measurement of the induced gap in the bulk will enable a better classification of the observed subgap states. In conclusion, once this technology is applied to nanowire networks, it will allow verifying topological parity read-out schemes, which is a milestone toward verifying the Majorana states' exotic exchange statistics.

SAMENVATTING

Een eeuw na de ontwikkeling van de kwantummechanische beschrijving van de natuur, heeft de wetenschappelijke gemeenschap de basis gelegd om de eigenschappen van de natuur in ons voordeel in te zetten. Het toekomstperspectief van kwantumtechnologie broedt voort uit het idee om munt te slaan uit deze principes in verscheidende sectoren, zoals computerberekeningen en communicatie. In tegenstelling tot klassieke computers, wordt het encoderen en verwerken van kwantuminformatie echter bemoeilijkt door de gevoeligheid van kwantumtoestanden voor omgevingsruis. Om deze kwetsbaarheid te omzeilen, suggereerden baanbrekende voorstellen om informatie te versleutelen in niet-lokale vrijheidsgraden, zoals in paren van gedelokaliseerde Majorana toestanden in topologische supergeleiders. Alhoewel dergelijke materialen vooralsnog ongrijpbaar zijn in de natuur, is het wel mogelijk om de benodigde eigenschappen te construeren in vastestof apparaatjes, zoals in hybride halfgeleidende-supergeleidende nanodraden.
Experimentele tekenen van nul-energie Majorana toestanden op basis van dit idee zijn de afgelopen jaren onderhevig geweest aan continue theoretische validatie en verwerping. De verfijning van het theoretische begrip gaat hand in hand met rappe ontwikkelingen aan de experimentele kant, en dit proefschrift vindt zijn plaats in deze fase van de ontwikkeling, zich richtend op de rijke natuurkundige fenomenen van de bouwstenen van Majorana kwantumbits en met voorstellen voor oplossingen voor verschillende uitdagingen in nanofabricage. In het bijzonder, wijden we aandacht aan de uitdaging om de informatie van Majorana's uit te lezen via veranderingen in de fase van de transmissie. Het minimale circuit hiervoor, bestaat uit een fasecoherente interferometer met daarin een halfgeleidend-supergeleidend segment. Ondanks de veronderstelde eenvoud van dit experiment, blijven kenmerkende signalen van Majorana's grotendeels onverkend door de complexiteit van de bouwstenen van het circuit. Gemotiveerd door deze uitdaging, begint onze zoektocht door elk onderdeel van de puzzel apart onder de loep te nemen.

We beginnen door gebruik te maken van recente doorbraken in de groei van interferometers gebaseerd op nanodraden om de fase in de transmissie van een grote kwantumdot te bestuderen, een opstelling die vergelijkbaar is met de opstelling benodigd om Majorana's uit te lezen. De geleiding van deze Aharonov-Bohm lus vertoont Fano resonanties veroorzaakt door elektrische gate spanningen en magneetvelden, die voortkomen uit de interferentie tussen elektronen die zich door de referentiearm bewegen en een resonant tunneleffect ondergaan in de kwantumdot. Dit experiment toont de beperkingen van nanodraad netwerken die momenteel beschikbaar zijn aan en biedt cruciaal inzicht in een verbeterd het ontwerp van toekomstige interferometers. Vervolgens duiken we in de rijke fysica van Coulomb halfgeleidende-supergeleide nanodraden, beter bekend als hybride eilanden. Hierin tonen we voor het eerst aan dat InSb nanodraden gekoppeld aan een dunne laag van supergeleidend Al ladingseffecten vertonen veroorzaakt door Cooper paren van elektronen. Deze waarneming duidt erop dat laagenergiespectrum van

de halfgeleider volledig bepaald is door het supergeleidende nabijheidseffect, wat een fundamentele vereiste is voor controle over de pariteit in topologische circuits. Vanuit een condensaat van Cooper paren met een even pariteit, kunnen we grondtoestand van het eiland beïnvloeden met experimentele knoppen, zoals een magneetveld en elektrische gate spanningen. In het bijzonder, wanneer een spinvolle toestand binnen de bandkloof vanaf de rand van de geïnduceerde supergeleide bandkloof naar nul energie beweegt, dan kunnen enkele elektronen het eiland opladen, met geleidingsoscillaties waarvan de periodiciteit de helft is vergeleken met het geval van Cooper paren tot gevolg. Door deze overgang van 2e naar 1e in kaart te brengen over een groot bereik van elektrische gate spanning en magneetveld, bepalen we potentiële topologische gebieden waar de 1e oscillaties veroorzaakt worden door discrete subkloof toestanden die rond nul energie oscilleren.

Een deel van de uitdagingen rondom de verwezenlijking van schaalbare hybride nanodraden, komt voort uit de complexiteit van hun nanofabricage en de open vragen in de desbetreffende materiaalkunde. Gestimuleerd door deze vragen, introduceert het tweede deel van dit proefschrift significante vooruitgang op het gebied van hybride nanodraden. Na ons tot zover gericht te hebben op InSb nanodraden met een maximale lengte van ongeveer $\sim 3\,\mu$m, richten we onze aandacht op de groei en karakterisatie van veel langere InSb nanodraden met een hogere chemische zuiverheid dan hun voorgangers en een elektronmobiliteit van meer dan $40000\,\mathrm{cm}^2/\mathrm{Vs}$. Na hun aanzienlijke spinbaankoppelingssterkte te hebben gekwantificeerd, is het toevoegen van een supergeleider de volgende logische stap. Ten tijde van deze experimenten werden hybride nanodraden gemaakt door de twee materialen in-situ op elkaar aan te brengen, direct na de groei van de halfgeleider. Alhoewel dit proces een barrièrevrij halfgeleider-supergeleider grensvlak oplevert, heeft deze aanpak significante nadelen bij het vormen van juncties die beïnvloedbaar zijn door een elektrische gate, vanwege uitdagingen rondom het selectief en precies chemisch etsen. Doordat het halfgeleider-supergeleider grensvlak zelf instabiel is op kamertemperatuur, zorgt het uitvoerige en onbetrouwbare fabricageproces voor een ernstig verminderde kwaliteit van de nanodraad apparatuur, de doorlooptijd en reproduceerbaarheid.
Om deze barrières te vermijden, hebben we een nieuw fabricage paradigma ontworpen gebaseerd op schaduwmuren op de chip en een schaduwopdamp proces dat aanzienlijke voordeel biedt wat betreft nanodraad kwaliteit en reproduceerbaarheid. Onze aanpak resulteert in een harde geïnduceerde supergeleidende bandkloof en ballistische hybride juncties. In Josephson juncties observeren we grote, elektrische gate stuurbare superstromen en meervoudige Andreev reflecties van hoge orde, duidend op een uitzonderlijke coherentie in de junctie. Bovendien maakt onze aanpak het mogelijk om nanodraden met drie elektrische aansluitingen te realiseren, waarin nulspanning geleidingspieken aan beide zijdes van de eendimensionale hybride verschijnen in een magneetveld. In de nabije toekomst zal de correlatie van zulke Majorana tekenen, in combinatie met de meting van een geïnduceerde bandkloof in de bulk van de nanodraad, een verbeterde classificatie van de geobserveerde toestanden binnen de bandkloof opleveren. Concluderend, wanneer deze technologie ingezet zal worden voor netwerken van nanodraden, zal het de toetsing van meetschema's voor de topologische pariteit mogelijk maken, wat

een mijlpaal is op de weg naar het verifiëren van de exotische verwisellingsstatistiek van Majorana toestanden.

1

INTRODUCTION

The possession of knowledge does not kill the sense of wonder and mistery, there is always more mistery.

Anais Nin

1

1.1. QUANTUM TECHNOLOGY TODAY

The quantum theory describing the physics of small particles such as atoms and molecules was developed in the dawn of 1900. Scientists such as N. Bohr, M. Plank, A. Einstein, W. Heisenberg, E. Schrödinger, W. Pauli and M. Curie (which distinguishes from the others at the Solvay conferences for being the only woman, and for winning two Nobel prizes – Fig. 1.1) have marked with their ideas the first quantum revolution.

Figure 1.1: **The founding fathers** of quantum mechanics at the Solvay conference in 1927 (in false colors).

The thesis work at hand has been conducted at QuTech – faculty of TU Delft – one of the hottest research centers in quantum in the world. Here, teamed scientists are contributing to the birth of a second quantum revolution. If we – as humankind – survive to the effects of climate warming, we will remember these years as an extraordinary period of fruitful progress. We live in a time in which the scientific community – with the support of the society and the policymakers – has laid the basis for using the properties that nature offers us to our advantage. The quantum technology vision stems from the idea of capitalizing these quantum principles in sectors such as computation, secure communications, chemistry, metrology, and sensing.

In this thesis, we focus on a novel, and yet to be demonstrated, platform to form qubits. Qubits are the quantum analogous of classical bits. A qubit is a two-level system described by a state that can be in any quantum superposition of the two levels. Several quantum systems have been proposed and demonstrated to form reliable, coherent qubits. Primary examples in solid-state platforms are spin and superconducting qubits, which – upon taking advantage of mature technologies – have rallied in the last two decades [1, 2]. Despite being somewhat scalable platforms, the stored quantum information has a finite

lifetime, known as coherence time. The loss of the information is originated from the quantum states susceptibility to noise from the surrounding environment. Correcting for these losses requires additional qubits that operate next to the logical qubits. Altogether, the implementation of error-correction schemes might hinder their full scalability. Alternatively, we can think about storing the information in topological materials. Here, the qubit is encoded in a non-local degree of freedom in a way that minimizes decoherence effects [3, 4]. The concept of storing the information non-locally, in distant entangled objects creates the bridge between quantum technology and topology in condensed matter systems. This link defines the context of this thesis.

Before transitioning to the topology in condensed matter, let us introduce a necessary basic concept. In general, collective behaviours of particles have been mathematically (and intuitively) treated considering quasiparticles instead – see classical analogous in Fig. 1.2. Renowned examples are holes for missing electrons, plasmons for electronic waves, Bogoliubov quasiparticles for the electron-hole excitations in superconductors, and excitons for bound states of electrons and holes. These objects have been and will be continued to be studied intensively.

Figure 1.2: **Classical quasiparticles.** The motion of the six-body system can be simplified to the one of a two-body system. With some imagination, we can make an analogy between the Kitaev chain where the low-energy spectrum hosts end Majoranas and this series of pendula where only the outer spheres swing.

A landmark milestone was set with Kitaev's theoretical demonstration that certain superconductors [1] are capable of hosting (quasi)particles which have been long sought, and not yet found [3, 7, 8]. The particles under the lens are Majorana fermions, named after the genius Italian physicist Ettore Majorana. Majorana – one of the brightest Enrico Fermi's students [2] – introduced into theoretical physics an equation that describes a fermionic particle with a real, rather than complex, wave function. Opposite to Dirac fermions

[1] Notably, Sr_2RuO_4 might be an intrinsic p-wave superconductor [5, 6].

[2] Enrico Fermi about Majorana, Rome 1938: "There are several categories of scientists in the world; those of

described by complex wave functions, a particle with a real wave function is equal to its own antiparticle. Although there are speculations, not yet proven, regarding the neutrino, no fundamental particles behave as Majorana fermions [10]. The particle physicists community has been looking into space for the last century, but the zero-energy, zero-mass, zero-charge did not make their detection simple and successful. Instead, condensed matter physicists have started to look at the spatial boundaries of p-wave superconductors where Majoranas should appear. The search for these particles has since then posed considerable challenges in materials science.

Let us take a step back for a second. Mathematically, two Majorana fermions combine into one Dirac fermion, just as two real numbers form a complex number [10], but a clarification is in order at this point. Ettore Majorana's particles are indeed fermions in three-dimensions that exchange according to the Fermi-Dirac statistics. In contrast, Majorana quasiparticles (also called bound states, or zero-energy modes) confined in one-dimensional systems exchange unlike bosons and fermions. Exchanging fermions or bosons does not have a measurable effect, whereas braiding Majorana quasiparticles – that obey Ising-type non-abelian statistics [3] – changes the quantum state fundamentally, with detectable effects [10]. This unveiled phenomenon motivates the scientific significance of Majorana modes and triggers technological applications for quantum information processing [4].

From 2012 onward, Majorana signatures in solid-state systems have been accompanied by continuous theoretical validations and rejections, which are the expression of a field that is still in a rapid development phase. The refinement in the theoretical understanding aligns with the swift advances on the experimental side. This thesis finds its place in this phase of advancement. This stage is a necessary transition period in between the years of the first Majorana signatures and the final development of the required architectures. Along my venture in the Topo group, I touched several aspects of the Majorana systems varying from their technological improvement to fundamental studies.

1.2. THIS VENTURE

The Lutchyn and Oreg recipe for creating Majorana modes in solid-state devices comprises pristine semiconductor nanowires with appreciable spin-orbit energy coupled to a superconductor in a magnetic field [7, 8]. The state of two emerging Majoranas can either be empty or filled with a single delocalized electron. When the system is infinite, the two states are truly degenerate with zero-energy. Upon coupling the system to an electron reservoir, the occupation of the two states constantly flips as electrons flow in and out from the wire. If we were able to take a snapshot of the system and to count the electrons

second or third rank do their best but never get very far. Then there is the first rank, those who make important discoveries, fundamental to scientific progress. But then there are the geniuses, like Galilei and Newton. Majorana was one of these."[9].

[3] The term non-abelian stems from the fact that subsequent braids do not commute. Examples of abelian particles are fermions, bosons and broadly speaking anyons which acquire an intermediate phase $e^{i\phi}$ such as fractional electrons in the fractional quantum Hall effect [11].

in the wire, we would find that, when the electron number is even, the Majoranas are in the empty state because even electrons form Cooper pairs that vanish in the bosonic condensate. Oppositely, in the odd configuration, the extra electron is absorbed in the two Majoranas.

Distinguishing between the two parity states is as vital for quantum computing as complex to achieve. Theoretical proposals suggested that the tunnelling phase via two Majoranas depends on their topological parity and thus serves for their read-out [12]. Because this concept is not yet demonstrated experimentally, it forms the starting interrogative of my PhD venture. To tackle this long-standing question, we first split the problem into simpler pieces.

In chapter 4, we investigate the implementation of such phase-detector circuit on a two-path nanowire interferometer. Here, we characterize the phase-coherent transport across a large semiconducting quantum dot embedded in the loop. The large dot mimics a Coulomb-blockaded Majorana island that is the object of our investigations in chapters 5 and 6. Although the two elements are the essential ingredients for the aforementioned hybrid interferometry circuit, the combination of the two experiments was at the time technologically impossible. In brief, several problems interfere with our quest. First, nanowire interferometers are arduous to grow and are relatively short; second, a superconducting film deposited *in-situ* on the entire nanostructure cannot be etched without introducing disorder; third, together with the evaporation of a superconducting film on a nanowire segment, standard lithography techniques do not proximitize the wire for electron parity control.

The second part of this thesis is devoted to solving these limitations. Starting from the semiconductor, in chapter 7, we contribute to the development and the characterization of a new generation of extremely long quantum wires. The improvement of the growth conditions enables to enhance the electron mobility by a factor of two compared to previous growth methods. Eventually, in chapters 8 and 9, we overcome the limitations for creating hybrid nanowire devices. Our newly developed shadow-wall lithography method allows for the implementation of novel devices such as hybrid interferometers and ultimately topological qubits while eliminating many fabrication steps such as lithography and etching. Crucially, simple devices such as normal-superconducting junctions and various others can be realized in a single-shot. These advancements open new avenues ranging from experiments to material improvements. Once this technology is applied to nanowire networks, it enables topological parity read-out, which is a landmark achievement to verify the exotic exchange statistics of elusive Majorana states [10].

1

REFERENCES

[1] J. Koch, T. M. Yu, J. Gambetta, A. A. Houck, D. I. Schuster, J. Majer, A. Blais, M. H. Devoret, S. M. Girvin, and R. J. Schoelkopf, *Charge-insensitive qubit design derived from the Cooper pair box,* Phys. Rev. A **76**, 042319 (2007).

[2] D. Loss and D. P. DiVincenzo, *Quantum computation with quantum dots,* Phys. Rev. A **57**, 120 (1998).

[3] A. Y. Kitaev, *Unpaired Majorana fermions in quantum wires,* Phys.-Uspekhi **44**, 131 (2001).

[4] R. M. Lutchyn, E. P. A. M. Bakkers, L. P. Kouwenhoven, P. Krogstrup, C. M. Marcus, and Y. Oreg, *Majorana zero modes in superconductor–semiconductor heterostructures,* Nat. Rev. Mater. **3**, 52 (2018).

[5] T. M. Rice and M. Sigrist, *Sr2RuO4: an electronic analogue of 3He?* J. Phys.: Condens. Matter **7**, L643 (1995).

[6] A. P. Mackenzie and Y. Maeno, *The superconductivity of Sr2RuO4 and the physics of spin-triplet pairing,* Rev. Mod. Phys. **75**, 657 (2003).

[7] R. M. Lutchyn, J. D. Sau, and S. Das Sarma, *Majorana fermions and a topological phase transition in semiconductor-superconductor heterostructures,* Phys. Rev. Lett. **105**, 077001 (2010).

[8] Y. Oreg, G. Refael, and F. von Oppen, *Helical liquids and Majorana bound states in quantum wires,* Phys. Rev. Lett. **105**, 177002 (2010).

[9] F. Wilczek, *Majorana returns,* Nat. Phys. **5**, 614 (2009).

[10] P. W. Brouwer, *Enter the Majorana fermion,* Science **336**, 989 (2012).

[11] J. Alicea, *New directions in the pursuit of Majorana fermions in solid state systems,* Rep. Prog. Phys. **75**, 076501 (2012).

[12] L. Fu, *Electron teleportation via Majorana bound states in a mesoscopic superconductor,* Phys. Rev. Lett. **104**, 056402 (2010).

2

THEORY

Mathematically, two Majorana fermions combine into one Dirac fermion,
just as two real numbers form a complex number.

Piet W. Brouwer

This chapter describes theoretical concepts which are relevant for the understanding of the experiments reported in this thesis. The protagonists of this thesis are undoubtedly semiconducting quantum wires, which serve as (quasi) one-dimensional electronic channels. We will then introduce the second vital characters of this work: superconductors. Together, the two materials can be combined to form pairs of Majorana quasiparticles on solid-state devices. We will discuss this mechanism considering the energy dispersions of the system, and reveal how these states can be used as a delocalized two-level system for quantum computing. Eventually, we will show how electron tunnelling via two Majorana enables the read-out and manipulation of the quantum information.

2.1. SEMICONDUCTING WIRES

BALLISTIC AND DIFFUSIVE TRANSPORT

Semiconducting nanowires are an exciting platform to explore physics in reduced dimensionality and to develop novel quantum devices. Due to the strong confinement in two out of three spatial dimensions, let us assume the **y** and **z** directions, ballistic motion of electrons along **x** gives rise to an energy dispersion – in the $\mathbf{k}\cdot\mathbf{p}$ approximation – formed by n discrete subbands quadratic as a function of the wave vector k_x (Figs. 2.1a and b):

$$E_n(k_x) = E_{0,n} + \frac{\hbar^2 k_x^2}{2m^*} \tag{2.1}$$

where m^* is effective electron mass. When no external bias voltage is applied to the one-dimensional channel between source (S) and drain (D), states with positive and negative k_x are equally occupied up to the Fermi energy E_F. Upon the application of a voltage bias V, the symmetry is broken, and the energy difference $eV = \mu_S - \mu_D$ creates a current I. At zero-temperature, this reads [1, 2]:

$$I = e\sum_{n=1}^{N}\int_{\mu_S}^{\mu_D}\frac{1}{2}\rho_n(E)\cdot v_n\cdot T_n(E)dE \tag{2.2}$$

where e is the electron charge, N is the total number of channels, $\rho_n(E) = \frac{2}{\pi}\frac{dk_x}{dE_n}$ is the one-dimensional density of states, $v_n = \frac{dE_n}{\hbar dk_x}$ is the effective electron velocity and T_n is the channel transparency. The conductance $G = I/V$ results:

$$G = \frac{2e^2}{h}\sum_{n=1}^{N} T_n(E) \tag{2.3}$$

For ideal transparencies ($T_n = 1$), the conductance becomes quantized in multiples of $2e^2/h$, where the factor 2 takes into consideration the two spin eigenstates. Upon increasing the chemical potential in the channel μ (i. e., by electrostatic gating), we observe the increase in steps of the conductance (Fig. 2.1c). Note, this beautiful phenomenon occurs only when the separation l between the source and drain leads is at maximum of the order of the mean free path l_e. For this reason, the observation of conductance quantization has become the hallmark of ballistic transport in nanostructures [3–10].

In the opposite limit, when the semiconducting channel is much longer than the mean free path ($l \gg l_e$), electrons undergo a series of scattering events and transport becomes diffusive. In this regime, the experiments are well described by the Drude model, where transport is classical [11, 12]. In this context, the time (τ) between two scattering events is directly linked to the carrier mobility (μ_m) as

$$\mu_m = \frac{e\tau}{m^*} \tag{2.4}$$

The mobility is a measurable quantity in field-effect nanowire transistors, where scattering stems from several mechanisms such as the presence of crystal defects, surface roughness, and chemical impurities [13–17]. In this scenario, the conductance increases linearly with gate voltage (V_g):

$$G = \frac{\mu_m C}{l^2}(V_g - V_{th}) \tag{2.5}$$

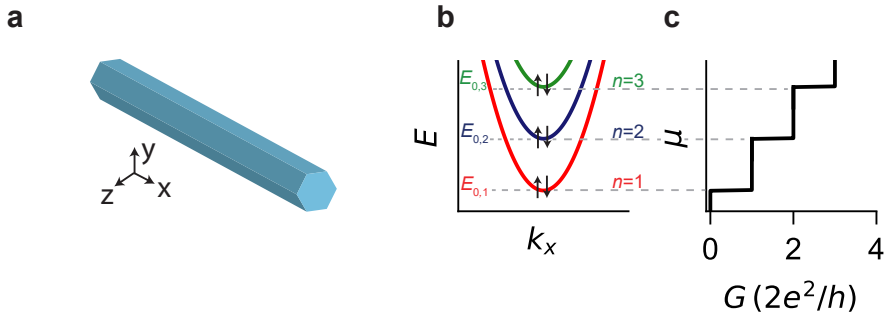

Figure 2.1: **Confinement and ballistic transport in quantum wires. a** Illustration of a hexagonal nanowire similar to the ones used in this thesis. **b** Energy dispersion of a quantum wire comprising discrete spin-degenerate subbands. **c** Upon increasing the chemical potential (μ), the wire subbands become populated and consequently the conductance rises in quantized steps of $2e^2/h$.

where V_{th} is the threshold voltage and C is the gate capacitance.

SPIN-ORBIT COUPLING

When electrons move with velocity **v** in the electric field **E** of an atom, they are subjected to an effective magnetic field **B** in their rest-frame

$$\mathbf{B} = -\frac{1}{c^2}\mathbf{v}\cdot\mathbf{E} \tag{2.6}$$

The magnetic moment of the electrons interacts with such magnetic field leading to the so-called spin-orbit interaction. Our research group focuses on transport on InSb nanowires, where this effect is extremely pronounced. In this thesis, we deal with InSb nanowires with zinc-blend crystal structure, where it is expected that the Rashba spin-orbit interaction dominates over the the Dresselhaus interaction. The latter is expected to vanish for electrons propagating along the [1,1,1] crystal direction, which is also the nanowire growth direction [18–20]. In this approximation, the Rashba Hamiltonian in a one-dimensional nanowire is:

$$H_R = \alpha_R p_x \sigma_y \tag{2.7}$$

where σ_y is one of three Pauli spin matrices $\sigma = (\sigma_x, \sigma_y, \sigma_z)$, and α_R is the Rashba coupling constant, which is a material-dependent parameter. This interaction results in an effective spin-orbit field ($\mathbf{B}_{SO}$) perpendicular to the electric field and the momentum:

$$\mathbf{B}_{SO} \propto \alpha_R \mathbf{k} \times \mathbf{E} \tag{2.8}$$

To quantify this interaction, it is often useful to define the spin-orbit energy E_{SO} and the spin-orbit length l_{SO}:

$$E_{SO} = \frac{m^* \alpha_R^2}{2\hbar^2} \tag{2.9}$$

$$l_{SO} = \frac{\hbar^2}{m^* \alpha_R} \tag{2.10}$$

The spin-orbit length l_{SO} corresponds to the length scale of the spin procession around $\mathbf{B}_{SO}$ of 2 radiants. In Tab. 2.1, we give an overview of the quantities discussed so far for InSb and InAs, the two most common materials to investigate Majorana zero modes [21–24].

Parameter	InSb	InAs
m^*	0.014	0.023
α_R (eVÅ)	0.23 - 1.04	0.18-0.81
E_{SO} (meV)	0.05 - 1	0.05-1
l_{SO} (nm)	50 - 230	40-180

Table 2.1: **Material parameters.** Bulk properties of InSb and InAs.

2.2. SUPERCONDUCTORS

In a superconductor, electrons close to the Fermi level bind together in Cooper pairs thanks to the attractive interaction mediated by lattice vibrations (phonons). Altogether, Cooper pairs form a bosonic condensate. At a macroscopic level, the superconducting state was explained by the Ginzburg-Landau theory as a low-temperature phase transition [25]. Later, Bardeen, Cooper and Schrieffer provided the well-know BCS microscopic description [26]. In brief, single-particle excitations are found at an energy $|\Delta|$ above the superconducting condensate, where $\Delta = |\Delta| e^{i\phi}$ is the complex order parameter. For an s-wave superconductor, these excitations are well described by the Bogoliubov de Gennes (BdG) formalism. The BdG effective Hamiltonian in the second quantization and in the mean field approximation reads [27]

$$H = \sum_{k,\sigma} \epsilon_k a^\dagger_{k,\sigma} a_{k,\sigma} + \sum_k \Delta \left(a^\dagger_{k,\uparrow} a^\dagger_{-k,\downarrow} + a_{-k,\downarrow} a_{k,\uparrow} \right) \tag{2.11}$$

where the operators $a^\dagger_{k,\sigma}$ and $a_{k,\sigma}$ create and annihilate respectively an electron with momentum $\hbar k$, spin σ and energy $\epsilon_k = \hbar^2 k^2/(2m^*) - \mu$. In eq. 2.11, we also have made the approximation that Δ does not depend on the momentum. The resulting BdG excitations are quasiparticles $b_{k,\sigma}$ with energies E_k that are coherent superpositions of electrons and holes

$$\begin{aligned} b_{k,\uparrow} &= u_k a_{k,\uparrow} - v_k a^\dagger_{-k,\downarrow} \\ b^\dagger_{k,\downarrow} &= v_k a_{k,\uparrow} + u_k a^\dagger_{-k,\downarrow} \\ E_k &= \pm\sqrt{\epsilon_k^2 + |\Delta|^2} \end{aligned}$$

The coherence factors u and v are displayed in Fig. 2.2a and can be seen as the electron and hole weights of a quasiparticle:

$$\begin{aligned} |u_k|^2 + |v_k|^2 &= 1 \\ |u_k|^2 &= \frac{1 + \epsilon_k/|E_k|}{2} \end{aligned} \tag{2.12}$$

The single-particle density of states (ρ_s) – shown in Fig. 2.2b – becomes gapped at $[-\Delta, \Delta]$, symmetric around the Fermi energy, and reads

$$\rho_s = \rho_n \frac{E_k}{\sqrt{E_k^2 - \Delta^2}} \tag{2.13}$$

with ρ_n the density of the states in the normal regime.

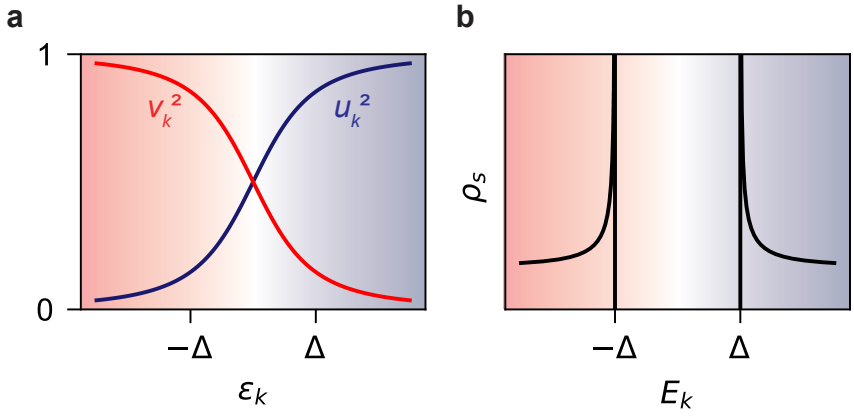

Figure 2.2: **Quasiparticle excitations.** **a** Coherence factors around $\epsilon_k = 0$: at $\epsilon_k \gg \Delta$ BdG excitations are electron-like quasiparticles (blue), whereas for $\epsilon_k \ll \Delta$ excitations are hole-like quasiparticles (red). **b** Single-particle density of states (ρ_s) plotted in arbitrary units versus E_k.

2.3. SEMICONDUCTING-SUPERCONDUCTING MAJORANA WIRES

The combination of semiconducting quantum wires and superconductors enables the synthesis of solid-state devices that can undergo a topological phase transition to a p-wave superconductor. At a mathematical level, this means that the topological invariant of the class D Hamiltonian in one dimension switches value [28]. At a physical level, this indicates that superconducting pairing occurs between electrons with the same spins [29–32].

While such transition is predicted for a variety of systems, such as two-dimensional electron gases [33, 34], atomic chains [35, 36], topological insulators [37, 38], and fractional quantum Hall effect systems [39, 40], the most studied platform consists of a semiconducting nanowire coupled to a superconductor [41–47]. When the two materials are put in close contact, the semiconductor inherits an induced superconducting gap Δ thanks to the Andreev reflections at the interface. We now consider a proximitized wire in the single-subband regime oriented along the **x** direction and subjected to an external electric field along **z**. In this case, a spin-orbit field B_{SO} is originated along **y**, and the Hamiltonian of the system reads [30, 31]

$$H = \left(\epsilon_k + \epsilon_{SO}\sigma_y + \epsilon_B\sigma_x\right)\tau_z + \Delta\tau_x \tag{2.14}$$

where $\epsilon_{SO} = \alpha_R k$ is the Rashba contribution, $\epsilon_B = \frac{1}{2} g\mu_B B$ is the Zeeman energy with g the Landé g-factor, μ_B the Bohr magneton and B the magnetic field along **x**. The operators σ and τ are the Pauli matrices which act respectively in the spin and particle-hole space. Because of these two degrees of freedom (electrons and holes), we diagonalize the Hamiltonian using the basis $(a_{k,\uparrow}, a_{k,\downarrow}, a^\dagger_{k,\uparrow}, a^\dagger_{k,\downarrow})$. The energy spectrum results:

$$E_\pm = \left(\epsilon_k^2 + \epsilon_{SO}^2 + \epsilon_B^2 + \Delta^2 \pm 2\sqrt{\epsilon_k^2 \cdot (\epsilon_{SO}^2 + \epsilon_B^2) + \epsilon_B^2\Delta^2}\right)^{\frac{1}{2}} \tag{2.15}$$

In the top row of Fig. 2.3, we highlight the contributions of each ingredient towards the topological phase transition. We start from the energy dispersion of the conduction band of a one-dimensional wire with a single spin-degenerate subband (Fig. 2.3a). Then, we introduce the spin-orbit interaction, which splits the two spin subbands in the momentum space by $k_{SO} = m^*\alpha_R/\hbar^2$. In this scenario, spins are parallel and anti-parallel to the effective spin-orbit magnetic field (Fig. 2.3b). The Zeeman field splits the states at $k = 0$ opening the so-called helical gap, and tilts the spins toward the field direction [48–52]. A larger magnetic field increases the size of the helical gap and further competes with the spin-orbit field polarizing the spins along the field direction. Notably, the spin-orbit interaction vanishes at $k = 0$, where the spins are aligned to the external magnetic field (Fig. 2.3c). If the chemical potential lies inside the helical gap, and superconductivity is added into the picture, a gap is created around the Fermi energy, where superconducting pairing occurs among electrons with opposite momenta and the same spin component, creating a p-wave superconductor (Fig. 2.3d) [53].

We can follow this transition from a different perspective, that is by increasing the magnetic field in the presence of spin-orbit coupling and induced superconductivity. This in fact provides a better picture on how the electron-like and hole-like bands invert at the topological transition. At zero magnetic field, the superconducting pairing opens a

gap with size Δ around the Fermi energy (Fig. 2.3e). The magnetic field shrinks the gap (Fig. 2.3f), which eventually vanishes (Fig. 2.3g), and then reopens (Fig. 2.3h). Notably, states around $k = 0$ have switched character, with electron-like states now above and hole-like states below the Fermi energy.
This inversion of electron and hole bands corresponds to a change in the value of the topological invariant, and this transition coexists with the appearance of Majorana bound states γ_1, γ_2 at the two extremes of the wire, where the hole- and electron-like bands cross each other (Fig. 2.3i). In an infinite system, the two Majoranas are completely delocalized and do not interact. In contrast, in finite-size wires, the spatial distribution of each Majorana matters, as their characteristic length scale ξ might be comparable with their separation.

2.4. MAJORANA PROPERTIES

A generic fermionic operator a can always be written in terms of two Majorana operators γ_1 and γ_2 by distinguishing its real and imaginary parts

$$\begin{aligned} a &= \frac{1}{2}(\gamma_1 + i\gamma_2) \\ a^\dagger &= \frac{1}{2}(\gamma_1 - i\gamma_2) \end{aligned} \tag{2.16}$$

From these equations, we can derive the following properties and some relevant observations:

$$\begin{aligned} \gamma_i &= \gamma_i^\dagger \\ \{\gamma_i, \gamma_j\} &= \gamma_i\gamma_j + \gamma_j\gamma_i = 2\delta_{i,j} \end{aligned} \tag{2.17}$$

First, it turns out that the Majoranas are their own antiparticles (or in other words, γ_i is Hermitian), and second, that the two Majoranas – together – can be either filled or empty. A single Majorana is only half of a fermion, therefore it is not possible to define a Majorana number operator. Rather, the occupation of the global fermionic state is given by $n = a^\dagger a$, which can be either 0 (empty state), or 1 (filled state). For future considerations, is also useful to define the fermionic parity $P = -i\gamma_1\gamma_2$, which consequently results in ±1. Both even and odd configurations have zero energy, therefore they form a twofold degenerate ground state. A system with 4 Majoranas has a fourfold degenerate ground state, because both fermions can be either filled or empty with the same (zero) energy $P_1 = \pm 1$, $P_2 = \pm 1$. It is clear now that a system with $2N$ Majoranas (N fermions) has a ground state degeneracy of 2^N, but by fixing the overall parity, this decreases to 2^{N-1}. It turns out that Majoranas obey a non-abelian exchange statistic, and exchanging – braiding – γ_i and γ_j via the operator $U_{i,j}$ enables to switch from one ground state to another [53]

$$U_{i,j} = \frac{1}{\sqrt{2}}(1 \pm \gamma_i\gamma_j) = \frac{1}{\sqrt{2}}(1 \pm iP_{i,j}) \tag{2.18}$$

where ± differentiates between clockwise and counter-clockwise exchange. Exchanging two Majoranas in solid-state devices does not require their physical movement as suggested in early proposals [54]. Rather it can be achieved by adiabatically tuning their

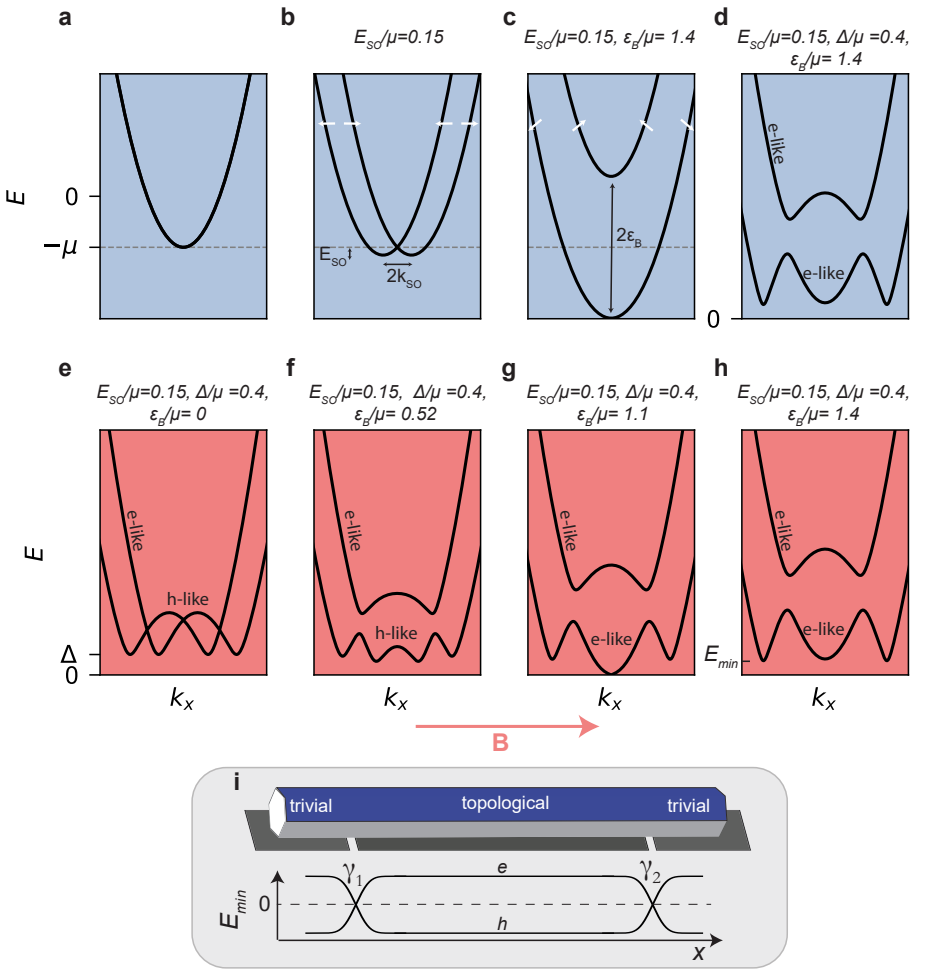

Figure 2.3: **Energy dispersion of a Majorana wire. a** Parabolic dispersion of a semiconducting wire; **b** the spin-orbit interaction splits the two spin-degenerate bands; and **c**, a magnetic field opens the helical gap around $k = 0$. **d** Superconductivity is added to the system in the spinless regime allowing p-wave pairing. In the second row, we look at the transition to this regime in a different perspective. **e** Energy dispersion of a quantum wire with induced superconductivity. We do not display the particle-hole symmetric bands at negative energy. **f** A Zeeman magnetic field splits the bands and tends to polarize the spin of the states close to $k = 0$. **g**, **h** The gap closes and reopens signalling the transition to the topological regime. These panels are calculated using realistic values for InSb/Al wires, such as $\Delta = 0.2\,\text{meV}$, and $E_{SO} = 0.07\,\text{meV}$. We also set $\mu = 0.5\,\text{meV}$ and, assuming $g = 30$, the magnetic fields of the central panels are respectively $0, 0.3, 0.62$, and $0.8\,\text{T}$. **i** Qualitative evolution of the lowest energy state (E_{min}) along a trivial-topological-trivial nanowire emphasizing the inversion of the bands. At the two zero-energy crossings, Majorana quasiparticles γ_1 and γ_2 emerge. In this illustration, a modification of the chemical potential along the wire with three bottom gates (in grey) determines the topological order.

tunnel- or Coulomb-interactions via specific sequences of operations on electrostatic gates or magnetic fluxes [55, 56].

2.5. MAJORANA QUBITS AND INTERFEROMETRIC READ-OUT

In an infinite system, the occupancy of the Majoranas comes at no energy cost, hence the twofold degeneracy of the ground state. The two degenerate states differ in the electron parity, which can be either even or odd, and therefore might form the basis of a qubit. Quantum information stored in far-away Majoranas is topologically protected against parity-preserving local perturbations, and for this reason, is considered an important pathway to a large-scale quantum computer [29, 55–59]. Another relevant property of Majorana particles is their unconventional exchange statistics [53, 60]. Rather than obeying Fermi-Dirac or Bose-Einstein statistics, they exchange according to the rules of non-Abelian anyons. In brief, this means that the order in which Majoranas are moved around determines the final state. This property results from the ground-state degeneracy and can be exploited to perform qubit manipulations [61]. Reviewing non-Abelian particles and their link with topological quantum computing is beyond the scope of this section. We instead focus on a possible implementation of a topological qubit and some of the physical requirements, which represent the cores of several experiments described in this thesis.

While several theoretical proposals have been put forward in the last decade, we concentrate on the topological qubit illustrated in Fig. 2.4a [58]. Two topological nanowire segments (TS) with length L_W are coupled by an s-wave superconductor (S) [1], and by a semiconducting reference arm (R). We suppose that the emerging Majoranas $\gamma_1, \gamma_2, \gamma_3, \gamma_4$ are far apart such that their interaction is negligible and that the coherence length (L_Φ) in the reference arm is much longer than the nanowire separation (L_R). The whole de-

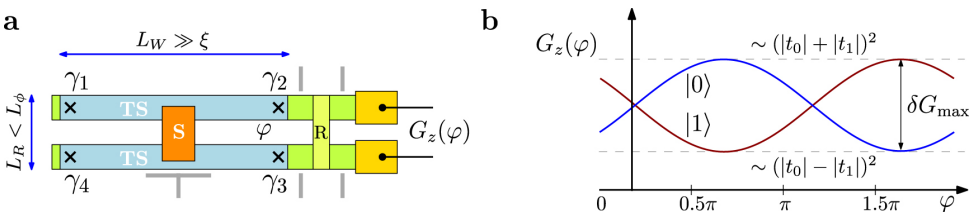

Figure 2.4: **Majorana box qubit. a** Physical implementation of the box qubit: two topological wires (TS) are connected by a superconductor (S). To evaluate the transmission phase via Majoranas γ_2 and γ_3, an interferometric circuit is realized by adding a semiconducting reference path (R) in parallel. **b** Conductance (G_z) detection as a function of the phase difference between the two paths (φ) enables to read-out the two parity states. The figure is taken from ref. [58].

vice is known as the Majorana box qubit. Its name stems from the fact that adjustable tunnel barriers (in grey) can completely isolate the two interconnected wires forming a large Coulomb-blockaded box. The finite charging energy of the system prevents extra electrons from jumping in and from flipping the total box parity (i.e., also known as quasiparticle poisoning). The global parity can be written as the product of all Majorana operators γ_i, and, in the absence of quasiparticle poisoning, is a conserved quantum

[1] It is relevant to stress that S needs to be a parity-preserving superconductor, forming a single-electron blocker, otherwise single quasiparticles can move freely flipping the parity of each topological segments. Examples of parity-preserving superconductors are Al [62], Pb [63], and Sn in the crystal phase β, which has a tetragonal tetragonal unit cell [64].

number:

$$P = \gamma_1\gamma_2\gamma_3\gamma_4 = \pm 1 \tag{2.19}$$

The 4-Majorana system can be mapped to a degenerate spin-1/2 degree of freedom, with the corresponding Pauli operators [65–68]:

$$\hat{x} = i\gamma_1\gamma_2 \qquad \hat{y} = i\gamma_3\gamma_1 \qquad \hat{z} = i\gamma_2\gamma_3 \tag{2.20}$$

The device shown in Fig. 2.4a enables the read-out of the $\hat{z}$ component, but a generalization of the circuit allows for the application of the entire set of Pauli operators [58, 59]. The qubit state can be inferred by detecting the electron tunnelling coefficients via the Majorana states and justifies the need for the reference arm. In brief, cotunnelling electrons can momentarily tunnel from a (metallic) lead in the box via γ_2 and tunnel out via γ_3. The amplitude of the process is dependent on the bilinear product $i\gamma_2\gamma_3$ accounting for the $\hat{z}$ operator [67, 68]. Hence, interferometric conductance measurements can be used to both read-out and initialize the qubit in one of the two $\hat{z}$ eigenstates. In fact, the conductance measured across the two leads is given by:

$$G(\varphi) = g_0 + i\gamma_2\gamma_3 g(\varphi) = g_0 \pm g(\varphi) \tag{2.21}$$

where g_0 is the background conductance, and $g(\varphi)$ is h/e-periodic signal in magnetic flux arising from the Aharonov-Bohm effect. At optimal magnetic flux, the two qubit states can be distinguished and mapped into a high- and a low- conductance values (Fig. 2.4b). Such projective measurements are at the core of the measurement-only quantum computing approach, where consecutive measurements project the qubit states in eigenstates of the Pauli matrices, enabling rotations of 90° in the Bloch sphere [69, 70]. A sequence of projective measurements also allows for braiding two Majoranas. The qubit state can also be read out by exploiting the interaction between the Majorana box and one (or more) quantum dot(s) embedded in the reference arm. The idea is simple: electrons from the dot can cotunnel in and out the Majorana box qubit acquiring a $\hat{z}$-dependent transmission coefficient which modifies the dot energy dispersion. This can be read-out via quantum capacitance or spectroscopy measurements.

Independently of the read-out method, realising this device presents challenges under several angles. First, a quasiparticle-protected Majorana box requires a charging energy much higher than the thermal energy, which at the base temperature of common dilution refrigerators of 20 mk is about 7 μeV. However, the charging energy scales as $\sim 1/L_W$, providing an upper bound to the Majoranas separation. Even though the unwanted Majorana overlap decreases as $e^{-2L_W/\xi}$, it is also true that ξ remains experimentally unknown, leaving open the question of whether a suitable sweet spot actually exists. One way to solve this problem is to minimise ξ by maximising the topological gap, which can be achieved by increasing Δ and E_{SO}. A second challenge is the fabrication of the device itself. While the realisation of a full qubit is still far, we will provide a method to realise the simplest qubit version, analogous to the one shown in Fig 2.4. The third challenge is to my belief the most relevant and scientifically interesting. The dilemma is the following: do experiments actually obey equation 2.21?

2.6. THE PHASE-LAPSE DILEMMA IN MAJORANA CIRCUITS

Answering this question is crucial because several topological qubit schemes rely on the one-to-one correspondence between the transmission phase and encoded fermionic parity.

Measuring the transmission phase in the topological regime requires embedding a semiconducting-superconducting segment in a two-path interferometer (Fig. 2.5a), but, from the nanofabrication perspective, this is not trivial. In fact, at the moment of writing, only one experiment of this sort has been conducted in a hybrid two-dimensional gas, and the results remain not conclusive [71]. Due to the lack of experimental observations, we review the minimal theoretical model reported in the work of Drukier *et al.* [72], which supports eq. 2.21.

The interferometer in Fig. 2.5a hosts a large semiconducting-superconducting quantum dot, which we will also refer to as a Coulomb-blockaded island. At zero magnetic field, transport through the island is mediated by Cooper pairs; thus the conductance is 2e-periodic in the gate-induced charge n_{el}. In the topological regime, charge transport is enabled by the coherent single-electron transmission via delocalized Majoranas [73–76]. Here, the transmission of the island at gate voltages between two Coulomb resonances ($E_{N_0} < eV_G < E_{N_0+1}$) can be approximated by a Breit-Wigner function:

$$T_{\sigma\sigma} = \sum_{N=N_0,N_0+1} \frac{\rho_F \lambda_{\sigma,L}(N)\lambda^*_{\sigma,R}(N)}{eV_G - E_N + i\pi\rho_F \sum_{\sigma'}\left[|\lambda_{\sigma',L}(N)|^2 + |\lambda_{\sigma',R}(N)|^2\right]} + O\left(\frac{\rho_F^2\lambda^4}{(eV_G)^2}\right) \tag{2.22}$$

where σ denotes the spin, ρ_F is the density of the states at the Fermi energy in the two leads, $\lambda_{\sigma,L}$ and $\lambda_{\sigma,R}$ represent the complex coupling of the single N-state in the wire to the left (L) and right (R) leads. When the gate voltage V_G is swept across a resonance, the transmission phase exhibits a π-shift. In between two resonances, two scenarios are possible: a phase lapse or a phase plateau (Fig. 2.5c). The first behaviour occurs when the resonances N_0 and N_0+1 have the same phase:

$$\arg\left[\lambda_{\sigma,L}(N_0)\lambda^*_{\sigma,R}(N_0)\right] = \arg\left[\lambda_{\sigma,L}(N_0+1)\lambda^*_{\sigma,R}(N_0+1)\right] \tag{2.23}$$

in contrast to the second, where the two phases differ by π:

$$\arg\left[\lambda_{\sigma,L}(N_0)\lambda^*_{\sigma,R}(N_0)\right] = \arg\left[\lambda_{\sigma,L}(N_0+1)\lambda^*_{\sigma,R}(N_0+1)\right] \pm \pi \tag{2.24}$$

To demonstrate that a Majorana wire obeys the second case, we assume that transport flows through the wire via one Bogoliubov quasiparticle close to zero energy. Its electron operator c_0 can be written in term of Bogoliubov electron- and hole-components, and Majorana operators:

$$c_0(y) = u(y)\beta_0 + v^*(y)\beta_0^\dagger = \xi_L(y)\gamma_1 + \xi_R(y)\gamma_2 \tag{2.25}$$

When the ground state parity is even, c_0 is empty, and tunnelling of an additional electron is mediated by the particle-like part of the BdG wave function [77]. On the other hand, when the parity is odd, the state is filled with one electron, and the hole-like part favours the transfer (Fig. 2.5b). Thus, we can approximate

$$\lambda_{\sigma,L,R}(2M) \propto u_\sigma(y_{L,R};2M); \quad \lambda_{\sigma,L,R}(2M+1) \propto v^*_\sigma(y_{L,R};2M+1) \tag{2.26}$$

Moreover, supposing that the coefficients u and v do not depend on the particle numbers, we can estimate the phase difference between two charge states:

$$\frac{\lambda_{\sigma,L}(2M+1)\lambda^*_{\sigma,R}(2M+1)}{\lambda_{\sigma,L}(2M)\lambda^*_{\sigma,R}(2M)} \sim \frac{u_\sigma(y_L)u^*_\sigma(y_R)}{v^*_\sigma(y_L)v_\sigma(y_R)} = \frac{1\cdot 1}{1\cdot(-1)} = -1 \tag{2.27}$$

The last identity derives from the non-locality of the Majorana wave functions ($\xi_L(y = R) = 0$, and $\xi_R(y = L) = 0$), from the fact that γ_1, γ_2 are Hermitian and from the anticommutation relations of $\beta_0, \beta_0^\dagger$. Importantly, it demonstrates that consecutive charge states have opposite tunnel couplings, and therefore, according to eq. 2.22, phase lapses should be absent. Interestingly, single-electron transfer via Majoranas has also been named

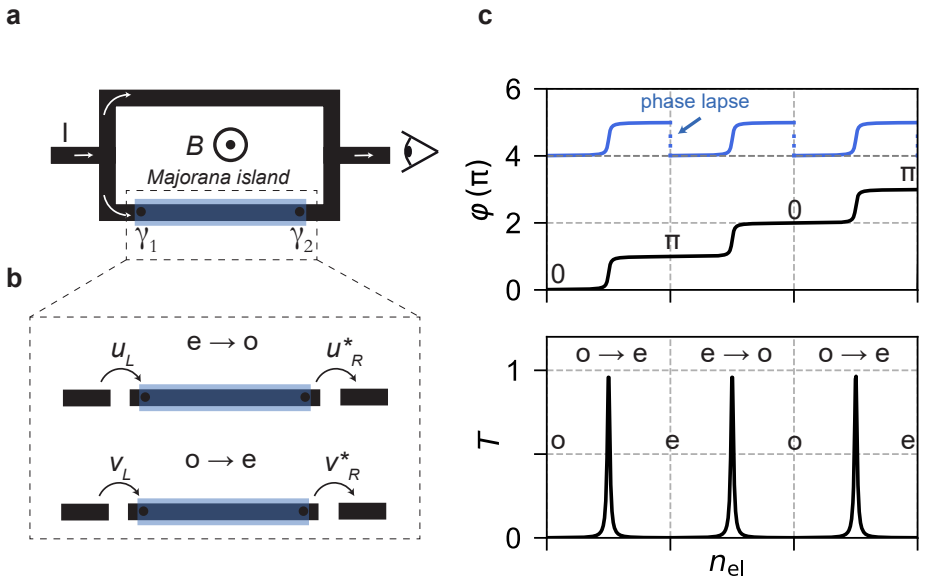

Figure 2.5: **A Majorana interferometer.** **a** A two-path interferometer (in black) with a proximitized section (in light blue) driven in the topological regime. A magnetic field perpendicular to the device plane tunes the magnetic flux enabling the study of the transmission amplitude and phase across the Coulomb-blockaded Majorana island. The two arrows illustrate the two electron paths. **b** At the charge degeneracy points (cf. resonances in panel **c**), the transition from the even (e) to the odd (o) parity ground states is mediated by the electron-like coherent factor u. In contrast, the hole-like factor v is involved in the odd-to-even transition. **c** Transmission phase (top) and amplitude (bottom) versus induced charge in the island (n_{el}). In the topological regime, the fermionic parity has a bijective relation with the transmission phase (black trace), whereas, in the trivial regime, phase lapses are expected (light-blue trace, offsetted for clarity).

teleportation because it is expected to be phase-coherent independently of the Majorana separation [73]. As a result, long Majorana islands are promising coherent links in large topological architectures [57–59].

REFERENCES

[1] L. P. Kouwenhoven, *Quantum adiabatic electron transport in ballistic conductors,* in *Physics of Low-Dimensional Semiconductor Structures*, edited by P. Butcher, N. H. March, and M. P. Tosi (Springer US, Boston, MA, 1993) pp. 463–498.

[2] T. Ihn, *Semiconductor Nanostructures* (Oxford University Press, 2010).

[3] B. J. van Wees, H. van Houten, C. W. J. Beenakker, J. G. Williamson, L. P. Kouwenhoven, D. van der Marel, and C. T. Foxon, *Quantized conductance of point contacts in a two-dimensional electron gas,* Phys. Rev. Lett. **60**, 848 (1988).

[4] D. A. Wharam, T. J. Thornton, R. Newbury, M. Pepper, H. Ahmed, J. E. F. Frost, D. G. Hasko, D. C. Peacock, D. A. Ritchie, and G. A. C. Jones, *One-dimensional transport and the quantisation of the ballistic resistance,* J. Phys. C: Solid State Phys. **21**, L209 (1988).

[5] S. J. Koester, B. Brar, C. R. Bolognesi, E. J. Caine, A. Patlach, E. L. Hu, H. Kroemer, and M. J. Rooks, *Length dependence of quantized conductance in ballistic constrictions fabricated on InAs/AlSb quantum wells,* Phys. Rev. B **53**, 13063 (1996).

[6] A. C. Ford, S. B. Kumar, R. Kapadia, J. Guo, and A. Javey, *Observation of degenerate one-dimensional sub-bands in cylindrical InAs nanowires,* Nano Lett. **12**, 1340 (2012).

[7] S. Chuang, Q. Gao, R. Kapadia, A. C. Ford, J. Guo, and A. Javey, *Ballistic InAs nanowire transistors,* Nano Lett. **13**, 555 (2013).

[8] I. van Weperen, S. R. Plissard, E. P. A. M. Bakkers, S. M. Frolov, and L. P. Kouwenhoven, *Quantized conductance in an InSb nanowire,* Nano Lett. (2013).

[9] J. Kammhuber, M. C. Cassidy, H. Zhang, m. Gül, F. Pei, M. W. A. de Moor, B. Nijholt, K. Watanabe, T. Taniguchi, D. Car, S. R. Plissard, E. P. A. M. Bakkers, and L. P. Kouwenhoven, *Conductance quantization at zero magnetic field in InSb nanowires,* Nano Lett. **16**, 3482 (2016).

[10] S. Heedt, W. Prost, J. Schubert, D. Grützmacher, and T. Schäpers, *Ballistic transport and exchange interaction in InAs nanowire quantum point contacts,* Nano Lett. **16**, 3116 (2016).

[11] Ö. Gül, D. J. van Woerkom, I. van Weperen, D. Car, S. R. Plissard, E. P. A. M. Bakkers, and L. P. Kouwenhoven, *Towards high mobility InSb nanowire devices,* Nanotechnology **26**, 215202 (2015).

[12] S. M. Sze, *Physics of semiconductor devices (2nd edition)* (Wiley, 1981).

[13] M. D. Schroer and J. R. Petta, *Correlating the nanostructure and electronic properties of InAs nanowires,* Nano Lett. **10**, 1618 (2010).

[14] A. V. Kretinin, R. Popovitz-Biro, D. Mahalu, and H. Shtrikman, *Multimode Fabry-Pérot conductance oscillations in suspended stacking-faults-free InAs nanowires,* Nano Lett. **10**, 3439 (2010).

[15] H. Shtrikman, R. Popovitz-Biro, A. V. Kretinin, and P. Kacman, *GaAs and InAs nanowires for ballistic transport,* IEEE Journal of Selected Topics in Quantum Electronics **17**, 922 (2011).

[16] N. Gupta, Y. Song, G. W. Holloway, U. Sinha, C. M. Haapamaki, R. R. LaPierre, and J. Baugh, *Temperature-dependent electron mobility in InAs nanowires,* Nanotechnology **24**, 225202 (2013).

[17] M. J. L. Sourribes, I. Isakov, M. Panfilova, H. Liu, and P. A. Warburton, *Mobility enhancement by Sb-mediated minimisation of stacking fault density in InAs nanowires grown on silicon,* Nano Lett. **14**, 1643 (2014).

[18] S. R. Plissard, D. R. Slapak, M. A. Verheijen, M. Hocevar, G. W. G. Immink, I. van Weperen, S. Nadj-Perge, S. M. Frolov, L. P. Kouwenhoven, and E. P. A. M. Bakkers, *From InSb nanowires to nanocubes: looking for the sweet spot,* Nano Lett. **12**, 1794 (2012).

[19] S. Gazibegovic, D. Car, H. Zhang, S. C. Balk, J. A. Logan, M. W. A. de Moor, M. C. Cassidy, R. Schmits, D. Xu, G. Wang, P. Krogstrup, R. L. M. Op het Veld, K. Zuo, Y. Vos, J. Shen, D. Bouman, B. Shojaei, D. Pennachio, J. S. Lee, P. J. van Veldhoven, S. Koelling, M. A. Verheijen, L. P. Kouwenhoven, C. J. Palmstrøm, and E. P. A. M. Bakkers, *Epitaxy of advanced nanowire quantum devices,* Nature **584**, 434 (2017).

[20] G. Badawy, S. Gazibegovic, F. Borsoi, S. Heedt, C.-A. Wang, S. Koelling, M. A. Verheijen, L. P. Kouwenhoven, and E. P. A. M. Bakkers, *High mobility stemless InSb nanowires,* Nano Lett. **19**, 3575 (2019).

[21] M. Levinshtein, S. Rumyantsev, and M. Shur, *Handbook Series on Semiconductor Parameters* (WORLD SCIENTIFIC, 1996).

[22] J. Shabani, M. Kjaergaard, H. J. Suominen, Y. Kim, F. Nichele, K. Pakrouski, T. Stankevic, R. M. Lutchyn, P. Krogstrup, R. Feidenhans'l, S. Kraemer, C. Nayak, M. Troyer, C. M. Marcus, and C. J. Palmstrøm, *Two-dimensional epitaxial superconductor-semiconductor heterostructures: A platform for topological superconducting networks,* Phys. Rev. B **93**, 155402 (2016).

[23] R. M. Lutchyn, E. P. A. M. Bakkers, L. P. Kouwenhoven, P. Krogstrup, C. M. Marcus, and Y. Oreg, *Majorana zero modes in superconductor–semiconductor heterostructures,* Nat. Rev. Mater. **3**, 52 (2018).

[24] I. van Weperen, B. Tarasinski, D. Eeltink, V. S. Pribiag, S. R. Plissard, E. P. A. M. Bakkers, L. P. Kouwenhoven, and M. Wimmer, *Spin-orbit interaction in InSb nanowires,* Phys. Rev. B **91**, 201413 (2015).

[25] L. D. Landau and V. Ginzburg, Zh. Eksp. Teor. Fiz. **20**, 1064 (1950).

[26] J. Bardeen, L. N. Cooper, and J. R. Schrieffer, *Theory of superconductivity,* Phys Rev **108**, 1175 (1957).

[27] M. Tinkham, *Introduction to superconductivity* (Dover Publications, 1996).

[28] S. Ryu, A. P. Schnyder, A. Furusaki, and A. W. W. Ludwig, *Topological insulators and superconductors: tenfold way and dimensional hierarchy,* New J. Phys. **12**, 065010 (2010).

[29] A. Y. Kitaev, *Unpaired Majorana fermions in quantum wires,* Phys.-Uspekhi **44**, 131 (2001).

[30] R. M. Lutchyn, J. D. Sau, and S. Das Sarma, *Majorana fermions and a topological phase transition in semiconductor-superconductor heterostructures,* Phys. Rev. Lett. **105**, 077001 (2010).

[31] Y. Oreg, G. Refael, and F. von Oppen, *Helical liquids and Majorana bound states in quantum wires,* Phys. Rev. Lett. **105**, 177002 (2010).

[32] J. Alicea, *New directions in the pursuit of Majorana fermions in solid state systems,* Rep. Prog. Phys. **75**, 076501 (2012).

[33] P. San-Jose, J. L. Lado, R. Aguado, F. Guinea, and J. Fernández-Rossier, *Majorana zero modes in graphene,* Phys. Rev. X **5**, 041042 (2015).

[34] F. Pientka, A. Keselman, E. Berg, A. Yacoby, A. Stern, and B. I. Halperin, *Topological superconductivity in a planar Josephson junction,* Phys. Rev. X **7**, 021032 (2017).

[35] S. Nadj-Perge, I. K. Drozdov, J. Li, H. Chen, S. Jeon, J. Seo, A. H. MacDonald, B. A. Bernevig, and A. Yazdani, *Observation of Majorana fermions in ferromagnetic atomic chains on a superconductor,* Science **346**, 602 (2014).

[36] H. Kim, A. Palacio-Morales, T. Posske, L. Rózsa, K. Palotás, L. Szunyogh, M. Thorwart, and R. Wiesendanger, *Toward tailoring Majorana bound states in artificially constructed magnetic atom chains on elemental superconductors,* Sci. Adv. **4** (2018).

[37] B. A. Bernevig, T. L. Hughes, and S.-C. Zhang, *Quantum spin Hall effect and topological phase transition in HgTe quantum wells,* Science **314**, 1757 (2006).

[38] J.-P. Xu, M.-X. Wang, Z. L. Liu, J.-F. Ge, X. Yang, C. Liu, Z. A. Xu, D. Guan, C. L. Gao, D. Qian, Y. Liu, Q.-H. Wang, F.-C. Zhang, Q.-K. Xue, and J.-F. Jia, *Experimental detection of a Majorana mode in the core of a magnetic vortex inside a topological insulator-superconductor* $\mathrm{bi_2te_3/nbse_2}$ *heterostructure,* Phys. Rev. Lett. **114**, 017001 (2015).

[39] N. Read and D. Green, *Paired states of fermions in two dimensions with breaking of parity and time-reversal symmetries and the fractional quantum Hall effect,* Phys. Rev. B **61**, 10267 (2000).

[40] D. J. Clarke, J. Alicea, and K. Shtengel, *Exotic non-Abelian anyons from conventional fractional quantum Hall states,* Nat. Commun. **4**, 1348 (2013).

[41] V. Mourik, K. Zuo, S. M. Frolov, S. Plissard, E. P. A. M. Bakkers, and L. P. Kouwenhoven, *Signatures of Majorana fermions in hybrid superconductor-semiconductor nanowire devices,* Science **336**, 1003 (2012).

[42] M. T. Deng, S. Vaitiekėnas, E. B. Hansen, J. Danon, M. Leijnse, K. Flensberg, J. Nygård, P. Krogstrup, and C. M. Marcus, *Majorana bound state in a coupled quantum-dot hybrid-nanowire system,* Science **354**, 1557 (2016).

[43] S. M. Albrecht, A. P. Higginbotham, M. Madsen, F. Kuemmeth, T. S. Jespersen, J. Nygård, P. Krogstrup, and C. M. Marcus, *Exponential protection of zero modes in Majorana islands,* Nature **531**, 206 (2016).

[44] F. Nichele, A. C. C. Drachmann, A. M. Whiticar, E. C. T. O'Farrell, H. J. Suominen, A. Fornieri, T. Wang, G. C. Gardner, C. Thomas, A. T. Hatke, P. Krogstrup, M. J. Manfra, K. Flensberg, and C. M. Marcus, *Scaling of Majorana zero-bias conductance peaks,* Phys. Rev. Lett. **119**, 136803 (2017).

[45] M. W. A. de Moor, J. D. S. Bommer, D. Xu, G. W. Winkler, A. E. Antipov, A. Bargerbos, G. Wang, N. van Loo, R. L. M. O. het Veld, S. Gazibegovic, D. Car, J. A. Logan, M. Pendharkar, J. S. Lee, E. P. A. M. Bakkers, C. J. Palmstrøm, R. M. Lutchyn, L. P. Kouwenhoven, and H. Zhang, *Electric field tunable superconductor-semiconductor coupling in Majorana nanowires,* New J. Phys. **20**, 103049 (2018).

[46] S. Heedt, M. Quintero-Pérez, F. Borsoi, A. Fursina, N. van Loo, G. P. Mazur, M. P. Nowak, M. Ammerlaan, K. Li, S. Korneychuk, J. Shen, M. A. Y. van de Poll, G. Badawy, S. Gazibegovic, K. van Hoogdalem, E. P. A. M. Bakkers, and L. P. Kouwenhoven, *Shadow-wall lithography of ballistic superconductor-semiconductor quantum devices,* ArXiv e-prints **2007.14383** (2020).

[47] F. Borsoi, G. P. Mazur, N. van Loo, M. P. Nowak, L. Bourdet, K. Li, S. Korneychuk, A. Fursina, E. Memisevic, G. Badawy, S. Gazibegovic, K. van Hoogdalem, E. P. A. M. Bakkers, L. P. Kouwenhoven, S. Heedt, and M. Quintero-Pérez, *Single-shot fabrication of semiconducting-superconducting nanowire devices,* ArXiv e-prints **2009.06219** (2020).

[48] P. Středa and P. Šeba, *Antisymmetric spin filtering in one-dimensional electron systems with uniform spin-orbit coupling,* Phys. Rev. Lett. **90**, 256601 (2003).

[49] Y. V. Pershin, J. A. Nesteroff, and V. Privman, *Effect of spin-orbit interaction and in-plane magnetic field on the conductance of a quasi-one-dimensional system,* Phys. Rev. B **69**, 121306 (2004).

[50] C. H. L. Quay, T. L. Hughes, J. A. Sulpizio, L. N. Pfeiffer, K. W. Baldwin, K. W. West, D. Goldhaber-Gordon, and R. de Picciotto, *Observation of a one-dimensional spin–orbit gap in a quantum wire,* Nat. Phys. **6**, 336 (2010).

[51] S. Heedt, N. Traverso Ziani, F. Crépin, W. Prost, S. Trellenkamp, J. Schubert, D. Grützmacher, B. Trauzettel, and T. Schäpers, *Signatures of interaction-induced helical gaps in nanowire quantum point contacts,* Nat. Phys. **13**, 563 (2017).

[52] J. Kammhuber, M. C. Cassidy, F. Pei, M. P. Nowak, A. Vuik, Ö. Gül, D. Car, S. R. Plissard, E. P. A. M. Bakkers, M. Wimmer, and L. P. Kouwenhoven, *Conductance through a helical state in an Indium antimonide nanowire,* Nat. Commun. **8**, 478 (2017).

[53] M. Leijnse and K. Flensberg, *Introduction to topological superconductivity and Majorana fermions,* Semicond. Sci. Technol. **27**, 124003 (2012).

[54] J. Alicea, Y. Oreg, G. Refael, F. von Oppen, and M. P. A. Fisher, *Non-Abelian statistics and topological quantum information processing in 1d wire networks,* Nat. Phys. **7**, 412 (2011).

[55] T. Hyart, B. van Heck, I. C. Fulga, M. Burrello, A. R. Akhmerov, and C. W. J. Beenakker, *Flux-controlled quantum computation with Majorana fermions,* Phys. Rev. B **88**, 035121 (2013).

[56] D. Aasen, M. Hell, R. V. Mishmash, A. Higginbotham, J. Danon, M. Leijnse, T. S. Jespersen, J. A. Folk, C. M. Marcus, K. Flensberg, and J. Alicea, *Milestones toward Majorana-based quantum computing,* Phys. Rev. X **6**, 031016 (2016).

[57] S. Vijay and L. Fu, *Teleportation-based quantum information processing with Majorana zero modes,* Phys. Rev. B **94**, 235446 (2016).

[58] S. Plugge, A. Rasmussen, R. Egger, and K. Flensberg, *Majorana box qubits,* New J. Phys. **19**, 012001 (2017).

[59] T. Karzig, C. Knapp, R. M. Lutchyn, P. Bonderson, M. B. Hastings, C. Nayak, J. Alicea, K. Flensberg, S. Plugge, Y. Oreg, C. M. Marcus, and M. H. Freedman, *Scalable designs for quasiparticle-poisoning-protected topological quantum computation with Majorana zero modes,* Phys. Rev. B **95**, 235305 (2017).

[60] D. A. Ivanov, *Non-abelian statistics of half-quantum vortices in p-wave superconductors,* Phys. Rev. Lett. **86**, 268 (2001).

[61] C. Nayak, S. H. Simon, A. Stern, M. Freedman, and S. Das Sarma, *Non-Abelian anyons and topological quantum computation,* Rev. Mod. Phys. **80**, 1083 (2008).

[62] T. M. Eiles, J. M. Martinis, and M. H. Devoret, *Even-odd asymmetry of a superconductor revealed by the Coulomb blockade of Andreev reflection,* Phys. Rev. Lett. **70**, 1862 (1993).

[63] T. Kanne, M. Marnauza, D. Olsteins, D. J. Carrad, J. E. Sestoft, J. de Bruijckere, L. Zeng, E. Johnson, E. Olsson, K. Grove-Rasmussen, and J. Nygård, *Epitaxial Pb on InAs nanowires,* ArXiv e-prints **2002.11641** (2020).

[64] M. Pendharkar, B. Zhang, H. Wu, A. Zarassi, P. Zhang, C. P. Dempsey, J. S. Lee, S. D. Harrington, G. Badawy, S. Gazibegovic, J. Jung, A. H. Chen, M. A. Verheijen, M. Hocevar, E. P. A. M. Bakkers, C. J. Palmstrøm, and S. M. Frolov, *Parity-preserving and magnetic field resilient superconductivity in indium antimonide nanowires with tin shells,* arXiv e-prints **1912.06071** (2019).

[65] B. Béri and N. R. Cooper, *Topological Kondo effect with Majorana fermions,* Phys. Rev. Lett. **109**, 156803 (2012).

[66] A. Altland and R. Egger, *Multiterminal Coulomb-Majorana junction,* Phys. Rev. Lett. **110**, 196401 (2013).

[67] L. A. Landau, S. Plugge, E. Sela, A. Altland, S. M. Albrecht, and R. Egger, *Towards realistic implementations of a Majorana surface code,* Phys. Rev. Lett. **116**, 050501 (2016).

[68] S. Plugge, L. A. Landau, E. Sela, A. Altland, K. Flensberg, and R. Egger, *Roadmap to Majorana surface codes,* Phys. Rev. B **94**, 174514 (2016).

[69] P. Bonderson, M. Freedman, and C. Nayak, *Measurement-only topological quantum computation,* Phys. Rev. Lett. **101**, 010501 (2008).

[70] P. Bonderson, M. Freedman, and C. Nayak, *Measurement-only topological quantum computation via anyonic interferometry,* Ann. Phys. **324**, 787?826 (2009).

[71] A. M. Whiticar, A. Fornieri, E. C. T. O'Farrell, A. C. C. Drachmann, T. Wang, C. Thomas, S. Gronin, R. Kallaher, G. C. Gardner, M. J. Manfra, C. M. Marcus, and F. Nichele, *Coherent transport through a Majorana island in an Aharonov–Bohm interferometer,* Nat. Commun. **11**, 3212 (2020).

[72] C. Drukier, H.-G. Zirnstein, B. Rosenow, A. Stern, and Y. Oreg, *Evolution of the transmission phase through a Coulomb-blockaded Majorana wire,* Phys. Rev. B **98**, 161401 (2018).

[73] L. Fu, *Electron teleportation via Majorana bound states in a mesoscopic superconductor,* Phys. Rev. Lett. **104**, 056402 (2010).

[74] B. van Heck, R. M. Lutchyn, and L. I. Glazman, *Conductance of a proximitized nanowire in the Coulomb blockade regime,* Phys. Rev. B **93**, 235431 (2016).

[75] R. M. Lutchyn and L. I. Glazman, *Transport through a Majorana island in the strong tunneling regime,* Phys. Rev. Lett. **119**, 057002 (2017).

[76] M. Hell, K. Flensberg, and M. Leijnse, *Distinguishing Majorana bound states from localized Andreev bound states by interferometry,* Phys. Rev. B **97**, 161401 (2018).

[77] E. B. Hansen, J. Danon, and K. Flensberg, *Probing electron-hole components of subgap states in Coulomb blockaded Majorana islands,* Phys. Rev. B **97**, 041411 (2018).

3

FABRICATION AND EXPERIMENTAL METHODS

In this chapter, we review the fabrication methods used to investigate semiconducting and proximitized nanowire devices. We divide our discussion into two parts: in the first, we discuss the fabrication methods to realise high-quality devices. In the second, we provide an overview of the electrical measurement setups.

3.1. FABRICATION METHODS

InSb nanowires employed in this thesis are grown by prof. Erik Bakkers group at the Eindhoven University of Technology. Depending on the growth mechanism (chapter 7), wires with (InP) stem and wires without stem can be respectively at max 3.5 and even > 15 μm long. Recent advancement in the stemmed wires platform enabled the synthesis of simple 2x2 nanowire networks and the formation of shadowed hybrid nanowire junctions [1]. To transfer these nanostructures onto substrates, we used micromanipulators installed in a scanning electron microscope (SEM) or under an optical microscope. In both cases, the transfer involves accurate movements with a sharp needle (tungsten or indium) that collects and breaks the vertical wires from the growth chip, and leaves them on the other substrate thanks to van der Waals forces [2]. SEM or high-resolution optical pictures allows to align and design the components of the electrical circuit via CAD software (e.g. AutoCAD). A full circuit might comprise not only ohmic contacts, gates, bond pads, and dielectric layers, but also shadowing objects employed to engineer the selective superconducting proximity effect.

3.1.1. SEMICONDUCTING NANOWIRE DEVICES

In this thesis, semiconducting nanowire devices are realised by using standard electron-beam lithography and evaporation techniques. In brief, an electron-sensitive polymer resist, such as PMMA, is spun over the chip forming a uniform layer of few hundreds of nanometers. The parts of interest on the chip are exposed to a beam of 100 kV (in a Raith EBPG 5000 or 5200 system), which weakens the chemical bonds of the exposed positive resist. After that, the chip is dipped in a solution of MIBK:IPA 1:3 for 1' where the exposed resist is dissolved, and then in pure IPA for 1' to stop the reaction. To remove organic residuals, we then expose the chip to a remote oxygen plasma for 2' at 2 mbar and 100 W. Then, we evaporate a metal (e.g. typically a double layer of Ti/Au 10/150 nm for ohmics and gates, where the Ti acts as a sticking layer), which is removed from undesired locations with the resist in a lift-off process in acetone at 50° for several hours.
InSb nanowires are surrounded by a chemically stable ~ 3 nm native oxide layer and forming high-quality and transparent metal contacts requires removing this layer with minimal damage to the crystal beneath. This can be achieved by sulfur-passivating the III-V surface for 30' in ammonium polysulfide diluted in water (1:200 $(NH_4)_2S_x : H_2O$) at 60° C, as first demonstrated for InAs nanowires [3, 4]. After the deposition of Ti/Au on a clean surface, it is preferred not to heat up the substrate to prevent diffusion of gold particles into the channel. While we did not study in detail what is the activation temperature of the process, we observed that 3 hours at 110 °C leave the wire intact and gate-tunable, but 10 minutes at 175 °C lead to largely not gate-tunable devices.
Electrostatic gating can be implemented in several ways: from the side, the top, and/or the bottom of the nanostructure. The choice really depends on the actual application. While side gates present the advantage of being easy to integrate into the fabrication of the ohmic leads, side gates can be realised in a reproducible way only at a 50 – 100 nm separation from the channel. Hence, the side-gate coupling is generally low. With top gates on 10-20 nm thin dielectrics, we can achieve the maximum coupling, but this costs some extra fabrication steps that might hinder the device yield. Bottom gates are a good compromise between the two. They provide an intermediate gate-coupling and can be

prefabricated simultaneously on several chips before the nanowire transfer. Moreover, the bottom-gate dielectric can be grown at high temperature (300 – 600 °C) via ALD or PECVD processes, whereas the growth temperature of the top-gate dielectric is limited by the activation of Au diffusion in the channel.
At the beginning of this PhD research, we focused on the implementation of top gates, because side gates were found not effective in tuning the carrier density in the large nanowires (with diameter ~ 120 nm) that compose the nano-networks employed in chapter 4. To test the fabrication recipe, quantum dot devices were fabricated as described above employing a 12 nm-Al_2O_3 global gate-dielectric layer grown at 110 °C via ALD (Figs. 3.1a, b, and c). While the doped-Si/SiOx substrate enabled global back gate functionality (Figs. 3.1d), the three top gates were used to tune local nanowire sections. Conductance traces versus the two cutter gates TG1 and TG2 and the plunger gate PG voltages exhibited sharp and low-hysteresis response (Figs. 3.1e, f and g), and enabled the definition of stable quantum dots in several nanowire devices. An alternative solution to ALD Al_2O_3 was a sputtered layer of Si_3N_4 (typically 35 nm). Results are shown in the quantum-point-contact devices in chapter 7.

3.1.2. SUPERCONDUCTING-SEMICONDUCTING NANOWIRE DEVICES

Despite the success of the ALD dielectrics on InSb nanowires, TEM experiments later revealed that proximitized InSb/Al nanowires could not withstand the not-so-high temperature of the ALD process (110 °C) [5]. The limited temperature budget stems from chemical intermixing at the InSb/Al interface which promotes the formation of compounds such as AlSb and $Al_xIn_{1-x}Sb$. Remarkably, this process is also active at room temperature and leads to the short shelf life of InSb/Al nanowires [6, 7].
For this reason, different gating strategy had to be implemented. First, we employed top gates with a room-temperature sputtered layer of Si_3N_4 (experiments in chapters 5 and 6) and then – with the introduction of our shadow-wall lithography technique – we switched to bottom gates covered by ALD grown Al_2O_3 at 300 °C (experiments in chapters 8 and 9). Here, the high-temperature process could be, in fact, carried out on the substrates without nanowires. Other standard fabrication steps such as resist baking (e.g. PMMA resist requires baking at 175 °C) had to be removed from the fabrication flow of these hybrid devices.

Phase one

At the beginning of this PhD research, InSb nanowires freshly grown on trenches were sent from Erik Bakkers' lab in Eindhoven to Chris Palmstrøm lab at UC Santa Barbara. Here, the wires were coated with Al by shadow evaporation via molecular beam epitaxy after the removal of the native oxide. Eventually, the growth chip was sent back to Eindhoven and then Delft where respectively the nanowire transfer and the final fabrication would take place (Fig. 3.2) [1]. This is, in short, the story of the nanowire devices employed in chapters 5 and 6, but also in de Moor *et al.* [8]. Despite the initial success of this approach, it turned out not to be a systematically reproducible cycle. The growth of the nanowire in trenches discussed in ref. [1] is not a trivial process, the thin Al layer is prone to oxidation, the nanowire transfer is complicated, and the nanofabrication of the few wires was intrinsically challenging. Overall, this cycle could take at best 1-2 months, and, after leaving

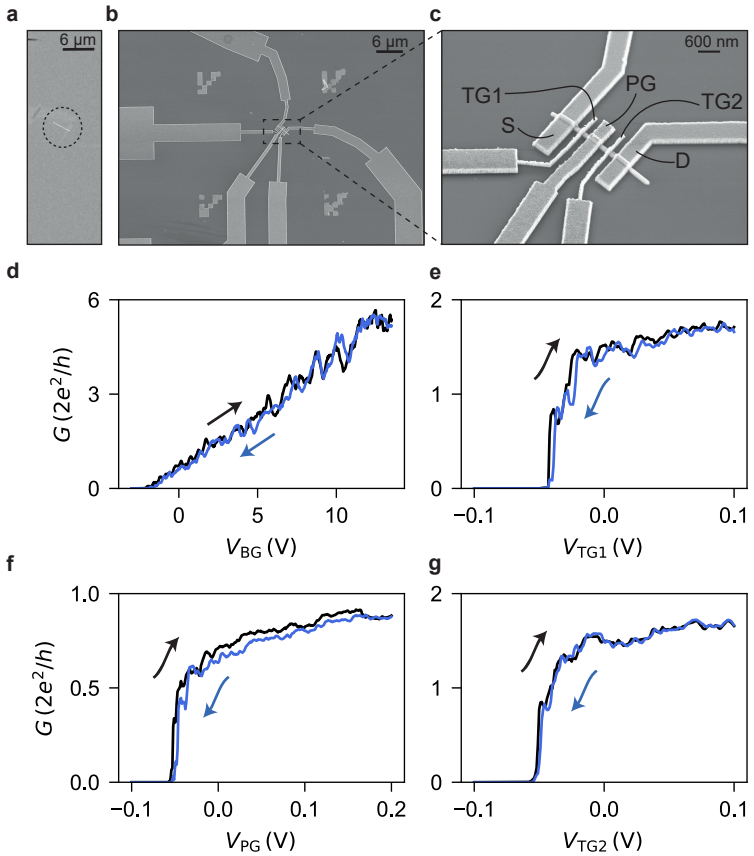

Figure 3.1: **Fabrication and characterisation of gate-tunable InSb devices.** Microscopies of a nanowire after the transfer (**a**) and after the fabrication of contacts, dielectric layer and gates (**b, c**). Conductance of the device versus global backgate voltage (V_{BG}) in **d**, cutter-gate voltages (V_{TG1} and V_{TG2}) in **e**, **g** and plunger-gate voltage (V_{PG}) in **f**. The source-drain voltage (V_{SD}) is kept at 2 mV, except for panel **f**, where it is 3 mV.

Santa Barbara, the degradation of the interface started the clock of the devices' lifetime.

Phase two

To mitigate all these problems, we developed a novel fabrication approach. The core difference with respect to the previous approach is the use of on-chip dielectric pillars rather than standing wires as shadowing objects. The goal of this section is not to review the entire process (for this, we invite the reader to study chapters 8 and 9), but instead to enlighten the differences between the two techniques. Except for the nanowire growth, the entire process takes place in Delft alleviating the need to deliver samples around the globe (Fig. 3.3). This method reduces the time and enables a rapid feedback loop between fabrication and transport measurements. Moreover, it facilitates the creation of complex devices with minimum fabrication hassle and eliminates the necessity of etching the

superconductor from the nanowire. The latter is of fundamental relevance because, in many years of intense research, a selective etching process for InSb/Al wires has not been found yet [9]. Crucially, with this technique, the realization of complex hybrid devices is now a matter of one/two days.

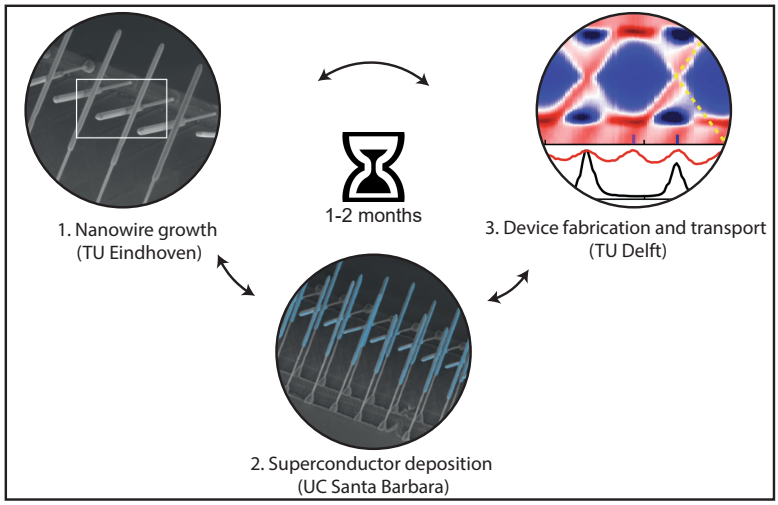

Figure 3.2: **Phase 1:** fabrication cycle of InSb/Al nanowire devices at the beginning of this PhD. Nanowires grown in trenches at the TU Eindhoven are sent to UC Santa Barbara where the native oxide is removed prior to the Al deposition (in light blue in the central panel). They are then sent back to our group at the TU Delft for transport studies. Figures are adapted from [1, 10].

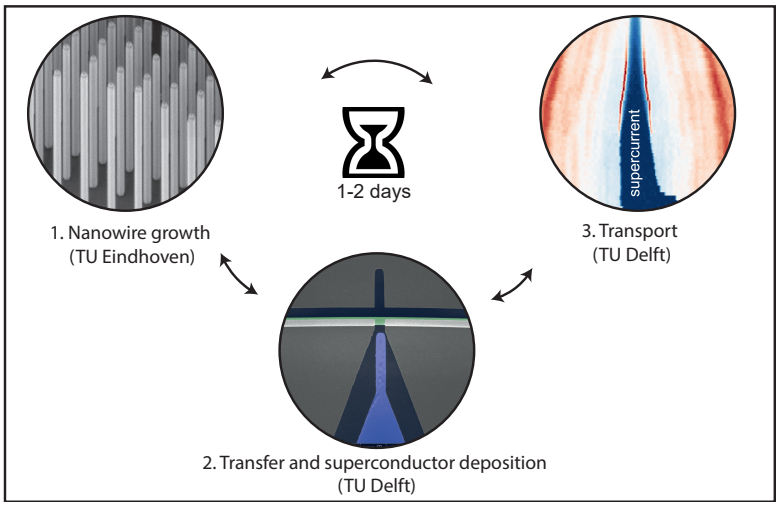

Figure 3.3: **Phase 2:** fabrication cycle of InSb/Al nanowire devices at the end of this PhD. Nanowires are grown on planar substrates at the TU Eindhoven and sent to our group at the TU Delft where are further processed to realize hybrid devices via a shadow evaporation of the superconductor (in grey in the central panel) after removal of the native oxide. Transport studies follow thereafter. Figures are adapted from [11, 12].

3.2. LOW-TEMPERATURE ELECTRICAL MEASUREMENT SETUP

Transport measurements were carried out using Oxford and Leiden Cryogenics dilution fridges. The base temperature of these refrigerators can be as low as 15 mK, with electron temperature reaching 20 – 30 mK. Several simple characterizations and test experiments were performed in dipsticks in a 4 K He_4 bath.

For electrical measurements, we always made use of the IVVI racks, which are low-noise electronic systems developed and built by the team of Raymond Schouten and DEMO at the TU Delft. Each IVVI rack comes with a series of modules such as voltage/current sources, and voltage/current detectors. IVVI racks are powered by batteries, communicate with computers for data acquisition via optical links and are linked to standard commercial electronics (e.g. Keithley 2000 multimeter, Stanford Research 830 lock-in amplifiers etc.) which are connected to computers via GPIB connection.

Most of the measurements discussed in this thesis are, in principle, relatively simple. They often involve VI (and sometimes IV) characteristics versus other parameters such as gate voltages and magnetic fields. Due to the presence of series resistances in the circuit (R_s), the applied bias voltage (V_{ap}) does not correspond directly to the source-drain voltage across the device (V_d). Therefore, the device conductance (G_d) in DC reads

$$G_d(V_{ap}) = \frac{I}{V_{ap} - IR_s} \tag{3.1}$$

where I is the current. Obviously, when $R_d = 1/G_d$ is much bigger than R_s, one can discard the line resistances, obtaining simply $G_d(V_{ap}) = \frac{I}{V_{ap}}$. In our measurement circuits, R_s is the sum of various components such as the fridge line filters (few kΩ depending on the fridge), the PCB resistors (usually 0 – 800 Ω), the input resistance of the current-measure module (that is 3 kΩ for a gain of 1MV/A in the current-measure module M1b in the low-noise setting) and the internal resistor of the voltage bias module (that is 10 – 100 Ω for the module S3B at amplifications respectively of 10mV/V and 1mV/V) [13]. Moreover, the electrical lines of the diluition fridges have three kinds of filters at the mixing chamber plate: low-pass RC-filters (<50 KHz), low-pass π-filters (<100 MHz-1GHz) and low pass Cu-powder filters (<1GHz) [13].

In our experiments, we are often interested in detecting the differential conductance $\frac{dI}{dV}$. To achieve so, we superpose to the DC bias voltage a small AC sinusoidal signal $\delta V_{ap,AC}$ of 5 – 20 μV with frequency f in the 10-90 Hz regime. The amplitude of the AC current δI_{AC} component is amplified and read-out via a lock-in amplifier that filters out the noise in the narrow band $f \pm \tau^{-1}$, where τ is the measurement integration time (typically 0.1-0.3 s) [14]. It is important to remark that – due to the finite series resistances – a good measure of the differential conductance is given by

$$\frac{dI}{dV} \sim \frac{\delta I_{AC}}{\delta V_{ap,AC} - \delta I_{AC} R_s} \tag{3.2}$$

When measuring the 'lock-in' differential conductance, it is relevant to know how to deal with systematic errors arising from complicate circuit artefacts. A complete review of the most common origins of complications is being written at the moment by components of the Topo group and soon to be published [14].

DATA AVAILABILITY

The data and the codes that create the figures in this chapter are available at https://doi.org/10.4121/13395482.v1.

REFERENCES

[1] S. Gazibegovic, D. Car, H. Zhang, S. C. Balk, J. A. Logan, M. W. A. de Moor, M. C. Cassidy, R. Schmits, D. Xu, G. Wang, P. Krogstrup, R. L. M. Op het Veld, K. Zuo, Y. Vos, J. Shen, D. Bouman, B. Shojaei, D. Pennachio, J. S. Lee, P. J. van Veldhoven, S. Koelling, M. A. Verheijen, L. P. Kouwenhoven, C. J. Palmstrøm, and E. P. A. M. Bakkers, *Epitaxy of advanced nanowire quantum devices,* Nature **584**, 434 (2017).

[2] K. Flöhr, M. Liebmann, K. Sladek, H. Y. Günel, R. Frielinghaus, F. Haas, C. Meyer, H. Hardtdegen, Th. Schäpers, D. Grützmacher, and M. Morgenstern, *Manipulating InAs nanowires with submicrometer precision,* Rev. Sci. Instrum. **82**, 113705 (2011).

[3] D. B. Suyatin, C. Thelander, M. T. Björk, I. Maximov, and L. Samuelson, *Sulfur passivation for ohmic contact formation to InAs nanowires,* Nanotechnology **18**, 105307 (2007).

[4] M. J. L. Sourribes, I. Isakov, M. Panfilova, and P. A. Warburton, *Minimization of the contact resistance between InAs nanowires and metallic contacts,* Nanotechnology **24**, 045703 (2013).

[5] S. Gazibegovic, *Bottom-up grown InSb nanowire quantum devices*, Ph.D. thesis, Department of Applied Physics (2019).

[6] F. Boscherini, Y. Shapira, C. Capasso, C. Aldao, M. del Giudice, and J. H. Weaver, *Exchange reaction, clustering, and surface segregation at the Al/InSb(110) interface,* Phys. Rev. B **35**, 9580 (1987).

[7] C. Thomas, R. E. Diaz, J. H. Dycus, M. E. Salmon, R. E. Daniel, T. Wang, G. C. Gardner, and M. J. Manfra, *Toward durable Al-InSb hybrid heterostructures via epitaxy of 2ML interfacial InAs screening layers,* Phys. Rev. Mater. **3**, 124202 (2019).

[8] M. W. A. de Moor, J. D. S. Bommer, D. Xu, G. W. Winkler, A. E. Antipov, A. Bargerbos, G. Wang, N. van Loo, R. L. M. O. het Veld, S. Gazibegovic, D. Car, J. A. Logan, M. Pendharkar, J. S. Lee, E. P. A. M. Bakkers, C. J. Palmstrøm, R. M. Lutchyn, L. P. Kouwenhoven, and H. Zhang, *Electric field tunable superconductor-semiconductor coupling in Majorana nanowires,* New J. Phys. **20**, 103049 (2018).

[9] M. W. A. de Moor, *Quantum transport in nanowire networks*, Ph.D. thesis, Delft University of Technology (2019).

[10] J. Shen, S. Heedt, F. Borsoi, B. van Heck, S. Gazibegovic, R. L. M. Op het Veld, D. Car, J. A. Logan, M. Pendharkar, S. J. J. Ramakers, G. Wang, D. Xu, D. Bouman, A. Geresdi, C. J. Palmstrøm, E. P. A. M. Bakkers, and L. P. Kouwenhoven, *Parity transitions in the superconducting ground state of hybrid InSb-Al Coulomb islands,* Nat. Commun. **9**, 4801 (2018).

[11] G. Badawy, S. Gazibegovic, F. Borsoi, S. Heedt, C.-A. Wang, S. Koelling, M. A. Verheijen, L. P. Kouwenhoven, and E. P. A. M. Bakkers, *High mobility stemless InSb nanowires,* Nano Lett. **19**, 3575 (2019).

[12] S. Heedt, M. Quintero-Pérez, F. Borsoi, A. Fursina, N. van Loo, G. P. Mazur, M. P. Nowak, M. Ammerlaan, K. Li, S. Korneychuk, J. Shen, M. A. Y. van de Poll, G. Badawy, S. Gazibegovic, K. van Hoogdalem, E. P. A. M. Bakkers, and L. P. Kouwenhoven, *Shadow-wall lithography of ballistic superconductor-semiconductor quantum devices,* ArXiv e-prints **2007.14383** (2020).

[13] R. Schouten, *Qt designed instrumentation,* http://qtwork.tudelft.nl/ schouten/ivvi/index-ivvi.htm (2020).

[14] M. d. M. Guanzhong Wang, Jouri Bommer, *Notes on transport measurements using a lock-in,* Forum Kavli TuDelft (retrieved on date June 2020).

4

TRANSMISSION PHASE READ-OUT OF A LARGE QUANTUM DOT IN A NANOWIRE INTERFEROMETER

The world makes room for passionate people.

Lewis Howes

Detecting the transmission phase of a quantum dot via interferometry can reveal the symmetry of the orbitals and details of electron transport. Crucially, interferometry will enable the read-out of topological qubits based on one-dimensional nanowires. However, measuring the transmission phase of a quantum dot in a nanowire has not yet been established. Here, we exploit recent breakthroughs in the growth of one-dimensional networks and demonstrate interferometric read-out in a nanowire-based architecture. In our two-path interferometer, we define a quantum dot in one branch and use the other path as a reference arm. We observe Fano resonances stemming from the interference between electrons that travel through the reference arm and undergo resonant tunnelling in the quantum dot. Between consecutive Fano peaks, the transmission phase exhibits phase lapses that are affected by the presence of multiple trajectories in the interferometer. These results provide critical insights for the design of future topological qubits.

This chapter has been published as, F. Borsoi, K. Zuo, S. Gazibegovic, R. L. M. Op het Veld, E. P. A. M. Bakkers, L. P. Kouwenhoven, and S. Heedt, *Transmission phase read-out of a large quantum dot in a nanowire interferometer*, Nature Communications 11, 3666 (2020) [1].

4.1. INTRODUCTION

Similar to a light wave, an electron wave acquires a phase when interacting with a scattering centre. Studying this effect requires an interferometer with phase-coherent transport such as semiconducting or metallic rings [2–4]. In these nanostructures, the phase difference between the two paths ($\Delta\varphi$) can be tuned by a magnetic flux via the Aharonov-Bohm (AB) effect:

$$\Delta\varphi = 2\pi\frac{\Phi_B}{\Phi_0} \tag{4.1}$$

with Φ_B the magnetic flux through the interferometer and $\Phi_0 = h/e$ the flux quantum. When the scattering centre is a quantum dot (QD), as depicted in Fig. 4.1a, the transmission phase φ provides information complementary to the transmission probability $T = |t|^2$, with t the transmission amplitude $t = \sqrt{T}e^{i\varphi}$. It can reveal insights into microscopic details of electron transport and into the spatial symmetries of the orbitals [5–8]. Recently, theoretical proposals suggested using interferometry as a read-out method of

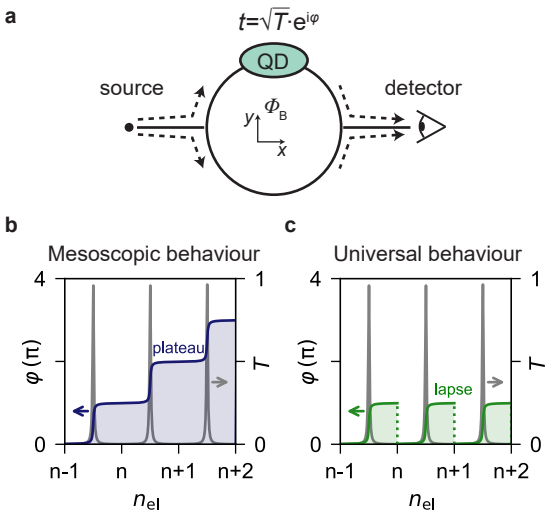

Figure 4.1: Mesoscopic and universal phase behaviours. **a** The minimum setup to study the transmission phase via a quantum dot (in light green) is a two-path interferometer. **b**, **c** Transmission phase φ and probability T as a function of the electron number n_{el} in a quantum dot. A Breit-Wigner function describes each of the resonances (in grey). **b** The mesoscopic regime: phase plateaus in the Coulomb valleys appear at 0 and π. **c** The universal regime: phase lapses occur between transmission resonances.

topological qubits, where quantum information is encoded in the electron parity of Majorana modes in semiconducting-superconducting nanowires [9–15]. Here, opposite qubit states are characterised by different transmission phases similar to the mesoscopic phase behaviour observed in few-electron quantum dots (Fig. 4.1b) [16–19]. When Majorana modes are absent, the phase is expected to exhibit the universal behaviour detected in many-electron quantum dots. In these systems, abrupt phase lapses break the simple parity-to-phase relation (Fig. 4.1c) [6, 19–23].

Despite the critical application in topological qubits, the phase read-out of a quantum dot in a nanowire interferometer has not been demonstrated yet. While pioneering works employed two-dimensional electron gases [19–21, 23], here we take advantage of the recent advances in the growth of nanowire networks [24, 25] and demonstrate interferometric read-out of a quantum dot defined in a nanowire. Our findings provide crucial insights for future topological qubits based on hybrid one-dimensional nanowire systems.

4.2. COTUNNELLING AHARONOV-BOHM INTERFERENCE

Our device is shown in Fig. 4.2a and consists of a hashtag-shaped network of hexagonal InSb nanowires of high crystalline quality [25]. In the top-right arm, negative voltages (V_{T1} and V_{T2}) on the top gates, T1 and T2, create two tunnel barriers that define an X-shaped quantum dot (pink region). The voltage on the plunger gate PG (V_{PG}) tunes its electron occupation. Likewise, the transmission in the bottom-left branch – the reference arm – can be varied from pinch-off to the open regime by adjusting the voltage V_{RG} on the reference gate (RG). The p-doped-Si/SiO_x substrate allows global back-gate (BG) functionality. A DC bias voltage with a small AC excitation, $V_{SD} + \delta V_{AC}$, is applied between source and drain, yielding a current $I + \delta I_{AC}$. Both the DC current and the differential conductance $G = \delta I_{AC}/\delta V_{AC}$ are measured in a dilution refrigerator with an electron temperature of $T_{el} \sim 35\,\mathrm{mK}$ at its base temperature. When the QD is not defined, the conductance at zero bias voltage displays Aharonov-Bohm oscillations as a function of the magnetic field perpendicular to the substrate ($B_\perp$) with period $\Delta B_\perp \sim 16 - 20\,\mathrm{mT}$ (Fig. 4.2b). This periodicity corresponds to a loop area of $\Phi_0/\Delta B_\perp \sim 0.21 - 0.26\,\mu\mathrm{m}^2$, which is consistent with the actual area of the device of $\sim 0.23\,\mu\mathrm{m}^2$ measured up to the centre of the nanowires.

When the quantum dot is defined, we adjust the plunger-gate voltage between two resonances, as indicated by the red arrow in Fig. 4.2c, where the horizontal axis is the QD electrochemical potential ($E_{QD} = e \cdot \alpha \cdot V_{PG}$, with α the lever arm and e the electron charge). In this regime, the electron-electron repulsion in the dot suppresses the current almost completely, which is known as Coulomb blockade. Transport is then allowed only via virtual, higher-order processes. At zero bias, elastic cotunnelling is predominant and its phase coherence is critical for parity-protected read-out schemes of Majorana wires [14, 15].

When we balance the current distribution in the two arms of our device, the AB oscillations in the cotunnelling regime become visible with an amplitude of $\sim 20 - 30\%$ of the average conductance (Fig. 4.2d). The large visibility demonstrates that cotunnelling across the large Coulomb-blockaded dot is phase-coherent, fulfilling a fundamental requirement of future parity read-out circuits.

4.3. FROM COULOMB TO FANO RESONANCES

In order to characterize the quantum dot, we first pinch off the reference arm. The green trace in Fig. 4.3a displays a series of nearly equally spaced conductance peaks stemming from tunnelling via the dot. Their separation is also known as the addition energy and arises from two effects: the quantum confinement and the Coulomb interaction [26]. In a large dot, the second effect dominates over the first, leading to a series of peaks that are

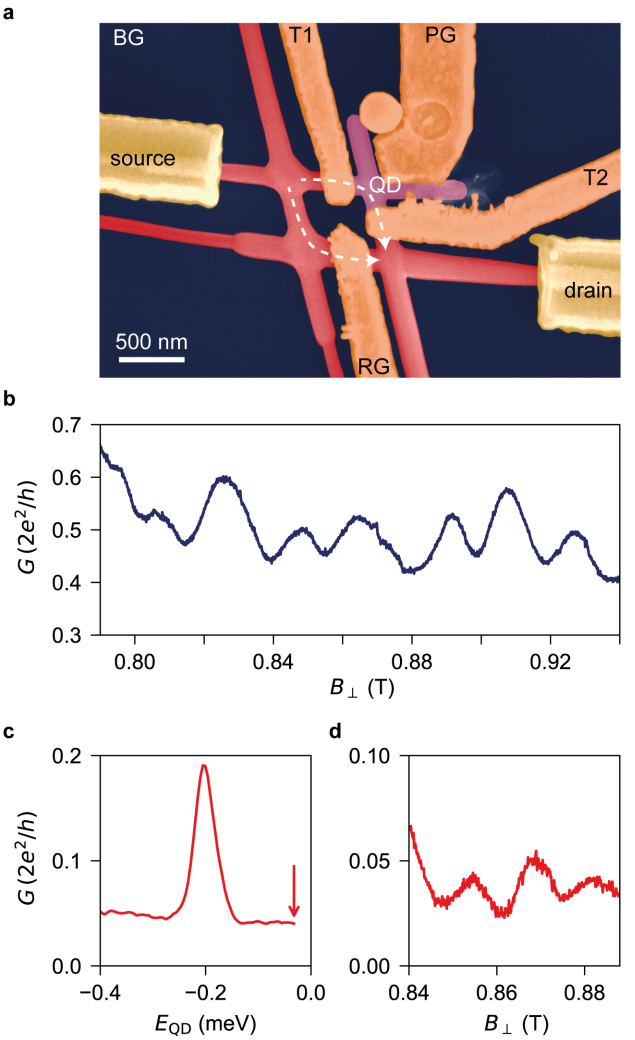

Figure 4.2: Aharonov-Bohm oscillations in an InSb nanowire network. **a** False-colour scanning electron micrograph of the device: in red the nanowire network, in gold the leads, in orange the gates and in pink the quantum dot region. An additional illustration and a schematic of the device are shown in the Methods. **b** Conductance at zero bias voltage $G(V_{SD} = 0)$ as a function of the perpendicular field $B_\perp$ in the open regime (i.e., with no QD defined) manifesting AB oscillations. **c** $G(V_{SD} = 0)$ vs. E_{QD} (the dot electrochemical potential) when the quantum dot is defined. **d** $G(V_{SD} = 0)$ vs. $B_\perp$ when the dot is in the cotunnelling regime (cf. Coulomb valley indicated by the red arrow in panel **c**).

equidistant [26, 27]. From the bias spectroscopy in Fig. 4.3b, we estimate the Coulomb charging energy $E_c = e^2/C \sim 0.35 - 0.45$ meV (with C the overall capacitance) and the level spacing due to confinement $\delta \sim 0.020 - 0.035$ meV. We evaluate the first parameter from the size of the diamonds in bias voltage, and the second from the separation between the

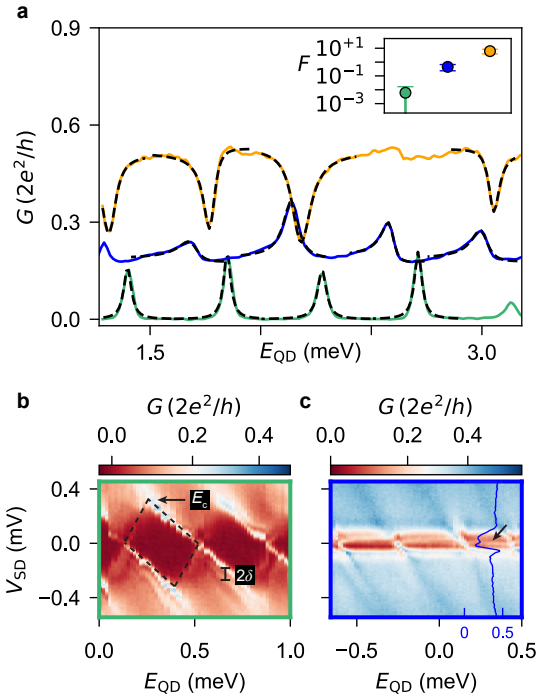

Figure 4.3: From Coulomb to Fano resonances. **a** Differential conductance G as a function of E_{QD} with the reference arm fully pinched-off (green trace), partially conducting (blue trace) and transparent (orange trace). Dashed lines are best fits. Inset: Fano parameter $F = t_{ref}/\sqrt{J_L J_R}$, averaged across four peaks in each of the three regimes. **b**, **c** G versus E_{QD} and V_{SD} in the first and second regime, respectively. The blue line-cut in **c** is taken at $E_{QD} = 0.32$ meV, the blue values on the horizontal axis refer to conductance G in $2e^2/h$. In **b**, E_c indicates the charging energy (at the apex of the diamond) and δ denotes the level spacing due to quantum confinement.

lines that confine the Coulomb diamonds and the lines that are due to the excited states. The large ratio of $E_c/\delta \gg 1$ indeed arises from the large size of the dot, which is designed to be comparable with the typical micron-long semiconducting-superconducting dots of near-future explorations [28–30]. Assuming a typical open-channel electron density of $2\cdot10^{17}\,\mathrm{cm}^{-3}$ [31] and the dot volume of $1.4\cdot10^{-2}\,\mu\mathrm{m}^3$, we estimate the maximum number of electrons on the QD to be $\sim 1-3\cdot10^3$.

We now start to activate transport in the reference arm. Upon increasing its transparency, the Coulomb peaks first evolve into the asymmetric peaks of the blue trace and then into the dips in the orange one of Fig. 4.3a. The variation of their line-shapes stems from the Fano effect, a phenomenon observed in multiple contexts in physics: from Raman scattering [32, 33] to photon absorption in quantum-well structures [34, 35], from transport in single-electron transistors [36] to Aharonov-Bohm interferometers [37–42]. The effect originates from the interference between two partial waves: one is undergoing a resonant scattering and the other is travelling through a continuum of states. In our experiment, the first is mediated by the discrete dot spectrum provided by Coulomb

blockade and confinement, and the second by the continuum of the density of states in the reference path. Bias spectroscopy with the reference path being partially conducting – similarly to the blue trace in Fig. 4.3a – shows Fano peaks extending into the Coulomb valleys at $V_{SD} \sim 0\,\text{mV}$ (cf. black arrows in Fig. 4.3c). To the best of our knowledge, this is the first observation of Fano physics in a nanowire-based interferometer.
To distinguish the three regimes of Fig. 4.3a, we fit the line-shapes of the peaks using a generalized Fano model [38]. The relevant ingredients are the coupling terms between the dot and the two leads (J_L and J_R), the transmission through the reference arm (t_{ref}) and the magnetic flux through the ring (Φ_B). A schematic illustration and more information are shown in the Methods and the result of the fits are listed in Tables 4.1, 4.2 and 4.3.
We extract the Fano parameter $F = t_{ref}/\sqrt{J_L J_R}$ from each peak (or dip). The inset of Fig. 4.3a shows that the averages of F across each trace extend over three orders of magnitude, reflecting the large tunability of the device.

4.4. THE UNIVERSAL PHASE BEHAVIOUR

Upon sweeping the magnetic field, the Fano line-shapes vary periodically owing to the Aharonov-Bohm effect. In particular, Fig. 4.4a shows that two adjacent Fano resonances evolve in-phase.
We use the model described above to fit both peaks as a function of magnetic field, and we illustrate the result in Fig. 4.4b. The model captures well the main features of the experimental data, and the good agreement is visible in the line-cuts presented in Fig. 4.4c. Here, the three traces are taken at the positions denoted by the black, red, and green lines in both panels a and b. A π-shift in the AB oscillations is visible between both the black and red as well as the red and green traces. The complete evolution of the phase φ as a function of E_{QD} is extracted by tracking the maximum of the AB pattern and shown in the top panel of Fig. 4.4d. In the bottom panel, we present horizontal line-cuts of Figs. 4.4a and 4.4b at the positions indicated by the coloured lines.
Here, we observe two main features: a phase variation of π at the resonances over an energy scale similar to the broadening of the peaks, and a phase lapse in the Coulomb valley. These are distinctive features of the universal phase behaviour and are consistent with the in-phase evolution of the two adjacent CPs in Fig. 4.4a [6, 19–22]. The observation of the universal rather than the mesoscopic behaviour can be explained by taking a look at the energy scales of the transport. In our measurement, the typical dot coupling energy ($\Gamma = \sqrt{|J_L J_R|} \sim 0.1\,\text{meV}$) is a few times larger than the level spacing in the dot ($\delta \sim 0.02 - 0.035\,\text{meV}$). Therefore, tunnelling occurs via multiple dot-levels, a condition for which theory predicts the observation of the universal behaviour [6, 22].
Because previous experiments focused on the single-level regime ($\Gamma < \delta$) [19–21] and in the crossover ($\Gamma \sim \delta$) [23], finding both phase lapses and phase plateaus, our investigation in the fully multi-level regime ($\Gamma \gg \delta$) seems to complete the complex dot-interferometry puzzle.

4.5. MULTI-PATH TRANSPORT EFFECTS

In the following, we highlight that an optimal read-out of the transmission phase requires an interferometer close to the one-dimensional limit in the sense that it shoud comprise

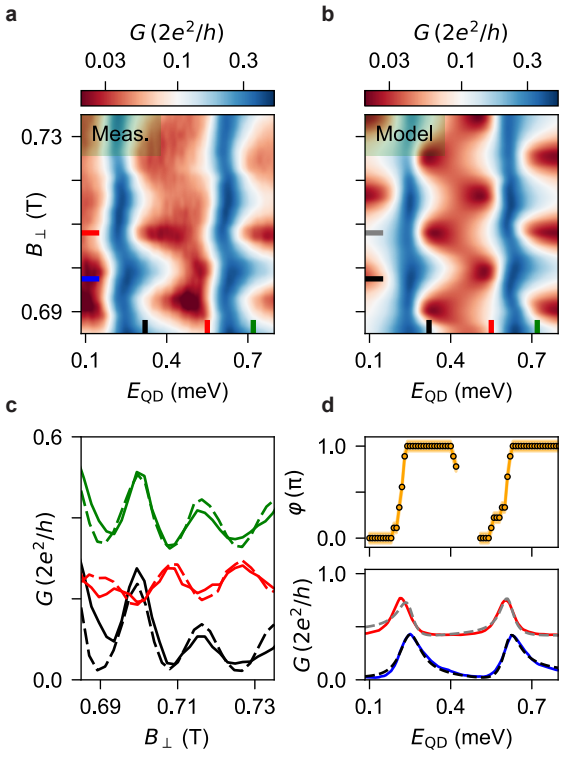

Figure 4.4: The universal phase behaviour. **a** G versus E_{QD} and $B_\perp$ at zero bias voltage, describing the evolution of two adjacent Coulomb peaks as a function of magnetic field. Data are taken at back-gate voltage $V_{BG} = 1.5\,V$. **b** Fit of the data in panel **a**. **c** Solid and dashed traces are vertical line-cuts from panels **a** and **b**, respectively, indicated by black, red, and green lines. The three pairs of curves are displaced by an offset of $0.15 \cdot 2e^2/h$ for clarity. **d** Bottom panel: solid and dashed lines are horizontal line-cuts of panels **a** and **b**, respectively, at the positions indicated by the blue/black and red/grey lines. Top panel: transmission phase φ extracted from the AB pattern. The shaded region indicates the error bars that stem from the uncertainty in extracting the oscillation maxima that is $\sim 1-2\,mT$.

thin nanowires enclosing a relatively large hole. For a gate configuration different from the previous regime, the transmission phase varies smoothly between several pairs of adjacent CPs. Here, the phase displays a behaviour in between the universal and the mesoscopic regimes (Fig. 4.5a). The two configurations differ in the back-gate voltage that has been lowered from $V_{BG} = 1.5\,V$ in Fig. 4.4 to $V_{BG} = -1.5\,V$ in Fig. 4.5. Voltages on the tunnel gates are also re-adjusted to retain a similar transmission, whereas the plunger gate remains at $V_{PG} \sim 0\,V$. We estimate a reduction of the electron density by no more than $\sim 20\%$ compared to the first case, leaving the dot still in the many-electron regime (see Figure 4.8).

In Fig. 4.5a, we show a color map of G vs. E_{QD} and $B_\perp$, exhibiting the evolution of 4 CPs. The red features in the cotunnelling regions oscillate as a function of $B_\perp$ owing to the AB

effect. Several vertical line-cuts are shown in Fig. 4.5c. The maxima of the AB oscillations around $B_\perp \sim 0.68\,\mathrm{T}$ are converted into transmission phase via the magnetic field period (here $\Delta B_\perp = 19\,\mathrm{mT}$) and displayed in the top panel of Fig. 4.5d. In the bottom panel of Fig. 4.5d, we show a horizontal line-cut taken at the position indicated by the blue line in Fig. 4.5a. Similar to the data in Fig. 4.4, the phase exhibits a $\sim \pi$ variation concomitant with the peak in the conductance. However, the phase lapse in the Coulomb valley is replaced by a smooth evolution. This slow phase variation is not universal, but depends on the specific gate setting.

We interpret this anomaly as a consequence of the relatively large width of the nanowires ($\sim 100 - 150\,\mathrm{nm}$). Microscopically, we speculate that consecutive charge states might not couple to the same loop trajectory. The presence of at least two paths gives rise to beatings in the magneto-conductance that conceal the evolution of the transmission phase [38]. Our interpretation is well-supported by the large width of the Aharonov-Bohm peak in the Fourier spectrum shown in Fig. 4.9.

While in reality multiple trajectories could couple to each QD orbital, we reproduce our observation in the model by linking each resonance to a possibly different AB periodicity. This simple assumption enables to capture the main features of the measurement (Fig. 4.5b).

The coexistence of the two distinct phase behaviours (Fig. 4.4 vs. Fig. 4.5) in the same mesoscopic device is hard to fully explain, and might be correlated with the exact coupling mechanism between the dot orbitals and the leads.

4.6. DISCUSSION

In summary, we report interferometric measurements on a quantum dot embedded in a network of four conjoint InSb nanowires. The observation of pronounced quantum interference in the cotunnelling regime and the presence of Fano resonances suggest that interferometry is a viable tool for parity read-out of future topological qubits in nanowire networks. Theory suggests that the transmission probability of a semiconducting-superconducting quantum dot in the topological regime should exhibit phase plateaus [16, 17]. However, transmitting channels other than the teleportation via Majorana bound states were not taken into account. In experiments, extended topologically trivial modes without an underlying topological bulk phase can mimic Majoranas. Hence, quasiparticle transport via these modes might offer parallel paths to the Majorana teleportation [43, 44]. Altogether, these can cause phase lapses that hinder the simple correspondence between the transmission phase and the electron parity. We conclude by remarking that future interferometers for parity-state discrimination via phase read-out should be designed with a large ratio between circumference and nanowire diameter.

AUTHOR CONTRIBUTIONS

F.B., K.Z. and S.H. fabricated the devices. F.B., S.H. and K.Z. performed the measurements. F.B. analysed the transport data. F.B., S.H. and L.P.K. discussed the results. S.G. and R.L.M.O.h.V. carried out the growth and the transfer of the interconnected InSb nanowires under the supervision of E.P.A.M.B.. F.B. wrote the manuscript with contributions from S.H. and all authors provided critical feedback. S.H. and L.P.K. supervised the project.

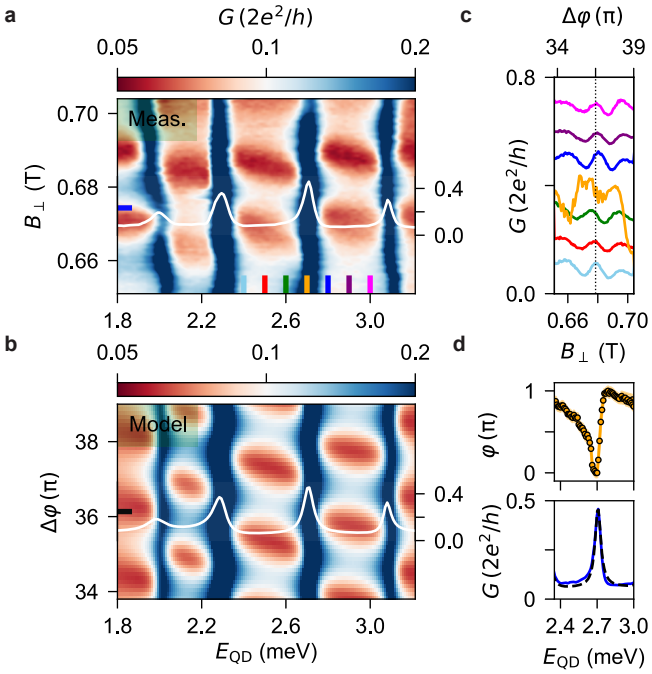

Figure 4.5: Multi-path transport effects. **a** G vs. E_{QD} and $B_\perp$ exhibiting the evolution of four CPs. Data are taken at back-gate voltage $V_{BG} = -1.5$ V. **b** Calculated conductance assuming a multi-path interferometer, details are reported in the Methods. The white traces in **a** and **b** correspond to the values indicated by the horizontal lines, and the vertical axes refer to conductance G in $2e^2/h$. **c** Vertical line-cuts of panel **a** showing the evolution of AB oscillations across a charge transition in the QD. Traces are displaced by $0.1 \cdot 2e^2/h$ for clarity, except for the orange one taken on resonance. **d** Top panel: the trend of the AB maxima across the third CP. The shaded region indicates the error bars stemming from the uncertainty in extracting the oscillation maxima that is $\sim 1-2$ mT. Bottom panel: solid and dashed lines are horizontal line-cuts of panels **a** and **b**, respectively, at the position indicated by the blue/black lines.

DATA AVAILABILITY

The data and the codes that create the figures in this chapter are available at https://doi.org/10.4121/uuid:9e625b55-11cf-4de2-8b81-32b5bf04d53d.

4.7. METHODS

DEVICE FABRICATION

InSb networks are grown by combining the bottom-up synthesis of four monocrystalline nanowires and the accurate positioning of the nanowire seeds along trenches on an InP substrate. Further details on the nanowire growth are presented in refs. [24] and [25].
After the growth, we transfer nanowire networks from the InP growth chip onto a p-doped Si/SiO_x substrate (oxide thickness of 285 nm) using a mechanical nanomanipulator installed in a scanning electron microscope. Ti/Au contact leads are patterned using electron-beam lithography and e-gun evaporation, following surface treatment of the InSb for 30 minutes in a sulfur-rich ammonium polysulfide solution diluted in water (1 : 200) at 60°C. The devices are covered with ~ 30 nm of sputtered Si_xN_y acting as a gate dielectric. The second layer of Ti/Au electrodes is patterned and evaporated to define the top gates. The chip is then diced, mounted and bonded onto a commercial printed circuit board.

TRANSPORT MEASUREMENTS

The device is cooled down in a dry dilution refrigerator equipped with a 6-2-2 T vector magnet. The base electron temperature is $T_{el} \sim 35$ mK. Conductance across the device is measured via a standard low-frequency lock-in technique at an AC signal amplitude of $\delta V_{AC} \sim 20\,\mu$V. The data presented so far and in Figures 4.8, 4.9, and 4.10 are taken from a single device. In the Supplementary Information, Figures 4.11 and 4.12, we present data taken from a second and third device, respectively. The AC conductance in Figs. 4.2, 4.3, 4.4, and 4.10 was corrected for a constant offset that was later identified to arise from the setup.

MODEL OF THE AHARONOV-BOHM INTERFEROMETER

The Landauer formula ($G = (2e^2/h) \cdot T$) connects the single-channel conductance of the system with the transmission probability T. In Fig. 4.6, we show a schematic of the multi-path Aharonov-Bohm interferometer (a simple generalization of the single-path counterpart) next to an illustration of the actual device. The QD electrochemical potential ladder is represented as a series of discrete states, separated by the charging energy $E_c = e^2/C$ [27]. For the single-path case, hopping terms J_L and J_R couple the source (L) and drain (R) to the QD, respectively, with the Aharonov-Bohm phase included in $J_L = j_L \cdot \exp(i2\pi\Phi_B/\Phi_0)$, and j_L and J_R being real parameters. Φ_B is the magnetic flux through the loop. When multiple-path are considered, we define the phase of J_L as $2\pi\Phi_B/\Phi_0[1 + x(n)]$, with the parameter $x(n)$ distinct for every CP.

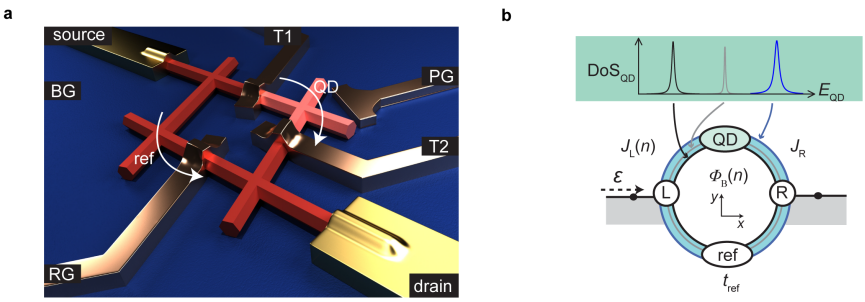

Figure 4.6: The multi-path interferometer. **a** Illustration of the device: in red the nanowire, in gold the leads, in copper the gates and in pink the quantum dot. **b** Schematic of the device: the quantum dot exhibits a density of states ($\mathrm{DoS_{QD}}$) comprised of discrete levels with distinct energy broadening. In the model, we assume that the dot states might couple to different interferometer trajectories that are sketched as rings of different colour.

The reference site has a slowly varying spectrum that we will assume for simplicity to be constant. The leads are assumed to be one-dimensional (lattice constant a) with hopping matrix elements $-J$ and a typical energy dispersion of $\varepsilon = -2J\cos(ka)$. The resulting transmission probability T through the AB interferometer is [38]:

$$T = \frac{4|S_{\mathrm{LR}}|^2 \cdot \sin^2(ka)}{\left||S_{\mathrm{LR}}|^2 - (S_{\mathrm{LL}} + e^{-ika})(S_{\mathrm{RR}} + e^{-ika})\right|^2} \tag{4.2}$$

with

$$S_{XY} = \sum_{n=0}^{N} \frac{J_{\mathrm{X}}(n) J_{\mathrm{Y}}(n)^*}{J\left(\varepsilon - E_{\mathrm{QD}} + E_{\mathrm{n}}\right)} + t_{\mathrm{ref}} \tag{4.3}$$

where E_{n} represent the positions of the N levels relevant in the tunnelling process on the E_{QD}-axis. For the fit of our results, we add an offset to eq. (4.2) to capture the incoherent contribution of the current through the device.

4.8. SUPPLEMENTARY INFORMATION

4.8.1. TRANSFER OF NANOWIRE NETWORK DEVICES

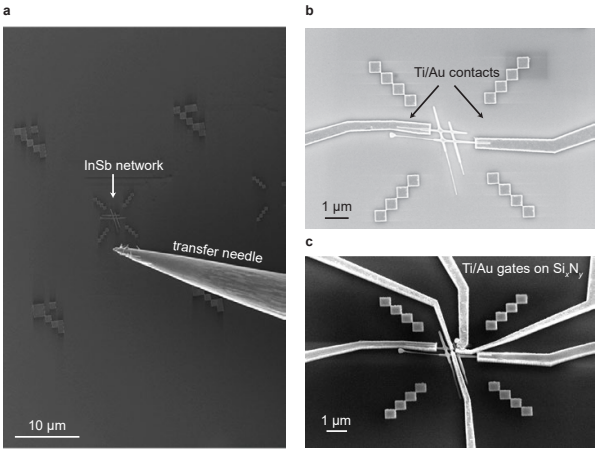

Figure 4.7: Transfer of the InSb nanowire networks. **a** Mechanical transfer of a nanowire network with a nanomanipulator in a scanning electron microscope. The device is placed in the vicinity of pre-patterned alignment markers. **b**, **c** Scanning electron micrographs of the device after the fabrication of the Ti/Au contacts and the Ti/Au top gates that are deposited onto a dielectric layer of Si_xN_y, respectively.

4.8.2. BACK-GATE DEPENDENCE

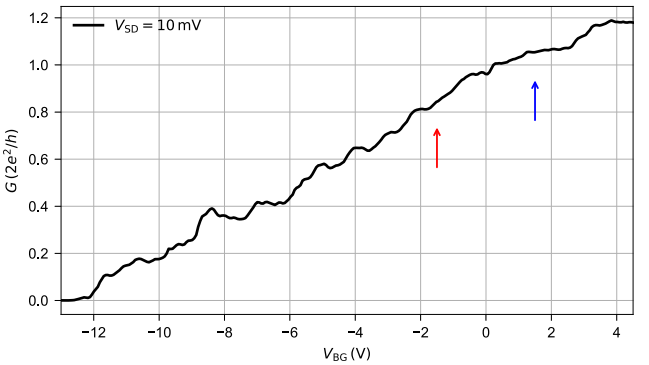

Figure 4.8: G vs. V_{BG} at 10 mV bias voltage. The conductance increases linearly with respect to the global back gate in agreement with the Drude model. The blue and red arrows at 1.5 V and −1.5 V, respectively, indicate the two working points at which the data are taken. In the second case, the electron density (roughly proportional to the conductance) is only ~ 20% lower than in the first case. Therefore, we can conclude that the quantum dot is in both cases in the many-electron regime.

4.8.3. FOURIER SPECTRUM OF THE MAGNETO-CONDUCTANCE OSCILLATIONS

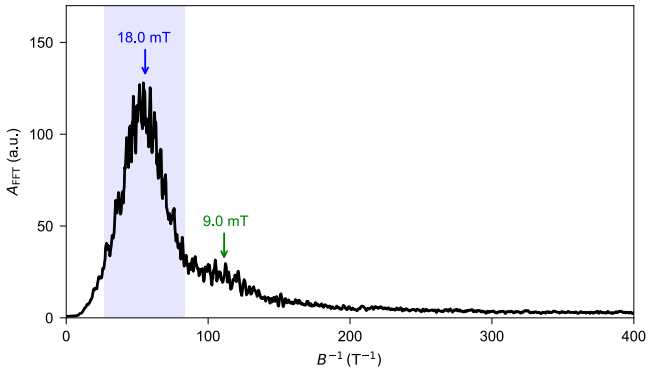

Figure 4.9: Averaged Fourier spectrum of the magneto-conductance oscillations. Eight different magneto-conductance traces are measured and filtered with the Savitzky-Golay algorithm to remove slow oscillations such as universal conductance fluctuations. The Fourier transforms are then calculated and averaged to obtain the trace in the figure. The light blue window identifies the width of the spectrum expected from the area enclosed by the loop. The peak maximum at $55\,\mathrm{T}^{-1}$ corresponds to the Aharonov-Bohm periodicity of 18 mT and perfectly matches the expected value considering the area enclosed by the centre of the interconnected nanowires. A smaller, but discernible peak at $110\,\mathrm{T}^{-1}$ indicates the presence of Altshuler-Aronov-Spivak oscillations.

4.8.4. ADDITIONAL DATA IN THE MULTI-PATH AHARONOV-BOHM REGIME

Two methods were used to study the phase evolution of the magneto-conductance oscillations. The data shown in Figs. 4.4 and 4.5 are taken by sweeping V_{PG} as the fast axis and $B_\perp$ as the slow axis. Oppositely, in Fig. 4.10 we present data taken with $B_\perp$ and V_{PG} being the fast and slow axis, respectively. The data presented here are taken at $V_{BG} = 1.5\,\mathrm{V}$ as in Fig. 4.4. For each value of V_{PG} (proportional to E_{QD}) the maxima of the AB oscillations are tracked, and their positions in $B_\perp$ are converted into the transmission phase φ via the AB periodicity and plotted in Figure 4.10a. In Figure 4.10b, we show the corresponding conductance trace (blue data points) exhibiting CPs. The phase displays a rapid evolution close to the charge degeneracy points. At the two inner CPs, the phase φ evolves by $\sim \pi$, and gradually shifts back to the original value. For the first and fourth CPs, the variation is much smaller than π. For all displayed Coulomb valleys, the phase is neither constant, nor does it exhibit a rapid phase lapse. Instead, gradual variations are observed, compatible with the picture in which multiple trajectories with different enclosed areas in the nanowire interferometer couple to different QD orbitals.

4.8.5. PHASE VARIATIONS AND FUNDAMENTAL SYMMETRIES

The top panel of Fig. 4.4d shows that the transmission phase swings from 0 to π at resonance over an energy range of $\sim \Gamma$. This continuous variation differs significantly from what has been reported in the pioneering experiment of ref. [20] where the phase was mysteriously locked to 0 and π with abrupt switches in between. Later on, their finding was understood in term of fundamental symmetries.

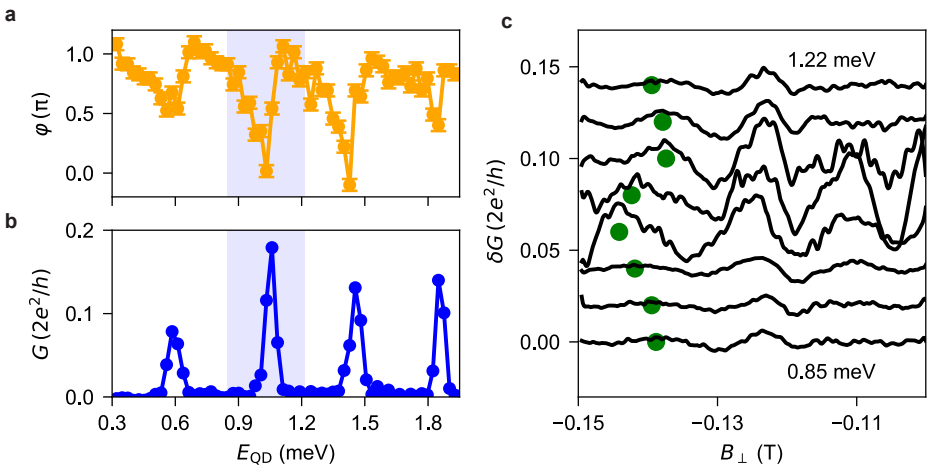

Figure 4.10: Additional data in the multi-path Aharonov-Bohm regime. **a** Phase φ of the magneto-conductance oscillations as a function of E_{QD}, **b** G vs. E_{QD} exhibiting four CPs. **c** Aharonov-Bohm oscillations measured in the proximity of the second CP. δG is obtained by subtracting a slowly varying background from the magneto-conductance traces. The green circles identify the maxima of the oscillations in the first period. The traces are displaced for clarity.

Time-reversal symmetry imposes, in fact, the two-terminal conductance to be an even function of the magnetic field (the Casimir-Onsager relation: $G(B) = G(-B)$). In an Aharonov-Bohm interferometer, the conductance displays sinusoidal oscillations on top of a background, and the symmetry around zero field imposes on their phase to assume only two values: 0 or π. However, in our experiment we find the opposite: the phase variation at resonance is smooth and not abrupt. We associate this behaviour with the fact that time-reversal symmetry does not hold in our context due to the large magnetic fields applied.

4.8.6. FITTING RESULTS

FIG. 4.3

We obtain the dashed lines in Fig. 4.3a by fitting each peak independently with the single-trajectory model Aharonov-Bohm interferometer. For this and other fits, we use $J = 1$ and $ka = 1.57 \sim \pi/2$ similarly to ref. [45]. The phase of J_{L} is a fitting parameter that is not relevant and therefore not displayed. We report the other values in Table 4.1 subdivided into the three characteristic regimes in Fig. 4.3a.

FIG. 4.4

We obtain Fig. 4.4b by fitting the data of Fig. 4.4a with the single-trajectory model Aharonov-Bohm interferometer with $N = 2$. The fitting procedure is facilitated by fixing two parameters globally (i.e., for the entire measurement): a constant offset to the traces of $0.02 \cdot 2e^2/h$ and $t_{\mathrm{ref}} = 0.07$. The phase of J_{L} is an independent parameter that increases

	Regime		
Average parameter	green trace	blue trace	high orange trace
j_L (μeV)	31 ± 1	34 ± 6	14 ± 8
J_R (μeV)	140 ± 6	202 ± 17	206 ± 26
t_{ref}	$< 10^{-3}$	0.04 ± 0.01	0.28 ± 0.02

Table 4.1: Average and standard deviations of the best-fit parameters of four peaks in the three different regimes in Fig. 4.3a.

with the magnetic field along the y-axis. We display in Table 4.2 the best-fit parameters averaged along the magnetic field axis. Peak numbers are ordered from left to right.

	Peak number	
Average parameter	1	2
j_L (μeV)	192 ± 22	182 ± 12
J_R (μeV)	57 ± 10	59 ± 5
E_n (meV)	0.241 ± 0.001	0.618 ± 0.011

Table 4.2: Best-fit parameters averaged along the magnetic field axis of Fig. 4.4. The errors presented are the standard deviations of the distributions of the parameters.

FIG. 4.5

In order to obtain Fig. 4.5b, we first consider the line-cut of the data at $B_\perp = 0.667\,\mathrm{T}$ and fit the peaks independently with the single-path interferometer model. We fix some of the parameters to simplify the procedure as $t_{ref} = 0.05$ and the added offset to the trace at $0.06 \cdot 2e^2/h$. In this procedure, the phase of J_L is used as a free parameter and not relevant here. The other values are shown in Table 4.3, where the peak names in Fig. 4.5a are ordered numerically from left to right.

We then extrapolate the trace with the best-fit parameters by varying the phase of J_L and adjusting the values of $x(n) \in [0.025,\ 0.01,\ 0,\ -0.016]$ to qualitatively reproduce the experimental data.

	Peak number			
Parameter	1	2	3	4
j_L (μeV)	178 ± 2	165 ± 4	153 ± 5	167 ± 2
J_R (μeV)	33.4 ± 0.2	60.9 ± 0.1	51.4 ± 1.1	37.3 ± 0.04
E_n (meV)	2.000 ± 0.001	2.293 ± 0.002	2.710 ± 0.002	3.092 ± 0.001

Table 4.3: Fitting parameters obtained at $B_\perp = 0.667\,\mathrm{T}$ of Fig. 4.5a.

4.8.7. COTUNNELLING AHARONOV-BOHM EFFECT IN A SECOND DEVICE

Here, we report additional measurements of Aharonov-Bohm interference in the cotunnelling regime for a second device. The electron density in this device (Figure 4.11a) is tunable by voltages on a global back gate and several top gates. The top dielectric used

here is Al_2O_3 grown via atomic layer deposition. A T-shaped quantum dot is formed in the bottom branch of the interferometer and has a charging energy of $E_c \sim 0.5$ meV, with the tunnel coupling to the leads adjustable using the tunnel gates T1 and T2. Although the conductance around $V_{SD} = 0$ is strongly suppressed owing to the Coulomb blockade (inset of Figure 4.11b), the magneto-conductance exhibits clear Aharonov-Bohm oscillations with a periodicity of $9 - 11$ mT (Figure 4.11b, main panel). The oscillation amplitude is sizable despite the cotunnelling conductance being as low as $\sim 0.025 \cdot 2e^2/h$. This value corresponds to a typical dwell time in the QD in the order of $5 - 10$ ps. The magnitude of the Fast Fourier Transform (FFT) of these oscillations is displayed in Figure 4.11c, together with the FFTs of the AB oscillations at gradually stronger cotunnelling conductance, until the Coulomb blockade is fully quenched (red trace corresponding to the 'open regime' with $G \sim 2e^2/h$). We observe here that the width of the FFT peak of the AB signal increases when quenching the Coulomb blockade by making the barriers more transparent (in particular, see the difference between the red and the other traces). This fact might suggest that, when the quantum dot is defined, fewer trajectories play a role in the transport through the interferometer, reducing the spread of the enclosed area.

4.8.8. TEMPERATURE DEPENDENCE OF THE AHARONOV-BOHM EFFECT

In Figures 4.12a and 4.12e, we show the scanning electron micrographs of two nanowire loops (second and third devices) used to study the temperature dependence of the Aharonov-Bohm oscillations. In Figures 4.12b and 4.12f, we plot two typical magneto-conductance traces of each device. They both exhibit AB oscillations superimposed on a slowly varying background. In the data analysis, we subtract this background and calculate the Fast Fourier Transform. The amplitudes A_{FFT} shown in Figs. 4.12c and 4.12g are the averaged Fast Fourier Transforms of several scans taken in the same magnetic field window. The peaks in the spectra are fitted with a Gaussian obtaining the power spectrum of the AB oscillations A_{AB}. For the third device, we find that the sum of two Gaussian curves better describes the broad FFT peak due to the presence of the second harmonic. In panels d and h, we demonstrate the decrease of A_{AB} as a function of temperature. The amplitudes of each harmonic (with index n) are expected to decrease as $\exp(-n \cdot L/l_\phi)$, with l_ϕ being the phase coherence length and L being the effectively travelled path length [27]. In ballistic systems, we have $l_\phi \propto T^{-1}$, while $l_\phi \propto T^{-1/2}$ in the diffusive regime [46]. We fitted the experimental decay of the Aharonov-Bohm amplitude with the function $A \cdot \exp(-\alpha T^k)$, with free parameters A, α, k, and the Aharonov-Bohm phase coherence length defined as $l_\phi = (L/\alpha) T^{-k}$. The best-fit curves are shown in black, and correspond to $k_{best} = 0.72$ and $k_{best} = 0.45$ for the second and third devices, respectively. For comparison, we also show the best-fit curves obtained for $k = 1$. The values of the fitted exponents k reflect the nature of the transport in the semiconducting loops, which is in the crossover between completely ballistic and diffusive. In fact, the typically travelled length is $\sim 1\,\mu$m, which is only a few times larger than the estimated mean free path of $\sim 0.1 - 0.3\,\mu$m [47, 48]. We expect that at higher temperatures and for the longer loops (cf. device 2) the diffusive model with $k = 0.5$ captures the experimental trend better than the ballistic one, but the experimental data do not provide conclusive evidence.
From our analysis, we derive $l_\phi(35\,\text{mK}) = \frac{L}{\alpha} T^{-k} \sim 8\,\mu$m for the second device, and $l_\phi(35\,\text{mK}) \sim 2.5\,\mu$m for the third loop. It can be argued that these values are probably

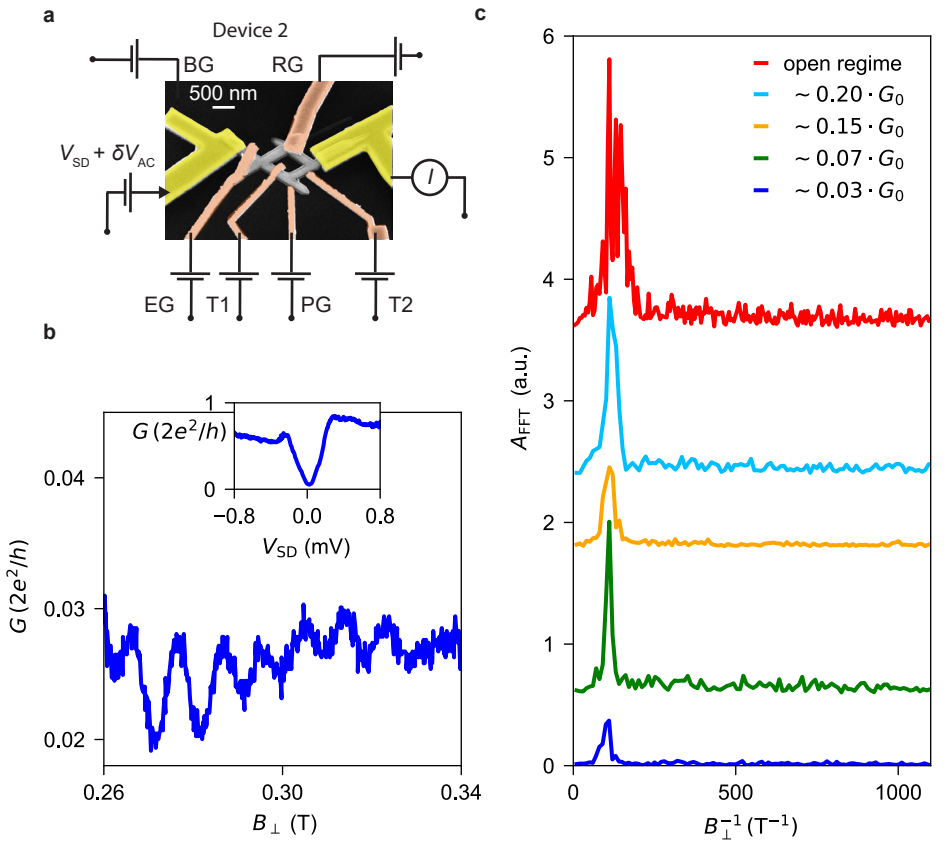

Figure 4.11: Cotunnelling Aharonov-Bohm effect in a second device. **a** False-color scanning electron microscopy image of a second device. A quantum dot with a T-shape is formed in the bottom branch of the network by applying negative voltages to the two tunnel gates (T1 and T2). The induced charge is tuned via the plunger gate (PG). We use the top branch of the network as the reference arm of the interferometer, with a transmission tunable by the reference gate (RG). **b** Differential conductance G at zero bias voltage V_{SD} as a function of the perpendicular field $B_\perp$ in the cotunnelling regime manifesting AB oscillations with a period of $\sim 9-11$ mT. Inset: G vs. V_{SD} taken at $B_\perp = 0.34$ T. **c** Magnitude of the Fast Fourier Transforms for different tunnel gate settings. The legend indicates the average value of the cotunnelling conductance of the raw magneto-conductance traces.

underestimating the actual coherence length since the amplitude of the AB oscillations (more generally all odd harmonics) are additionally suppressed by the energy averaging effect.

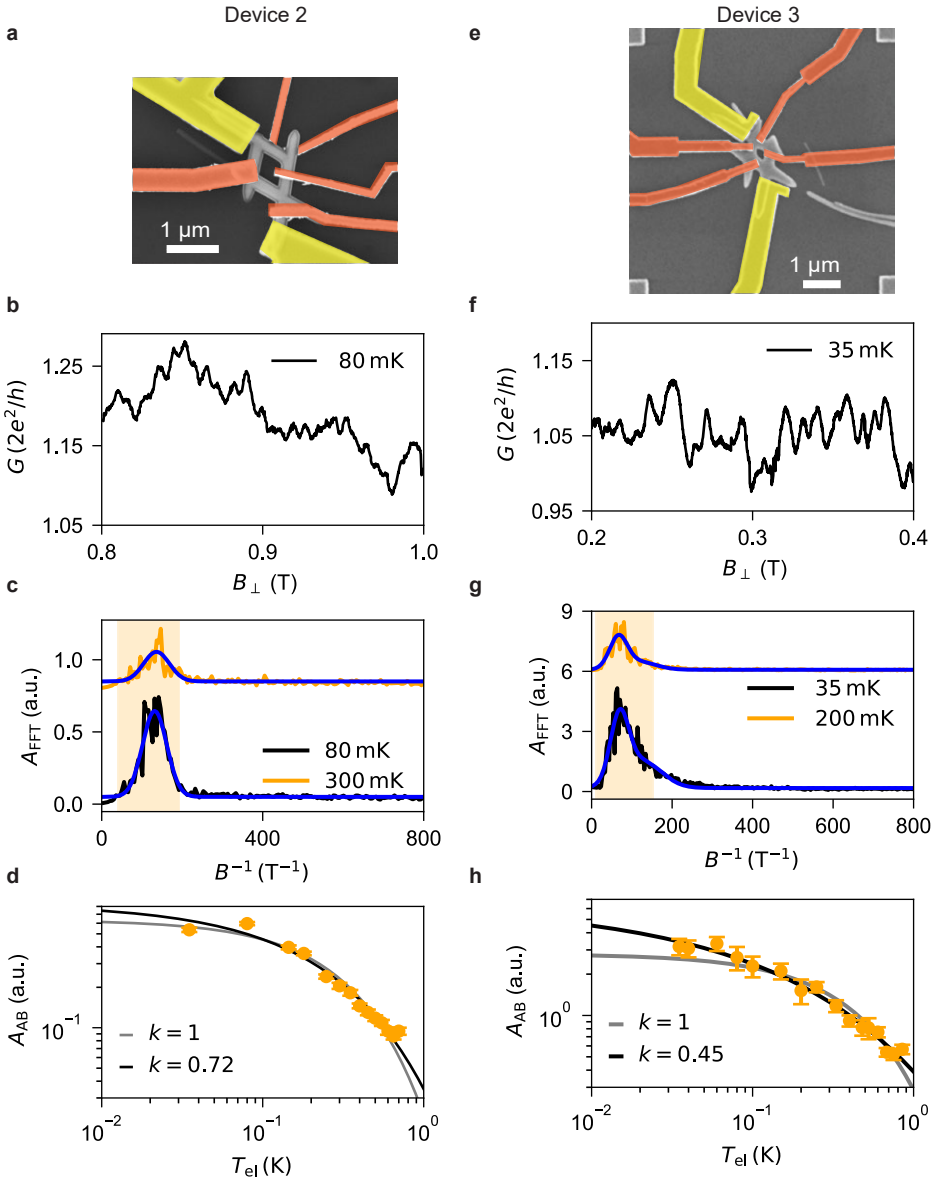

Figure 4.12: Aharonov-Bohm temperature dependence of the second and third device. **a**, **e** Scanning electron micrographs of devices 2 and 3, respectively. **b**, **f** Typical magneto-conductance traces for the two devices exhibiting oscillations superimposed on a slowly varying background. **c**, **g** Average of several Fast Fourier Transforms of oscillations at two different temperatures fitted with a Gaussian in **c** and a sum of two Gaussians in **g**. The yellow shaded area denotes the expected range of the first harmonic (Aharonov-Bohm) according to the sizes of the loops. In **d**, **h** the temperature dependence of the AB amplitudes is presented for both the devices (orange points). Black and grey traces are the best fits of the data.

REFERENCES

[1] F. Borsoi, K. Zuo, S. Gazibegovic, R. L. M. Op het Veld, E. P. A. M. Bakkers, L. P. Kouwenhoven, and S. Heedt, *Transmission phase read-out of a large quantum dot in a nanowire interferometer,* Nat. Commun. **11**, 3666 (2020).

[2] R. A. Webb, S. Washburn, C. P. Umbach, and R. B. Laibowitz, *Observation of h/e Aharonov-Bohm oscillations in normal-metal rings,* Phys. Rev. Lett. **54**, 2696 (1985).

[3] A. Bachtold, C. Strunk, J.-P. Salvetat, J.-M. Bonard, L. Forró, T. Nussbaumer, and C. Schönenberger, *Aharonov-Bohm oscillations in carbon nanotubes,* Nature **397**, 673 (1999).

[4] S. Russo, J. B. Oostinga, D. Wehenkel, H. B. Heersche, S. S. Sobhani, L. M. K. Vandersypen, and A. F. Morpurgo, *Observation of Aharonov-Bohm conductance oscillations in a graphene ring,* Phys. Rev. B **77**, 085413 (2008).

[5] H.-W. Lee, *Generic transmission zeros and in-phase resonances in time-reversal symmetric single channel transport,* Phys. Rev. Lett. **82** (1998).

[6] Y. Oreg, *Universal phase lapses in a noninteracting model,* New J. Phys. **9**, 122 (2007).

[7] P. G. Silvestrov and Y. Imry, *Towards an explanation of the mesoscopic double-slit experiment: A new model for charging of a quantum dot,* Phys. Rev. Lett. **85**, 2565 (2000).

[8] J. A. van Dam, Y. V. Nazarov, E. P. A. M. Bakkers, S. De Franceschi, and L. P. Kouwenhoven, *Supercurrent reversal in quantum dots,* Nature **442**, 667 (2006).

[9] A. Y. Kitaev, *Unpaired Majorana fermions in quantum wires,* Phys.-Uspekhi **44**, 131 (2001).

[10] R. M. Lutchyn, J. D. Sau, and S. Das Sarma, *Majorana fermions and a topological phase transition in semiconductor-superconductor heterostructures,* Phys. Rev. Lett. **105**, 077001 (2010).

[11] Y. Oreg, G. Refael, and F. von Oppen, *Helical liquids and Majorana bound states in quantum wires,* Phys. Rev. Lett. **105**, 177002 (2010).

[12] J. Alicea, *New directions in the pursuit of Majorana fermions in solid state systems,* Rep. Prog. Phys. **75**, 076501 (2012).

[13] S. Vijay and L. Fu, *Teleportation-based quantum information processing with Majorana zero modes,* Phys. Rev. B **94**, 235446 (2016).

[14] S. Plugge, A. Rasmussen, R. Egger, and K. Flensberg, *Majorana box qubits,* New J. Phys. **19**, 012001 (2017).

[15] T. Karzig, C. Knapp, R. M. Lutchyn, P. Bonderson, M. B. Hastings, C. Nayak, J. Alicea, K. Flensberg, S. Plugge, Y. Oreg, C. M. Marcus, and M. H. Freedman, *Scalable designs for quasiparticle-poisoning-protected topological quantum computation with Majorana zero modes,* Phys. Rev. B **95**, 235305 (2017).

[16] L. Fu, *Electron teleportation via Majorana bound states in a mesoscopic superconductor,* Phys. Rev. Lett. **104**, 056402 (2010).

[17] C. Drukier, H.-G. Zirnstein, B. Rosenow, A. Stern, and Y. Oreg, *Evolution of the transmission phase through a Coulomb-blockaded Majorana wire,* Phys. Rev. B **98**, 161401 (2018).

[18] M. Hell, K. Flensberg, and M. Leijnse, *Distinguishing Majorana bound states from localized Andreev bound states by interferometry,* Phys. Rev. B **97**, 161401 (2018).

[19] M. Avinun-Kalish, M. Heiblum, O. Zarchin, D. Mahalu, and V. Umansky, *Crossover from mesoscopic to universal phase for electron transmission in quantum dots,* Nature **436** (2005).

[20] A. Yacoby, M. Heiblum, D. Mahalu, and H. Shtrikman, *Coherence and phase sensitive measurements in a quantum dot,* Phys. Rev. Lett. **74**, 4047 (1995).

[21] R. Schuster, E. Buks, M. Heiblum, D. Mahalu, V. Umansky, and H. Shtrikman, *Phase measurement in a quantum dot via a double-slit interference experiment,* Nature **385**, 417 (1997).

[22] C. Karrasch, T. Hecht, A. Weichselbaum, Y. Oreg, J. von Delft, and V. Meden, *Mesoscopic to universal crossover of the transmission phase of multilevel quantum dots,* Phys. Rev. Lett. **98**, 186802 (2007).

[23] H. Edlbauer, M. Y. S. Takada and, G. Roussely and, S. Tarucha, A. Ludwig, A. D. Wieck, T. Meunier, and C. Bäuerle, *Non-universal transmission phase behaviour of a large quantum dot,* Nat. Commun. **8** (2017).

[24] D. Car, J. Wang, M. A. Verheijen, E. P. A. M. Bakkers, and S. R. Plissard, *Rationally designed single-crystalline nanowire networks,* Adv. Mater. **26**, 4875 (2014).

[25] S. Gazibegovic, D. Car, H. Zhang, S. C. Balk, J. A. Logan, M. W. A. de Moor, M. C. Cassidy, R. Schmits, D. Xu, G. Wang, P. Krogstrup, R. L. M. Op het Veld, K. Zuo, Y. Vos, J. Shen, D. Bouman, B. Shojaei, D. Pennachio, J. S. Lee, P. J. van Veldhoven, S. Koelling, M. A. Verheijen, L. P. Kouwenhoven, C. J. Palmstrøm, and E. P. A. M. Bakkers, *Epitaxy of advanced nanowire quantum devices,* Nature **584**, 434 (2017).

[26] L. P. Kouwenhoven, D. G. Austing, and S. Tarucha, *Few-electron quantum dots,* Rep. Prog. Phys. **64**, 701 (2001).

[27] T. Ihn, *Semiconductor Nanostructures* (Oxford University Press, 2010).

[28] S. M. Albrecht, A. P. Higginbotham, M. Madsen, F. Kuemmeth, T. S. Jespersen, J. Nygård, P. Krogstrup, and C. M. Marcus, *Exponential protection of zero modes in Majorana islands,* Nature **531**, 206 (2016).

[29] J. van Veen, A. Proutski, T. Karzig, D. I. Pikulin, R. M. Lutchyn, J. Nygård, P. Krogstrup, A. Geresdi, L. P. Kouwenhoven, and J. D. Watson, *Magnetic-field-dependent quasiparticle dynamics of nanowire single-Cooper-pair transistors,* Phys. Rev. B **98**, 174502 (2018).

[30] J. Shen, S. Heedt, F. Borsoi, B. van Heck, S. Gazibegovic, R. L. M. Op het Veld, D. Car, J. A. Logan, M. Pendharkar, S. J. J. Ramakers, G. Wang, D. Xu, D. Bouman, A. Geresdi, C. J. Palmstrøm, E. P. A. M. Bakkers, and L. P. Kouwenhoven, *Parity transitions in the superconducting ground state of hybrid InSb-Al Coulomb islands,* Nat. Commun. **9**, 4801 (2018).

[31] S. R. Plissard, I. van Weperen, D. Car, M. A. Verheijen, G. W. G. Immink, J. Kammhuber, L. J. Cornelissen, D. B. Szombati, A. Geresdi, S. M. Frolov, L. P. Kouwenhoven, and E. P. A. M. Bakkers, *Formation and electronic properties of InSb nanocrosses,* Nat. Nanotechnol. **8**, 859 (2013).

[32] F. Cerdeira, T. A. Fjeldly, and M. Cardona, *Effect of free carriers on zone-center vibrational modes in heavily doped p-type Si,* Phys. Rev. B **8**, 4734 (1973).

[33] R. Gupta, Q. Xiong, C. K. Adu, U. J. Kim, and P. C. Eklund, *Laser-induced Fano resonance scattering in silicon nanowires,* Nano Lett. **3**, 627 (2003).

[34] J. Faist, F. Capasso, C. Sirtori, K. W. West, and L. N. Pfeiffer, *Controlling the sign of quantum interference by tunnelling from quantum wells,* Nature **390**, 589 (1997).

[35] H. Schmidt, K. L. Campman, A. C. Gossard, and A. Imamoglu, *Tunneling induced transparency: Fano interference in intersubband transitions,* Appl. Phys. Lett. **70**, 3455 (1997).

[36] J. Göres, D. Goldhaber-Gordon, S. Heemeyer, M. A. Kastner, H. Shtrikman, D. Mahalu, and U. Meirav, *Fano resonances in electronic transport through a single-electron transistor,* Phys. Rev. B **62**, 2188 (2000).

[37] K. Kobayashi, H. Aikawa, S. Katsumoto, and Y. Iye, *Tuning of the Fano effect through a quantum dot in an Aharonov-Bohm interferometer,* Phys. Rev. Lett. **88 25**, 256806 (2002).

[38] A. Aharony, O. Entin-Wohlman, T. Otsuka, S. Katsumoto, H. Aikawa, and K. Kobayashi, *Breakdown of phase rigidity and variations of the Fano effect in closed Aharonov-Bohm interferometers,* Phys. Rev. B **73**, 195329 (2006).

[39] L. Huang, Y.-C. Lai, H.-G. Luo, and C. Grebogi, *Universal formalism of Fano resonance,* AIP Adv. **5** (2015), https://doi.org/10.1063/1.4906797.

[40] C.-M. Ryu and S. Y. Cho, *Phase evolution of the transmission coefficient in an Aharonov-Bohm ring with Fano resonance,* Phys. Rev. B **58**, 3572 (1998).

[41] K. Kobayashi, H. Aikawa, S. Katsumoto, and Y. Iye, *Mesoscopic Fano effect in a quantum dot embedded in an Aharonov-Bohm ring,* Phys. Rev. B **68**, 235304 (2003).

[42] S. Katsumoto, K. Kobayashi, H. Aikawa, A. Sano, and Y. Iye, *Quantum coherence in quantum dot - Aharonov-Bohm ring hybrid systems,* Superlattices Microstruct **34**, 151 (2003).

[43] A. M. Whiticar, A. Fornieri, E. C. T. O'Farrell, A. C. C. Drachmann, T. Wang, C. Thomas, S. Gronin, R. Kallaher, G. C. Gardner, M. J. Manfra, C. M. Marcus, and F. Nichele, *Coherent transport through a Majorana island in an Aharonov–Bohm interferometer,* Nat. Commun. **11**, 3212 (2020).

[44] E. Prada, P. San-Jose, M. W. A. de Moor, A. Geresdi, E. J. H. Lee, J. Klinovaja, D. Loss, J. Nygård, R. Aguado, and L. P. Kouwenhoven, *From Andreev to Majorana bound states in hybrid superconductor–semiconductor nanowires,* Nature Reviews Physics **2**, 575 (2020).

[45] A. Aharony, O. Entin-Wohlman, and Y. Imry, *Phase measurements in open and closed Aharonov-Bohm interferometers,* Phys. E **29**, 283 (2005).

[46] T. Ludwig and A. D. Mirlin, *Interaction-induced dephasing of Aharonov-Bohm oscillations,* Phys. Rev. B **69**, 193306 (2004).

[47] I. van Weperen, B. Tarasinski, D. Eeltink, V. S. Pribiag, S. R. Plissard, E. P. A. M. Bakkers, L. P. Kouwenhoven, and M. Wimmer, *Spin-orbit interaction in InSb nanowires,* Phys. Rev. B **91**, 201413 (2015).

[48] Ö. Gül, D. J. van Woerkom, I. van Weperen, D. Car, S. R. Plissard, E. P. A. M. Bakkers, and L. P. Kouwenhoven, *Towards high mobility InSb nanowire devices,* Nanotechnology **26**, 215202 (2015).

5

PARITY TRANSITIONS IN THE SUPERCONDUCTING GROUND STATE OF HYBRID INSB-AL COULOMB ISLANDS

The number of electrons in small metallic or semiconducting islands is quantised. When tunnelling is enabled via opaque barriers this number can change by an integer. In superconductors the addition is in units of two electron charges (2e), reflecting that the Cooper pair condensate must have an even parity. This ground state (GS) is foundational for all superconducting qubit devices. Here, we study a hybrid superconducting-semiconducting island and find three typical GS evolutions in a parallel magnetic field: a robust 2e-periodic even-parity GS, a transition to a 2e-periodic odd-parity GS, and a transition from a 2e- to a 1e-periodic GS. The 2e-periodic odd-parity GS persistent in gate-voltage occurs when a spin-resolved subgap state crosses zero energy. For our 1e-periodic GSs we explicitly show the origin being a single zero-energy state gapped from the continuum, i.e., compatible with an Andreev bound states stabilized at zero energy or the presence of Majorana zero modes.

This chapter has been published as, J. Shen*, S. Heedt*, F. Borsoi*, B. van Heck, S. Gazibegovic, R. L. M. Op het Veld, D. Car, J. A. Logan, M. Pendharkar, S. J. J. Ramakers, G. Wang, D. Xu, D. Bouman, A. Geresdi, C. J. Palmstrøm, E. P. A. M. Bakkers, and L. P. Kouwenhoven, *Parity transitions in the superconducting ground state of hybrid InSb-Al Coulomb islands*, Nature Communications 9, 4801 (2018) [1].
*These authors contributed equally to this work.

5.1. INTRODUCTION

A superconductor can proximitize a semiconductor and open a gap in its energy spectrum. If the two materials are strongly coupled, the induced gap can be as large as the original gap in the superconductor. The two gaps respond differently to an applied magnetic field, e.g. when the Landé g-factors differ in the two materials. A large g-factor in the semiconductor can cause the induced gap to close long before the closing of the original gap. If, in addition, the semiconductor has strong spin-orbit interaction, the induced gap can re-open, signalling a transition to a topological superconducting phase [2, 3]. This phase contains pairs of Majorana zero modes (MZMs) that can accommodate either zero or one fermion, and thus allows for both even- and odd-parity GSs [4, 5].

When a conductor has a finite size, it forms an island restricting the charge to an integer times the elementary charge, e [6]. The resulting Coulomb blockade effects have been widely studied in metallic and superconducting islands, the latter often referred to as Cooper pair boxes [7, 8]. A major breakthrough was the demonstration of charge quantization in units of $2e$ in aluminium (Al) islands [9–14], indicating that the even-parity superconducting GS was not poisoned by quasiparticles on the time scale of the measurement. The $2e$ quantization could be destroyed by subjecting the Al to an external magnetic field, B, which causes a transition to the metallic state with $1e$ charge quantization [11, 12]. Hybrid superconducting-semiconducting islands have also shown a $2e$ charge quantization at low B-fields [15–17]. These observations imply that the low-energy spectrum in the semiconductor is completely proximitized with no Andreev bound states (ABSs) at low energies. Also, for these hybrid islands a B-field can cause a $2e$ to $1e$ transition [16, 17]. A recent breakthrough demonstrated that under particular circumstances the $1e$ quantization is not due to the transition to the metallic state - but rather due to a topological superconducting phase [16]. These pioneering experiments used InAs as the semiconductor.

Here, we harness the large g-factor ($g \sim 50$) and the ballistic transport properties of InSb nanowires [18, 19], and find additional B-field induced transitions, including a recurrence of a $2e$ quantization at higher B-fields.

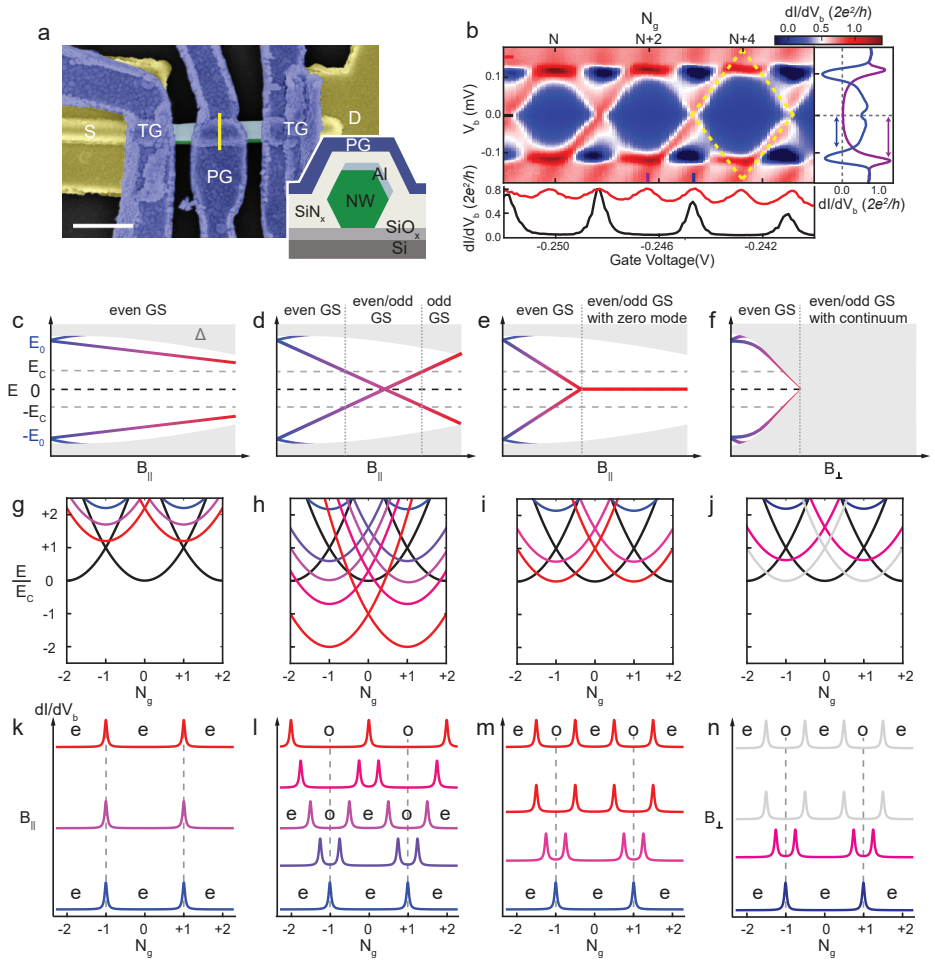

Figure 5.1: Hybrid semiconducting-superconducting island and its energy spectrum. **a** False-colour scanning electron microscope image of the device consisting of an InSb nanowire (green) with an 800-900 nm long Al-shell (light-blue) covering the top facet and one side facet. Inset: schematic cross-section at the centre of the plunger gate (PG) indicated by the yellow line. The Si/SiOx substrate contains a global back gate that we keep at zero voltage. The InSb wire is contacted by Cr/Au leads (yellow) and then covered by a 30 nm thick dielectric layer of SiNx (light-grey). Ti/Au top gates (blue) that wrap around the wire allow for local electrostatic control of the electron density. Two gates are used to induce tunnel barriers (TG) and one plunger gate (PG) controls the electron number on the island. The scale bar indicates 500 nm. **b** dI/dV_b versus tunnel gate voltage and V_b showing *2e*-periodic Coulomb diamonds (one diamond is outlined by yellow dashed lines). The lower panel shows horizontal linecuts with *2e*-periodic Coulomb oscillations at $V_b = 0$ (black trace) and *1e*-periodic oscillations at $V_b = 150\,\mu V$ (red trace). The panel on the right shows a vertical linecut through the Coulomb peak at the degeneracy point (blue trace) and through the centre of the Coulomb diamond (purple trace). Below are four scenarios for the B-dependence of a single Andreev level (**c**, **d**, **e** and **f**), the resulting energies as a function of the induced charge, N_g, (**g**, **h**, **i** and **j**) and the Coulomb oscillations (**k**, **l**, **m** and **n**). In panels **c**-**f**, the grey regions represent the continuum of states above Δ. The coloured traces represent the energy, E_0, of the lowest-energy subgap state. Panels **g**-**j** show the energies of the island with N excess electrons, $E(N_g) = E_c(N_g - N)^2 + p_N E_0$, where N_g is the gate-induced charge, N is the electron occupancy number, and $p_N = 0\,(1)$ for N = even (odd). Parabolas for N = even are shown in black, while parabolas for N = odd are shown in colours in correspondence to the colours in the other rows. Crossings in the lowest-energy parabolas correspond to Coulomb peaks as sketched in panels **k**-**n**, again with the same colour coding. Labels in the Coulomb valleys between the peaks indicate the GS parity being either even (e) or odd (o).

5.2. DIFFERENT GROUND-STATE EVOLUTIONS AT CONTROLLABLE GATE CONFIGURATIONS

Our device (Fig. 5.1a) consists of a hexagonal InSb nanowire with two of its facets covered by a thin epitaxial layer of Al (see ref. [20] for materials details). Two top gates (TG) can induce adjustable tunnel barriers separating the InSb-Al island from the two normal leads. The voltage, V_{PG}, applied to the top plunger gate (PG), can be used to tune the charge on the island as well as the spatial charge density profile in the semiconductor. A bias voltage, V_b, is applied between source (S) and drain (D), yielding a current, I, that is measured in a dilution refrigerator at a base temperature of $\sim$ 15 mK.

Fig. 5.1b shows the differential conductance, dI/dV_b, versus V_b and the voltage applied to the tunnel gate at $B = 0$. The charge is fixed in the current-blockaded Coulomb diamonds (with mostly blue colour) with a periodicity in gate voltage corresponding to a charge increment of *2e*. For $V_b > 120\,\mu$V the periodicity is halved to *1e*, indicating the onset of single electron transport. Linecuts in the right panel show that dI/dV_b can be enhanced as well as suppressed, even down to negative values (black colour). These are known features for hybrid islands and can be used to extract values for the charging energy, $E_c = e^2/2C \sim 25\,\mu$eV and the lowest-energy subgap state, $E_0 = 50-90\,\mu$eV (Fig. 5.6). The Al superconducting gap, $\Delta = 220\,\mu$eV, is extracted from tunnelling spectroscopy measurement (Fig. 5.7).

To understand parity transitions induced by a B-field, we illustrate four different scenarios in Fig. 5.1c-f. We sketch a slow reduction of Δ for a B-field, $B_\parallel$, along the nanowire axis (Fig. 5.1c-e) and a rapid decrease of Δ for a perpendicular field, $B_\perp$ (Fig. 5.1f). We consider a single lowest-energy subgap state (i.e. an ABS) with energy E_0, which is two-fold spin-degenerate at $B = 0$ and becomes spin-split in a B-field. Fig. 5.1c sketches the case where E_0 decreases very slowly with $B_\parallel$ remaining above E_c such that the GS parity remains even. This translates to *2e*-periodic conductance oscillations for all $B_\parallel$-fields (Fig. 5.1k). Note that conductance peaks occur when the lowest-energy parabolas cross. In Fig. 5.1g the lowest crossings are always between even-charge parabolas. These crossings, for instance at $N_g = -1$ and $+1$, are *2e*-periodic. The odd-charge parabolas remain above these lowest-energy crossings and thus do not participate in the low-energy transport.

Fig. 5.1d sketches a second case where E_0 varies more rapidly with $B_\parallel$. When E_0 crosses E_c the odd-charge parabolas pass the lowest-energy crossings of the even parabolas, thereby adding degeneracy points between even-charge and odd-charge parabolas (Fig. 5.1h). This results in alternating smaller and larger peak spacings, where the smaller valleys have odd-parity for $E_0 > 0$ and even-parity for $E_0 < 0$. Note that an equal spacing with *1e*-periodicity occurs when $E_0 = 0$. At negative energies, when E_0 crosses $-E_c$ the *2e*-periodicity is restored, however, now with an odd-parity GS. In terms of the charge parabolas this corresponds to odd-charge parabolas being always lower in energy than the even ones (red parabolas in Fig. 5.1h). This case of *2e*-periodicity for an odd-parity GS has not been reported before.

In the third case we illustrate the possible consequence of strong spin-orbit interaction. The zero-energy crossing of the subgap state can now be followed by a transition to a topological phase containing MZMs rigidly fixed at $E_0 = 0$ (Fig. 5.1e). (Note that the re-opening of the gap is not shown in Fig. 5.1e since only the lowest-energy subgap state

is sketched.) As E_0 decreases below E_c, the peak spacing gradually evolves from *2e* to *1e* with alternating even- and odd-parity GSs (Fig. 5.1i and m). It is important to note that the even/odd degeneracy of the topological phase in bulk materials is lifted here by the charging energy [4, 21]. This fundamental degeneracy is however visible by comparing the lowest energies for the even and odd parity GSs, which are both zero, albeit at different gate voltages. We note that ABSs confined by a smooth potential may also give rise to a similar phenomenon as sketched in Fig. 5.1e [22].

Finally, in the fourth case (Fig. 5.1f), the superconducting gap in Al closes at its critical perpendicular magnetic field (Fig. 5.1j and n). This transition to the normal state also causes equidistant *1e*-periodic oscillations, which in the peak evolution is similar to the topological case. However, we show below that finite-bias spectroscopy is significantly different in these two cases.

In Fig. 5.2, we present exemplary data for the four cases illustrated in Fig. 5.1k-n. Fig. 5.2a-d show four panels of dI/dV_b measured at zero bias as a function of V_{PG} and B-field ($B_\parallel$ or $B_\perp$). The bottom row of panels shows representative linecuts at high B-fields. Fig. 5.2e-h show the corresponding peak spacings for even (S_e) and odd (S_o) GSs. These spacings are converted from gate voltage to energy via the gate lever arm and reflect the energy difference between even- and odd-parity states. In Fig. 5.2a the peaks are *2e*-periodic with even-parity GS up to a field of ~ 0.9 T. This observation reflects that up to this B-field our Al thin film remains superconducting without any low-energy subgap state. Above ~ 0.9 T the gap is significantly suppressed such that *1e*-transport sets in [12].

In Fig. 5.2b, the conductance peaks split into pairs around 0.11 T with alternating small and large spacings. These split peaks merge with neighbouring split peaks, leading to the recurrence of *2e*-periodic oscillations, but strikingly with an odd-parity in the valleys (cf. Fig. 5.1l). The parity transition is also illustrated in Fig. 5.2f by the single crossing between S_e and S_o. Similar to Fig. 5.2a, above 0.9 T the oscillation becomes *1e*-periodic (see linecuts).

For the case shown in Fig. 5.2c (cf. Fig. 5.1m), the *2e*-periodicity gradually changes to uniform *1e*-periodicity above ~ 0.35 T. S_e and S_o exhibit slight but visible parity-changing oscillations up to 0.9 T, whose amplitude decreases with field. This case resembles the experiment of ref. [16] where the *1e* oscillations are associated with MZMs. Additionally, we found that the peaks are alternating in height. To quantify this effect, we extract from the data an asymmetry parameter $\Lambda = G_{e\to o}/(G_{e\to o} + G_{o\to e})$, which amounts to 0.5 for peaks with equal heights [23]. Here, $G_{e\to o}$ ($G_{o\to e}$) is the peak height at an even-to-odd (odd-to-even) transition occurring upon increasing V_{PG}. Fig. 5.2g shows that Λ undergoes drastic oscillations around 0.5 as $B_\parallel$ is varied, and levels off at 0.5 above 0.9 T.

The data in Fig. 5.2d are taken for the same gate configuration as Fig. 5.2c but in a perpendicular B-field, which turns the Al into a normal state around $B_\perp = 0.18$ T (see also Fig. 5.7). In the normal state the oscillations are 1e-periodic and both Λ and S_e/S_o are constant, in agreement with established expectations [7].

The four columns in Fig. 5.1 and 5.2 represent distinct phases at high B: an even-parity GS, an odd-parity GS, a superconducting phase of alternating even and odd parities due to a single state at zero energy, and a gapless normal phase of alternating even and odd parities. These distinct phases can be reached by varying V_{PG} and thereby the spatial profile of the wave functions, which determines the coupling strength to Al and to the

external magnetic field [24–26]. In Fig. 5.2a, a very negative V_{PG} pushes the wave functions against and partly into the Al, leading to a robust-induced gap with weak sensitivity to the B-field, which indeed never induces a parity change. Fig. 5.2b, at more positive V_{PG}, reflects the presence of a subgap state with larger weight in the InSb (as indicated by its estimated g-factor, $g \sim 7-15$, see another example in Fig. 5.3f). In Fig. 5.2c, at even more positive V_{PG}, the involved wave function has an even larger weight in the semiconductor, yielding a large g-factor of ~ 10, possibly augmented by orbital effects [27]. This leads to the appearance of robust zero-energy modes at B-fields much lower than the critical field of the thin Al shell. This V_{PG}-dependent *2e*- to *1e*-periodic transition has been repeated for another device, which is not depicted here.

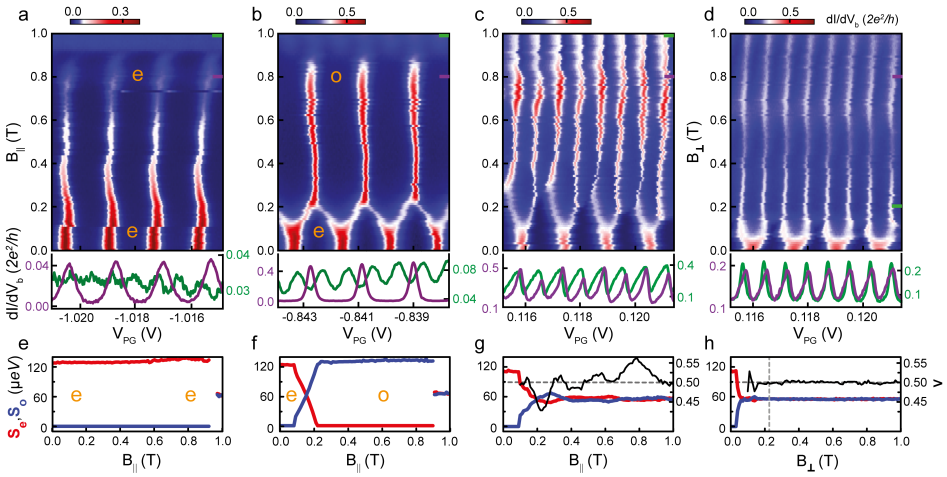

Figure 5.2: Four representative evolutions of Coulomb peaks, corresponding to the four columns (**c**-**n**) in Fig. 5.1. Top row panels: dI/dV_b as a function of V_{PG} and $B_\parallel$ (**a**, **b**, **c**) or $B_\perp$ (**d**). Below are typical linecuts at different B-fields indicated by the purple and green lines. (**e**, **f**, **g**, and **h**) Even and odd peak spacings, S_e (red) and S_o (blue) on the left axis, and peak height ratio, Λ (black) on the right axis, versus B-field, for the valleys labelled e/o in **a** and **b** and for the average spacings in **c** and **d**, respectively. Here and in other figures, the linewidths of S_e and S_o curves correspond to 5 μeV, in accordance with the lock-in excitation energy. **a** The *2e*-periodicity with even-parity valleys persists up to 0.9 T, above which quasiparticle poisoning occurs. **b** The *2e*-periodic peaks split at ~ 0.11 T and merge again at ~ 0.23 T. For $B_\parallel > 0.23$ T, the oscillations are again *2e*-periodic, but here the GS parity is odd, consistent with Fig. 5.1**h**. **c** *2e*-periodicity transitioning to uniform *1e*-periodicity at $B_\parallel \sim 0.35$ T, accompanied by peak spacing and peak height ratio oscillations up to 0.9 T (see also panel **g**). **d** *2e*-periodicity transitioning to *1e*-periodicity at $B_\perp = 0.18$ T (the vertical dashed line), coinciding with the critical B-field of the Al layer (see Fig. 5.7). Above the critical field, peak heights are constant (see linecuts) and the even/odd peak spacings are equal (**h**). A few common offsets in V_{PG} are introduced to compensate the shifts in gate voltage, and the raw data are listed in Fig. 5.8.

5.3. *2e*-PERIODIC ODD-PARITY GROUND STATE

Fig. 5.3 is dedicated to the new observation of a *2e*-periodic, odd-parity GS. The combined system of a superconducting island weakly coupled to a quantum dot with an odd electron number can also have odd parity [28]. In our case all states are strongly hybridized with the superconductor and one bound state drops below $-E_c$, which causes the even-parity

state to become an excited state above the odd-parity GS. (We describe different types of bound states in subsection 5.7.5.) Fig. 5.3a-c show Coulomb diamond for the gate settings of Fig. 5.2b at three values of $B_\parallel$. Fig. 5.3a at $B_\parallel = 0$ shows *2e*-periodic diamonds with *1e* and *2e* linecuts shown at the bottom (similar data was presented in Fig. 5.1b). Fig. 5.3b at $B_\parallel = 0.17$ T corresponds to the even-odd regime. Note that the conductance near $V_b = 0$ is suppressed, indicating that the subgap state causing the even-to-odd transition is weakly coupled to at least one of the normal leads (see also linecuts). Fig. 5.3c at $B_\parallel = 0.35$ T shows again *2e*-periodic diamonds but now the GS inside the diamonds has an odd parity. The diamond structure, including the presence of regions with negative dI/dV_b, is very similar to the even-parity GS diamonds, except for the shift in gate charge by *1e*.
Fig. 5.3f shows another example of the transition from the *2e*-periodic even GS, via a region of even-odd spacings, to a *2e*-periodic odd GS. Note again that the even-odd peak heights are significantly suppressed. These peaks correspond to a crossing of an even-parity parabola with an odd-parity parabola in Fig. 5.1h, where transport occurs via single electron tunnelling. In contrast, transport at the *2e*-periodic peaks, both for even and odd GSs, occurs via Andreev reflection. The two cartoons (Fig. 5.3d and e) illustrate these different transport mechanisms.

5.4. ISOLATED ZERO-ENERGY MODES AND COULOMB VALLEY OSCILLATIONS

Richer sequences of GS transitions as a function of magnetic field are also possible. For instance, the sketch in Fig. 5.4a illustrates the occurrence of multiple zero-energy crossings at low $B_\parallel$ followed by the appearance of a stable zero-energy state at higher $B_\parallel$. This type of behaviour is observed in Fig. 5.4b, showing large oscillations of S_e and S_o for $B_\parallel < 0.6$ T, and a stable *1e*-periodicity for $B_\parallel > 0.7$ T (see Fig. 5.4c). Similarly, Fig. 5.4d also shows large oscillations of S_e and S_o below 0.6 T, followed by a region of almost equally-spaced peaks above 0.6 T (see Fig. 5.4e). The features at low $B_\parallel$ (such as the position where the *2e*-periodic peaks first split) can depend on the precise value of V_{PG}. In contrast, the features at high $B_\parallel$ are strikingly regular, with only a weak dependence on V_{PG}. This suggests that the *1e*-periodicity at high fields originates from a state which is remarkably robust against gate variations. Furthermore, we note how the alternation of the conductance peak heights, already seen in Fig. 5.2c, is clearly visible in Fig. 5.4e even in the *1e*-periodic regime. The origin of these peak height oscillations lies in the difference between tunnelling amplitudes involving the electron and hole components of the subgap states [23]. It was recently proposed that in an idealized model for MZMs in a finite-length wire, the oscillations of Λ should be correlated with the oscillations in S_e and S_o, i.e. that Λ would be maximal or minimal when $S_e = S_o$ and vice versa that $|S_e - S_o|$ would be maximal for $\Lambda = 0.5$ [23]. In Fig. 5.4e, we find that the oscillations in Λ are similar in number and period to the corresponding oscillations in S_e and S_o, indeed suggesting a possible connection between the two (another example is presented in Figs. 5.11c-f). Fig. 5.4f shows finite-bias spectroscopy in the *1e*-periodic regime of Fig. 5.4d, at a high parallel field $B_\parallel = 0.7$ T. This spectroscopy reveals that the marked asymmetry of the peak heights originates from a discrete state that is gapped from a continuum of states at higher bias. As a comparison, Fig. 5.4g shows that for Al in the normal state no discrete features

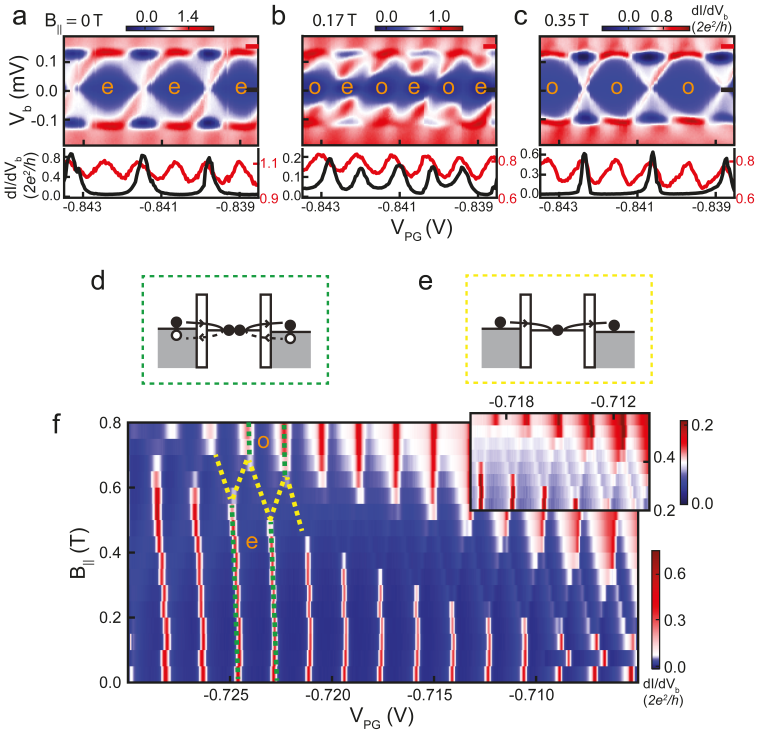

Figure 5.3: Transport via an odd-parity GS. (**a**-**c**) Coulomb diamonds for the gate settings in Fig. 5.2b at different $B_\parallel$. Below are linecuts at $V_b = 0$ (black trace) and $V_b = 150\,\mu V$ (red trace), respectively. **f** Another example of an even- to odd- GS transition. The inset is a zoom-in of the even-odd regime with a different scale bar. The sketch in **d** illustrates the Cooper pair tunnelling process in both even- and odd- GS regimes (marked by green dashed lines in **f**), while **e** illustrates the single electron tunnelling process in the alternating even-odd parity GS regime (marked by yellow dashed lines in **f**).

are observed. These are important verifications that substantiate our conclusion that the scenario in Fig. 5.1e is the proper description of the *1e* oscillations in the experimental figures (Fig. 5.2c and 5.4d) at high $B_\parallel$.

5.5. DISCUSSION

In summary, we have revealed distinct types of fermion parity transitions occurring as a function of magnetic field and gate voltages in a Coulomb-blockaded InSb-Al island. These transitions provide a complete picture of all the parity phases in mesoscopic Cooper pair boxes [29]. Among these, in a finite field we find a novel odd-parity phase with *2e* periodicity in gate voltage. Additionally, we find *1e*-periodic oscillations at high field originate from isolated zero-energy modes. The thorough understanding of the involved physics is important since such islands form the building blocks of future Majorana qubits [30–32].

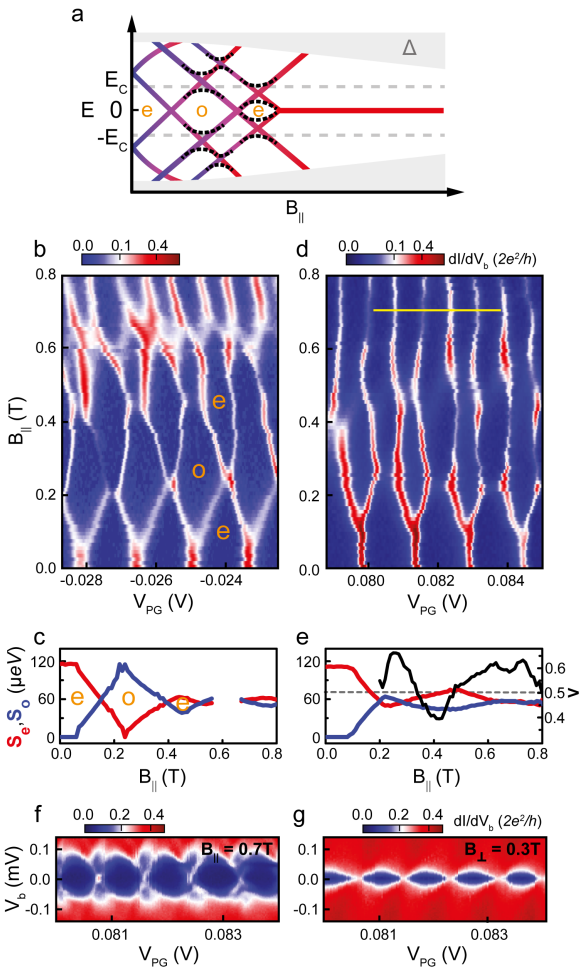

Figure 5.4: Evolution of multiple subgap states. **a** Schematic B-field dependence for the case of three subgap states with GS parity transitions at each zero-energy crossing. Dashed lines indicate level repulsion between different subgap states, leading to large oscillations of the lowest energy E_0. **b** One example of Coulomb peaks reflected by the scenario in panel **a**. The extracted peak spacings for the valleys labelled by e and o are shown below in **c**. The evolution of the peak spacings is compatible with the type of energy spectrum shown in **a**, characterized by large oscillations of E_0. Note that the odd-parity GS around ~ 0.2 T develops a full $2e$-periodicity. (The spacings near ~ 0.6 T are absent because the exact peak positions are unclear.) **d** Another example of Coulomb oscillations with a pronounced B-field dependence. Extracted peak spacings and the height ratio are shown in **e** (averaged over the three periods in **d**). **f** Coulomb diamonds at $B_\parallel = 0.7$ T along the V_{PG}-range indicated by the yellow line in **d**. This bias spectroscopy reveals isolated zero-bias peaks at the charge-degeneracy points that are separated from the continuum. As in Fig. 5.2c, neighbouring zero-bias peaks have different heights (also visible in **d** at high $B_\parallel$). **g** Bias spectroscopy with Al in the normal state ($B_\perp = 0.3$ T) where the isolated zero-bias peaks are absent.

AUTHOR CONTRIBUTIONS

J.S. fabricated the devices. J.S., F.B. and S.J.J.R. performed the measurements. J.S., S.H., B.V.H. and L.P.K. analysed the data. G.W., D.X., D.B., and A.G. contributed to the discussion of data and the optimization of the fabrication recipe. S.G., R.L.M.O.H.V., D.C., J.A.L., M.P., C.J.P. and E.P.A.M.B. carried out the growth of materials. J.S., B.V.H., S.H., F.B. and L.P.K. co-wrote the paper. All authors commented on the manuscript.

DATA AVAILABILITY

The data and the codes that create the figures in this chapter are available at `https://doi.org/10.4121/uuid:e0ecafef-7f45-4475-b2f8-351c2af4a2b0`.

5.6. METHODS

DEVICE FABRICATION

An isolated Al segment is formed by selectively shadowing the nanowire during Al evaporation. InSb-Al nanowires with double shadows (Fig. 5.5) were transferred from the InP growth chip to a doped-Si/SiOx substrate using a mechanical nanomanipulator installed inside an SEM. Au is used as leads and top gates. A 30 nm dielectric of SiNx separates the nanowire from the top gates.

TRANSPORT MEASUREMENTS

The device is cooled down to ~ 15 mK in an Oxford dry dilution refrigerator. The effective electron temperature is estimated to be 20-50 mK. Conductance across the devices was measured using a standard low-frequency lock-in technique (amplitude is 5 μV). The voltage bias $V_b = V_S - V_D$ is applied symmetrically between the two leads ($V_S = -V_S = V_b/2$). A magnetic field is applied using a 6-1-1 T vector magnet. The direction of the magnetic field is aligned carefully with respect to the nanowire axis (Fig. 5.7). The sweeping rate of the datapoints is very slow and one V_{PG}-dependent linetrace at fixed B in Fig. 5.2 takes a few minutes. We measure from 0 to 1 T with 0.01 T steps, bringing the measurement time for each panel to 3-4 hours. Because of this, we suffer from an ultra-slow drift that effectively changes the island potential. It is important to stress, however, that the slow drift affects the peak positions but not the peak spacings (since each trace only takes a few minutes to acquire). We extract subgap states and parity transitions from peak spacings and thus our conclusions are not affected by the ultra-slow drift.

5.7. SUPPLEMENTARY INFORMATION

5.7.1. GROWTH OF EPITAXIAL INSB/AL NANOWIRE ISLANDS

5.7.2. EXTRACTING E_c AND E_0 FROM *2e*-PERIODIC COULOMB DIAMONDS AT ZERO MAGNETIC FIELD

The energy parabolas in Fig. 5.6a illustrate that the degeneracies of the even-parity ground-state parabolas occur at E_c. In the Coulomb valley (at $N_g = 0$) the even-parity parabolas cross at $4E_c$ (indicated by the yellow dot in Fig. 5.6a). In finite-bias Coulomb diamonds, the voltage drop at the top of the *2e*-periodic Coulomb diamonds corresponds to $8E_c/e$

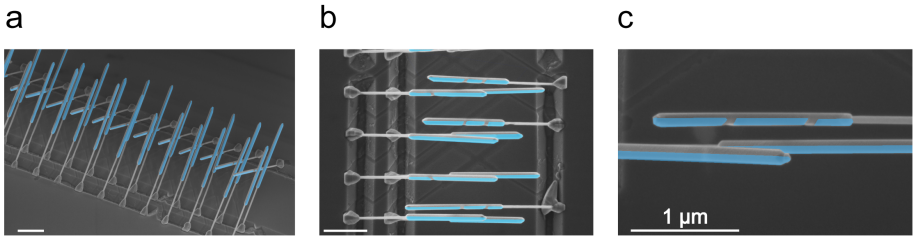

Figure 5.5: Scanning electron microscope (SEM) image of shadowed InSb/Al nanowires. The Al shell on the nanowires is coloured in light blue. **a** InSb nanowires are grown in a metal-organic vapour-phase epitaxy (MOVPE) reactor from catalyst droplets (Au), positioned along etched trenches. First, InP stems are grown to facilitate the nucleation of InSb nanowires. After nanowire growth, hydrogen cleaning is used to remove the native oxide layer of the nanowires and Al is evaporated in a direction parallel to the trenches. The positioning of Au droplets together with the tilting of the Al evaporation direction with respect to the horizontal plane allows the shadowing of predefined sections on the nanowires. **b** Zoomed-in SEM image of InSb nanowires with either one or two shadows. **c** During the Al evaporation, two sacrificial nanowires at the bottom are used to shadow two short segments (~ 100 nm) on a third wire at the top. The island length, set by the separation between two shadows, varies between 0.2 and 1 µm. Note that this 'shadow-growth' mechanism avoids the need of etching the Al, leaving pristine nanowire facets on the junction regions. We create a hybrid superconducting-semiconductor island of Al-InSb by interrupting the Al shell in two narrow regions allowing local electrostatic gating of two semiconducting junctions. At these two regions tunnel barriers can be introduced by the top gates to confine the superconducting-semiconducting hybrid island.

(dashed yellow diamond in Fig. 5.6b). As a result, E_c extracted from the yellow-dashed diamond in Fig. 5.1b is ~ 22 µeV. Over the entire gate range E_c varies between 22 – 27 µeV (see typical diamonds in Fig. 5.6c and d at different gate values). Above the degeneracy points of the GSs, the onset of quasiparticle transport causes a blockade of Andreev reflection and results in a region of negative differential conductance (NDC) starting from a threshold voltage bias $V_{NDC} \sim 2(E_0 - E_c)/e$ (see the blue arrows in Fig. 5.6a) [14]. For example, $V_{NDC} = 90\,\mu V$ in Fig. 5.1b, so $E_0 \sim 67\,\mu eV$. On the other hand, at finite bias, the onset of *1e*-periodicity is due to single-particle transport via co-tunnelling events (see the red arrow in Fig. 5.6a), corresponding to $2E_0/e$ [33]. In Fig. 5.1b, E_0 extracted from the onset of *1e*-periodicity is close to the number extracted from NDC in the same diamond ($E_0 \sim 67\,\mu eV$). Over the entire gate range E_0 varies between 50 – 90 µeV (see diamonds in Fig. 5.6c and d).

5.7.3. SUPERCONDUCTING CRITICAL MAGNETIC FIELDS OF THE INSB/AL NANOWIRE FOR THREE ORIENTATIONS

We performed tunnelling spectroscopy at one of the two junctions as a function of the magnetic field strength in three directions: parallel to the nanowire $B_\parallel$ (Fig. 5.7a), perpendicular to the substrate $B_{\text{out of plane}}$ (Fig. 5.7b) and perpendicular to the nanowire in the plane of the substrate $B_{\text{in plane}}$ (Fig. 5.7c). The local tunnel gate voltage is -1 V for this spectroscopy junction (the weak-tunnelling regime). The voltages are +2 V for the other tunnel gate and the plunger gate to make sure the chemical potential is smooth for the entire island except at the local tunnel gate. When B is applied parallel to the nanowire (Fig. 5.7a), the hard superconducting gap persists up to 1.0 T, with $\Delta(B_\parallel = 0) = 220\,\mu eV$

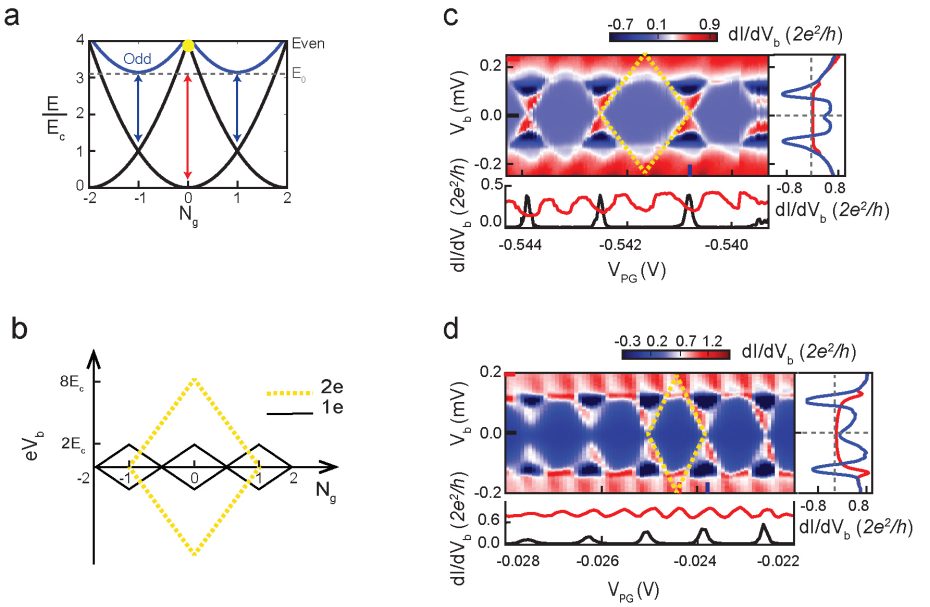

Figure 5.6: Derivation of E_c and E_0 from Coulomb diamonds. **a** The energy level parabolas of the superconducting island. The black parabolas describe the charge states for even parity, and blue parabolas for odd parity. Odd parabolas are lifted by E_0, consistent with $E_0 \gg E_c$ in Fig. 5.1b. **b** Finite-bias Coulomb diamonds for *1e*- (solid black diamonds) and *2e*-periodicity (dashed yellow diamond). **c** and **d**, Coulomb diamonds for two different gate configurations. In the bottom panels, horizontal linecuts show the *2e* (in black) versus *1e*-periodic (in red) conductance oscillations taken respectively at $V_b = 0\,\mu V$ and $V_b = 250\,\mu V$ (in **c**) / $V_b = 200\,\mu V$ (in **d**). In the right panels, vertical linecuts at different V_{PG} voltages show the presence of NDC regions above the degeneracy point (blue linecuts) and conductance enhancement in the valley (red linecuts). For **c**, we estimate $E_c \sim 25\,\mu eV$, while the onset of NDC is found at $V_b(\text{NDC}) \sim 70\,\mu V$, so $E_0 \sim 60\,\mu eV$. In **d**, $E_c \sim 22\,\mu eV$ and $V_b(\text{NDC}) \sim 70\,\mu V$, so $E_0 \sim 57\,\mu eV$.

and $\Delta(B_\parallel = 0.8\,\text{T}) = 90\,\mu eV$ (the bottom panel in Fig. 5.7a). The gap closes completely at $B_\parallel^c > 1\,\text{T}$, which is out of range for the employed 3D vector magnet. For the other two orientations, our device undergoes a transition to the normal state at $B^c_{\text{out of plane}} \sim 0.12\,\text{T}$ and $B^c_{\text{in plane}} = 0.18\,\text{T}$. In the text so far, $B_\perp$ means $B_{\text{in plane}}$ for simplicity. This observation is consistent with the SEM images of the device in Fig. 5.1a, showing the Al shell covering the top facet and one of the side facets of the nanowire.

5.7.4. RAW DATA FOR dI/dV_b AS A FUNCTION OF V_{PG} AND B

5.7.5. COMPARISON OF THE *2e*-PERIODIC ODD-PARITY GROUND STATE WITH PREVIOUS OBSERVATIONS OF FERMION PARITY CROSSINGS

The ground state fermion parity of a superconducting system can be changed by the Fermi-level crossing of a spin-resolved subgap state. The subgap state causing the GS transition may, for instance, be bound to an impurity in a bulk superconductor, as in the case of Shiba-Yu-Rusinov states [34]; or it may be an Andreev bound state in a Josephson junction

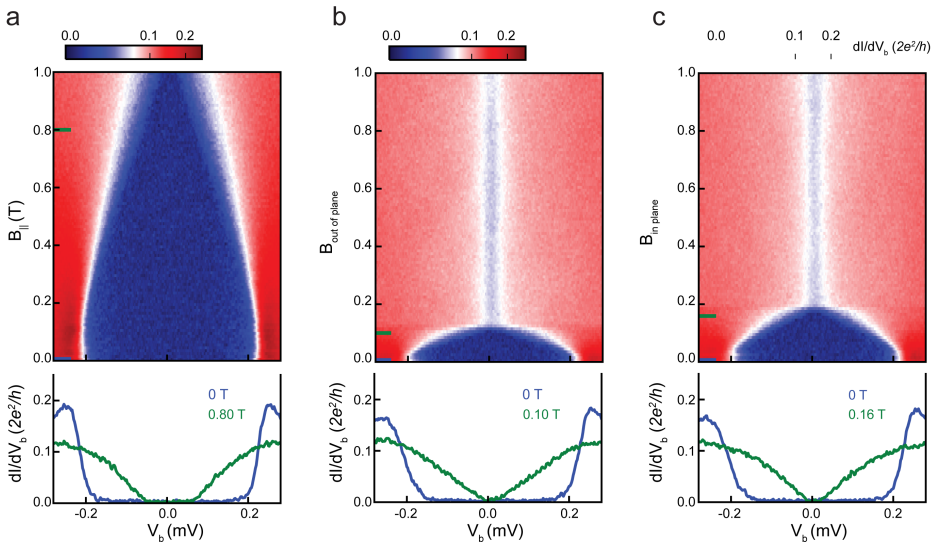

Figure 5.7: Tunnelling spectroscopy at magnetic fields of different orientations. Top panels show dI/dV_b tunnelling spectroscopy as a function of $B_\parallel$ (**a**), $B_{\mathrm{out\,of\,plane}}$ (**b**) and $B_{\mathrm{in\,plane}}$ (**c**). Typical linecuts at selected B are shown in the bottom panels. The zero-bias dip above the critical magnet field in **b** and **c** are likely due to the confinement at the second junction.

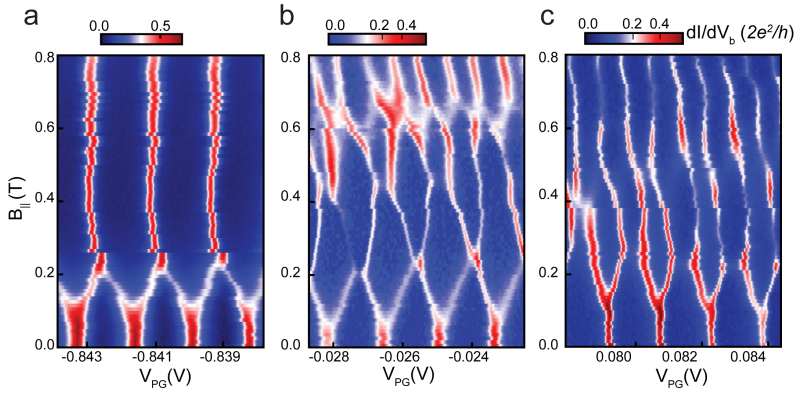

Figure 5.8: Raw data for dI/dV_b as a function of V_PG and $B_\parallel$. **a**, **b**, and **c** correspond to Fig. 5.2b, Fig. 5.4b and Fig. 5.4d, respectively. The plunger gate is sometimes drifting and gate-voltage jumps can occur because of charge trapping in the dielectric, so that raw dI/dV_b data here are not always stable. However, the conductance peaks from different parity states are still easily identified. A few common offsets in V_PG are introduced to compensate for the shifts in gate voltage.

(see [35] for instance). In our case, the fermion parity switch is due to a subgap state localized in the mesoscopic InSb/Al superconducting island. In this case, when the energy gap for emptying the subgap state exceeds the charging energy of the island, the odd

parity GS caused by the fermion parity switch is stable at all value of the induced charge of the island and the sequential process is Cooper pair tunnelling/Andreev reflection. This condition was not reached in previous studies of hybrid superconducting-semiconductor islands, which always observed either an even-parity GS or an alternation of even- and odd-parity GS [15, 16]. Furthermore, our observation is also distinct from the parity transitions observed in semiconducting quantum dots proximitized by a superconducting lead [28], where the charging energy applies only to the semiconductor but not to the superconductor. In this case, reducing the strength of the proximity effect (by varying the coupling between the dot and the superconductor) may cause a change from even to odd parity in the ground state of the dot, but only at values of the induced charge which would favour an odd occupation of the dot in the absence of the superconducting lead. In other words, the effect does not require a change of the GS parity of the superconducting lead itself.

5.7.6. EFFECT OF PARALLEL AND PERPENDICULAR MAGNETIC FIELDS ON THE PERIODICITY OF COULOMB PEAKS

For Fig. 5.2c and 5.4d, we just show typical Coulomb diamonds (Fig. 5.4f) at a specific value of $B_\parallel$. The additional figures at different $B_\parallel$ and $B_\perp$ (presented in Fig. 5.9) demonstrate the robustness of the isolated zero-bias state at all $B_\parallel$, as well as the obvious difference between the superconducting state at $B_\parallel$ and the normal state at $B_\perp$.Figs. 5.9a-c correspond to the same gate settings as Fig. 5.4d and Fig. 5.9d relates to Fig. 5.2c-d. The diamonds at different $B_\parallel$ (Fig. 5.9b and the top two panels in Fig. 5.9d) show the consistence of the isolated zero-mode. The finite bias spectroscopy (Fig. 5.9a) at the degeneracy point of Fig. 5.4d, as well as Fig. 5.9b, proves there is a zero-energy crossing at low $B_\parallel$ and a sticking zero-energy state at high $B_\parallel$, which fits the sketch in Fig. 5.4a. The normal transition in Fig. 5.9c shows equal peak spacings and heights, which is used to distinguish the normal and superconducting *1e*-periodic Coulomb peaks. For Fig. 5.2c and d, we can also see the isolated zero-mode for different $B_\parallel$ and a continuum in the normal regime (Fig. 5.9d).

5.7.7. FITTING OF THE COULOMB RESONANCES

The Coulomb resonances are analysed by fitting all peaks simultaneously using an identical electron temperature T_{el} that takes into account the temperature-broadening of the Coulomb resonances. A single resonance is described by a Breit-Wigner distribution [36, 37]

$$G_{\mathrm{BW}}(V_{\mathrm{PG}}, V_0, E) = \frac{2e^2}{h} \frac{(h\Gamma/2)^2}{(h\Gamma/2)^2 + (e\alpha(V_{\mathrm{PG}} - V_0) - E)^2} \tag{5.1}$$

where V_0 is the centre of the Coulomb peak and α is the plunger gate lever arm. The line shape is thermally broadened according to [38]

$$G(V_{\mathrm{PG}}, V_0) \propto \int_{-\infty}^{+\infty} G_{\mathrm{BW}}(V_{\mathrm{PG}}, V_0, E) \left[-\frac{\delta f(T,E)}{\delta E} \right] dE \tag{5.2}$$

with the Fermi-Dirac distribution $f(T,E)$. Hence, the total fitting function is given by a sum over a number of these line shapes and the tunnel coupling to the leads Γ. The

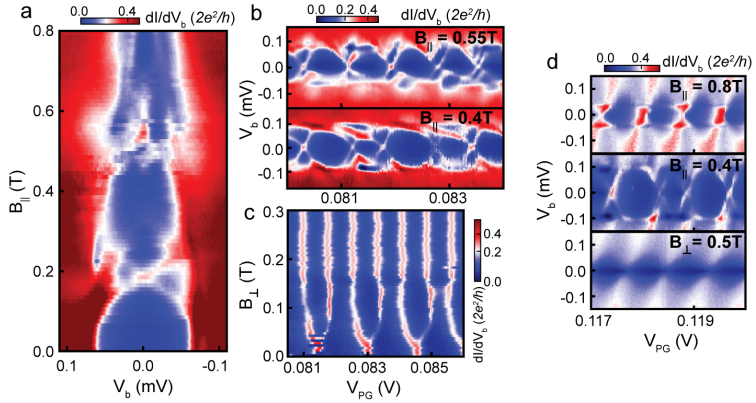

Figure 5.9: Zero-bias resonances at different $B_\parallel$ and $B_\perp$. **a**, **b** and **c** are measured for a similar gate-voltage regime as Fig. 5.4d. **a** dI/dV_b as a function of V_b and $B_\parallel$ at V_PG close to one degeneracy point in Fig. 5.4d. A charge degeneracy point at first crosses the Fermi level at $B_\parallel \sim 0.2$ T, while a more persistent zero-bias peak occurs for $B_\parallel = 0.5 - 0.65$ T. **b** Coulomb diamonds at $B_\parallel \sim 0.4$ T and 0.55 T. Both of them show a discrete state at the degeneracy points, isolated by an energy gap. $G_{\mathrm{e}\to\mathrm{o}}$ and $G_{\mathrm{o}\to\mathrm{e}}$ also show alternating amplitudes. **c** Evolution of zero-bias conductance peaks with $B_\perp$. The state becomes normal at $B_\perp \sim 0.18$ T ($B^c_{\text{in plane}}$ in Fig. 5.7 c), and the peak oscillations become *1e*-periodic with equal peak heights. **d** Coulomb diamonds at different $B_\parallel$ and $B_\perp$ at the same gate-voltage regime as Fig. 5.2c and d. Both of the top and middle panels at finite $B_\parallel$ show a discrete level at the degeneracy points and alternating peak heights, whereas the diamonds in the normal regime in the bottom panel show normal *1e* oscillations without isolated peaks at the charge degeneracy points.

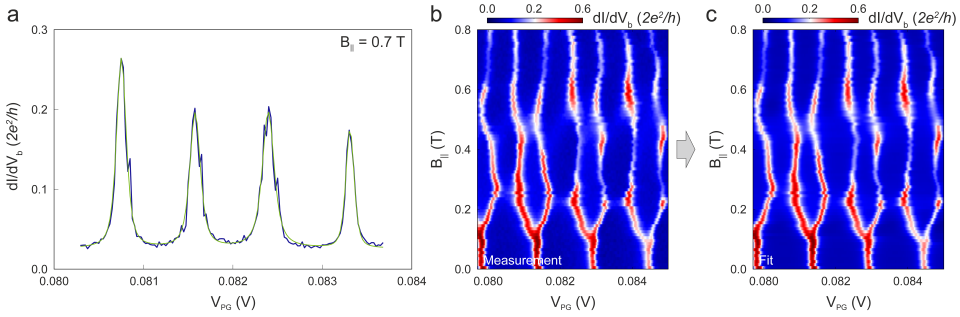

Figure 5.10: Fitting of the Coulomb resonances. **a** Fitting of the zero-bias linecut at $B_\parallel = 0.7$ T from the data presented in Fig. 5.4d. **b** and **c** are measurement (**b**) and fitting result (**c**) using $G_\mathrm{sum} = \sum_i G(V_\mathrm{PG}, V_{0,i})$, with $G(V_\mathrm{PG}, V_{0,i})$ given by eq. 5.2, for the data presented in Fig. 5.4d.

peak position V_0 and the peak height are individual fitting parameters for each resonance, while the electron temperature T_el and a constant offset are used as common fitting parameters. In conclusion, by fitting the data as depicted exemplarily in Fig. 5.10a (blue) the fitted curve (green) describes the data very well and we find an electron temperature of about 20-50 mK and a typical tunnel coupling of about $h\Gamma = 5\,\mu$eV. As depicted in Fig. 5.4b (bottom panel) the Coulomb peak spacing of the even and odd valleys oscillates

as a function of magnetic field. The oscillation amplitude is strongly reduced above 0.6 T. In Fig. 5.4b also the relative Coulomb peak height Λ is shown averaged for the three pairs of Coulomb peaks in Fig. 5.9b. This quantity is given by

$$\Lambda = \frac{G_{\mathrm{e}\to\mathrm{o}}}{G_{\mathrm{e}\to\mathrm{o}} + G_{\mathrm{o}\to\mathrm{e}}} \tag{5.3}$$

where $G_{\mathrm{e}\to\mathrm{o}}$ is the conductance peak height at resonance between an even and an odd parity Coulomb diamond and $G_{\mathrm{o}\to\mathrm{e}}$ is the consecutive resonance between the odd and the next even parity Coulomb diamond [23]. Clearly, the relative peak height undergoes oscillations as well that extend also into the regime of stable *1e* oscillations above 0.6 T. The fitting result for the data in Fig. 5.10b, which is used to extract the Coulomb peak spacings and peak heights, is depicted in Fig. 5.10c.

5.7.8. THE RELATION BETWEEN PEAK SPACING AND PEAK HEIGHT RATIO

We observe that the oscillations in Λ are similar in number and period to the corresponding oscillations in S_{e} and S_{o} (Fig. 5.11a, b and d), indeed suggesting a possible connection between the two.

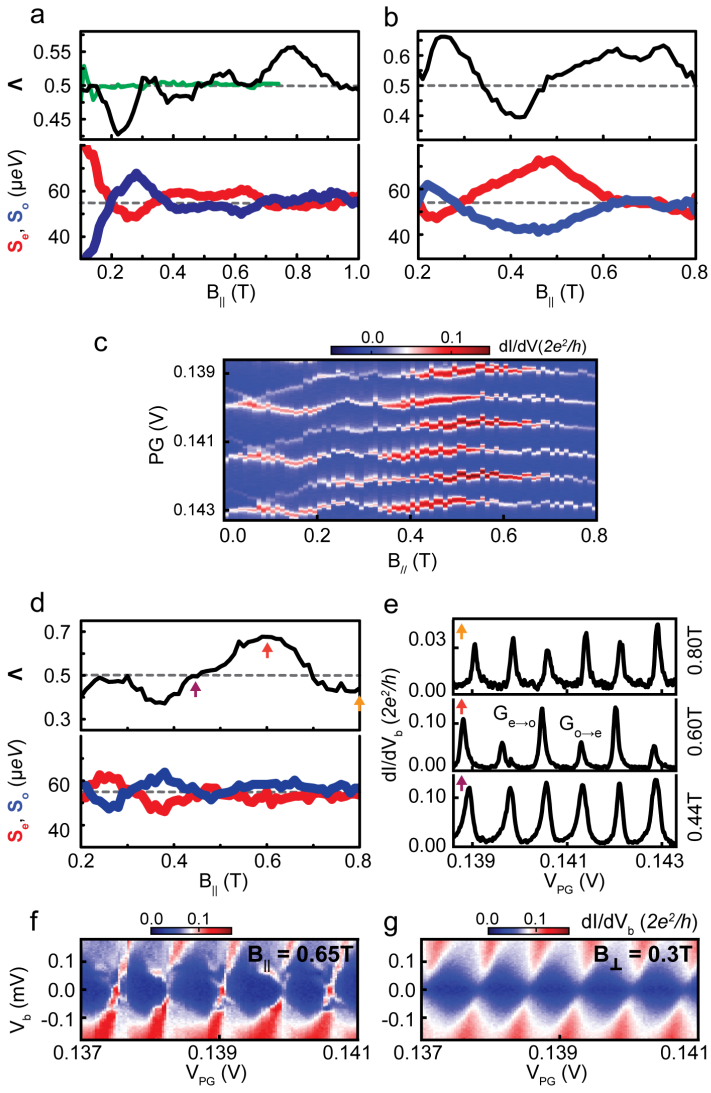

Figure 5.11: Evolution of peak heights and spacings. Peak height ratio Λ and peak pacings for even (S_e) and odd (S_o) parities as a function of $B_\parallel$ extracted from Fig. 5.2c (shown in **a**), Fig. 5.4d (shown in **b**) and Fig. 5.11c (shown in **d**). For comparison, the green curve in **a** is extracted from the normal state data of Fig. 5.2d. **e** Exemplary Coulomb oscillations for the data in **c** at different fields $B_\parallel$ = 0.44 T (Λ ~ 0.5), 0.60 T (Λ > 0.5), and 0.80 T (Λ < 0.5) indicated by arrows. **f** Coulomb diamonds at a large value of Λ in **c**, indicating the isolated zero mode. **g** Coulomb diamonds in the same gate-voltage regime as **f**, but measured in the normal state ($B_\perp$ = 0.3 T), showing the continuum at finite bias.

REFERENCES

[1] J. Shen, S. Heedt, F. Borsoi, B. van Heck, S. Gazibegovic, R. L. M. Op het Veld, D. Car, J. A. Logan, M. Pendharkar, S. J. J. Ramakers, G. Wang, D. Xu, D. Bouman, A. Geresdi, C. J. Palmstrøm, E. P. A. M. Bakkers, and L. P. Kouwenhoven, *Parity transitions in the superconducting ground state of hybrid InSb-Al Coulomb islands,* Nat. Commun. **9**, 4801 (2018).

[2] R. M. Lutchyn, J. D. Sau, and S. Das Sarma, *Majorana fermions and a topological phase transition in semiconductor-superconductor heterostructures,* Phys. Rev. Lett. **105**, 077001 (2010).

[3] Y. Oreg, G. Refael, and F. von Oppen, *Helical liquids and Majorana bound states in quantum wires,* Phys. Rev. Lett. **105**, 177002 (2010).

[4] L. Fu, *Electron teleportation via Majorana bound states in a mesoscopic superconductor,* Phys. Rev. Lett. **104**, 056402 (2010).

[5] S. D. Sarma, M. Freedman, and C. Nayak, *Majorana zero modes and topological quantum computation,* npj Quantum Inf. **1**, 15001 (2015).

[6] L. P. Kouwenhoven, C. M. Marcus, P. L. Mceuen, S. Tarucha, R. M. Westervelt, and N. S. Wingreen, *Electron transport in quantum dots. In Mesoscopic Electron Transport.* (Springer, 1997).

[7] Y. V. N. D. V. Averin, *Macroscopic quantum tunneling of charge and co-tunneling. In Single Charge Tunneling.* (Springer, 1992).

[8] M. Tinkham, *Introduction to superconductivity* (Dover Publications, 1996).

[9] L. J. Geerligs, V. F. Anderegg, J. Romijn, and J. E. Mooij, *Single Cooper-pair tunneling in small-capacitance junctions,* Phys. Rev. Lett. **65**, 377 (1990).

[10] M. T. Tuominen, J. M. Hergenrother, T. S. Tighe, and M. Tinkham, *Experimental evidence for parity-based 2e periodicity in a superconducting single-electron tunneling transistor,* Phys. Rev. Lett. **69**, 1997 (1992).

[11] M. T. Tuominen, J. M. Hergenrother, T. S. Tighe, and M. Tinkham, *Even-odd electron number effects in a small superconducting island: Magnetic-field dependence,* Phys. Rev. B **47**, 11599 (1993).

[12] J. G. Lu, J. M. Hergenrother, and M. Tinkham, *Magnetic-field-induced crossover from 2e to e periodicity in the superconducting single-electron transistor,* Phys. Rev. B **53**, 3543 (1996).

[13] T. M. Eiles, J. M. Martinis, and M. H. Devoret, *Even-odd asymmetry of a superconductor revealed by the Coulomb blockade of Andreev reflection,* Phys. Rev. Lett. **70**, 1862 (1993).

[14] F. W. J. Hekking, L. I. Glazman, K. A. Matveev, and R. I. Shekhter, *Coulomb blockade of two-electron tunneling,* Phys. Rev. Lett. **70**, 4138 (1993).

[15] A. P. Higginbotham, S. M. Albrecht, G. Kiršanskas, W. Chang, F. Kuemmeth, P. Krogstrup, T. S. Jespersen, J. Nygård, K. Flensberg, and C. M. Marcus, *Parity lifetime of bound states in a proximitized semiconductor nanowire,* Nat. Phys. **11**, 1017 (2015).

[16] S. M. Albrecht, A. P. Higginbotham, M. Madsen, F. Kuemmeth, T. S. Jespersen, J. Nygård, P. Krogstrup, and C. M. Marcus, *Exponential protection of zero modes in Majorana islands,* Nature **531**, 206 (2016).

[17] S. M. Albrecht, E. B. Hansen, A. P. Higginbotham, F. Kuemmeth, T. S. Jespersen, J. Nygård, P. Krogstrup, J. Danon, K. Flensberg, and C. M. Marcus, *Transport signatures of quasiparticle poisoning in a Majorana island,* Phys. Rev. Lett. **118**, 137701 (2017).

[18] J. Kammhuber, M. C. Cassidy, H. Zhang, m. Gül, F. Pei, M. W. A. de Moor, B. Nijholt, K. Watanabe, T. Taniguchi, D. Car, S. R. Plissard, E. P. A. M. Bakkers, and L. P. Kouwenhoven, *Conductance quantization at zero magnetic field in InSb nanowires,* Nano Lett. **16**, 3482 (2016).

[19] H. Zhang, Ö. Gül, S. Conesa-Boj, M. P. Nowak, M. Wimmer, K. Zuo, V. Mourik, F. K. de Vries, J. van Veen, M. W. A. de Moor, J. D. S. Bommer, D. J. van Woerkom, D. Car, S. R. Plissard, E. P. Bakkers, M. Quintero-Pérez, M. C. Cassidy, S. Koelling, S. Goswami, K. Watanabe, T. Taniguchi, and L. P. Kouwenhoven, *Ballistic superconductivity in semiconductor nanowires,* Nat. Commun. **8**, 16025 (2017).

[20] S. Gazibegovic, D. Car, H. Zhang, S. C. Balk, J. A. Logan, M. W. A. de Moor, M. C. Cassidy, R. Schmits, D. Xu, G. Wang, P. Krogstrup, R. L. M. Op het Veld, K. Zuo, Y. Vos, J. Shen, D. Bouman, B. Shojaei, D. Pennachio, J. S. Lee, P. J. van Veldhoven, S. Koelling, M. A. Verheijen, L. P. Kouwenhoven, C. J. Palmstrøm, and E. P. A. M. Bakkers, *Epitaxy of advanced nanowire quantum devices,* Nature **584**, 434 (2017).

[21] B. van Heck, R. M. Lutchyn, and L. I. Glazman, *Conductance of a proximitized nanowire in the Coulomb blockade regime,* Phys. Rev. B **93**, 235431 (2016).

[22] C.-K. Chiu, J. D. Sau, and S. Das Sarma, *Conductance of a superconducting Coulomb-blockaded Majorana nanowire,* Phys. Rev. B **96**, 054504 (2017).

[23] E. B. Hansen, J. Danon, and K. Flensberg, *Probing electron-hole components of subgap states in Coulomb blockaded Majorana islands,* Phys. Rev. B **97**, 041411 (2018).

[24] A. E. Antipov, A. Bargerbos, G. W. Winkler, B. Bauer, E. Rossi, and R. M. Lutchyn, *Effects of gate-induced electric fields on semiconductor Majorana nanowires,* Phys. Rev. X **8**, 031041 (2018).

[25] B. D. Woods, T. D. Stanescu, and S. Das Sarma, *Effective theory approach to the Schrödinger-Poisson problem in semiconductor Majorana devices,* Phys. Rev. B **98**, 035428 (2018).

[26] A. E. G. Mikkelsen, P. Kotetes, P. Krogstrup, and K. Flensberg, *Hybridization at superconductor-semiconductor interfaces,* Phys. Rev. X **8**, 031040 (2018).

[27] G. W. Winkler, D. Varjas, R. Skolasinski, A. A. Soluyanov, M. Troyer, and M. Wimmer, *Orbital contributions to the electron g factor in semiconductor nanowires,* Phys. Rev. Lett. **119**, 037701 (2017).

[28] E. J. H. Lee, X. Jiang, M. Houzet, R. Aguado, C. M. Lieber, and S. De Franceschi, *Spin-resolved Andreev levels and parity crossings in hybrid superconductor–semiconductor nanostructures,* Nat. Nanotechnol. **9**, 79 (2014).

[29] M. H. Devoret and R. J. Schoelkopf, *Superconducting circuits for quantum information: An outlook,* Science **339**, 1169 (2013).

[30] T. Karzig, C. Knapp, R. M. Lutchyn, P. Bonderson, M. B. Hastings, C. Nayak, J. Alicea, K. Flensberg, S. Plugge, Y. Oreg, C. M. Marcus, and M. H. Freedman, *Scalable designs for quasiparticle-poisoning-protected topological quantum computation with Majorana zero modes,* Phys. Rev. B **95**, 235305 (2017).

[31] S. Vijay and L. Fu, *Teleportation-based quantum information processing with Majorana zero modes,* Phys. Rev. B **94**, 235446 (2016).

[32] S. Plugge, A. Rasmussen, R. Egger, and K. Flensberg, *Majorana box qubits,* New J. Phys. **19**, 012001 (2017).

[33] Y. V. Nazarov and Y. M. Blanter, *Quantum Transport: Introduction to Nanoscience* (Cambridge University Press, 2009).

[34] A. V. Balatsky, I. Vekhter, and J.-X. Zhu, *Impurity-induced states in conventional and unconventional superconductors,* Rev. Mod. Phys. **78**, 373 (2006).

[35] W. Chang, V. E. Manucharyan, T. S. Jespersen, J. Nygård, and C. M. Marcus, *Tunneling spectroscopy of quasiparticle bound states in a spinful Josephson junction,* Phys. Rev. Lett. **110**, 217005 (2013).

[36] G. Breit and E. Wigner, *Capture of slow neutrons,* Phys. Rev. **49**, 519 (1936).

[37] C. W. J. Beenakker, *Theory of Coulomb-blockade oscillations in the conductance of a quantum dot,* Phys. Rev. B **44**, 1646 (1991).

[38] E. B. Foxman, P. L. McEuen, U. Meirav, N. S. Wingreen, Y. Meir, P. A. Belk, N. R. Belk, M. A. Kastner, and S. J. Wind, *Effects of quantum levels on transport through a Coulomb island,* Phys. Rev. B **47**, 10020 (1993).

6

A FULL PARITY PHASE DIAGRAM OF A MAJORANA ISLAND

The conductance oscillations of a mesoscopic island are a powerful source to understand the properties of both semiconducting and superconducting devices. Recent measurements of hybrid semiconducting-superconducting islands have shown a complex behavior that interpolates between that of the individual materials and suggests the presence of Majorana zero modes. Here, we measure the charge periodicity of Coulomb blockade conductance oscillations of a hybrid InSb–Al island as a function of gate voltage and parallel magnetic field. The periodicity changes from $2e$ *to* $1e$ *at a gate-dependent value of the magnetic field,* B^**, decreasing from a high to a low limit upon increasing the gate voltage. In the gate voltage region between the two limits, which our numerical simulations indicate to be the most promising for locating Majorana zero modes, we observe correlated oscillations of peak spacings and heights. Our measurements demonstrate the importance of a careful exploration of the entire available phase space of a proximitized nanowire as a prerequisite to define future topological qubits.*

This chapter has been published as, J. Shen, G.W. Winkler, F. Borsoi, S. Heedt, V. Levajac, J.-Y. Wang, D. van Driel, D. Bouman, S. Gazibegovic, R. L. M. Op het Veld, D. Car, A. Logan, M. Pendharkar, C. J. Palmstrøm, E. P. A. M. Bakkers, L. P. Kouwenhoven, and B. van Heck *A full parity phase diagram of a Majorana island*, arXiv:2012.10118 (2020) [1].

6.1. INTRODUCTION

Coulomb blockade conductance oscillations can provide quantitative information about the charge and energy spectrum of a mesoscopic island [2]. In particular, the charge periodicity of the oscillations can be directly related to the free energy difference between even and odd fermion parity states of the island [3]. In superconducting Al islands, the periodicity is $2e$ [3–6], reflecting the presence of a superconducting ground state with even fermion parity. In gate-defined semiconducting dots, on the other hand, the periodicity is $1e$, up to peak-to-peak variations due the individual energy levels of the dot [7–9]. Recent measurements have shown that hybrid semiconducting-superconducting islands can be tuned to exhibit both periodicities [10–21]. In particular, a magnetic field can be used to change the periodicity from $2e$ to $1e$, with an intermediate "even-odd" regime characterized by a bimodal distribution of peak spacings [11]. This change in periodicity can be associated with the exciting possibility of a transition into a topological phase with Majorana zero modes [22–24], with potential applications in topological quantum computing [25, 26]. The $2e$-to-$1e$ transition, however, is a necessary but not sufficient condition to determine the presence of a topological phase [27], since it can be caused by any Andreev bound state [28] whose energy decreases below the charging energy of the island. In fact, in these early experiments on InAs–Al and InSb–Al islands, some findings were not fully consistent with a Majorana interpretation: in particular, the decreasing amplitude of even-odd peak spacing oscillations with magnetic field [29–32], as well as the low value of the magnetic field at which $1e$-periodicity appeared with respect to the expected critical field of the topological transition. In this work, we report an exhaustive measurement of the Coulomb oscillations in an InSb–Al island as a function of gate voltage and magnetic field. Our goal is to map out the entire measurable phase space of the island in order to identify potential topological regions and compare their locations to the expected topological phase diagram resulting from state-of-the-art numerical simulations. We find that the $2e$-to-$1e$ transition happens at a value of the magnetic field, B^*, which decreases with increasing gate voltage in agreement with simulations. Regions with a very low B^* are unlikely to be topological, while the most promising gate range occurs at intermediate values of B^*.

6.2. 2E-1E PHASE DIAGRAM

The experiment is carried out in a device with the layout shown in Fig. 6.1. It consists of a hybrid InSb–Al nanowire [33], in which two crystallographic facets of the hexagonal InSb cross-section are covered by $8-15$ nm of epitaxial Al film. The length of the proximitized segment of the nanowire is $\sim 1\,\mu$m. The nanowire is contacted with metallic source and drain leads, and coupled to three gates for electrostatic control. The two gates on the sides act as tunnel gates, tuning the magnitude of the potential barriers at the junctions and thus the conductance, while the middle gate acts as a plunger gate controlling the electron occupation of the island as well as the cross-sectional profile of the electron density in the semiconductor. A magnetic field B, parallel to the nanowire axis, can be applied to the device. The device under consideration shows a hard superconducting gap [33] as well as $2e$-periodic Coulomb oscillations at $B = 0$ [14]. An example of the latter is shown in Fig. 6.1c, with a $2e$ peak spacing ~ 1.2 mV. From the measurement of the

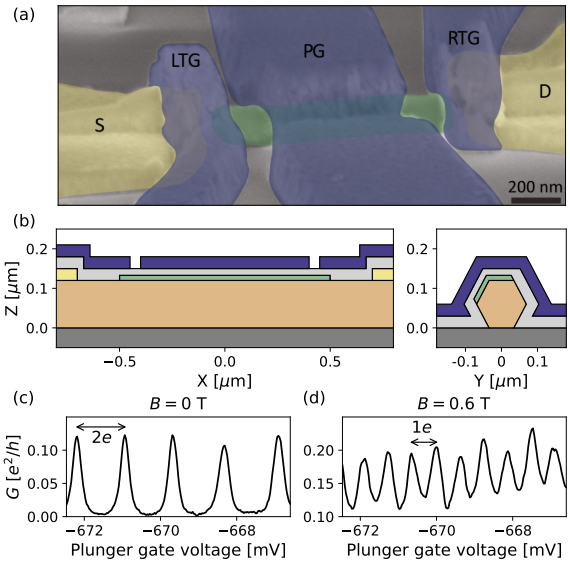

Figure 6.1: *(a)* Scanning electron microscopy image of the experimental device with false colors. Labels indicate source (S), drain (D), left and right tunnel gates (LTG, RTG) and plunger gate (PG). The Al shell, which is ~ 1 μm long, is colored in green. *(b)* Longitudinal (left) and cross-sectional (right) cuts of the device model used in the simulations: substrate (dark grey), InSb nanowire (orange), Al (green), ohmic contacts (yellow), dielectric (grey) and gates (blue). *(c)* Conductance oscillations measured at zero bias voltage as a function of plunger gate voltage exhibit $2e$ peak spacings at $B = 0$. *(d)* Same as (c), but showing $1e$ peak spacings at $B = 0.6$ T.

$2e$-periodic Coulomb diamonds (see Fig. 6.5), we extract a single-electron charging energy $E_C = e^2/2C \sim 20\,\mu$eV for the island. In a large magnetic field, the Coulomb oscillations become $1e$-periodic, as shown in Fig. 6.1d. The magnetic field B^* at which the periodicity changes from $2e$ to $1e$ is a function of the plunger gate voltage. To determine this, we have measured the Coulomb oscillations of the conductance as a function of B and over different gate voltage intervals, covering a range spanning 3.6 V in plunger gate and 0.9 T in magnetic field. In each gate interval, we measured a sequence of Coulomb blockade oscillations and extracted the peak spacing distribution. A telling picture emerges when plotting the median of the peak spacing distribution at each point in parameter space, see Fig. 6.2a. This experimental phase diagram can be heuristically described by dividing the data in three different plunger gate voltage regions, which we denote regions I, II, III going from negative to positive gate voltages. In region I, the $2e$-to-$1e$ transition occurs at a roughly constant magnetic field $B^* \sim 0.65$ T. This transition is likely caused by quasiparticle poisoning in the superconducting shell, favored by the suppression of superconducting pairing in Al [34]. In region II, the transition field B^* decreases gradually with gate voltage, albeit in an irregular fashion. In region III, the field B^* is again constant and equal to a low value $B^* \sim 50$ mT. In Fig. 6.2b we show the field dependence of the peak spacing distribution for each region. We note that an even-odd regime with a bimodal peak distribution, which is present each time the transition

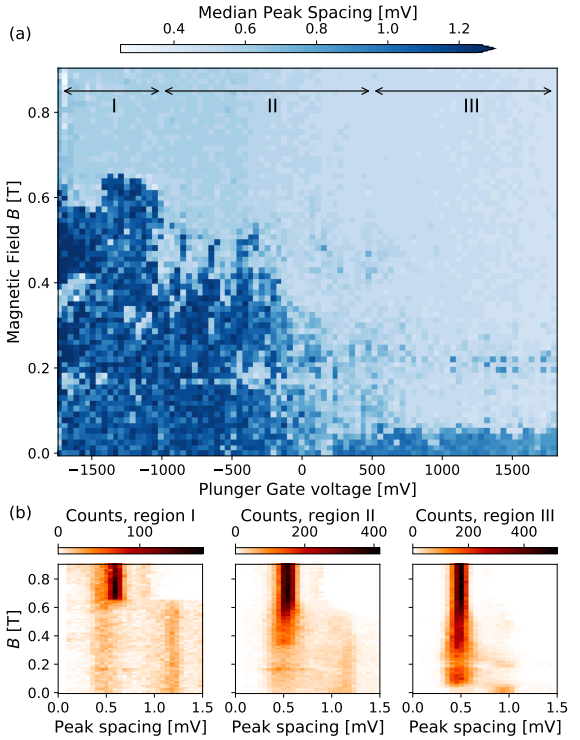

Figure 6.2: *(a)* Median peak spacing of Coulomb blockade oscillations as a function of magnetic field and gate voltage. Dark blue areas correspond to predominant $2e$ periodicity, light blue to $1e$ periodicity. For each pixel, the median is determined from a window of 20 mV in plunger gate voltage, corresponding to $\sim 20-40$ conductance oscillations. *(b)* Peak spacing distributions for regions I, II, III as labeled in panel (a). We attribute the presence of a residual $1e$ peak at low B in region I to the possible poisoning of the island [12] as well as to the occasional presence of subgap states [14].

from $2e$- to $1e$-periodicity occurs, is not visible in Fig. 6.2a, possibly because of the averaging procedure. The even-odd regime is weakly visible in the standard deviation of the peak spacing distribution, which is larger in the low-field $1e$ regime of regions II and III than in the high-field metallic regime of region I (see Fig. 6.10). It is also interesting to notice a weak resurgence of $2e$ spacings at $B \sim 0.2$ T in region III. Similar results were obtained on another phase diagram measurement, shown in the Fig. 6.11 and performed on the device we previously studied in Ref. [14]. Possible sources of noise in the processed data of Fig. 6.2 are the following. First, although we compensated the tunnel gates during the plunger gate sweep (see Fig. 6.7), the conductance level varied over the measurements, leading to a varying amplitude of the background signal. Second, the occurrence of uncontrolled resonances under the tunnel gates sometimes leads to conductance oscillations with spurious periodicity. Third, the lever arm of the plunger gate changes slightly over the entire measurement range, as can be noticed by the shift of the median peak spacing magnitude in the $1e$ regime at high B. Fourth, charge

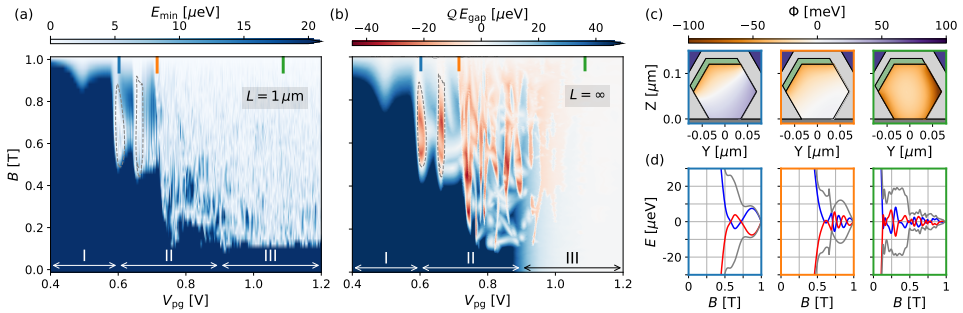

Figure 6.3: *(a)* Quasiparticle energy gap E_{min} as a function of plunger voltage V_{pg} and magnetic field for the simulated island. Two topological regimes with large gap and small coherence length are marked by the dashed grey lines. We also indicate regimes I, II and III as in Fig. 6.2. The energy scale is saturated at 20 μeV because this is the estimated charging energy in the experimental device and thus the expected boundary at which the $2e \rightarrow 1e$ transition would start to occur. *(b)* Bulk topological phase diagram indicating the bulk gap E_{gap} and the sign of the topological index $\mathcal{Q} = \pm 1$. Red regions are topological. *(c)* Electrostatic potential profiles in the nanowire cross-section for the three plunger gate values indicated by blue, orange and green bars in panels (a) and (b). *(d)* Magnetic field dependence of the lowest (red/blue) and first excited (grey) energy levels for three different plunger values. The left panel (blue) crosses a topological region of the phase diagram, while the two other panels (orange and green) correspond to topologically trivial regions.

fluctuations in the dielectric led to the occurrence of undetected gate jumps during the long measurement, causing missing or doubly-counted peaks and, thus, irregularities in the resulting peak spacing distributions. While these factors contribute to fluctuations in the peak spacing distributions extracted in Fig. 6.2b, in particular in the $2e$ regime of region I, overall they do not obfuscate the emerging structure of the parity phase diagram.

6.3. NUMERICAL SIMULATIONS

To shed light on the latter, we perform numerical simulations of a proximitized InSb island. Advances in the modelling of semiconductor-superconductor hybrid structures allow the inclusion of important effects such as self-consistent electrostatics, orbital magnetic field contribution and strong coupling between semiconductor and superconductor [35–40]. By integrating out the superconductor into self-energy boundary conditions, we can simulate three-dimensional wires with realistic dimensions including all of the aforementioned effects [18, 41]. With this approach we also fully take into account the renormalization of semiconductor properties like g-factor and spin-orbit coupling due to the strong coupling to the superconductor [42]. We model a hexagonal InSb wire with 120 nm facet-to-facet distance and two facets covered by 15 nm Al. The longitudinal and cross-sectional cuts of the simulated device are shown in Fig. 6.1, while in Fig. 6.3c we show the simulated electrostatic potential inside of the InSb wire for three representative plunger voltages. The electrostatic potential is solved on the level of the Thomas-Fermi approximation, which works very well for these hybrid devices [36]. Consistent with the large induced gap observed in InSb–Al devices [43], we assume an

electron accumulation layer at the InSb–Al interface [36, 37, 39, 44]. We take the band offset to be 50 meV and the critical field $B_{c,\mathrm{Al}} = 1$ T for the parent Al shell. Additional details on the simulation and precise material parameters are included in section 6.5.2. In Fig. 6.3a we show the simulated energy gap E_{min} of a $L = 1$ μm InSb–Al wire, dividing the data in three different plunger gate voltage regions as done in Fig. 6.2 [1]. In region I, InSb is strongly proximitized by Al, subgap states are absent and the induced gap only vanishes when B is close to $B_{c,\mathrm{Al}}$, which explains the large experimental value of B^* in this region. We note that the simulations do not include pair-breaking effects in the Al shell, which in reality lead to a regime of gapless superconductivity at B slightly lower than $B_{c,\mathrm{Al}}$ [45]. On the opposite end, in region III E_{min} reaches zero at very small magnetic fields mostly independent of plunger gate voltage, very similar to what is observed in the experiment. We now show that this surprising feature is a result of finite-size and orbital effects. For this purpose, in Fig. 6.3b we show the bulk energy gap computed from the bandstructure of an infinitely long wire, with the cross-sectional electrostatic potential chosen to be identical to that which we find in the middle of the 1 μm island. We find that in region III the bandstructure is gapless, which can be explained by the weakening of the proximity effect due to electron accumulation away from the Al interface [39]. We believe that the difference between panels (a) and (b) of Fig. 6.3 arises because, in the finite length system, scattering due to the inhomogeneous electrostatic potential at the ends of the wire suppresses long-wavelength modes and is effective in proximitizing all semiconducting states [46, 47]. This results in the presence of a gap at $B = 0$ at positive plunger gates voltages in Fig. 6.3a, but not in the bandstructure calculation of Fig. 6.3b. However, this gap is fragile: the orbital effect of the magnetic field is strong [38] and leads to the gap closing at a field scale corresponding to half of a flux quantum threading the cross-section area A: $B^*_{\mathrm{III}} \sim h/(4eA) \sim 0.1$ T [39]. A comparison with a simulation in which orbital effects are absent, shown in the Fig. 6.16, confirms that orbital effects are crucial to explain the data. For the purpose of inducing topological superconductivity with well-separated Majorana zero modes, region III is unsuitable due to the vanishing bulk gap. Instead, region II is more promising: in the infinite length limit, it hosts topological phases with a sizable gap, as indicated by the dashed grey lines in Fig. 6.3b. In the finite-length island, however, identifying these topological phases is hard due to the energy splitting between Majorana zero modes [29, 32]. Numerical simulations indicate that the shortest coherence length achievable in the topological phase is ∼ 200 nm (see Fig. 6.15), leading to a sizable splitting with characteristic field oscillations of increasing amplitude, see Fig. 6.3d. To complicate the matter further, oscillations of the lowest energy level as a function of magnetic field can also be observed in the topologically trivial regions for different plunger gate voltage values in both regions II and III, as also shown in Fig. 6.3d. We note that in our simulations the oscillation amplitude increases with field in the topological phase, but not necessarily in the trivial phase, as was pointed out using simpler models [27, 29, 32]. These energy oscillations can be measured in detail in the experiment as they reveal themselves in the even-odd peak spacings of conductance oscillations [11]. An example measured in the promising region II is shown in Fig. 6.4a. The $2e$-spaced peaks first split at $B \sim 0.3$ T, initially leading to a brief $2e$ odd-parity regime [14] and then

[1] This correspondence is only qualitative; we do not aim at matching the precise gate intervals since the charge environment present in the experimental device is not precisely known.

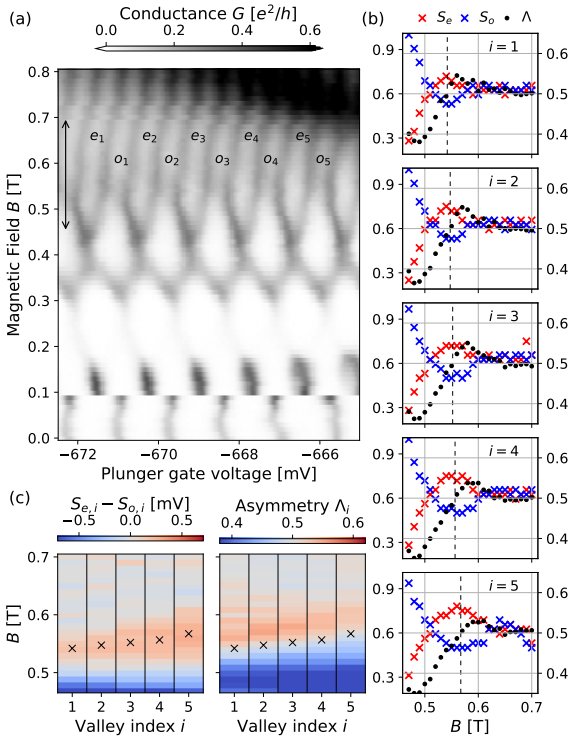

Figure 6.4: *(a)* Coulomb blockade oscillations measured versus plunger gate and magnetic field in region II of the phase diagram. The measurement covers five pairs of even-odd Coulomb valleys (labeled by index $i = 1,\ldots,5$) in the field range indicated by the black arrow. *(b)* Field dependence of the even and odd peak spacings $S_{\mathrm{e,o}}$ (left y axis, in mV) and of the peak height asymmetry Λ (right y axis) for each pair of Coulomb valleys. Vertical dashed lines denote the linearly interpolated values of B at which $\Lambda = 0.5$, corresponding to equal peak heights. These values of B closely match extremal points in $S_{\mathrm{e,o}}$. *(c)* Peak spacing difference and peak height asymmetry as a function of magnetic field. Black crosses correspond to the values of B denoted by vertical dashed lines in panel (b).

to an even-odd regime, for which we show peak spacing oscillations in Fig. 6.4b. In both the even and odd valleys, the peak spacings undergo one oscillation in magnetic field before the onset of regularly spaced $1e$-peaks at $B \sim 0.65$ T, likely due to poisoning in the Al shell. We also notice that the amplitude and position of the peak spacing oscillations change across neighboring valleys, increasing with gate voltage and conferring each valley an individual character, as shown in Fig. 6.4c. This shift could be attributed to the strong lever arm between the gate and the semiconductor causing a change in the effective chemical potential of the proximitized InSb bands. In correspondence with the peak spacing oscillations, we also observe oscillating peak heights. As we show in Fig. 6.4b, these can be captured by the asymmetry parameter $\Lambda = G_{\mathrm{e}\to\mathrm{o}}/(G_{\mathrm{e}\to\mathrm{o}} + G_{\mathrm{o}\to\mathrm{e}})$ where $G_{\mathrm{e}\to\mathrm{o}}$ and $G_{\mathrm{o}\to\mathrm{e}}$ are two neighboring peak heights[2]. The parameter Λ is related to the electron and hole components of the subgap state mediating the transport at the even-odd charge degeneracy point. In a minimal theory of two coupled Majorana zero modes, it is predicted to oscillate in anti-phase with the energy oscillations [48]. Such a correlation between peak spacing and peak heights is visible in Fig. 6.4b-c: in each valley, the symmetric peak heights ($\Lambda = 0.5$) occurring at $B \sim 0.55$ T have close-to-maximal peak spacings. Other datasets taken in region II show similar behavior, see Figs. 6.12 and 6.13. However, in the presence of only a single oscillation we cannot take this as conclusive evidence distinguishing Majorana zero modes from subgap states of trivial origin.

6.4. DISCUSSION

To conclude, our measurements and simulations have brought to light a new mechanism behind the $2e$-to-$1e$ transition in proximitized nanowires, distinct from the transition into a topological phase with Majorana zero-energy modes. A strategy to distinguish the two types of $2e$-to-$1e$ transitions would be to measure a sequence of large parity phase diagrams such as the one in Fig. 6.2 for wires of increasing length, in order to systematically decrease finite-size effects while also capturing the different plunger gate voltage regimes.

DATA AVAILABILITY

The data and the codes that create the figures in this chapter are available at `https://doi.org/10.4121/13333451.v2`.

[2] In Fig. 6.4b and c we plot the average value over two neighboring o → e peaks for each even valley.

6.5. SUPPLEMENTARY INFORMATION

6.5.1. ADDITIONAL EXPERIMENTAL DATA

We include in this Supplementary the following data:

- A voltage bias versus plunger gate scan showing $2e$-periodic Coulomb diamonds at $B = 0$, Fig. 6.5.
- A tunneling conductance measurement showing the parallel critical field of the Al shell, Fig. 6.6.
- A plunger gate versus tunnel gate conductance scan, which is a calibration measurement for the phase diagram measurement reported in Fig. 6.7.
- Two additional large-range conductance measurements of Coulomb blockade oscillations as a function of plunger gate and magnetic field, showing in larger detail the $2e$-$1e$ transition occuring at different fields in region I and III; see Fig. 6.8 and 6.9.
- The standard deviation of the peak spacing distribution measured as a function of plunger gate and magnetic field for the same data used in the phase diagram in Fig. 6.1, see Fig. 6.10.
- A second parity phase diagram obtained for a different device than considered in the main text, Fig. 6.11. This second device is the same previously studied in Ref. [14].
- Two additional datasets taken in region II of the device discussed in the main text, showing Coulomb peak and height oscillations as a function of magnetic field, see Fig. 6.12 and 6.13.
- In Fig. 6.14 we show numerical simulations of the energy gap similar to the left panel of Fig. 6.3, but with an uncorrelated disorder potential.
- In Fig. 6.15 we show numerical simulations of the topological coherence length in the bulk wire for the same parameters as the middle panel in Fig. 6.3.
- In Fig. 6.16 we show numerical simulations of the energy gap similar to the left panel of Fig. 6.3, but with the orbital effect of the magnetic field turned off.

As mentioned above, we refer to our earlier study of a nominally identical device [14] for further technical details on growth, fabrication and measurements.

6.5.2. NUMERICAL SIMULATIONS

The numerical simulations are performed with the same code as described in Ref. [18]. In this code the superconductor is integrated out into a self-energy boundary condition. The normal-state Hamiltonian used in the numerical simulations is given by

$$H_0 + \left[(\vec{p} + e\vec{A})^T/(2m(\vec{r}))(\vec{p} + e\vec{A}) - E_F(\vec{r}) + \Phi(\vec{r})\right]\sigma_0 + \frac{1}{2}\left[\vec{\alpha}(\vec{r}) \cdot \left(\vec{\sigma} \times (\vec{p} + e\vec{A})\right) + \left(\vec{\sigma} \times (\vec{p} + e\vec{A})\right) \cdot \vec{\alpha}(\vec{r})\right] + Bg(\vec{r})\frac{\mu_B}{2}\sigma_z, \tag{6.1}$$

where E_F is the Fermi level, Φ is the potential energy and $\vec{\alpha}$ is the spin-orbit coupling. We solve for the electrostatic potential in a separate step using the Thomas-Fermi approximation, analogous to what is done in Ref. [39]. In the electrostatic calculations, all surface and dielectric charge density are set to zero. In the semiconductor (InSb) we take $m_{\text{semi}} = 0.013\, m_0$, $E_{\text{F,semi}} = 0$, $\vec{\alpha} = (0, 0.1, 0)$ eV nm and $g_{\text{semi}} = -50$ [49]. In the superconductor (Al) we take $m_{\text{super}} = m_0$, $E_{\text{F,super}} = 11.7$ eV and $\vec{\alpha} = 0$. For simplicity we also set $g_{\text{super}} = 0$. The vector potential $\vec{A} = \left(0, 0, By\right)$ corresponds to a spatially homogeneous magnetic field in x-direction.

The Bogoliubov-de-Gennes Hamiltonian is given by

$$H_{\text{BdG}} = \begin{bmatrix} H_0(\vec{r}, \vec{A}) & \Delta(B, \vec{r}) \\ \Delta^*(B, \vec{r}) & -\sigma_y H_0(\vec{r}, -\vec{A})^* \sigma_y \end{bmatrix}, \tag{6.2}$$

with the pairing in the superconductor given by

$$\Delta(B, \vec{r}) = \Delta_0 e^{i\varphi(B,\vec{r})} \left(1 - \frac{B^2}{B_{\text{crit}}^2}\right), \tag{6.3}$$

where $\varphi(B, \vec{r})$ is the superconducting phase obtained by minimizing the supercurrent as in Ref. [39] and $B_{\text{crit}} = 1$ T is the critical magnetic field of the superconductor.

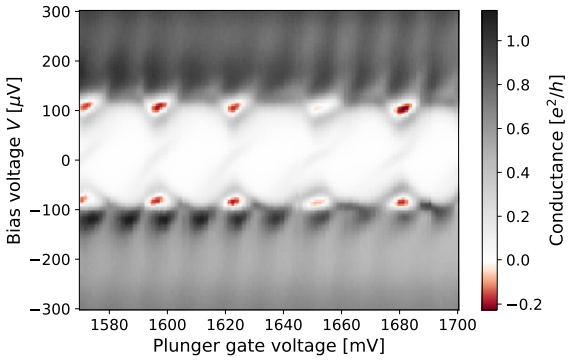

Figure 6.5: Conductance versus bias voltage and plunger gate at $B = 0$, showing $2e$-periodic Coulomb oscillations around zero bias voltage. From the onset of $1e$-periodic Coulomb oscillations at a high bias voltage $\sim 160\,\mu$V, we extract a charging energy $E_c \sim 20\,\mu$eV.

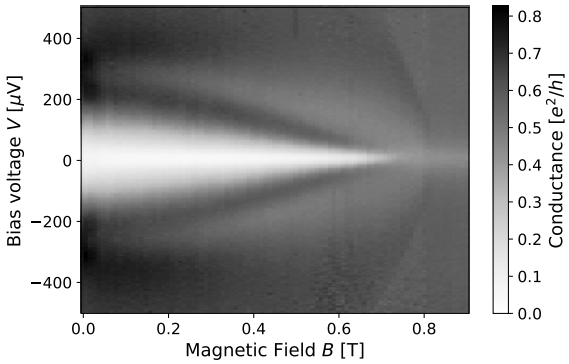

Figure 6.6: Measurement of the parallel critical field of the Al shell of the island via tunneling conductance. This measurement is performed by opening the left tunnel gate ($V_{\mathrm{LTG}} = 2$ V), while keeping the right tunnel gate in the tunneling regime ($V_{\mathrm{RTG}} = -2$ V). The critical field is $B_c \sim 0.8$ T.

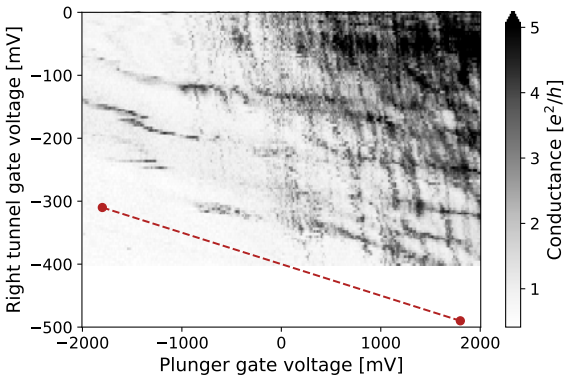

Figure 6.7: Right tunnel gate versus plunger gate conductance map, measured at zero bias voltage, that illustrates the tunnel gate compensation implemented during the phase diagram measurement of Fig. 6.2. In the phase diagram measurement, the left tunnel gate was kept fixed at $V_{\mathrm{LTG}} = -0.03$ V, while the right tunnel gate was varied together with the plunger gate following the red dashed line, in order to remain close to the tunneling regime throughout the measurement.

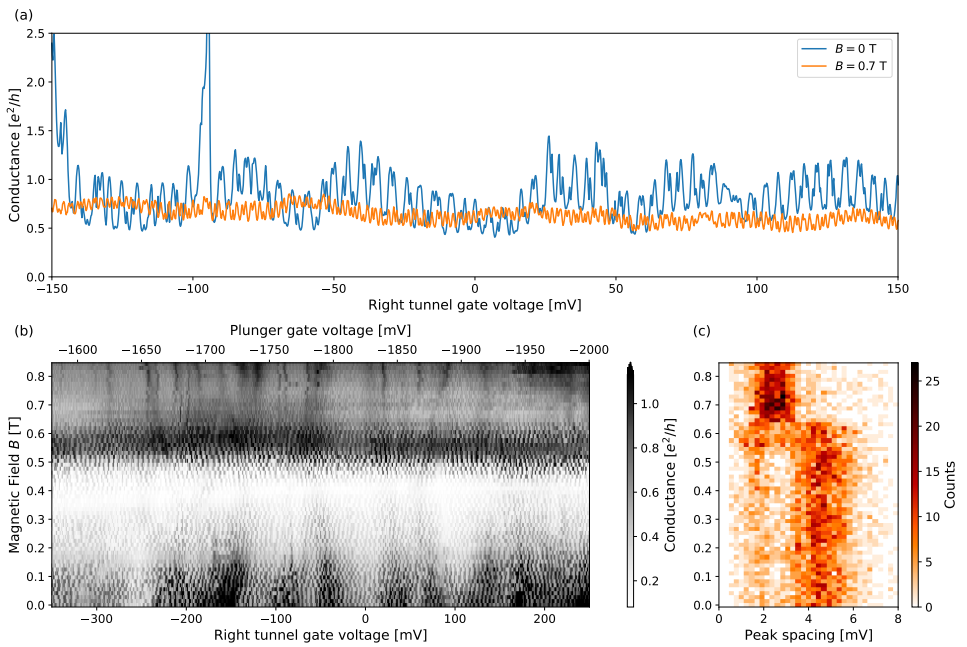

Figure 6.8: *(a-b)* Large-range conductance measurement in the negative plunger gate voltage (region I of the main text). Here the right tunnel gate is varied, with the left tunnel gate kept fixed at $V_{\mathrm{LTG}} = -0.03$ V. Panel (a) shows a selection of linetraces from panel (b). *(c)* Corresponding peak spacing histogram. The $2e$-$1e$ transition field is not affected by the compensation in tunnel gate voltage and fluctuations in the background conductance.

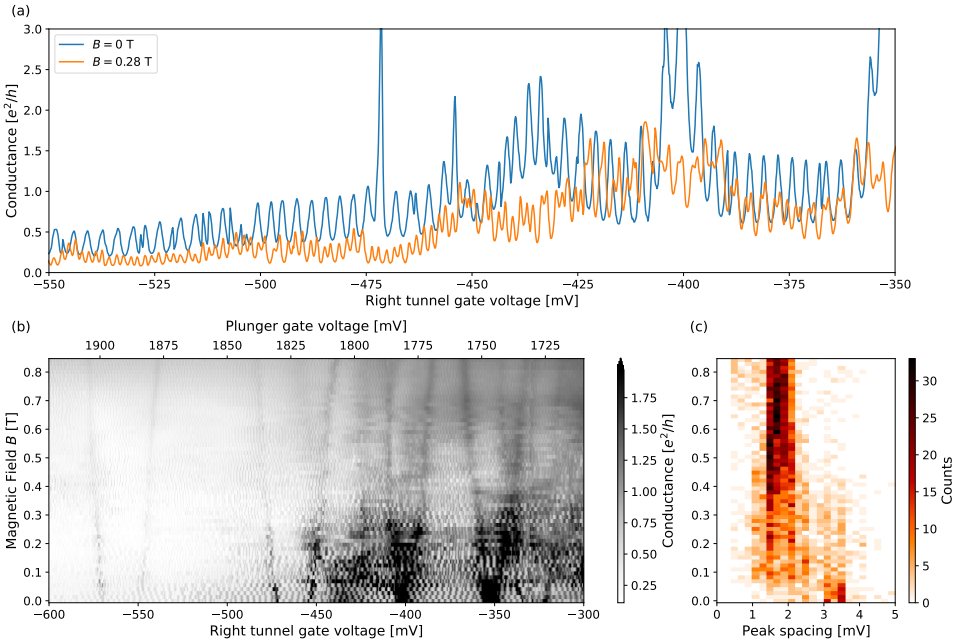

Figure 6.9: *(a- b)* Large-range conductance measurement in the positive plunger gate voltage (region III of the main text). Here the right tunnel gate is varied, with the left tunnel gate kept fixed at $V_{\mathrm{LTG}} = -0.03$ V. Panel (a) shows a selection of linetraces from panel (b). *(c)* Corresponding peak spacing histogram. As in the previous Fig. 6.8, the $2e$-$1e$ transition field is not affected by the compensation in tunnel gate voltage and fluctuations in the background conductance.

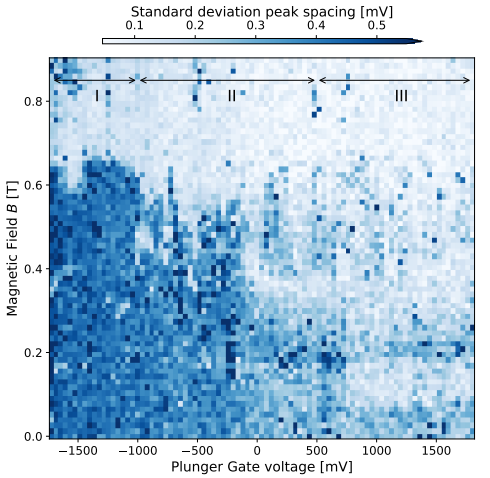

Figure 6.10: Standard deviation of the peak spacings as a function of magnetic field and plunger gate. Regions I, II, III are indicated in analogy to Fig. 6.2. The larger fluctuations occurring at $B \lesssim 0.65$T in regions II and III are an indication of the even-odd regime of Coulomb oscillations, distinguished from the more regular $1e$ regime occurring at $B \gtrsim 0.65$T.

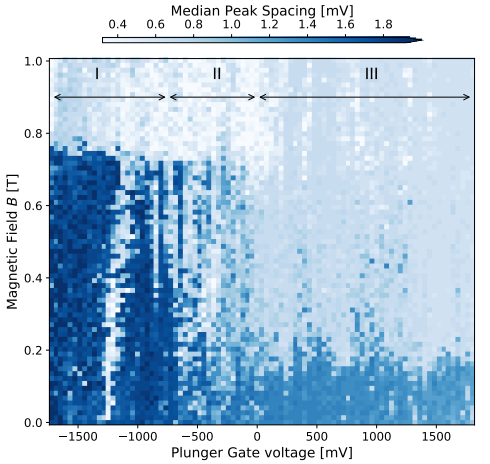

Figure 6.11: A second phase diagram measurement, executed on the same island device measured in Ref. [14]. This device also shows three characteristic regions as in Fig. 6.2, although the transition between region I and III is more abrupt. Also note the larger value of B^* in region III compared to the phase diagram of Fig. 6.2, which we attribute to the nanowire having a small diameter.

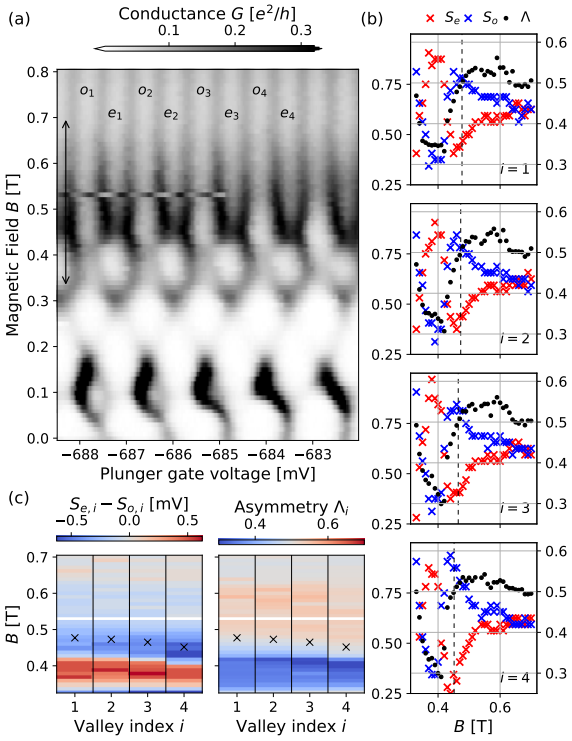

Figure 6.12: Coulomb peak spacings and oscillation analysis, analogous to Fig. 6.4, for an additional dataset measured in region II. In panels (b) and (c), data points at $B = 0.54$ T are omitted since their valley identification is ambiguous due to the gate jump visible in panel (a).

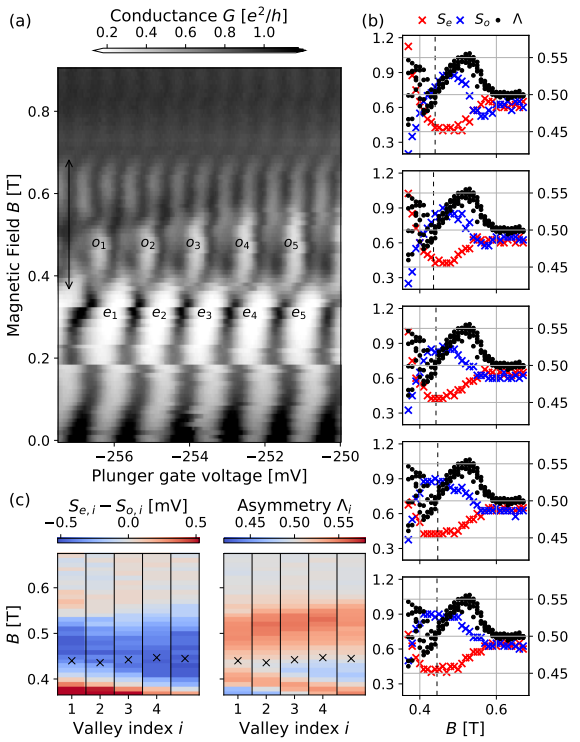

Figure 6.13: Coulomb peak spacings and oscillation analysis, analogous to Fig. 6.4, for an additional dataset measured in region II.

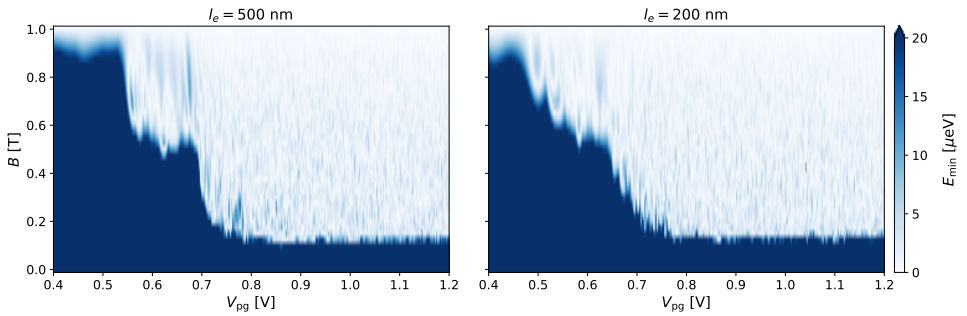

Figure 6.14: Energy gap as a function of plunger voltage and magnetic field in the simulated island for two different values of mean free path l_e. A single disorder realization is shown. We find that with increased disorder strength, and decreased mean free path, the boundaries between regions I, II and III become smeared.

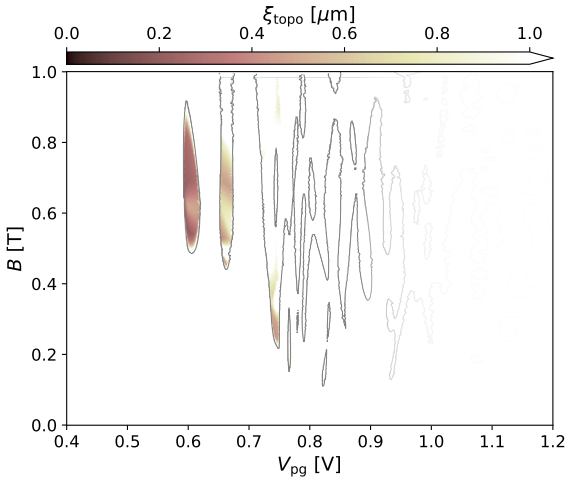

Figure 6.15: Topological coherence length as a function of plunger voltage and magnetic field in the bulk wire. The topological phase boundaries from the middle panel of Fig. 6.3b are shown as light grey lines. Only two topological phases at the lowest plunger values have a coherence length that is significantly shorter than the island length.

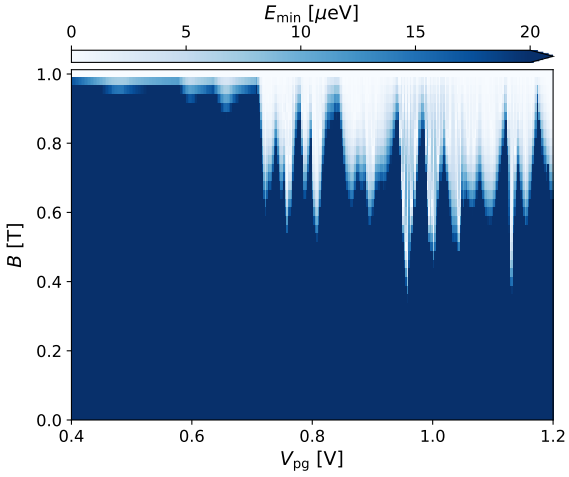

Figure 6.16: Energy gap as a function of plunger voltage and magnetic field in the simulated island with the orbital effect of the magnetic field turned off in the simulation. In comparison to the left panel of Fig. 6.3 the energy gap is not suppressed until much larger magnetic fields. Furthermore, the transition is strongly dependent on plunger gate voltage for voltages corresponding to region III in Fig. 6.3.

REFERENCES

[1] J. Shen, G. W. Winkler, F. Borsoi, S. Heedt, V. Levajac, J. Y. Wang, D. van Driel, D. Bouman, S. Gazibegovic, R. L. M. O. H. Veld, D. Car, J. A. Logan, M. Pendharkar, C. J. Palmstrøm, E. P. A. M. Bakkers, L. P. Kouwenhoven, and B. van Heck, *A full parity phase diagram of a majorana island,* (2020), arXiv:2012.10118 [cond-mat.mes-hall] .

[2] J. von Delft and D. Ralph, *Spectroscopy of discrete energy levels in ultrasmall metallic grains,* Phys. Rep. **345**, 61 (2001).

[3] P. Lafarge, P. Joyez, D. Esteve, C. Urbina, and M. H. Devoret, *Measurement of the even-odd free-energy difference of an isolated superconductor,* Phys. Rev. Lett. **70**, 994 (1993).

[4] L. J. Geerligs, V. F. Anderegg, J. Romijn, and J. E. Mooij, *Single Cooper-pair tunneling in small-capacitance junctions,* Phys. Rev. Lett. **65**, 377 (1990).

[5] M. T. Tuominen, J. M. Hergenrother, T. S. Tighe, and M. Tinkham, *Experimental evidence for parity-based 2e periodicity in a superconducting single-electron tunneling transistor,* Phys. Rev. Lett. **69**, 1997 (1992).

[6] T. M. Eiles, J. M. Martinis, and M. H. Devoret, *Even-odd asymmetry of a superconductor revealed by the Coulomb blockade of Andreev reflection,* Phys. Rev. Lett. **70**, 1862 (1993).

[7] A. T. Johnson, L. P. Kouwenhoven, W. de Jong, N. C. van der Vaart, C. J. P. M. Harmans, and C. T. Foxon, *Zero-dimensional states and single electron charging in quantum dots,* Phys. Rev. Lett. **69**, 1592 (1992).

[8] E. B. Foxman, P. L. McEuen, U. Meirav, N. S. Wingreen, Y. Meir, P. A. Belk, N. R. Belk, M. A. Kastner, and S. J. Wind, *Effects of quantum levels on transport through a Coulomb island,* Phys. Rev. B **47**, 10020 (1993).

[9] Y. Alhassid, *The statistical theory of quantum dots,* Rev. Mod. Phys. **72**, 895 (2000).

[10] A. P. Higginbotham, S. M. Albrecht, G. Kiršanskas, W. Chang, F. Kuemmeth, P. Krogstrup, T. S. Jespersen, J. Nygård, K. Flensberg, and C. M. Marcus, *Parity lifetime of bound states in a proximitized semiconductor nanowire,* Nat. Phys. **11**, 1017 (2015).

[11] S. M. Albrecht, A. P. Higginbotham, M. Madsen, F. Kuemmeth, T. S. Jespersen, J. Nygård, P. Krogstrup, and C. M. Marcus, *Exponential protection of zero modes in Majorana islands,* Nature **531**, 206 (2016).

[12] S. M. Albrecht, E. B. Hansen, A. P. Higginbotham, F. Kuemmeth, T. S. Jespersen, J. Nygård, P. Krogstrup, J. Danon, K. Flensberg, and C. M. Marcus, *Transport signatures of quasiparticle poisoning in a Majorana island,* Phys. Rev. Lett. **118**, 137701 (2017).

[13] E. C. T. O'Farrell, A. C. C. Drachmann, M. Hell, A. Fornieri, A. M. Whiticar, E. B. Hansen, S. Gronin, G. C. Gardner, C. Thomas, M. J. Manfra, K. Flensberg, C. M. Marcus, and F. Nichele, *Hybridization of subgap states in one-dimensional superconductor-semiconductor Coulomb islands,* Phys. Rev. Lett. **121**, 256803 (2018).

[14] J. Shen, S. Heedt, F. Borsoi, B. van Heck, S. Gazibegovic, R. L. M. Op het Veld, D. Car, J. A. Logan, M. Pendharkar, S. J. J. Ramakers, G. Wang, D. Xu, D. Bouman, A. Geresdi, C. J. Palmstrøm, E. P. A. M. Bakkers, and L. P. Kouwenhoven, *Parity transitions in the superconducting ground state of hybrid InSb-Al Coulomb islands,* Nat. Commun. **9**, 4801 (2018).

[15] S. Vaitiekenas, A. M. Whiticar, M.-T. Deng, F. Krizek, J. E. Sestoft, C. J. Palmstrøm, S. Marti-Sanchez, J. Arbiol, P. Krogstrup, L. Casparis, and C. M. Marcus, *Selective-area-grown semiconductor-superconductor hybrids: A basis for topological networks,* Phys. Rev. Lett. **121**, 147701 (2018).

[16] J. van Veen, A. Proutski, T. Karzig, D. I. Pikulin, R. M. Lutchyn, J. Nygård, P. Krogstrup, A. Geresdi, L. P. Kouwenhoven, and J. D. Watson, *Magnetic-field-dependent quasiparticle dynamics of nanowire single-Cooper-pair transistors,* Phys. Rev. B **98**, 174502 (2018).

[17] M. Pendharkar, B. Zhang, H. Wu, A. Zarassi, P. Zhang, C. P. Dempsey, J. S. Lee, S. D. Harrington, G. Badawy, S. Gazibegovic, J. Jung, A. H. Chen, M. A. Verheijen, M. Hocevar, E. P. A. M. Bakkers, C. J. Palmstrøm, and S. M. Frolov, *Parity-preserving and magnetic field resilient superconductivity in indium antimonide nanowires with tin shells,* arXiv e-prints **1912.06071** (2019).

[18] S. Vaitiekėnas, G. W. Winkler, B. van Heck, T. Karzig, M.-T. Deng, K. Flensberg, L. I. Glazman, C. Nayak, P. Krogstrup, R. M. Lutchyn, and C. M. Marcus, *Flux-induced topological superconductivity in full-shell nanowires,* Science **367** (2020).

[19] A. M. Whiticar, A. Fornieri, E. C. T. O'Farrell, A. C. C. Drachmann, T. Wang, C. Thomas, S. Gronin, R. Kallaher, G. C. Gardner, M. J. Manfra, C. M. Marcus, and F. Nichele, *Coherent transport through a Majorana island in an Aharonov–Bohm interferometer,* Nat. Commun. **11**, 3212 (2020).

[20] D. J. Carrad, M. Bjergfelt, T. Kanne, M. Aagesen, F. Krizek, E. M. Fiordaliso, E. Johnson, J. Nygård, and T. Sand Jespersen, *Shadow epitaxy for in Situ growth of generic semiconductor/superconductor hybrids,* Adv. Mater. **32**, 1908411 (2020).

[21] T. Kanne, M. Marnauza, D. Olsteins, D. J. Carrad, J. E. Sestoft, J. de Bruijckere, L. Zeng, E. Johnson, E. Olsson, K. Grove-Rasmussen, and J. Nygård, *Epitaxial Pb on InAs nanowires,* ArXiv e-prints **2002.11641** (2020).

[22] R. M. Lutchyn, E. P. A. M. Bakkers, L. P. Kouwenhoven, P. Krogstrup, C. M. Marcus, and Y. Oreg, *Majorana zero modes in superconductor–semiconductor heterostructures,* Nat. Rev. Mater. **3**, 52 (2018).

[23] L. Fu, *Electron teleportation via Majorana bound states in a mesoscopic superconductor,* Phys. Rev. Lett. **104**, 056402 (2010).

[24] B. van Heck, R. M. Lutchyn, and L. I. Glazman, *Conductance of a proximitized nanowire in the Coulomb blockade regime,* Phys. Rev. B **93**, 235431 (2016).

[25] C. Nayak, S. H. Simon, A. Stern, M. Freedman, and S. Das Sarma, *Non-Abelian anyons and topological quantum computation,* Rev. Mod. Phys. **80**, 1083 (2008).

[26] T. Karzig, C. Knapp, R. M. Lutchyn, P. Bonderson, M. B. Hastings, C. Nayak, J. Alicea, K. Flensberg, S. Plugge, Y. Oreg, C. M. Marcus, and M. H. Freedman, *Scalable designs for quasiparticle-poisoning-protected topological quantum computation with Majorana zero modes,* Phys. Rev. B **95**, 235305 (2017).

[27] C.-K. Chiu, J. D. Sau, and S. Das Sarma, *Conductance of a superconducting Coulomb-blockaded Majorana nanowire,* Phys. Rev. B **96**, 054504 (2017).

[28] E. Prada, P. San-Jose, M. W. A. de Moor, A. Geresdi, E. J. H. Lee, J. Klinovaja, D. Loss, J. Nygård, R. Aguado, and L. P. Kouwenhoven, *From Andreev to Majorana bound states in hybrid superconductor–semiconductor nanowires,* Nature Reviews Physics **2**, 575 (2020).

[29] S. Das Sarma, J. D. Sau, and T. D. Stanescu, *Splitting of the zero-bias conductance peak as smoking gun evidence for the existence of the Majorana mode in a superconductor-semiconductor nanowire,* Phys. Rev. B **86**, 220506 (2012).

[30] O. Dmytruk and J. Klinovaja, *Suppression of the overlap between Majorana fermions by orbital magnetic effects in semiconducting-superconducting nanowires,* Phys. Rev. B **97**, 155409 (2018).

[31] Z. Cao, H. Zhang, H.-F. Lü, W.-X. He, H.-Z. Lu, and X. C. Xie, *Decays of Majorana or Andreev oscillations induced by steplike spin-orbit coupling,* Phys. Rev. Lett. **122**, 147701 (2019).

[32] G. Sharma, C. Zeng, T. Stanescu, and S. Tewari, *Hybridization energy oscillations of Majorana and Andreev bound states in semiconductor-superconductor nanowire heterostructures,* Phys. Rev. B **101**, 245405 (2020).

[33] S. Gazibegovic, D. Car, H. Zhang, S. C. Balk, J. A. Logan, M. W. A. de Moor, M. C. Cassidy, R. Schmits, D. Xu, G. Wang, P. Krogstrup, R. L. M. Op het Veld, K. Zuo, Y. Vos, J. Shen, D. Bouman, B. Shojaei, D. Pennachio, J. S. Lee, P. J. van Veldhoven, S. Koelling, M. A. Verheijen, L. P. Kouwenhoven, C. J. Palmstrøm, and E. P. A. M. Bakkers, *Epitaxy of advanced nanowire quantum devices,* Nature **584**, 434 (2017).

[34] M. T. Tuominen, J. M. Hergenrother, T. S. Tighe, and M. Tinkham, *Even-odd electron number effects in a small superconducting island: Magnetic-field dependence,* Phys. Rev. B **47**, 11599 (1993).

[35] A. Vuik, D. Eeltink, A. R. Akhmerov, and M. Wimmer, *Effects of the electrostatic environment on the Majorana nanowire devices,* New J. Phys. **18**, 033013 (2016), arXiv:1511.08044 .

[36] A. E. G. Mikkelsen, P. Kotetes, P. Krogstrup, and K. Flensberg, *Hybridization at superconductor-semiconductor interfaces,* Phys. Rev. X **8**, 031040 (2018).

[37] A. E. Antipov, A. Bargerbos, G. W. Winkler, B. Bauer, E. Rossi, and R. M. Lutchyn, *Effects of gate-induced electric fields on semiconductor Majorana nanowires,* Phys. Rev. X **8**, 031041 (2018).

[38] G. W. Winkler, D. Varjas, R. Skolasinski, A. A. Soluyanov, M. Troyer, and M. Wimmer, *Orbital contributions to the electron g factor in semiconductor nanowires,* Phys. Rev. Lett. **119**, 037701 (2017).

[39] G. W. Winkler, A. E. Antipov, B. Van Heck, A. A. Soluyanov, L. I. Glazman, M. Wimmer, and R. M. Lutchyn, *Unified numerical approach to topological semiconductor-superconductor heterostructures,* Phys. Rev. B **99**, 245408 (2019).

[40] B. Nijholt and A. R. Akhmerov, *Orbital effect of magnetic field on the Majorana phase diagram,* Phys. Rev. B **93**, 235434 (2016).

[41] A. Kringhøj, G. W. Winkler, T. W. Larsen, D. Sabonis, O. Erlandsson, P. Krogstrup, B. van Heck, K. D. Petersson, and C. M. Marcus, *Andreev modes from phase winding in a full-shell nanowire-based transmon,* (2020), arXiv:2008.10013 [cond-mat.mes-hall] .

[42] W. S. Cole, S. Das Sarma, and T. D. Stanescu, *Effects of large induced superconducting gap on semiconductor majorana nanowires,* Phys. Rev. B **92**, 174511 (2015).

[43] O. Gul, H. Zhang, F. K. de Vries, J. van Veen, K. Zuo, V. Mourik, S. Conesa-Boj, M. P. Nowak, D. J. van Woerkom, M. Quintero-Pérez, M. C. Cassidy, A. Geresdi, S. Koelling, D. Car, S. R. Plissard, E. P. A. M. Bakkers, and L. P. Kouwenhoven, *Hard superconducting gap in InSb nanowires,* Nano Lett. **17**, 2690 (2017).

[44] M. W. A. de Moor, J. D. S. Bommer, D. Xu, G. W. Winkler, A. E. Antipov, A. Bargerbos, G. Wang, N. van Loo, R. L. M. O. het Veld, S. Gazibegovic, D. Car, J. A. Logan, M. Pendharkar, J. S. Lee, E. P. A. M. Bakkers, C. J. Palmstrøm, R. M. Lutchyn, L. P. Kouwenhoven, and H. Zhang, *Electric field tunable superconductor-semiconductor coupling in Majorana nanowires,* New J. Phys. **20**, 103049 (2018).

[45] A. Larkin, *Superconductor of small dimensions in a strong magnetic field,* Soviet Physics JETP **21**, 153 (1965).

[46] A. Haim and A. Stern, *Benefits of weak disorder in one-dimensional topological superconductors,* Phys. Rev. Lett. **122**, 126801 (2019).

[47] T. Laeven, B. Nijholt, M. Wimmer, and A. Akhmerov, *Enhanced proximity effect in zigzag-shaped Majorana Josephson junctions,* Phys. Rev. Lett. **125**, 086802 (2020).

[48] E. B. Hansen, J. Danon, and K. Flensberg, *Probing electron-hole components of subgap states in Coulomb blockaded Majorana islands*, Phys. Rev. B **97**, 041411 (2018).

[49] I. Vurgaftman, J. R. Meyer, and L. R. Ram-Mohan, *Band parameters for III–V compound semiconductors and their alloys*, Journal of applied physics **89**, 5815 (2001).

7

HIGH MOBILITY STEMLESS INSB NANOWIRES

High aspect-ratio InSb nanowires (NWs) of high chemical purity are sought for implementing advanced quantum devices. The growth of InSb NWs is challenging, generally requiring a stem of a foreign material for nucleation. Such a stem tends to limit the length of InSb NWs and its material becomes incorporated in the InSb segment. Here, we report on the growth of chemically pure InSb NWs tens of microns long. Using a selective-area mask in combination with gold as a catalyst allows complete omission of the stem, thus demonstrating that InSb NWs can grow directly from the substrate. The introduction of the selective-area mask gives rise to novel growth kinetics, demonstrating high growth rates and complete suppression of layer deposition on the mask for Sb-rich conditions. The crystal quality and chemical purity of these NWs is reflected in the significant enhancement of low temperature electron mobility, yielding an average of 4.4 $\times 10^4$ *cm*^{2}*/Vs, compared to previously studied InSb NWs grown on stems.*

This chapter has been published as, G. Badawy, S. Gazibegovic, F. Borsoi, S. Heedt, C. –A. Wang, S. Koelling, M. A. Verheijen, L. P. Kouwenhoven, and E. P. A. M. Bakkers, *High Mobility Stemless InSb Nanowires*, Nano Letters 19, 3575–3582 (2019) [1].

7.1. INTRODUCTION

Indium-antimonide (InSb) nanowires (NWs) have sparked interest in the past few years due to their potential to host Majorana zero modes (MZMs) [2–4], prime candidates for topological quantum computing [5–7]. InSb has further unfolded as an ideal material for spin-orbit quantum bits (qubits) [8–10] due to its giant Landé g-factor (≈ 51) and strong spin-orbit interaction (SOI) [11, 12]. Additionally, InSb offers other unique properties such as a large bulk electron mobility of 7.7×10^4 cm^2/VS at 300 K [11, 13], and provides a convenient platform for semiconducting-superconducting hybrid devices [14–17]. Despite its ability to outperform the majority of III-Vs in many aspects, synthesis of free-standing InSb nanostructures has proven to be rather challenging.

7.2. STEMMED VS STEMLESS NANOWIRES

The challenges associated with growing InSb NWs are primarily due to the low vapor pressure and surface energy of antimony (Sb). In particular, when in excess, the evaporation of Sb is less favorable causing it to stick to epitaxial surfaces [18]. Importantly, Sb is a *surfactant* — known to change the wetting properties of surfaces — likely to impede NW growth and affect the migration length of adatoms. More specifically, instead of being pushed up to promote NW growth [19], the metal catalysts are rather propelled on the substrate surface, leaving behind a streak of grown material [18]. The inhibition of vertical growth is attributed to a decrease in contact angle between the catalyst droplet, in this case gold, and the substrate in presence of Sb (Figure 7.1a).

It is possible to nucleate InSb NWs on top of a NW stem of a different material, such as indium phosphide (InP) or indium arsenide (InAs) [18, 20–24]; thus, inhibiting the metal catalyst from spreading due to the small footprint of the stem (Figure 7.1b). Although InSb NW growth is thereby enabled, deposition on the sample surface occurs, as shown in Figure 7.1c,d, and competes with NW growth [21]. Even if deposition on the surface (layer growth) were to be suppressed by adding a selective-area (SA) mask (Figure 7.1e-g), the downsides of growth on stems still persist. Namely, a foreign stem induces the incorporation of material impurities into the InSb NW segment [20], and limits the length of the InSb NW, to a maximum of approximately 3.5 μm [21, 23], as depicted in Figure 7.1e-g. In particular, the stem made of InP, evaporates during the InSb growth; and hence, is not able to maintain the weight of the growing InSb NW, as is the case of Figure 7.1g. This length restriction is likely to limit their utilization in complex devices. Specifically, longer NWs are preferred as they could reduce the overlap between the wavefunctions of MZMs at the NW ends by spatially separating them [25] and would also offer the possibility to accommodate multiple superconducting islands [26, 27] required by various schemes for topological quantum computing based on braiding of MZMs [28–30].

In this work, we demonstrate a method that enables InSb NWs to grow directly from the substrate without requiring a foreign NW stem. Stem omission is realized by positioning catalyst droplets within restricted openings of a selective-area (SA) mask, as shown in Figure 7.1h. As a consequence, Sb is impeded from changing the surface energy of the epitaxial substrate; thus, ensuring a catalyst contact angle that permits NW growth. Introduction of the silicon nitride (Si_xN_y) mask completely suppresses layer growth (see Figure 7.1i,j) and unveils entirely different growth kinetics and adatom diffusion behavior

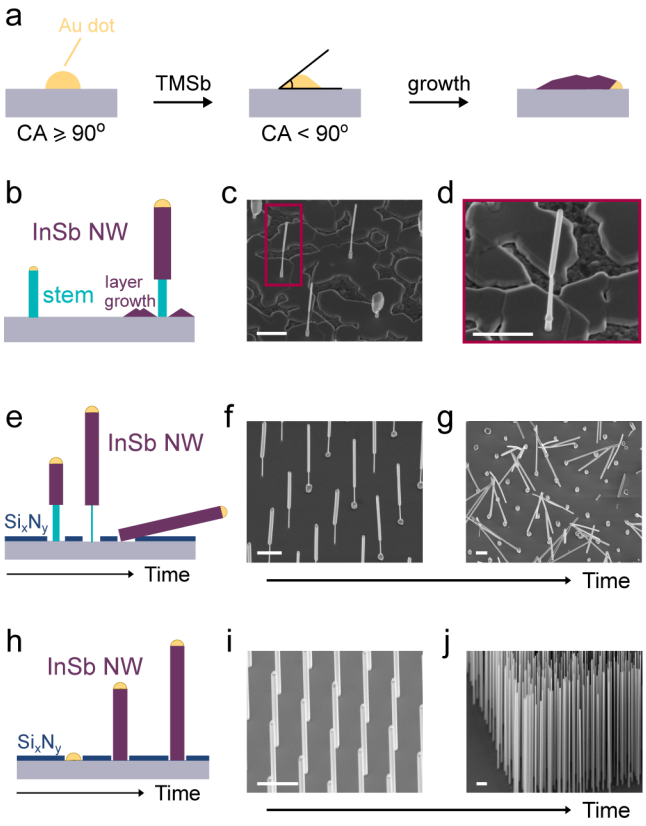

Figure 7.1: **Stem omission and stemless InSb NW growth**. (a) Response of the gold (Au) catalyst contact angle (CA) upon introduction of tri-methyl-antimony (TMSb). A reduction in CA to less than 90° prevails, which forbids NW growth. (b) Adding a NW stem (of a foreign material) allows for the nucleation of InSb NWs. (c) SEM images show InSb NWs grown on a stem. A red rectangle enlarged in (d) highlights the presence of layer growth on the substrate. (e) In order to suppress layer growth, a Si_xN_y mask is used. (f) The growth of stemmed InSb NWs on a masked substrate. (g) One limitation of growth on stems is, however, that as growth duration increases, the stem is thinned down due to evaporation and eventually perishes, leading InSb NWs to collapse on the substrate. (h) Since the presence of the Si_xN_y mask hinders the catalyst droplets from spreading, the stem is no longer needed, (i) demonstrating InSb NW growth directly from the substrate. (j) In contrast to stemmed growth, longer InSb NWs are achieved, up to tens of microns. All SEM images are 30°-tilt view and scale bars correspond to 1 μm.

in contrast to stemmed growth on unmasked substrates, as will be investigated in this paper. Most importantly, the presented technique gives rise to *stemless* InSb NWs. The length of these stemless wires reaches tens of microns, outperforming their stemmed counterparts in dimensions and electronic properties, marking them as promising candidates in various applications, such as mid-infrared photodetection [31, 32]. In particular, we show that InSb wires grown at T = 495 ^{o}C using metal organic vapor phase epitaxy (MOVPE) by this selective-area vapor liquid solid (SA-VLS) technique are chemically pure and, as a consequence, exhibit considerably higher electron mobility compared to previous studies on InSb NWs.

7.3. GROWTH KINETICS OF STEMLESS NANOWIRES

To investigate the emerging kinetics of the SA-VLS InSb NW growth, arrays of gold dots with different diameters spaced at varying distances are defined using electron beam lithography on an InSb (111)B substrate covered with a 20 nm Si_xN_y layer. Gold dots are positioned within differently sized nano-openings in the Si_xN_y (see Figure 7.2a I-III). The diameter of the openings is varied by means of wet-etching the Si_xN_y (details on substrate fabrication can be found in section 7.7.1). The interplay between gold droplet diameter and mask opening brings about new growth kinetics. To investigate the evolution of wire dimensions, we vary the mask opening diameter, denoted here by d_{mask}, for a given droplet size d_{Au} = 30 nm and perform a growth time series.

During early stages of the growth time series, we discern that the gold particle is consistently pushed to the edge of the mask opening, consistent with selective-area nucleation at edge sites (see section 7.7.3). This phenomenon persists until the opening is entirely covered by grown InSb. When that is achieved, the gold particle is centered with respect to the mask opening, which is already observed after 1 hour of growth (see Figure 7.2a IV-VI). The yield of these wires, estimated between 60 - 100%, is limited by the sliding of gold droplets under the mask during premature stages of growth, consequently leading to missing wires within one NW array (see section 7.7.3). Additionally, sometimes non-equal growth rates for wires within one NW array is noted caused by gold particle splitting during the sliding process, as shown in Figure 7.2a V. This sliding is dependent on NW pitch and gold diameter, being more probable for smaller gold diameters and bigger pitches.

Furthermore, we observe that the NW diameter increases with mask opening size and growth time. In fact, already after 1.5 hours of growth, the NW diameter exceeds d_{mask}, as shown in Figure 7.2b. Additionally, the alloyed gold droplet remains smaller in diameter compared to the NW diameter. These observations indicate the presence of a vapor-solid induced radial growth. The catalyst droplet thus drives the axial growth, which proceeds in a layer-by-layer fashion, determining the initial NW diameter. Therefore, a bigger gold droplet, results in a larger NW diameter for a given d_{mask}. The mask opening on the other hand determines the extent of radial growth, as depicted in Figure 7.2b. The complete absence of tapering in these wires together with the atomically flat side facets, however, signifies that if a new layer is formed it grows along the full length of the NW [33]. The low probability of nucleation on {110} side-walls commonly known for InSb NWs [20, 21], implies that the formation energy for a new step-edge is very high. As shown in Figure 7.2b, the enhanced radial growth observed for wires emanating from bigger openings together

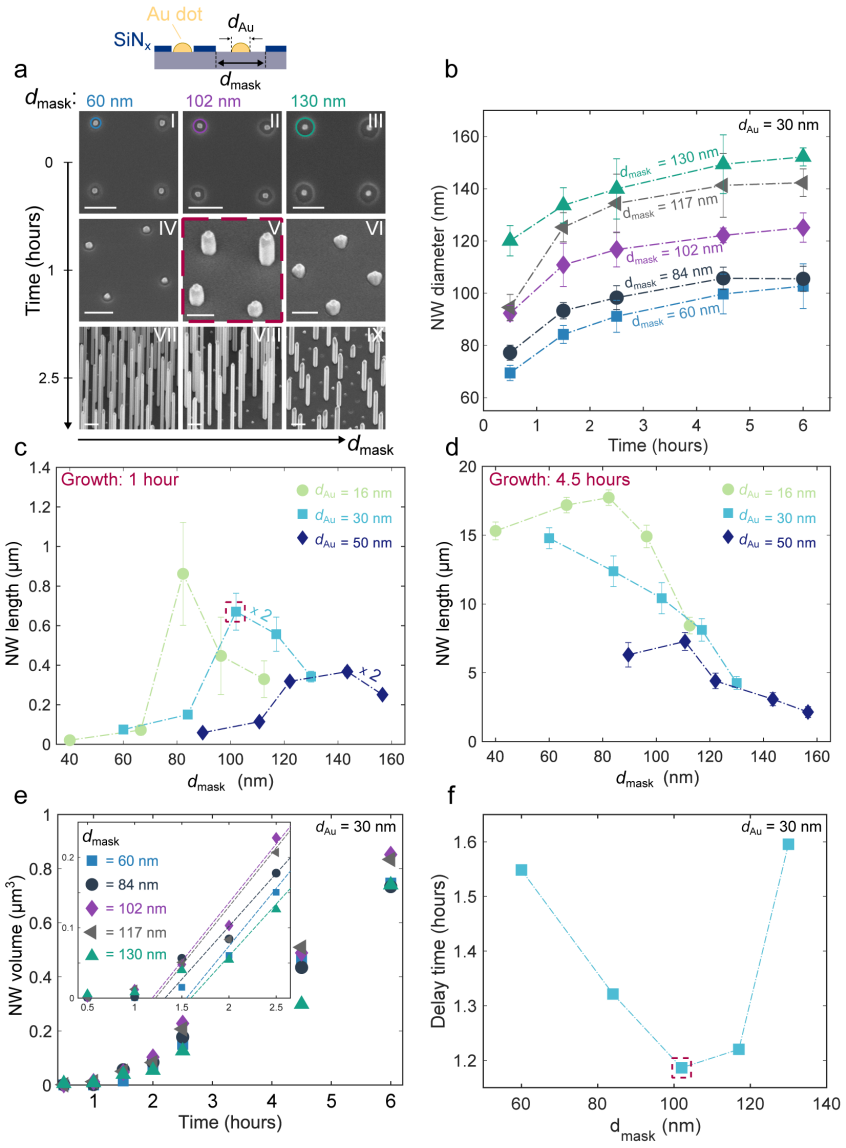

Figure 7.2: **Effect of gold dot diameter (d_{Au}) and mask opening (d_{mask}) on NW growth**. (a) SEM images, for a fixed d_{Au} = 30 nm, are organized in a matrix labeled with Roman numerals, where along a row, d_{mask} becomes larger and along a column, time increases (the scale bar is 0.25 μm for row 1 and 2, and 0.5 μm for row 3). (b) NW diameter increases with larger d_{mask} and longer growth time. (c) A peak in NW length exists after one hour of growth for all d_{Au} (curves for d_{Au} = 30 and 50 nm are multiplied by two for display purposes). (d) After 4.5 hours, the peak becomes less prominent. (e) The presence of these peaks is scrutinized by linear fits (inset) of the NW volume, for a fixed d_{Au} = 30 nm and various d_{mask}. Evolution of NW volume proceeds non-linearly with time during the first 1.5 hours, after which the growth rate becomes linear. The earliest intersection with the x-axis, indicates the fastest crossover to the linear regime. (f) The x-intercepts in (e) are shown as a function of d_{mask}, yielding the fastest crossover (minimum) for d_{mask} = 102 nm, which corresponds to the peak in (c) and V in (a) as marked by the dashed red square.

with the NW diameter not being defined by the gold particle size, highlights the dynamics affected by both d_{Au} and d_{mask}.

For a fixed d_{Au} = 30 nm and differently sized d_{mask} = [60, 84, 102, 117, 130] nm, we observe after 1 hour of growth, that NWs originating from d_{mask} = 102 nm grow the longest (≈ 350 nm), as shown in Figure 7.2a V and Figure 7.2c. Wires growing from smaller opening (d_{mask} = 60 nm, 84 nm), however, barely outgrow the mask thickness (Figure 7.2a IV and Figure 7.2c). For a diffusion limited growth process where the wire volume is constant, we would have expected wires grown from the smallest opening to have yielded the tallest NWs for a given growth time. Instead, we note that these wires experience a barrier towards the axial growth rate. We, therefore, propose an alternative mechanism governing the nucleation and growth of these wires, causing NWs arising from small openings to experience an *axial growth delay*. This delay could be attributed to a distinct droplet response to different mask openings. Particularly, during the early stages of nucleation, the gold particles positioned in the smallest mask openings experience a kinetic blockade; the catalyst particle increases in volume due to the uptake of precursors, but is confined by the mask opening and can therefore not yield the optimum contact angle for NW growth. Whereas growth from the biggest d_{mask} is governed by a diffusion-limited process. The optimum configuration thus exists for medium-sized openings, yielding the fastest axial growth rate during the first hour, as depicted in Figure 7.2a IV and Figure 7.2c. Once this blockade is overcome and the NW axial growth proceeds, a diffusion-limited process dominates the growth for all mask openings, yielding the shortest wires from the biggest openings after 4.5 hours, as shown in Figure 7.2d.

We further investigate this delay by including different gold particle sizes, d_{Au} = 16 nm and d_{Au} = 50 nm, respectively. As shown in Figure 7.2c,d, for d_{Au} = 16 nm, the mask opening encompasses the values d_{mask} = [40, 67, 82, 96, 112] nm and for d_{Au} = 50 nm, d_{mask} = [90, 111, 122, 144, 157] nm. After one hour of growth, a delay in axial growth indeed exists for all gold particle sizes, manifested by a peak in NW length for wires originating from openings with a ring of exposed substrate d_{mask} - d_{Au} < 66 nm (see Figure 7.2c). For instance, NWs grown for an hour from d_{Au} = 16 nm and d_{mask} < 82 nm have a length less than 100 nm, while those arising from d_{mask} = 82 nm are 0.86 μm long. After 4.5 hours of growth (Figure 7.2d), this peak becomes less distinguishable and shifts towards smaller openings for different gold droplet diameters. More specifically, this shift is observed for wires grown from d_{Au} = 30 nm and d_{Au} = 50 nm, as shown in Figure 7.2d. In contrast, NWs catalyzed by d_{Au} = 16 nm gold particles maintain a peak for the same mask opening after 4.5 hours, albeit the difference in NW length in comparison to wires growing from smaller d_{mask} becomes much less with time.

Whether the peak in NW length shifts or persists, could be derived from an interplay between two competing effects; the difference in NW length (ΔL) between wires originating from different d_{mask}, resulting from the axial growth delay and what we refer to as *volume effect*, which yields a slower axial growth rate for thicker wires (see section 7.7.4). Therefore, a peak shift towards smaller d_{mask} implies that as the growth time extends longer, the volume effect dominates, yielding the shortest wires from the biggest openings. A peak persistence, on the other hand would mean that ΔL was too big, causing the effect of the axial growth delay to last longer.

This delay is captured in more detail in Figure 7.2e, where NW volume is plotted as

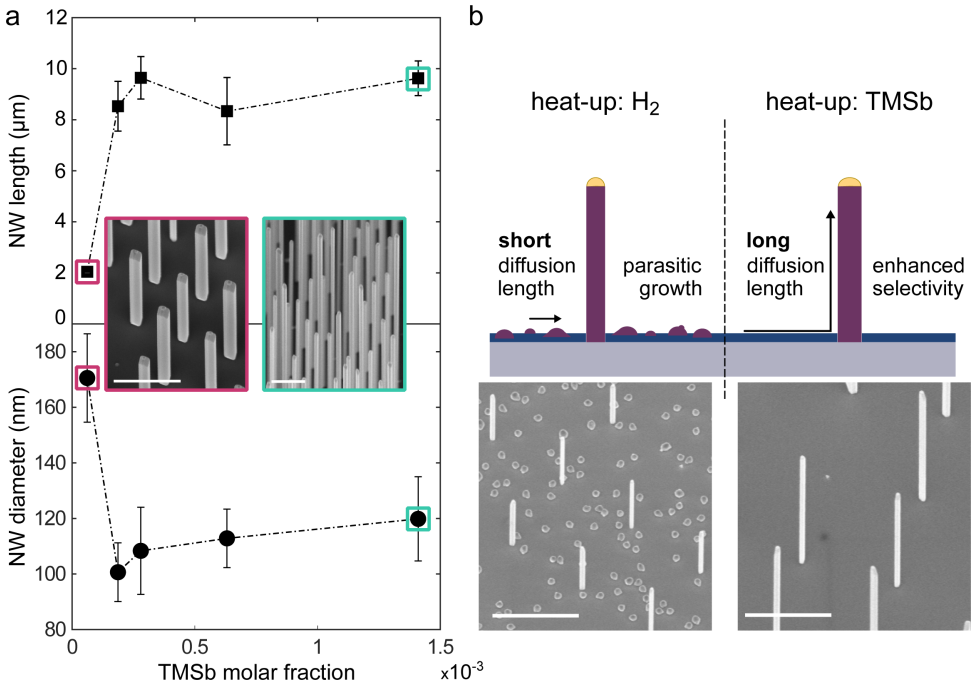

Figure 7.3: **Effect of TMSb molar fraction on InSb NW growth.** (a) A reduction in NW diameter and an increase in NW length are achieved in response to higher TMSb flow. Representative 30^o-tilt SEM images at the lowest and highest TMSb molar fractions reflect the improved aspect ratio (length/diameter) (scale bar corresponds to 1 µm) (b) Furthermore, TMSb flow has a direct influence on precursor diffusion length. In particular, heat-up under hydrogen leads to a short diffusion length reflected in parasitic growth on the SA mask. On the other hand, sample heat-up under TMSb flow enhances selectivity by entirely suppressing nucleation on the mask, as shown in the SEM images (scale bar is 2 µm).

7

a function of time for varying d_{mask} and a fixed d_{Au} = 30 nm. The NW growth rate is non-linear in the first ≈ 1.5 hours. After that, the volume increases linearly with time. A linear fit of these data points (inset of Figure 7.2e) shows that all NWs (irrespective of d_{mask}) grow with more or less the same rate (slope: 0.159 ± 0.009 µm^3/hour). The point of intersection with the x-axis, thus, reflects the onset of linear growth. Furthermore, the first x-intercept reflects which opening diameter experiences the least axial growth delay. The linear fit for d_{mask} = 102 nm intersects the x-axis the earliest, coinciding with the peak in NW length of Figure 7.2a V and Figure 7.2c and thus a minimal growth delay, as shown in Figure 7.2f.

After capturing the effect of substrate patterning on InSb NW growth kinetics, we turn our attention to the impact of growth parameters on these wires. Thus, in what follows we will discuss the effects of precursor flows on NW growth kinetics, more specifically the impact of TMSb flow on the NW growth dimensions and adatom diffusion.

We vary the TMSb molar fraction, while keeping the tri-methyl-indium (TMIn) flow constant and note the evolution of NW dimensions accordingly. As outlined in Figure 7.3a, a slight increase in TMSb molar fraction causes significant change in both NW diameter

and length. In accordance with these plots, it is shown that there is a threshold amount of TMSb flow required beyond which InSb wires grow with a high aspect ratio.

A slightly larger diameter for the highest examined TMSb molar fraction in comparison with the minimum observed diameter for a molar fraction of 1.87×10^{-4} could be ascribed to excess Sb reducing the nucleation barrier on NW side-facets, resulting in radial growth without compromising NW length. The considerable difference in NW length between low and high TMSb flows can possibly be attributed to the axial growth rate being group-V limited, which is unique to antimonide-based NWs and has been reported for InSb NWs on stems and gallium antimonide (GaSb) NWs on GaAs segments [21, 34] on bare substrates. Predominantly, for other III-V NWs, the group V precursors behave differently, due to their higher vapor pressure compared to Sb [18, 35].

Nonetheless, we would like to propose a different mechanism, namely a change of diffusion kinetics on the mask, which could be governing the growth of SA-VLS InSb NWs. We observe parasitic islands on the SA mask, if the sample is heated to the growth temperature under a flow of hydrogen (H_2). Deposition on the mask is also observed if the TMIn source is opened 30 seconds before growth starts (Figure 7.3b). In contrast, if the sample reaches the growth temperature for the same conditions under a flow of TMSb, parasitic growth is completely suppressed, thus confirming that deposition on the mask is initiated by In droplets. In fact, the density of nucleation points decreases with an increased TMSb flow during heat-up. The absence of parasitic islands further indicates that TMSb has a direct influence on the diffusion length of In precursors, as further shown in section 7.7.5. More generally, TMSb increases the diffusion length of In, inhibiting In from readily sticking on the Si_xN_y mask.

These observations are in stark contrast to reports on InSb NWs on stems grown on bare substrates, where layer growth is always present. Actually, these studies even report that an increase in V/III ratio eventually reduces the NW growth rate, because of favored parasitic growth on the substrate surface [21]. The growth parameter window seems to be much larger for SA-VLS stemless InSb NWs. Based on the reduction (increase) of parasitic growth on the mask with increasing TMSb flow (TMIn flow) together with the increase (decrease) in NW growth rate with a higher TMSb flow (TMIn flow), we thus conclude that the In precursor diffusion length is increased (decreased) with increasing TMSb (TMIn) flow and therefore the diffusion of In is rate limiting.

Upon examining the NW volume dependence on NW pitch, we extract a surface diffusion length on the Si_xN_y mask to be ≈ 2 μm (see section 7.7.6). The complete absence of tapering as noted earlier, however, indicates rather large diffusion lengths for incoming adatoms on the smooth {110} side-facets [18, 21].

7.4. CRYSTAL STRUCTURE AND CHEMICAL PURITY

In terms of crystal structure both types of InSb NWs, stemmed and stemless, are comparable, exhibiting the pure zinc blende crystal structure without defects, as verified by transmission electron microscopy (see section 7.7.8). With regards to chemical purity, atom probe tomography (APT) has been used to analyze the composition of both stemmed and stemless wires. As indicated in Figure 7.4, APT data shows four orders of magnitude reduction in As incorporation in the stemless wires. An average of five percent of As in NWs on stems indicates that we obtain an alloy of $InSb_{1-x}As_x$ rather than As being

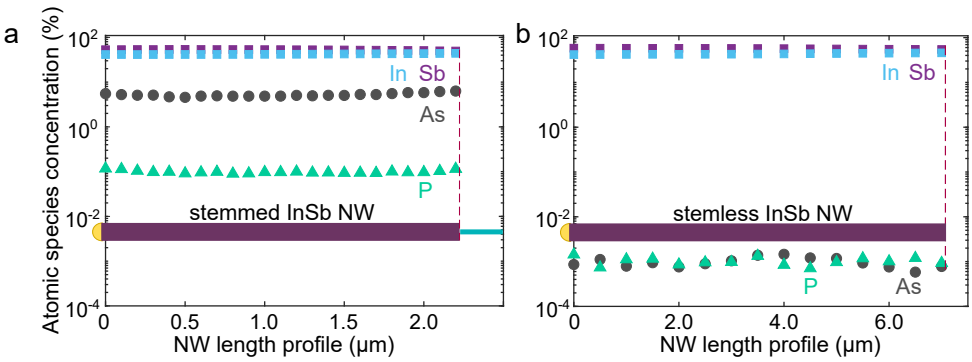

Figure 7.4: **Atomic species concentration along an InSb NW** for (a) stemmed and (b) stemless growth using atom probe tomography. A 50:50 concentration of In:Sb is observable in both graphs in accordance with the 1:1 ratio of III-V compounds. Significant reduction in arsenic (As) and phosphorus (P) incorporation in the stemless wires is realized. Specifically, arsenic is reduced from 5.5 ± 0.5% in NWs on stems to 0.0006 ± 0.0002% in stemless wires. While phosphorus is not as high as arsenic in stemmed InSb NWs, a noteworthy reduction is still achieved for the stemless wires, going from 0.11 ± 0.02% to 0.001 ± 0.0005%.

merely an impurity contaminant. Reduction in P contamination is also evident for stemless wires, showing two orders of magnitude less in P incorporation. The extremely low concentrations of P and As present in the stemless NWs are likely ascribed to background levels in the reactor chamber. Evidently, omission of the foreign stem together with using InSb substrates for growth notably reduces impurities in stemless InSb Nws.

7.5. QUANTUM TRANSPORT CHARACTERIZATION

To quantify the effects of impurity incorporation on the electronic properties of the NWs, we extract the electron mobility and investigate quantized conductance, the Landé g-factor and the spin-orbit energy. To obtain the electron mobility μ of the nanowire devices, field-effect transistor (FET) measurements are conducted at 4.2 K (inset Figure 7.5a) by accurately reproducing the conditions used in [36]. We fabricated 15 nanowire-FET devices (NW diameter in the range of 130 nm - 190 nm) with Ti/Au leads on degenerately p-doped Si/SiO_2 substrates to enable back-gate functionality. The source-drain contact separations are either $L = 1$ μm or 2 μm in order to ensure the diffusive long-channel transport regime. Gate-voltage sweeps $I(V_{BG})$ for both channel lengths are depicted in Figure 7.5a. Field-effect mobilities are extracted from fits of the pinch-off curves (cf. red dashed lines). The average of the mobility for the 15 devices yields $\mu = 4.4 \times 10^4$ cm^2/Vs, accounting for the weighted average of forward and reverse sweep directions. The obtained mobilities vary between $\mu = 3.4 \times 10^4$ cm^2/Vs and 5.7×10^4 cm^2/Vs (details are in table 7.1). These mobilities are significantly higher than obtained in previous studies on both InSb nanowires ($\mu = 2.0$ - 3.0×10^4 cm^2/Vs) [36] and InAs nanowires ($\mu = 1.0$ - 2.5×10^4 cm^2/Vs) [37–39] for ≈ 100 nm diameter wires. The lower mobility measured in InAs NW devices is likely attributed to surface electron accumulation, which enhances surface scattering. Surface adsorbates are thus known to strongly impact the field-effect mobility. In this work, adsorbates are efficiently removed from the nanowire surfaces by evacuating

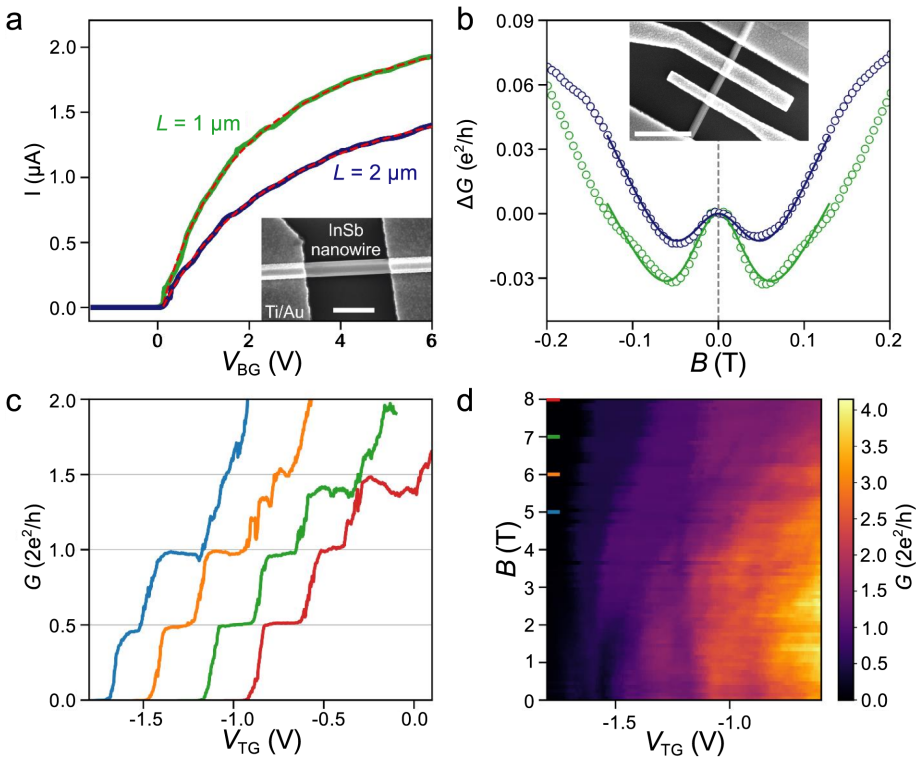

Figure 7.5: **Quantum transport characterization.** (a) FET measurements at V_{dc} = 10 mV for two nanowires of different lengths L. The fitting curves (red dashed lines) yield a mobility $\mu = 4.1 \times 10^4$ cm^2/Vs (blue trace) and $\mu = 4.6 \times 10^4$ cm^2/Vs (green trace). The inset shows an exemplary nanowire device with the scale bar equal to 500 nm . (b) WAL magnetoconductance correction at T = 0.3 K (excitation voltage V_{ac} = 20 µV) with data for both sweep directions being averaged. The fits (solid curves) are performed by utilizing the quasi-classical WAL model [12]. The back-gate voltage range for the blue curve is 2 V to 6 V and for the green curve 6 V to 10 V. The inset shows a top-gated NW device with a scale bar equal to 1 µm. (c) QPC conductance at V_{dc} = 1.0 mV. Due to the contact and line resistances and the unmodulated nanowire segments, a series resistance of R_c = 13.5 kΩ is subtracted, so that the conductance plateaus align with multiples of e^2/h. Here, the back-gate voltage V_{BG} = 7.5 V and the temperature T = 6 K . The gate traces are shifted in V_{TG} for clarity and the corresponding field values where the line cuts are taken are indicated by the colored dashes in panel (d). At B = 5 T (blue curve) the degeneracy between two subbands with opposite spin is evidenced by the fact that the plateau at $1.5 \times 2e^2/h$ vanishes. (d) QPC conductance G as a function of V_{TG} and B.

the sample space for at least 48 hours before measurements, similar to [36].

The highest mobilities —in the order of 10^5 cm^2/Vs—have been measured for InSb in conventional two-dimensional electron gases (2DEGs) [40], where the InSb quantum well is protected by epitaxial barrier layers. However, these barrier layers are incompatible with semiconducting/superconducting hybrid devices because they impede the exchange of carriers between the quantum well and the superconductor. Moreover, spin-orbit coupling, which is crucial for applications in spintronics and topological quantum computing, is generally more pronounced in bottom-up III-V nanowires compared with their 2DEG counterparts [12, 41].

The high mobilities reported for our nanowires translate into particularly long mean free paths over which the transport is ballistic. Accordingly, for sufficiently short channel length, the conductance is expected to vary in quantized steps of e^2/h as a function of top-gate voltage at finite magnetic field, which indicates the stepwise depopulation of the one-dimensional subbands [39, 42, 43]. This can be seen for instance in Figure 7.5c,d, where a 170-nm-wide top gate is used to form a local quantum point contact (QPC). The evolution of the conductance plateaus as a function of the applied magnetic field corresponds to the Zeeman splitting and the magnetic confinement that shifts the one-dimensional subband energies. The extracted Landé g-factor for the first subband is 38, in agreement with previous reports for InSb nanowires [42, 44].

An important prerequisite for realizing topological quantum computing in one-dimensional NWs is a large Rashba spin-orbit parameter. Superconductivity and a strong spin-orbit coupling in conjunction with an external magnetic field perpendicular to the uniaxial spin-orbit field allow for the formation of quasiparticle excitations, i.e. MZMs, in the topologically non-trivial phase at the opposite nanowire ends [5, 45]. The magnitude of the topological energy gap that protects these zero-energy states from poisoning by higher energy quasiparticles is enhanced by increasing the spin-orbit energy. Here, we extract the Rashba parameter from phase-coherent transport measurements by investigating the weak antilocalization effect (WAL). In Figure 7.5b, the magnetoconductance correction at $T = 0.3$ K is presented for two different back-gate voltage intervals. The blue trace refers to the back-gate voltage range from 2 V to 6 V, while the green trace corresponds to higher voltages between 6 V and 10 V . The solid lines represent the fits using the quasi-classical WAL model from Kurdak et al. [46]. The model parameters for magnetic and spin dephasing for hexagonal NWs were introduced in [12] (see section 7.7.8). Upon increasing the back-gate voltage, the spin-orbit energy is slightly enhanced from E_{so} = 0.17 meV to 0.18 meV, which corresponds to a change in the Rashba parameter from α_R = 0.43 eVÅ to 0.45 eVÅ. The spin-orbit energy derived from the WAL effect is quantitatively in line with previous studies on InSb nanowires grown from InP stems [12]. The extracted phase coherence length l_ϕ is approximately 480 nm and is nearly identical for the two curves. A second device is presented in section 7.7.8 yielding a comparable l_ϕ and a higher Rashba parameter of α_R = 0.64 eVÅ. For both devices, the Rashba parameters exceed α_R extracted for two-dimensional InSb heterostructures by more than one order of magnitude [46].

7.6. DISCUSSION

The stemless InSb wires characterized here are of particularly high chemical purity, which is reflected by the exceptionally large mobilities extracted from the FET characterization and the observation of quantized conductance—the hallmark of one-dimensional transport—in top-gate defined QPCs. These results pave the way toward the realization of high-quality hybrid semi-superconducting devices. The lack of impurities significantly suppresses the presence of subgap states, a prerequisite to achieve a large topological energy gap.

AUTHOR CONTRIBUTIONS

G.B., S.G. and E.P.A.M.B. conceived the concept of stemless nanowires. G.B and S.G. optimized the growth of the stemless nanowires. F.B. fabricated the field effect transistors and quantum point contact devices. F.B. and C.-A.W. performed the electrical measurements. F.B. and S.H. analysed the transport data. S.K. and M.A.V. carried out the material analysis. G.B., S.G., F.B. and S.H. wrote the manuscript and all the other authors provided critical feedback. E.P.A.M.B. and L.P.K. supervised the project.

DATA AVAILABILITY

The data and the codes that create the figures in this chapter are available at `https://data.4tu.nl/` with doi:10.4121/13469064.

7.7. SUPPLEMENTARY INFORMATION

7.7.1. SUBSTRATE FABRICATION

In what follows we describe the steps to fabricate the substrates used in this work.

SELECTIVE-AREA MASK DEPOSITION

- Start out with a 2-inch indium-antimonide (111)B wafer.
- The wafer as taken from the supplier box, is put in the plasma-enhanced chemical vapor deposition (PECVD) chamber, where around 20 nm of silicon nitride (SiN_x) are deposited.

POLYMER RESIST FOR ELECTRON-BEAM LITHOGRAPHY

- A primer (AR300-80) is spin coated on the sample at 4000 rpm for 60 seconds.
- The primer is baked on a hotplate for 2 minutes at 180^oC.
- An electron beam resist (AR-P 6200.04) is spin coated on the sample at 4000 rpm for 60 seconds.
- The resist is baked on a hotplate for 3 minutes at 150^oC.
- The sample is loaded to an electron beam lithography (EBL) tool where the design is written. The design consists of fields of nano-dots of varying sizes (16 nm - 50 nm) and varying inter-dot spacing (pitch) ranging from 0.25 μm to 4 μm.

RESIST DEVELOPMENT

- The sample is then taken out of the EBL tool for development. The sample is developed in Developer AR 600-546 for 60 seconds. It is then dipped in a beaker containing a Stopper AR 600-60 for 30 seconds. The sample is then rinsed in isopropanol (IPA) for 1 minute.

- The sample is dried using a nitrogen gun.

ETCHING OF SiN_x THROUGH RESIST NANO-HOLES

- **Wet etching:** the sample is dipped in a beaker containing buffered oxide etch BOE 7:1 ($HF : NH_4F$) for 14 - 25 seconds depending on the desired mask opening size. After that, the sample is rinsed in running ultra pure water (UPW) for at least 4 minutes.

- The sample is dried using a nitrogen gun.

GOLD EVAPORATION

- The samples are loaded in an electron-beam evaporator, where 8 nm of gold evaporated onto the sample with a deposition rate of 1 Å/second. Thereby gold is deposited within the holes in the SiN_x mask as well as everywhere on the resist.

LIFT-OFF

- The sample is dipped into PRS3000 (a photoresist stripper) for 30 minutes where a stir magnet continuously stirs the liquid.

- The sample is then transferred to an acetone beaker. There it is placed in a mildly sonicated bath for 5 minutes to ensure proper removal of gold residues.

- The sample is finally rinsed in an isopropanol beaker for 2 minutes.

- A nitrogen gun is used to dry the sample.

OXYGEN PLASMA

- The sample is then exposed to 300 Watt oxygen plasma with a gas flow of 55 standard cubic cm (sccm) for 2 minutes to remove any organic residues and ensure sample cleanliness.

7.7.2. GROWTH DETAILS

Growth in this work was done using a horizontal Aixtron 200 metal-organic vapor phase epitaxy (MOVPE) reactor. The samples were heated to the desired growth temperature of 495^oC by infrared lamps. The used precursors were trimethyl-indium (TMIn) and trimethyl-antimony (TMSb), where the TMIn molar fraction was kept constant at 1.95×10^{-7} and the TMSb was varied from 6.17×10^{-5} to 1.41×10^{-3}. The samples were heated up and cooled down under a flow of TMSb. The growth time was varied from 5 minutes to 6 hours. The carrier gas was H_2 and during growth the reactor pressure was kept constant at 50 mbar and a total volume of 6000 liters.

7.7.3. SEEDING OF SA-VLS INSB NWS

Growth of SA-VLS wires is consistent with selective-area seeding, where nucleation is preferred at edge sites. Therefore we observe the Au particles being consistently pushed to the edge of the mask opening, as shown in Figure 7.6. Once the opening is completely filled with precipitated InSb, the Au droplet is centered with respect to the mask opening, showing InSb NW diameters larger than the Au diameter.

It has been observed that Sb exposure has an effect on the morphology of Au particles in the early stages of growth causing nanowires to grow rather in-plane, leaving a streak of material behind, as the gold droplet moves [18]. As shown in Figure 7.6 a streak of material in the opening of the mask is visible after 5 minutes. As the Au particle encounters the mask edge, it does not like to wet it and hence bounces off (or it is being pushed around) the edges of the mask until the exposed substrate is filled. The resulting growth does not yield well-defined facets, causing the catalyst to reside on the smallest formed “facet", as no stable/defined planes are yet formed, as shown after 15 minutes of growth (see Figure 7.6). As growth proceeds, well-defined facets are slowly formed, possibly by catalyst wetting of more than one facet, until a (111) B plane is developed causing the gold catalyst to end up on it. Once this happens, normal NW growth takes place, where axial growth is driven by the catalyst whereas non-tapered radial growth is governed by VSS, resulting in slanted (111)A facets towards the catalyst, as shown in Figure 7.6 (60 minutes), similar to what has been observed for InAsSb wires [33]. This stable wire growth, with fully formed facets, results in hexagonal cross-section NWs, as shown in the inset of Figure 7.6.

The yield of these wires is sometimes limited by gold dots sliding under the mask during early growth stages, as indicated in Figure 7.7. The sliding is confirmed by closer examination yielding a brighter spot next to the holes with missing gold. This is observed for bigger inter-opening spacing (cf. with Figure 7.7).

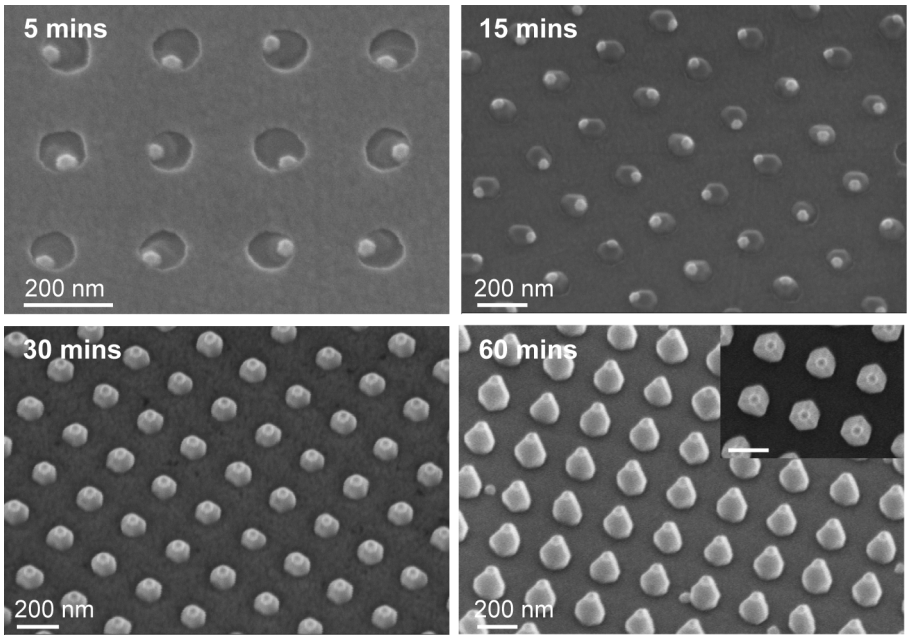

Figure 7.6: 30-degree tilt SEM images showing different growth stages of InSb Nws from 5 to 60 minutes of growth. The growth is performed for samples with the biggest examined openings in the SiN_x mask, around 130 nm openings. The gold droplet is approximately 30 nm in diameter prior to growth. Starting half an hour of growth, the gold droplet seems to take the stable configuration of being positioned on top of the growing wires. After 60 minutes of growth, stable facets and a hexagonal cross-section is discernable in the top-view inset. Scale bar corresponds to 200 nm for all SEM images.

7.7.4. VOLUME EFFECT

The volume effect refers to the fact, that if two objects have to grow to the same volume, the one with the smaller width (diameter) will grow higher, i.e. exhibit a higher aspect-ratio. The schematic in Figure 7.8 serves as a visualization of the volume effect.

7.7.5. TMSB INHIBITING PARASITIC GROWTH

The dependence of parasitic growth on pre-growth conditions. As shown in Figure 7.9, depending on the heat-up flow and the TMIn concentration prior to growth, parasitic growth is either favoured or suppressed. All the experiments shown in Figure 7.9 have the same growth parameters, they only differ in heat-up flow and TMIn filling of the gold droplet before growth commences. For the case where the gold catalyst is not filled with TMIn, we observe that parasitic growth decreases with increasing concentration of TMSb flow during heat-up. This observation indicates that parasitic growth is initiated by In deposition on the mask. TMIn diffusion is thus enhanced in presence of high enough TMSb concentration. Additionally, for the highest TMSb heat-up flow, parasitic growth is favoured as the TMIn filling duration increases. Thus indicating, that for a high enough TMIn concentration, nucleation on the mask becomes more probable.

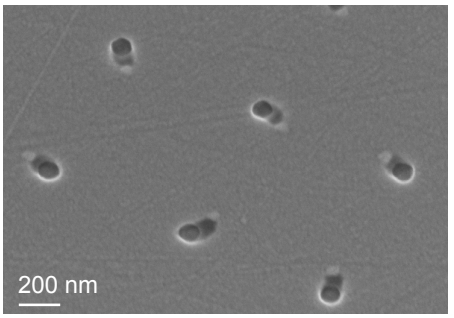

Figure 7.7: 30-degree tilt SEM image Au dots sliding under the selective-area mask, indicated by a bright dot next to the opening and empty holes. The image corresponds to 5 minutes of growth.

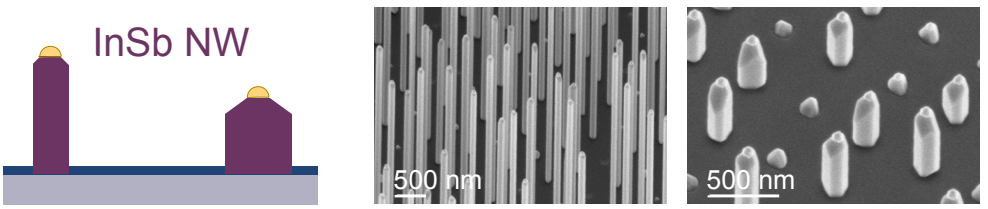

Figure 7.8: Visualization of the volume effect, reflecting lower (higher) axial growth rates for bigger (smaller) diameter wires for a given volume.

7.7.6. PITCH DEPENDENCE

Dependence of NW dimensions on pitch and extraction of surface diffusion length are discussed here. The data are collected from a growth run with low TMSb flow (molar fraction: 8.2×10^{-5}). Observing NW volume as a function of pitch (see Figure 7.10a), an increase in volume is barely discernible at a pitch of 2 μm. Thus, we can extract a diffusion length of about 2 μm. The plot of Figure 7.10b shows that the NW diameter is more or less independent of pitch, whereas the NW height is pitch-dependent. More generally, the NW height slowly saturates with pitch.

7.7.7. TEM ANALYSIS

Transmission electron microscopy (TEM) images were taken of the NWs to characterize their crystal quality. Stemless InSb NWs show pure zinc blende atomic ordering.

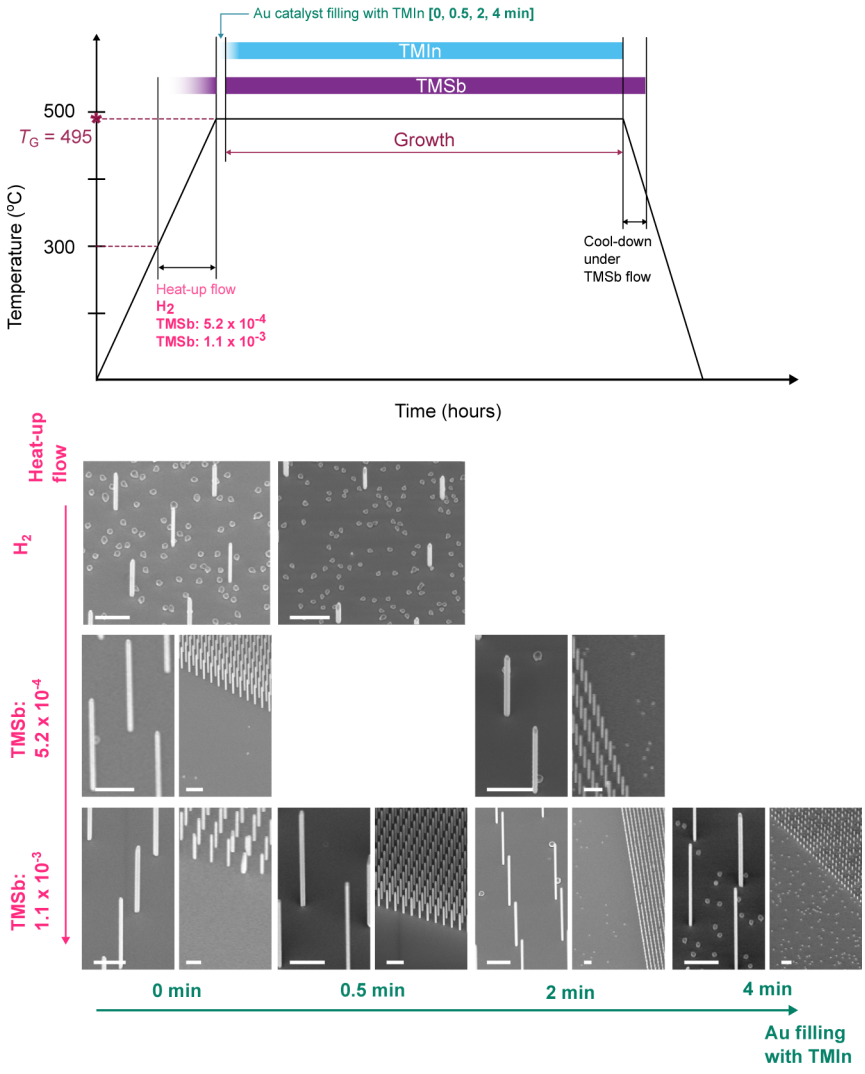

Figure 7.9: Top panel showing the growth scheme used to grow stemless InSb NWs. Temperature is ramped up from room temperature to the growth temperature (T_G) of 495 ^{o}C. In a few experiments (as shown in the bottom panel), the sample goes from 300 ^{o}C to 495 ^{o}C under a flow of TMSb. Once T_G is reached, the TMSb flow is switched off and the TMIn is opened for a short period of time to fill the gold catalyst with TMIn. The filling time is varied from 0 seconds and up to 4 minutes for different experiments, as shown in the bottom panel. As the Au filling is completed, the TMSb is switched on again, thus commencing growth. After growth is completed, the sample is cooled down from T_G to 370 ^{o}C under a flow of TMSb = 1.1 × 10^{-3}. The bottom panel shows representative SEM images from different experiments where different combinations of heat-up flow and Au filling durations are varied, while growth parameters are identical. Scale bar corresponds to 1 μm.

7.7.8. DEVICE FABRICATION

Here, we describe the fabrication process of both mobility and QPC devices:

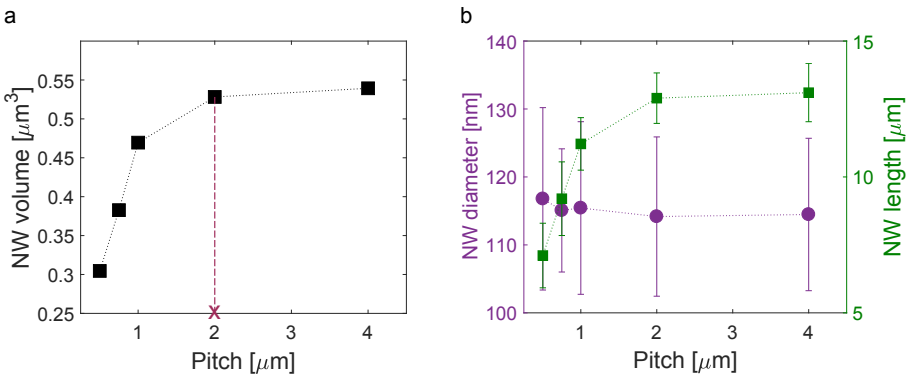

Figure 7.10: Plots showing dependence of NW dimensions on pitch. (a) NW volume increases with pitch up until an inter-wire spacing of 2 µm. At this pitch, the NW volume saturates where a surface diffusion length is concluded. (b) Plot of NW diameter and length against pitch. NW diameter is almost pitch-independent as opposed to NW length.

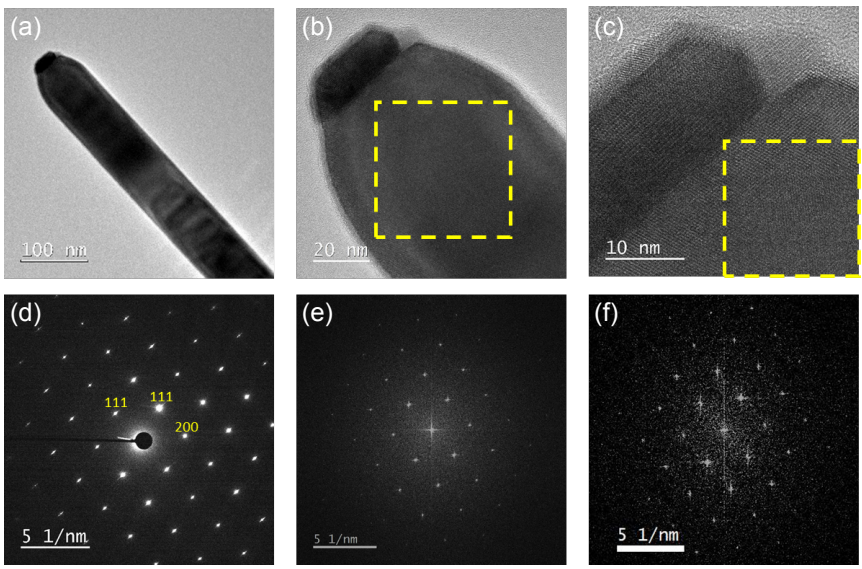

Figure 7.11: (a) Bright-field TEM image of a stemless InSb NW with a gold catalyst on top. (b), (c) HRTEM images of the top part of this wire. (d) Selected area electron diffraction pattern of the central part of the wire. (e), (f) Fast Fourier Transform patterns of the dashed regions of figures (b) and (c) respectively. All three patterns are characteristic for the <110> zone axis pattern of the zinc blende crystal structure of InSb.

- The substrates are made out of p^{++}-doped Si covered by 285 nm of thermal SiO_x via dry oxidation, onto which Ti/Au alignment markers are defined. The substrates are cleaned with 10 min of remote oxygen plasma at a pressure of 2 mbar and a power of 100 W.

- Nanowires are deterministically transferred by means of a nanomanipulator from

the growth chip onto the substrate. Optical images are taken in order to facilitate the design of the device with respect to the alignment markers.

- A double layer of resist (PMMA 495K A6 and PMMA 950K A2) is spin-coated on the substrate and each layer is baked for 10 min at 175 ^{o}C.
- The pattern of the contacts is defined by electron beam lithography (EBL). Source and drain contacts are designed to be separated by a 'long' InSb channel of length 1 or 2 μm.
- Development in a solution of MIBK:IPA (1:3) for 1 min, and in IPA for 1 min.
- Prior to the metal deposition, the chip is cleaned with 2 min of remote oxygen plasma at 2 mbar and a power 100 W, and left for 30 min in a sulphur-rich ammonium polysulfide solution diluted in water with a ratio of 1:200 at 60 ^{o}C.
- The chip is rinsed thoroughly with water and quickly loaded in an e-gun evaporator. Here it is exposed to 30 s of helium ion milling at a pressure of 1.6×10^{-2} mbar to facilitate the ohmic contact between InSb and metal, which is then evaporated in the sequence of 10 nm of Ti, and 170 nm of Au.
- Lift-off in acetone for 2 hours at 50 ^{o}C.

ADDITIONAL STEPS FOR QPC DEVICES:

- 40 nm of SiN_x gate dielectric is sputtered onto the entire chip.
- Resist (PMMA 495K A4) is spin-coated and baked for 10 min at 175 ^{o}C.
- The pattern of the top gates is defined by EBL; the designed gate widths lie in the range of 120 - 270 nm, comparable to the expected electron mean free path.
- Development in a solution of MIBK:IPA (1:3) for 1 min, and in IPA for 1 min.
- 20 nm of Ti and 210 nm of Au are deposited in an e-gun evaporator.
- Lift-off in acetone for 2 hours at 50 ^{o}C.

Experimental runs 1 and 2 hosting mobility devices (see Table 7.1) are performed respectively in a dilution refrigerator at a base temperature of ≈15 mK and in a dip-stick in helium at T = 4.2 K. QPC devices are loaded in a He-3 fridge with a base temperature of 300 mK. Prior to cool-down, the sample space is pumped for at least 48 hours, similarly to Ref. [36], in order to efficiently desorb adsorbates from the nanowires surface. The chips were imaged via SEM (scanning electron microscopy) only after the measurement to minimize carbon contamination, in order to evaluate diameter and length of the nanowires.

MOBILITY MEASUREMENTS

For the study of the field-effect mobility μ, we accurately reproduce the conditions used in Ref. [36]. Nanowire-FET devices were fabricated as described in section 7.7.8. Based on the channel lengths used, the diffusive long-channel regime is assumed. Hence the current I as a function of back-gate voltage V_{BG} and dc-bias voltage V_{dc} can be modeled by

$$I(V_{BG}, V_{dc}) = \frac{V_{dc}}{[L^2/\mu C(V_{BG} - V_{th})] + R_c} \tag{7.1}$$

The saturation current is limited by the series resistance R_c, which includes the contact, filter and line resistances. The current pinch-off is reached at the threshold voltage V_{th}. The value of the capacitance is evaluated via a 3D Laplace solver for a typical nanowire device geometry including two metallic leads. In this finite elements model the nanowire is treated as a metal. The capacitance is then reduced by 20% to include the effect of the quantum confinement. This reduction was in fact found from the comparison of the estimations of the capacitance obtained by a 2D Schrödinger-Poisson solver and by a 2D Laplace solver, as discussed in Ref. [36]. We expect that the inaccuracy in estimating the capacitance due to the unknown surface density of states leads to a relative error of 10-20% in the mobility – in line with what was evaluated in Ref. [47].

We present here in Table 7.1 the detailed summary of all devices measured to evaluate the electron mobility in the stemless InSb nanowires. Two chips (which we call experimental runs 1 and 2) have been fabricated and measured. Prior to the cool down, the sample space was evacuated at room temperature for 48 and 65 hours for run 1 and 2, respectively. Onto these chips, nanowires grown from two different growth batches (RB2252 and RB2669) were transferred. We did not observed any significant difference between both evacuation times, and both growth chips. The mobility and threshold voltage values presented in Table 7.1 are weighted averages of the parameters extracted from the up and down back-gate sweep at 10 mV bias. The error of the mobility reflects the weighted average of the values obtained from the least-square fits of current vs gate voltage traces for the up and down sweeps. The mobility values lie between 3.42 $\times 10^4$ Vs/cm^2 and 5.7 $\times 10^4$ Vs/cm^2, with an average value of 4.37 $\times 10^4$ Vs/cm^2.

ADDITIONAL QPC DATA

Here, we present data of a QPC device different from the one reported in the Fig. 7.5. Similarly, the QPC is defined in a nanowire segment by means of a 215-nm-wide top gate (Figure 7.12a), while an electric field can be applied by the global back gate across the entire nanowire. The magnetic field is applied perpendicularly to the substrate and breaks the spin degeneracy of the subbands. In case of ballistic transport, this translates in the conductance rising in steps of e^2/h versus top-gate voltage. From the Zeeman splitting ($E_Z = g\mu_B B$) of the first subband (see Figure 7.12b), we extracted a value of the g factor of 38, comparable to what was reported in Refs. [42, 44].

ADDITIONAL WAL DATA

Here, the weak antilocalization effect in the magnetoconductance data is modeled using the one-dimensional WAL formula of Kurdak et al. [46] given by

Table 7.1: Summary of FET devices

Exp. run	NW batch	Device	Diam. (nm)	Length (μm)	V_{th}	$\mu \pm \delta\mu$
1	RB2252	3	191	1.92	-1.50	44430±260
1	RB2252	5b	168	1.9	-1.13	43640±220
1	RB2252	6	182	1.96	-1.21	42740±200
1	RB2669	14a	175	1.87	-1.24	41240±250
1	RB2669	14b	169	1.89	-1.40	42900±260
1	RB2669	15a	159	1.94	-1.20	43910±210
1	RB2669	17a	171	1.92	-1.06	47960±180
1	RB2669	17b	166	1.92	-1.20	44150±220
1	RB2669	18	165	1.87	-0.99	39820±270
1	RB2669	19	183	1.75	-1.71	40000±290
1	RB2669	20	186	1.92	-1.12	47760±450
1	RB2669	21	189	1.93	-1.21	57000±410
2	RB2252	1	141	1.94	0.10	41040±190
2	RB2252	2	180	1.02	0.17	45590±150
2	RB2252	4	138	1.95	0.45	34280±90

$$\Delta G(B) = -\frac{e^2}{h}\frac{1}{L}\Big[3\Big(\frac{1}{l_\phi^2}+\frac{4}{3l_{SO}^2}+\frac{1}{l_B^2}\Big)^{-1/2}-\Big(\frac{1}{l_\phi^2}+\frac{1}{l_B^2}\Big)^{-1/2} -3\Big(\frac{1}{l_\phi^2}+\frac{4}{3l_{SO}^2}+\frac{d}{l_e^2}+\frac{1}{l_B^2}\Big)^{-1/2}+\Big(\frac{1}{l_\phi^2}+\frac{d}{l_e^2}+\frac{1}{l_B^2}\Big)^{-1/2}\Big]. \tag{7.2}$$

The diffusion in the nanowire with the scattering length l_e has the dimensionality $d = 3$. Here, $l_e = v_F\tau_e$ is extracted from the threshold voltage V_{th}, which yields the Fermi velocity v_F, and the mobility μ, providing the characteristic scattering time τ_e, that are both determined from FET traces. The magnetic dephasing length l_B and the spin relaxation length l_{SO} are given by [12]

$$l_B = \sqrt{\frac{C_m}{d}\frac{l_m^4}{w_f^{\gamma_m} l_e^{2-\gamma_m}}} \tag{7.3}$$

and

$$l_{SO} = \sqrt{\frac{C_s}{d}\frac{l_R^4}{w_f^{\gamma_s} l_e^{2-\gamma_s}}}, \tag{7.4}$$

respectively, with $C_m = 22.3$, $\gamma_m = 3.174$ and $C_s = 8.7$, $\gamma_s = 3.2$ determined from Monte Carlo simulations of the dephasing along closed-loop electron trajectories in a hexagonal nanowire [12]. Here, w_f refers to the facet-to-facet nanowire diameter and $l_R = \hbar^2/m^*\alpha_R$ is the Rashba spin precession length.

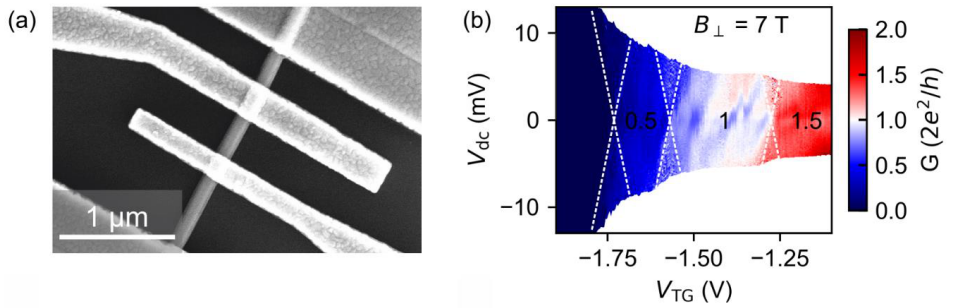

Figure 7.12: (a) InSb nanowire device comprising two top gates that can be used to electrostatically create QPCs. (b) Conductance as a function of bias voltage V_{dc} and top-gate voltage V_{TG} at $B = 7$ T. The top gate is 215-nm-wide and the measurement is performed at $T = 5$ K with $V_{TG} = 9$ V. The bias voltage is corrected for the voltage drop occurring due to additional series resistances.

Before fitting the magnetoconductance correction model of eq. 7.2 to the low-temperature transport data, the conductance background needs to be subtracted. To this end, for every magnetoconductance trace the average conductance at field values $|B| > 0.5$ T is subtracted. In Figure 7.13 the weak antilocalization effect is shown for another device, which is depicted in Figure 7.12a. Here, the magnetoconductance correction is averaged for a back-gate voltage interval from -1.5 V to 13.5 V. The orange curve in Figure 7.13 is the fit of the quasiclassical model in eq. 7.2, which yields a phase coherence length of $l_\phi = 510$ nm, comparable to the device presented in Fig. 7.5. The extracted spin-orbit energy is $E_{SO} = 0.37$ meV. This corresponds to a Rashba parameter of $\alpha_R = 0.64$ eVÅ.

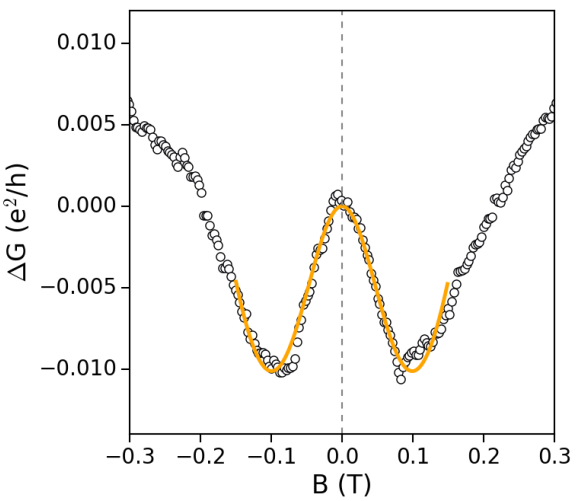

Figure 7.13: Magnetoconductance correction for the nanowire device depicted in Figure 7.13a at $T = 0.3$ K. For the fit (solid line) the quasi-classical WAL model from eq. 7.2 is utilized [12].

REFERENCES

[1] G. Badawy, S. Gazibegovic, F. Borsoi, S. Heedt, C.-A. Wang, S. Koelling, M. A. Verheijen, L. P. Kouwenhoven, and E. P. A. M. Bakkers, *High mobility stemless InSb nanowires,* Nano Lett. **19**, 3575 (2019).

[2] V. Mourik, K. Zuo, S. M. Frolov, S. Plissard, E. P. A. M. Bakkers, and L. P. Kouwenhoven, *Signatures of Majorana fermions in hybrid superconductor-semiconductor nanowire devices,* Science **336**, 1003 (2012).

[3] M. T. Deng, S. Vaitiekėnas, E. B. Hansen, J. Danon, M. Leijnse, K. Flensberg, J. Nygård, P. Krogstrup, and C. M. Marcus, *Majorana bound state in a coupled quantum-dot hybrid-nanowire system,* Science **354**, 1557 (2016).

[4] H. Zhang, C.-X. Liu, S. Gazibegovic, D. Xu, J. A. Logan, G. Wang, N. Van Loo, J. D. Bommer, M. W. De Moor, D. Car, R. L. M. Op het Veld, P. J. van Veldhoven, S. Koelling, M. A. Verheijen, M. Pendharkar, D. J. Pennachio, B. Shojaei, J. S. Lee, C. J. Palmstrøm, E. P. A. M. Bakkers, D. S. Sarma, and L. P. Kouwenhoven, *Quantized Majorana conductance,* Nature **556**, 74 (2018).

[5] Y. Oreg, G. Refael, and F. von Oppen, *Helical liquids and Majorana bound states in quantum wires,* Phys. Rev. Lett. **105**, 177002 (2010).

[6] A. Y. Kitaev, *Unpaired Majorana fermions in quantum wires,* Phys.-Uspekhi **44**, 131 (2001).

[7] A. Stern and N. H. Lindner, *Topological quantum computation–from basic concepts to first experiments,* Science **339**, 1179 (2013).

[8] K. D. Petersson, L. W. McFaul, M. D. Schroer, M. Jung, J. M. Taylor, A. A. Houck, and J. R. Petta, *Circuit quantum electrodynamics with a spin qubit,* Nature **490**, 380 (2012).

[9] S. Nadj-Perge, S. M. Frolov, E. P. A. M. Bakkers, and L. P. Kouwenhoven, *Spin–orbit qubit in a semiconductor nanowire,* Nature **468**, 1084 (2010).

[10] S. Nadj-Perge, V. S. Pribiag, J. W. G. Van den Berg, K. Zuo, S. R. Plissard, E. P. A. M. Bakkers, S. M. Frolov, and L. P. Kouwenhoven, *Spectroscopy of spin-orbit quantum bits in indium antimonide nanowires,* Phys. Rev. Lett. **108**, 166801 (2012).

[11] O. Madelung, ed., *Semiconductors,* 1st ed. (Springer-Verlag Berlin Heidelberg, Germany, 1991).

[12] I. van Weperen, B. Tarasinski, D. Eeltink, V. S. Pribiag, S. R. Plissard, E. P. A. M. Bakkers, L. P. Kouwenhoven, and M. Wimmer, *Spin-orbit interaction in InSb nanowires,* Phys. Rev. B **91**, 201413 (2015).

[13] I. Vurgaftman, J. R. Meyer, and L. R. Ram-Mohan, *Band parameters for III–V compound semiconductors and their alloys,* Journal of applied physics **89**, 5815 (2001).

[14] M. T. Deng, C. L. Yu, G. Y. Huang, M. Larsson, P. Caroff, and H. Q. Xu, *Anomalous zero-bias conductance peak in a Nb–InSb nanowire–Nb hybrid device,* Nano Lett. **12**, 6414 (2012).

[15] S. Gazibegovic, D. Car, H. Zhang, S. C. Balk, J. A. Logan, M. W. A. de Moor, M. C. Cassidy, R. Schmits, D. Xu, G. Wang, P. Krogstrup, R. L. M. Op het Veld, K. Zuo, Y. Vos, J. Shen, D. Bouman, B. Shojaei, D. Pennachio, J. S. Lee, P. J. van Veldhoven, S. Koelling, M. A. Verheijen, L. P. Kouwenhoven, C. J. Palmstrøm, and E. P. A. M. Bakkers, *Epitaxy of advanced nanowire quantum devices,* Nature **584**, 434 (2017).

[16] J. E. Sestoft, T. Kanne, A. N. Gejl, M. von Soosten, J. S. Yodh, D. Sherman, B. Tarasinski, M. Wimmer, E. Johnson, M. Deng, *et al.*, *Engineering hybrid epitaxial InAsSb/Al nanowires for stronger topological protection,* Phys. Rev. Mater. **2**, 044202 (2018).

[17] R. M. Lutchyn, E. P. A. M. Bakkers, L. P. Kouwenhoven, P. Krogstrup, C. M. Marcus, and Y. Oreg, *Majorana zero modes in superconductor–semiconductor heterostructures,* Nat. Rev. Mater. **3**, 52 (2018).

[18] B. M. Borg and L.-E. Wernersson, *Synthesis and properties of antimonide nanowires,* Nanotechnology **24**, 1 (2013).

[19] R. S. Wagner and W. C. Ellis, *Vapor-liquid-solid mechanism of single crystal growth,* Appl. Phys. Lett. **4**, 89 (1964).

[20] P. Caroff, J. B. Wagner, K. A. Dick, H. A. Nilsson, M. Jeppsson, K. Deppert, L. Samuelson, L. R. Wallenberg, and L.-E. Wernersson, *High-quality InAs/InSb nanowire heterostructures grown by metal–organic vapor-phase epitaxy,* Small **4**, 878 (2008).

[21] P. Caroff, M. E. Messing, B. M. Borg, K. A. Dick, K. Deppert, and L.-E. Wernersson, *InSb heterostructure nanowires: Movpe growth under extreme lattice mismatch,* Nanotechnology **20**, 1 (2009).

[22] M. de la Mata, R. Leturcq, S. R. Plissard, C. Rolland, C. Magén, J. Arbiol, and P. Caroff, *Twin-induced InSb nanosails: a convenient high mobility quantum system,* Nano Lett. **16**, 825 (2016).

[23] S. R. Plissard, D. R. Slapak, M. A. Verheijen, M. Hocevar, G. W. G. Immink, I. van Weperen, S. Nadj-Perge, S. M. Frolov, L. P. Kouwenhoven, and E. P. A. M. Bakkers, *From InSb nanowires to nanocubes: looking for the sweet spot,* Nano Lett. **12**, 1794 (2012).

[24] H. So, D. Pan, L. Li, and J. Zhao, *Foreign-catalyst-free growth of InAs/InSb axial heterostructure nanowires on Si (111) by molecular-beam epitaxy,* Nanotechnology **28**, 1 (2017).

[25] F. Domínguez, J. Cayao, P. San-Jose, R. Aguado, A. L. Yeyati, and E. Prada, *Zero-energy pinning from interactions in Majorana nanowires,* npj Quantum Materials **2**, 1 (2017).

[26] J. P. Stenger, B. D. Woods, S. M. Frolov, and T. D. Stanescu, *Control and detection of Majorana bound states in quantum dot arrays,* Phys. Rev. B **98**, 085407 (2018).

[27] Z. Su, A. B. Tacla, M. Hocevar, D. Car, S. R. Plissard, E. P. Bakkers, A. J. Daley, D. Pekker, and S. M. Frolov, *Andreev molecules in semiconductor nanowire double quantum dots,* Nat. Commun. **8**, 585 (2017).

[28] T. Karzig, C. Knapp, R. M. Lutchyn, P. Bonderson, M. B. Hastings, C. Nayak, J. Alicea, K. Flensberg, S. Plugge, Y. Oreg, C. M. Marcus, and M. H. Freedman, *Scalable designs for quasiparticle-poisoning-protected topological quantum computation with Majorana zero modes,* Phys. Rev. B **95**, 235305 (2017).

[29] S. Plugge, A. Rasmussen, R. Egger, and K. Flensberg, *Majorana box qubits,* New J. Phys. **19**, 012001 (2017).

[30] S. Vijay and L. Fu, *Teleportation-based quantum information processing with Majorana zero modes,* Phys. Rev. B **94**, 235446 (2016).

[31] H. Chen, X. Sun, K. W. Lai, M. Meyyappan, and N. Xi, *Infrared detection using an InSb nanowire,* in *2009 IEEE Nanotechnology Materials and Devices Conference* (IEEE, 2009) pp. 212–216.

[32] C.-H. Kuo, J.-M. Wu, S.-J. Lin, and W.-C. Chang, *High sensitivity of middle-wavelength infrared photodetectors based on an individual InSb nanowire,* Nanoscale research letters **8**, 327 (2013).

[33] D. Ercolani, M. Gemmi, L. Nasi, F. Rossi, M. Pea, A. Li, G. Salviati, F. Beltram, and L. Sorba, *Growth of InAs/InAsSb heterostructured nanowires,* Nanotechnology **23**, 115606 (2012).

[34] M. Jeppsson, K. A. Dick, J. B. Wagner, P. Caroff, K. Deppert, L. Samuelson, and L.-E. Wernersson, *GaAs/GaSb nanowire heterostructures grown by movpe,* J. Cryst. Growth **310**, 4115 (2008).

[35] S. P. Yip, L. Shen, and J. Ho, *Recent advances in iii-sb nanowires: from synthesis to applications,* Nanotechnology (2019).

[36] Ö. Gül, D. J. van Woerkom, I. van Weperen, D. Car, S. R. Plissard, E. P. A. M. Bakkers, and L. P. Kouwenhoven, *Towards high mobility InSb nanowire devices,* Nanotechnology **26**, 215202 (2015).

[37] A. C. Ford, J. C. Ho, Y.-L. Chueh, Y.-C. Tseng, Z. Fan, J. Guo, J. Bokor, and A. Javey, *Diameter-dependent electron mobility of InAs nanowires,* Nano Lett. **9**, 360 (2008).

[38] M. D. Schroer and J. R. Petta, *Correlating the nanostructure and electronic properties of InAs nanowires,* Nano Lett. **10**, 1618 (2010).

[39] S. Heedt, W. Prost, J. Schubert, D. Grützmacher, and T. Schäpers, *Ballistic transport and exchange interaction in InAs nanowire quantum point contacts,* Nano Lett. **16**, 3116 (2016).

[40] P. E. Thompson, J. L. Davis, J. Waterman, R. J. Wagner, D. Gammon, D. K. Gaskill, and R. Stahlbush, *Use of atomic layer epitaxy buffer for the growth of InSb on GaAs by molecular beam epitaxy,* J. Appl. Phys. **69**, 7166 (1991).

[41] R. L. Kallaher, J. J. Heremans, N. Goel, S. J. Chung, and M. B. Santos, *Spin-orbit interaction determined by antilocalization in an InSb quantum well,* Phys. Rev. B **81**, 075303 (2010).

[42] J. Kammhuber, M. C. Cassidy, H. Zhang, m. Gül, F. Pei, M. W. A. de Moor, B. Nijholt, K. Watanabe, T. Taniguchi, D. Car, S. R. Plissard, E. P. A. M. Bakkers, and L. P. Kouwenhoven, *Conductance quantization at zero magnetic field in InSb nanowires,* Nano Lett. **16**, 3482 (2016).

[43] I. van Weperen, S. R. Plissard, E. P. A. M. Bakkers, S. M. Frolov, and L. P. Kouwenhoven, *Quantized conductance in an InSb nanowire,* Nano Lett. (2013).

[44] H. A. Nilsson, P. Caroff, C. Thelander, M. Larsson, J. B. Wagner, L.-E. Wernersson, L. Samuelson, and H. Q. Xu, *Giant, level-dependent g factors in InSb nanowire quantum dots,* Nano Lett. **9**, 3151 (2009).

[45] R. M. Lutchyn, J. D. Sau, and S. Das Sarma, *Majorana fermions and a topological phase transition in semiconductor-superconductor heterostructures,* Phys. Rev. Lett. **105**, 077001 (2010).

[46] C. Kurdak, A. M. Chang, A. Chin, and T. Y. Chang, *Quantum interference effects and spin-orbit interaction in quasi-one-dimensional wires and rings,* Phys. Rev. B **46**, 6846 (1992).

[47] S. Heedt, I. Otto, K. Sladek, H. Hardtdegen, J. Schubert, N. Demarina, H. Lüth, D. Grützmacher, and T. Schäpers, *Resolving ambiguities in nanowire field-effect transistor characterization,* Nanoscale **7**, 18188 (2015).

8

SHADOW-WALL LITHOGRAPHY OF BALLISTIC SUPERCONDUCTOR–SEMICONDUCTOR QUANTUM DEVICES

If the road is easy, you are likely going the wrong way.

Terry Goodkind

The realization of a topological qubit calls for advanced techniques to readily and reproducibly engineer induced superconductivity in semiconductor nanowires. Here, we introduce an on-chip fabrication paradigm based on shadow walls that offers substantial advances in device quality and reproducibility. It allows for the implementation of novel quantum devices and ultimately topological qubits while eliminating fabrication steps such as lithography and etching. This is critical to preserve the integrity and homogeneity of the fragile hybrid interfaces. The approach simplifies the reproducible fabrication of devices with a hard induced superconducting gap and ballistic normal-/superconductor junctions. Large gate-tunable supercurrents and high-order multiple Andreev reflections manifest the exceptional coherence of the resulting nanowire Josephson junctions. Our approach enables, in particular, the realization of 3-terminal devices, where zero-bias conductance peaks emerge in a magnetic field concurrently at both boundaries of the one-dimensional hybrids.

This chapter has been published as, S. Heedt*, M. Quintero-Pérez*, F. Borsoi*, A. Fursina, N. van Loo, G. P. Mazur, M. P. Nowak, M. Ammerlaan, K. Li, S. Korneychuk, J. Shen, M. A. Y. van de Poll, G. Badawy, S. Gazibegovic, P. Aseev, K. van Hoogdalem, E. P. A. M. Bakkers, and L. P. Kouwenhoven, *Shadow-wall lithography of ballistic superconductor–semiconductor quantum devices*, arXiv:2007.14383 (2020) [1].

*These authors contributed equally to this work.

Hybrid superconducting/semiconducting nanowires are a promising material platform for the formation of one-dimensional topological superconductors bounded by pairs of Majorana modes [2–4]. Owing to their non-Abelian exchange statistics, these localized Majorana bound states (MBS) are the fundamental constituents for fault-tolerant topological quantum computing [5, 6]. Individual qubits comprise at least four MBS in several interconnected nanowire segments with a hard induced superconducting gap [7, 8]. Residual fermionic states within the gap would compromise the topological protection of the Majorana modes. Hence, a fundamental challenge in the development of topological qubits is the engineering of complex, interconnected hybrid devices with hard superconducting gaps and clean, homogenous interfaces [9, 10].

Here, we introduce a novel fabrication technique that resolves these challenges and provides high-quality hybrid quantum devices involving minimal nanofabrication steps compared with previously established methods [11, 12]. Our approach is based on the deposition of superconducting thin films at a shallow angle onto semiconducting nanowires, which have been selectively placed on substrates with pre-patterned gates and shadow-wall structures. It enables complex hybrid devices while eliminating lithography, etching, and other fabrication steps after the deposition of the superconductor, in the following referred to as *post-interface fabrication*. While shadow-wall lithography is compatible with a large variety of materials, we utilize InSb nanowires coated with Al half-shells to induce superconducting correlations – a suitable material combination to study Majorana physics [12, 13]. The homogeneity of the interface between InSb and Al ultimately determines the device quality, but it is known to have very limited chemical and thermal stability [10, 14]. Therefore, the reduction or elimination of post-interface fabrication steps represents a paradigm shift that enables pristine hybrid interfaces. Similar advances in quality and reproducibility were made possible by the reverse fabrication process established for carbon nanotube devices [15].

In this article, we investigate the transport properties of hybrid nanowire shadow-wall devices. Initially, we examine Josephson junctions and detect subharmonic gap features that arise from multiple Andreev reflections [16]. These junctions exhibit gate-tunable supercurrents of up to 90 nA, which is exceptionally large for InSb/Al nanowires [10, 17, 18]. The shadow-wall method also facilitates 3-terminal hybrid devices with two normal-metal–superconductor (N–S) interfaces, which are crucial to corroborate earlier Majorana signatures [19, 20]. We investigate the transport at a single N–S interface and observe a crossover between a hard induced gap and pronounced Andreev enhancement upon increasing the junction transparency, consistent with the expected behaviour for ballistic junctions [21, 22]. Finally, we report the emergence of discrete subgap states in the tunnelling conductance at both nanowire ends and detect stable zero-energy conductance peaks that coexist at certain magnetic fields and chemical potentials.

Our fabrication method paves the way for more advanced nanowire devices, including qubit implementations [7, 8, 23] and other multi-terminal devices that are essential for fundamental research on topological superconductors [20, 24]. The versatility of the shadow-wall technique introduces a convenient and quick way to implement new device geometries with various combinations of semiconductor and superconductor materials.

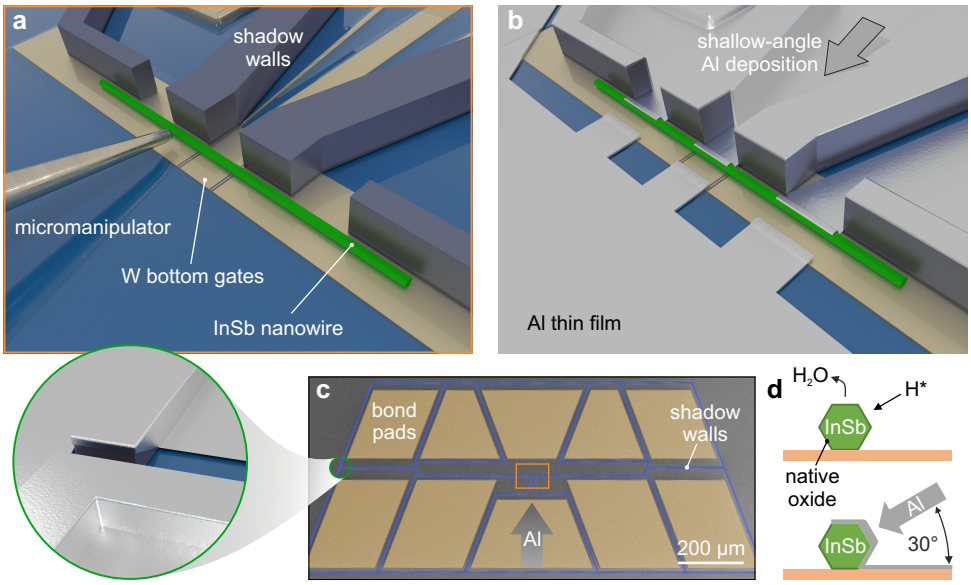

Figure 8.1: **Illustration of the shadow-wall technique. a** Micromechanical transfer of the nanowires onto local bottom gates (covered by Al_2O_3 dielectric) in the proximity of the Si_3N_4 shadow walls. **b** Illustration of a final device following the H radical cleaning and Al deposition at a shallow angle. **c** False-colour SEM image of an exemplary sample. Shadow walls are designated in blue and bond pads, which are enclosed by shadow walls, are shaded in dark yellow. Gaps are placed at critical locations along the shadow walls (cf. green circle and the illustration in the blow-up). This ensures that bond pads with leads are isolated from each other after the Al deposition. The area illustrated in panel (**a**) is indicated by the orange box. **d** Schematic of the InSb nanowire cross-section during H radical cleaning (top). The native oxide of the semiconductor is denoted by a dark green layer. The Al thin film deposited at a shallow angle of 30° forms an electrical connection to the substrate (bottom).

8.1. SHADOW-WALL LITHOGRAPHY

A well-established approach to realize hybrid devices is based on the epitaxial growth of nanowires followed by the in-situ evaporation of a superconductor [11, 25]. This method requires a subsequent etching step to expose gate-tunable wire segments without metal. Nanowires have also been grown on opposite crystal facets of etched trenches [12, 26], which enables the formation of shadowed junctions without the need to etch the superconductor [12]. The native oxide that forms during the ex-situ processing is removed prior to the deposition of the superconductor. Another recent study employed growth chips with bridges and trenches that act as selectively shadowing objects during the evaporation of a superconductor [27]. However, common to those methods is that the hybrid nanowires are removed from the growth substrate following the evaporation and undergo several post-interface fabrication steps such as alignment via scanning electron microscopy (SEM), electron-beam lithography involving resist coating, or etching. However, hybrid devices are prone to degradation. High-temperature processing (e.g. certain dielectric deposition methods or resist baking) cannot be performed, as it would lead to chemical intermixing at the super-/semiconductor interface [28, 29]. The limited chemi-

cal stability of the interface requires sample storage in vacuum at a temperature $T < 0\,^{\circ}\mathrm{C}$, which is hardly compatible with standard fabrication methods. The low thermal budget and the additional fabrication steps limit the achievable device performance in terms of electrical noise, lithographical alignment accuracy, contamination and disorder. The considerable variation from device to device imposes singular rather than standardized designs and results in a limited reproducibility of basic transport measurements.
In contrast, the core principle of our approach is to minimize or eliminate post-interface fabrication. We have engineered scalable substrates that comprise all desired functionalities without being subject to any fabrication restrictions (e.g. thermal budget limitations) since the semiconductor nanowires are only introduced right before the superconductor deposition. As depicted in Fig. 8.1a, we transfer InSb nanowires [30] to these substrates onto pre-patterned bottom gates covered by a continuous dielectric layer in the vicinity of shadow-wall structures. The nanowires are loaded into a customized evaporation chamber where the native oxide is removed at $T = 550\,\mathrm{K}$ by exposure to a directed flow of atomic hydrogen radicals. Without breaking the vacuum, Al is subsequently deposited onto the samples at $T = 140\,\mathrm{K}$. The superconductor is evaporated at a shallow angle of 30° with respect to the substrate plane, which creates a 3-facet nanowire shell that is connected to the leads and bond pads on the substrate (Fig. 8.1d). As illustrated in Fig. 8.1b, the shadow walls enable selective deposition on both the nanowires and the substrate. Adding gaps at critical locations along the shadow walls (Fig. 8.1c) ensures that the leads are electrically isolated from one another while eliminating the need for post-interface fabrication such as lift-off patterning or Al etching. Fig. 8.2a shows an exemplary device that is directly bonded to a printed circuit board for low-temperature transport measurements. Here, the p^+-doped Si substrate enables back-gate control of the electron density in the nanowire (see Fig. 8.2b).

8.2. MATERIALS ANALYSIS

The quality of the InSb nanowires, Al thin films, and InSb/Al interfaces is assessed by transmission electron microscopy (TEM) of cross-sectional lamellae prepared via focused ion beam (FIB). These lamellae are cut out from devices like the one depicted in Fig. 8.2a (cf. dashed line). A continuous high-quality polycrystalline Al layer is formed on three facets of the InSb nanowires and the samples exhibit a sharp superconductor–semiconductor interface (see Figs. 8.2c,e and Fig. 8.7). No oxide formation is observed between the Al grains, which is evident in the elemental energy-dispersive X-ray spectroscopy (EDX) composite image (Fig. 8.2c). The middle facet has twice the Al layer thickness (16 nm) compared to the top and bottom facets (8 nm) due to the evaporation angle of 30° with respect to the substrate plane. The InSb/Al interface is clean and there is no residual native oxide (see Figs. 8.2d,e), which confirms that our procedure of atomic hydrogen radical cleaning can effectively remove the oxide without damaging the InSb crystal structure. The nanowires are single-crystalline, defect-free, and exhibit a hexagonal geometry. The polycrystalline Al layer forms a continuous metallic connection from the nanowire to the substrate. This connection is crucial for the contact between the shell and the thin Al lead on the substrate and it is fundamental for more complex devices such as superconducting interferometers (see Fig. 8.31) and 3-terminal Majorana devices that can reveal the opening of a topological gap [20].

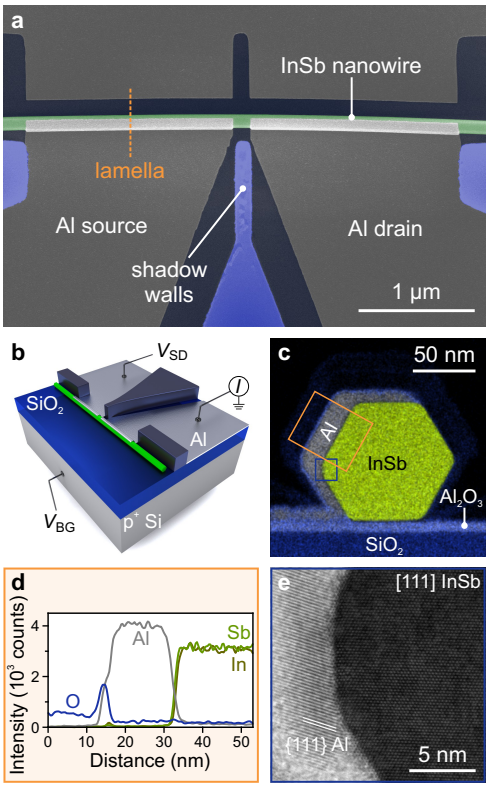

Figure 8.2: **TEM analysis of the InSb/Al interface. a** False-colour SEM image of an InSb nanowire Josephson junction. **b** Schematic of the measurement setup. The back-gate voltage, V_{BG}, is applied to the p^+-doped Si substrate to tune the electron density in the nanowire. **c** Cross-sectional EDX elemental composite image of the [111] InSb nanowire covered with the Al layer and a protective layer of SiN_x. **d** Line-cuts of the integrated elemental counts within the orange box in panel (**c**). **e** High-resolution bright-field scanning TEM image of the InSb/Al interface at the location indicated by the blue box in panel (**c**).

8.3. HIGHLY TRANSPARENT JOSEPHSON JUNCTIONS

We employ mesoscopic InSb/Al Josephson junctions like the one depicted in Fig. 8.2a to study the induced superconductivity in the nanowires. Each device comprises two Al contacts (1.8 µm wide) separated by a 110 – 150 nm long bare nanowire segment that is tunable by the back-gate voltage, V_{BG}. The source–drain voltage, V_{SD}, is applied or measured between the two Al electrodes (Fig. 8.2b). Fig. 8.3a shows the differential resistance, $R = \mathrm{d}V_{SD}/\mathrm{d}I_{SD}$, as a function of bias current, I_{SD}, and temperature for a typical device. The blue region ($R = 0\,\Omega$) denotes the superconducting phase, which persists up to ~ 1.8 K. At low temperatures ($T < 0.6$ K), the hysteretic behaviour of the asymmetric V_{SD}–I_{SD} traces indicates that the junction is in the underdamped regime according to the model of resistively and capacitively shunted junctions. Above 0.6 K, the thermal activation washes out the asymmetry of the traces. Remarkably, at $T = 30$ mK, the switching current, I_{sw}, i.e. the observable supercurrent, ranges from 30 to 90 nA across all devices in

the open-channel regime. The magnitude of the intrinsic supercurrent, I_c, in ballistic and short junctions can be predicted via the Ambegaokar–Baratoff formula: $I_c R_N = \pi\Delta_{ind}/2e$, with the normal-state resistance R_N, the induced gap Δ_{ind}, and the electron charge e [31]. Here, the typical $I_{sw}R_N$ product is ~ 110 µV, i.e. only one-third of $\pi\Delta_{ind}/2e \sim 360$ µV. The discrepancy between I_{sw} and I_c is consistent with previous experiments [17, 18, 32] and can be explained by premature switchings due to thermal activation and current fluctuations [33, 34]. In Fig. 8.3b, we show the differential conductance, $G = \mathrm{d}I_{SD}/\mathrm{d}V_{SD}$, as a

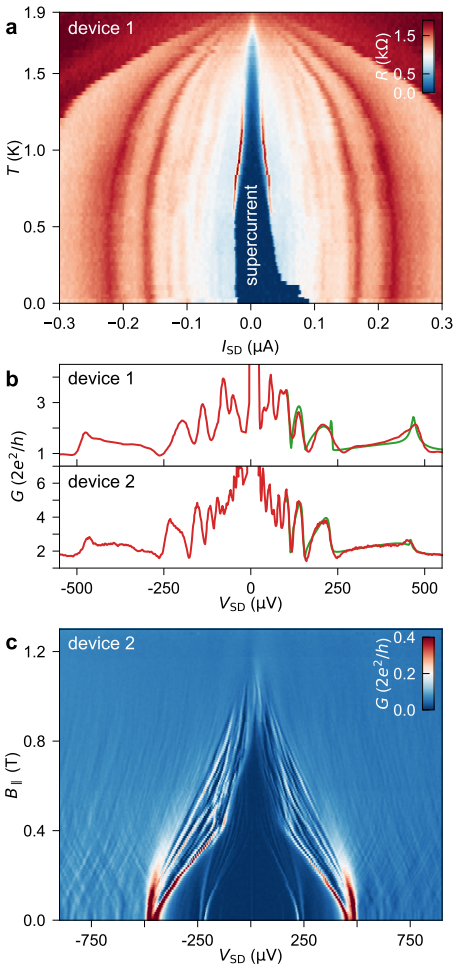

Figure 8.3: **Multiple Andreev reflections and supercurrent in InSb/Al Josephson junctions**. **a** Differential resistance, R, as a function of I_{SD} (upward sweep direction) and T for device 1 at $V_{BG} = 13.65$ V. The switching current reaches a maximum of ~ 90 nA at $T = 30$ mK and persists up to 1.8 K. **b** Conductance line traces (red) versus source–drain voltage for device 1 at $V_{BG} = 5.1$ V (top) and for device 2 at $V_{BG} = 3.0$ V (bottom). The theoretical fits (green) yield the transmissions, T_n, of the one-dimensional subbands with index n: $T_1 = 0.87$, $T_2 = 0.17$ (top) and $T_1 = 0.93$, $T_2 = 0.71$, $T_3 = 0.01$ (bottom). **c** Differential conductance, G, as a function of V_{SD} and magnetic field, $B_\parallel$, which is oriented along the nanowire, for device 2 at $V_{BG} = -0.9$ V.

function of V_{SD} (red curves) for the same Josephson junction (top) and for a second device (bottom). The traces display subharmonic conductance peaks originating from multiple Andreev reflection (MAR) processes [16]. By fitting the conductance with a coherent scattering model (green curves), we can estimate the induced superconducting gap, Δ_{ind} (233 μeV and 230 μeV for device 1 and 2, respectively), and the gate-tunable tunnelling probability of the different subbands (see Fig. 8.12) [35].
In Fig. 8.3c, we report the evolution of the MAR pattern as a function of magnetic field, $B_{\parallel}$, parallel to the nanowire axis of device 2. Here, the presence of subgap states close to the gap edge alters the typical MAR pattern and gives rise to an intricate energy dispersion in magnetic field that is further discussed in section 8.8.3. Eventually, the magnetic field quenches the superconductivity at a critical value of $B_c = 1.2 - 1.3$ T. This limit can be enhanced to about 2 T by using a thinner Al shell (Fig. 8.17). These values are well above the magnetic field at which a topological phase transition should occur in hybrid InSb/Al nanowires [36].

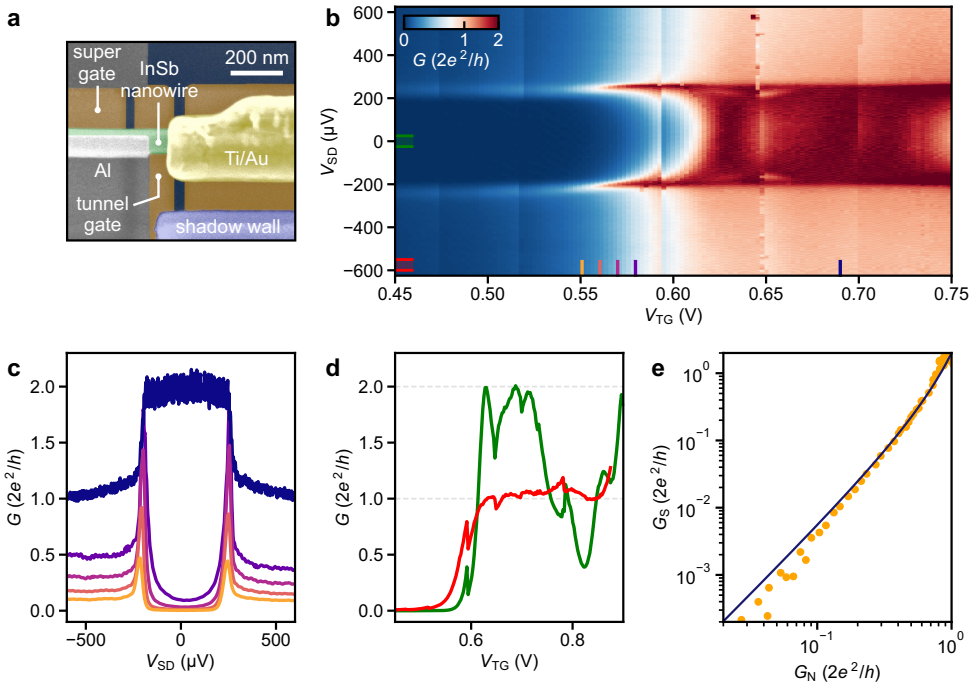

Figure 8.4: **Ballistic Andreev transport. a** False-colour SEM image of an exemplary N–S junction. The W bottom gates (brown) underneath the InSb nanowire (green) are covered by 18 nm of Al_2O_3 dielectric. **b** Differential conductance, G, as a function of source–drain voltage, V_{SD}, and bottom tunnel-gate voltage, V_{TG}. The so-called *super gate*, which controls the chemical potential of the hybrid nanowire segment, is grounded. **c** G versus V_{SD} line-cuts of the data in panel (**a**) at the locations designated by the coloured lines. **d** Subgap conductance (green) and above-gap conductance (red) averaged over the V_{SD} intervals designated in panel (**b**). **e** G_S (subgap conductance at zero bias) as a function of G_N (normal-state conductance at $V_{SD} = 650$ μeV) together with the theoretically predicted dependence, which assumes Andreev-dominated transport in a single channel (blue line trace).

In Fig. 8.3c, the out-of-gap conductance displays a dense pattern of faint peaks with an average spacing of about 30 μV and an effective Landé g factor of ~ 20 (extracted from the energy dispersion in magnetic field). This g factor is larger than in Al ($|g| = 2$) but smaller than in InSb ($|g| = 30 - 50$), which indicates that these peaks stem from discrete states of the nanowire hybridized with the ones in the metal [37]. The observation of this structure is a novelty and it might be correlated with our choice of nanowire surface treatment. In fact, the gentle atomic hydrogen cleaning preserves the pristine semiconductor crystal quality, unlike the invasive chemical or physical etching methods adopted in previous works [10, 17, 18, 32, 38].

8.4. HARD INDUCED GAP AND BALLISTIC SUPERCONDUCTIVITY

A common technique to search for evidence of Majorana bound states is N–S tunnelling spectroscopy, which probes the local density of states. Signatures of MBS in proximitized InSb nanowires are zero-bias peaks (ZBPs) in the differential conductance at moderately large magnetic fields [19]. The ZBP height in the zero-temperature limit is predicted to be $G_0 = 2e^2/h$, independent of the tunnel-coupling strength, due to resonant Andreev reflection via a Majorana zero mode [39]. ZBPs of non-topological origin, which mimic the subgap behaviour of MBS, may arise from disorder or potential inhomogeneities [40]. A major challenge is to reduce the detrimental role of disorder at the superconductor–semiconductor interface, which determines the final device quality. The measure of success is a hard induced gap at a finite magnetic field and quantized Andreev enhancement as a signature of ballistic transport [41].

An exemplary N–S device is depicted in Fig. 8.4a. Here, the N contact to the InSb nanowire was formed in an optional post-interface fabrication step. In Fig. 8.4b, we present voltage-bias spectroscopy at such an N–S junction where the transmission is tunable via a pre-fabricated bottom tunnel gate. The line-cuts in Fig. 8.4c at low tunnel-gate voltage, V_{TG}, highlight the pronounced suppression of the subgap conductance, G_S, by about two orders of magnitude compared with the normal-state conductance, G_N (cf. Fig. 8.24). As the first one-dimensional subband starts to conduct fully at $V_{TG} > 0.6$ V, the above-gap conductance reaches the conductance quantum, $2e^2/h$, and the quantization manifests itself as a plateau in the tunnel-gate dependence (Fig. 8.4d). At the same time, the conductance below the gap edge reaches $4e^2/h$ owing to two-particle transport via Andreev reflection [21]. This pronounced doubling of the normal-state conductance together with the quantization of G_N signifies a very low disorder strength in the junction and a strong coupling at the nanowire/Al interface [42]. While the subgap conductance reaches up to $2G_0$, it drops again before the chemical potential reaches the bottom of the second confinement subband due to inter-subband scattering [42, 43]. The plot of G_S versus G_N (Fig. 8.4e) follows the Beenakker model [22] without fitting parameter reasonably well, which shows that in the single-subband regime electrical transport below the gap edge is dominated by Andreev processes. The data are well-described by the BTK theory [21] across the entire gate voltage range, demonstrating a hard induced gap of $\Delta_{ind} \sim 230$ μeV (see Methods and Fig. 8.26). Discrete subgap states and ZBPs appear at a finite magnetic field and field-dependent voltage-bias spectroscopy for this N–S device is presented in

Fig. 8.27.

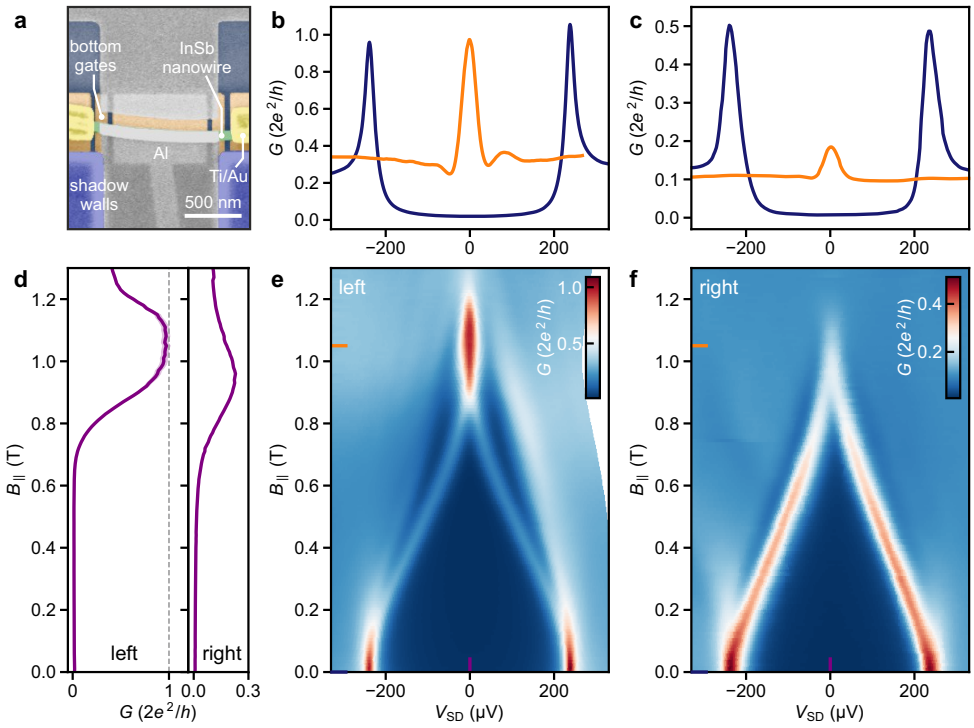

Figure 8.5: **Zero-bias conductance peaks at two opposite N–S boundaries.** **a** False-colour SEM image of the correlation device with a 1 μm long hybrid nanowire segment. **b**, **c** Line-cuts of the differential conductance at zero field (blue) and at $B_\parallel = 1.05\,\mathrm{T}$ (orange) taken from panel (**e**) and (**f**), respectively. **d** G versus $B_\parallel$ line-cut at $V_\mathrm{SD} = 0\,\mu\mathrm{V}$ taken from panel (**e**) (left) and (**f**) (right). Shaded areas (light purple) illustrate the variation in conductance assuming an uncertainty of $\pm 0.5\,\mathrm{k}\Omega$ in the series resistance. For the line-cut at the right N–S junction, this variation is less than the line width. **e**, **f** Differential conductance, $G = \mathrm{d}I_\mathrm{SD}/\mathrm{d}V_\mathrm{SD}$, as a function of bias voltage, V_SD, and magnetic field, $B_\parallel$, measured concurrently at the left and right junction, respectively. Here, the super gate underneath the hybrid nanowire segment is grounded ($V_\mathrm{SG} = 0\,\mathrm{V}$).

8.5. EMERGENCE OF ZERO-BIAS PEAKS AT BOTH NANOWIRE ENDS

The shadow-wall technique enables novel 3-terminal Majorana devices for nonlocal correlation experiments [20, 44] by harnessing the continuous connection of the Al shell to the substrate, as depicted in Fig. 8.5a. Here, the Al thin film serves as the superconducting drain lead. Established fabrication methods do not allow for the implementation of such devices since etching away the superconductor causes disorder at the InSb surface and contacting the Al shell requires selective removal of the native oxide of Al, which affects the integrity of the thin film. As shown in Fig. 8.5a, optional Ti/Au contacts are again added at both nanowire ends. With this device type, we can study the simultaneous emergence of ZBPs at both N–S boundaries in a magnetic field oriented along the wire. Here, the

hybrid nanowire segment is 1 µm long and the chemical potential, μ, is controlled via a bottom gate (*super gate*) at potential V_{SG}. The differential conductance is measured concurrently at both N–S boundaries by alternating the V_{SD} sweep between the left and right N terminals for every increment of $B_{\parallel}$ or V_{SG}. Using this technique, we demonstrate the formation of zero-energy subgap states at both nanowire ends for $V_{SG} = 0$ V (see Figs. 8.5e,f). The effective g factor extracted from the linear energy dispersion at the two boundaries is ∼ 10, albeit the values of g can be strongly gate-dependent [13]. Many experiments have demonstrated ZBPs in tunnelling spectroscopy at a single N–S boundary, indicating the presence of a robust state at zero energy [19, 45–47]. The robustness of ZBPs in the parameter space (defined by chemical potential and magnetic field) has been used to substantiate their topological origin [48]. So far, no experiment has revealed the emergence of ZBPs concurrently at both boundaries of a long hybrid nanowire. Recent experimental studies reported correlations between bound states at both ends of short (up to 400 nm long) hybrid nanowire devices [49, 50]. ZBPs often originate from trivial Andreev bound states (ABS) formed by overlapping MBS due to local variations in the chemical potential or random disorder, which emphasizes the need for long and pristine hybrids [40]. A topological phase with well-separated MBS requires that potential inhomogeneities along the hybrid segment are much smaller than the critical Zeeman energy, $E_Z^c = \sqrt{\Delta_{ind}^2 + \mu^2}$ [2, 51]. We see in Figs. 8.5e,f that the ZBPs at the two boundaries do not exhibit the same onset field, which could possibly be explained by the presence of long-range inhomogeneities that result in different values of E_Z^c at the two nanowire ends. At larger values of μ, potential variations are expected to be suppressed due to screening. This might be supported by another data set measured at a larger chemical potential ($V_{SG} \sim 0.5$ V) presented in Fig. 8.29, where we observe the same ZBP onset field at both N–S boundaries. The concomitant evolution as a function of V_{SG} at both nanowire ends is shown in Figs. 8.29 and 8.30. This observation might corroborate the signatures of MBS [44, 51], but it cannot be regarded as conclusive evidence for truly separated MBS [40].

Figs. 8.5b,c show differential conductance line-cuts, which reveal a zero-bias conductance close to $2e^2/h$ for the ZBP at the left boundary of the device, as highlighted in Fig. 8.5d. While ZBP conductance close to G_0 has been observed for several N–S boundaries, it depends on the fine-tuning of the tunnel barriers, which can be strongly affected by transmission resonances. Experimentally, ZBPs are in general substantially lower than the expected value of G_0 [39, 45]. Theoretical studies recently pointed out that partially or fully overlapping MBS can cause quantized ZBPs, indistinguishable from those resulting from isolated MBS [51–53]. Hence, the quantized ZBP conductance is a critical but not sufficient hallmark of MBS [50, 53].

8.6. DISCUSSION AND OUTLOOK

The 3-terminal hybrid nanowire devices provide a fundamental tool to study the evolution of the induced superconducting gap in the bulk of the hybrid, where electron- and hole-type bands become inverted at the topological phase transition. There, the closing and reopening of the induced gap are accompanied by the emergence of delocalized MBS, hallmarked by ZBPs at both boundaries of the hybrid nanowire. Here, we demonstrate

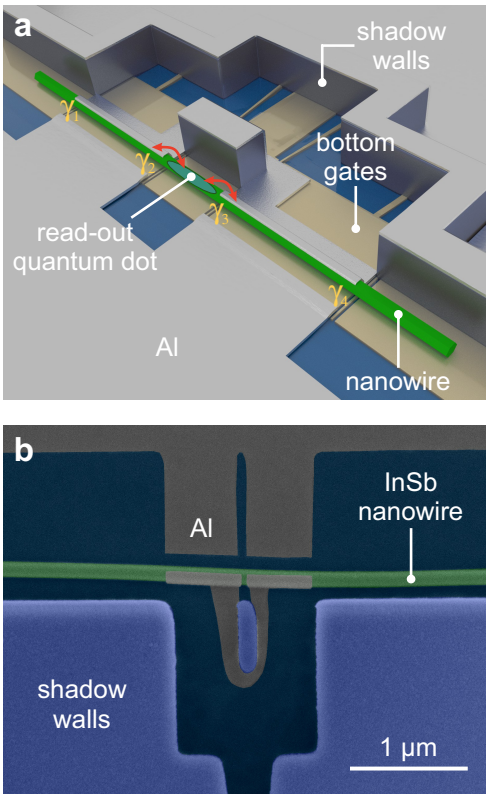

Figure 8.6: **Illustration of the proposed Majorana loop qubit. a** Schematic of a single-nanowire loop-qubit device. The presumable locations of the MBS at the boundaries of the two hybrid segments are denoted by γ_i, where $i \in \{1,2,3,4\}$. The electron parity is fixed due to the finite charging energy of the loop qubit. This configuration offers the desired ground-state degeneracy for a single qubit and can provide information on decoherence and quasiparticle poisoning. **b** False-colour SEM image of an InSb nanowire following the shadow-wall deposition. Two segments of the nanowire are covered with a superconducting 3-facet Al shell. These hybrid segments are interconnected via an Al loop running across the substrate.

hard-gap N–S junctions in a magnetic field where only discrete subgap states move to zero energy to form ZBPs at both boundaries and that respond similarly to variations in the chemical potential. While these are critical signatures of MBS, upcoming studies will attempt to correlate the local tunnelling conductance with the evolution of the induced bulk gap via the non-local conductance between the two N terminals [20].

Our approach promotes the development of intriguing nanowire-based quantum devices. The ballistic hard-gap N–S junctions together with the continuous thin Al connections across the substrate represent a vital starting point for realizing a topological qubit. A qubit implementation with a single read-out loop [8] would allow for measuring the projection of the qubit state on one axis of the Bloch sphere. A schematic of the *loop qubit* is presented in Fig. 8.6a. It is made from a single nanowire with two superconductor–semiconductor segments connected via a superconducting loop that encircles a central

shadow-wall pillar. Bottom gates at the centre of the device are used to define a read-out quantum dot in the nanowire with tunable tunnel couplings to the MBS denoted as γ_2 and γ_3 in the schematic. Parity read-out will be performed by measuring the quantum capacitance via radio-frequency gate reflectometry [7, 8, 54]. In Fig. 8.6b we present an exemplary realization of the basic elements of such a device via the shadow-wall technique. It comprises a superconducting loop to provide a connection for the exchange of Cooper pairs that acts a blocker for quasiparticle transport between the two hybridized nanowire segments. The shadow-wall technique is ideally suited to realize Al loops across the substrate and multi-terminal devices without the need for post-interface fabrication.

AUTHOR CONTRIBUTIONS

S.H., M.Q.P., F.B., P.A., K.v.H. and L.P.K. conceived the experiment. S.H., M.Q.P., F.B., N.v.L., G.P.M., J.S. and M.A.Y.v.d.P. contributed to the fabrication and/or electrical transport measurements of the devices. S.H. and F.B. analysed the transport data. A.F. fabricated the substrates. M.P.N. performed numerical simulations of the MAR processes. M.A. made critical upgrades to the equipment and provided technical support. G.B., S.G. and E.P.A.M.B. carried out the nanowire synthesis. K.L. prepared the FIB lamellae. S.K. performed the TEM analysis. S.H., M.Q.P. and F.B. wrote the manuscript. All authors provided critical feedback. L.P.K. supervised the project.

DATA AVAILABILITY

The data and the codes that create the figures in this chapter are available at `http://doi.org/10.5281/zenodo.3954465`.

8.7. METHODS

NANOWIRE GROWTH

The InSb nanowires are grown on InSb (111)B substrates covered with a pre-patterned SiN_x mask via metalorganic vapour-phase epitaxy (MOVPE). These nanowires are not grown on top of InP stems but nucleate instead directly on the growth substrate at Au catalyst droplets [30]. The investigated nanowires have an average diameter of 100 nm, which is controlled by the Au droplet size and the growth mask openings, and a typical length in the order of 10 µm.

DEVICE FABRICATION

Bottom gates are fabricated on Si/SiO_2 substrates via dry-etching of W thin films, which are subsequently covered by Al_2O_3 gate dielectric via atomic layer deposition (ALD). Shadow walls of ~ 600 nm height are created via reactive-ion etching of thick layers of Si_3N_4 formed via plasma-enhanced chemical vapour deposition (PECVD). Using a micromanipulator, individual nanowires are placed deterministically next to the shadow walls. The native oxide of the nanowires is removed via atomic hydrogen radical cleaning (see section 8.8.1). The Al thin films are deposited by evaporation under a shallow angle that forms continuous contacts between the nanowires and the substrate and creates

segments on the chip that are electrically isolated from one another. This allows to immediately cool down the devices without the need for additional post-interface fabrication steps. Additional Ti/Au leads, as depicted in Figs. 8.4 and 8.5, are optional. Alternatively, Al leads that are defined by the shadow walls – microns away from the N–S junction – can serve as N contacts but require additional bottom gates to render all nanowire segments fully conducting (cf. Fig. 8.1b).

TEM ANALYSIS

The cross-sectional lamellae for TEM are prepared using the focused ion beam technique with a Helios G4 UX FIB/SEM from Thermo Fisher Scientific after capping the devices with a protective layer of sputtered SiN_x. TEM analysis is carried out at an acceleration voltage of 200 kV with a Talos electron microscope from Thermo Fisher Scientific equipped with a Super-X EDX detector.

TRANSPORT MEASUREMENTS

Electrical transport measurements are carried out in dilution refrigerators equipped with 3-axes vector magnets. The base temperature is approximately 15 mK, corresponding to an electron temperature of about 30 mK measured with a metallic N–S tunnel junction thermometer. The sample space is evacuated for at least one day prior to the cool-down to remove surface adsorbates that limit the device performance. Conductance measurements are performed using a standard low-frequency lock-in technique. For voltage-bias measurements, the excitation voltage is $V_{AC} \leq 20\,\mu V$ at a lock-in frequency of at least 20 Hz. Current-driven measurements are carried out in a four-point configuration. After taking the data, we became aware of the relatively low bandwidth of the employed current-to-voltage amplifiers. Hence, we recalibrated the lock-in data via a mapping according to the measured DC conductance that does not suffer from any bandwidth limitations and is insensitive to the reactive response of the circuit (section 8.8.4).

SUPERCONDUCTING GAP EXTRACTION

The BCS–Dynes term is given by a smeared BCS density of states with the broadening parameter Γ [55]:

$$\frac{dI_{SD}}{dV_{SD}}(V_{SD}) = G_N \,\mathrm{Re}\left[\frac{eV_{SD} - i\Gamma}{\sqrt{(eV_{SD} - i\Gamma)^2 - \Delta_{ind}^2}}\right].$$

For all of our N–S devices, the fit of the BCS–Dynes term yields typical broadening parameters of less than 10 μeV. The model by Blonder, Tinkham, and Klapwijk (BTK) incorporates the transition between BCS tunnelling and Andreev reflection in the open channel [21]. Fits of the BCS–Dynes term and of the BTK model to the N–S junction data (including the data in Fig. 8.4b) are presented in section 8.8.4.
The subgap conductance for a ballistic N–S junction with a single subband, where the transport is dominated by Andreev processes, has been described by Beenakker [22]. At a

large enough chemical potential [56], it is given by

$$G_S = \frac{4e^2}{h}\frac{T^2}{(2-T)^2} = 2\frac{G_N^2}{(2G_0 - G_N)^2},$$

where the transmission probability, T, has been substituted with the normal-state conductance, G_N, in units of $2e^2/h$. This function is plotted together with the measured data in Fig. 8.4e.

8.8. SUPPLEMENTARY INFORMATION

8.8.1. FABRICATION RECIPES

CHIPS WITHOUT BOTTOM GATES

Chips that contain devices with a global back-gate like the ones presented in Figs. 8.2 and 8.3 are fabricated on p^+-doped Si wafers covered with 285 nm of thermal SiO_2. The first fabrication step consists of patterning the bond pads via electron-beam lithography (EBL), W sputtering and lift-off in acetone. Afterwards, plasma-enhanced chemical vapour deposition (PECVD) of 600 nm of Si_3N_4 is performed followed by EBL, reactive-ion etching (RIE) with CHF_3/O_2 gases, resist lift-off and an oxygen plasma descum step to remove carbon residues. Eventually, nanowires are deposited under an optical microscope using a micromanipulator equipped with tungsten needles [57].

CHIPS WITH BOTTOM GATES

Chips with additional local bottom gates (used e.g. for the experiments in Figs. 8.4 and 8.5) are fabricated by sputtering 17 nm of W on Si wafers covered with 285 nm of thermal SiO_x (protected by a thin Al_2O_3 etch-stop layer), followed by EBL patterning and RIE of the W layer with SF_6 gas. Next, 18 nm of a high-quality Al_2O_3 layer are deposited by atomic layer deposition (ALD), acting as bottom-gate dielectric. Shadow walls on top of the bottom gates are created by first depositing 600 nm of Si_3N_4 by PECVD, followed by EBL patterning with precise alignment of the shadow walls with respect to the underlying fine bottom gates. Then, RIE with CHF_3/O_2 gases is used to selectively etch Si_3N_4 while the Al_2O_3 gate dielectric acts as an etch-stop layer. Finally, after the resist lift-off an oxygen plasma descum step is used to remove carbon residues from the chips. The nanowires are then mechanically transferred on top of the bottom gates under an optical microscope using a micromanipulator equipped with tungsten needles [57].

ADDITIONAL FABRICATION STEPS FOR N–S DEVICES

For devices with additional Ti/Au normal-metal contacts, such as the ones presented in Figs. 8.4 and 8.5, an extra post-interface fabrication step is included. It consists of EBL patterning, 40 s of argon ion milling at $1.5\cdot10^{-3}$ mbar with a commercial Kaufmann source in the load lock of an electron-beam evaporator, and in-situ evaporation of 10 nm/150 nm of Ti/Au followed by lift-off in acetone. Note that this step is not essential and could have been omitted. Bottom gates underneath the nanowire can open up the channels and tune the conductance. Combining this electrostatic gate control with additional Al contacts that are defined by shadow walls microns away from the N–S junction allows to entirely avoid post-interface fabrication for these devices.

SEMICONDUCTOR SURFACE TREATMENT

To obtain a pristine, oxide-free semiconductor surface, we accomplish a gentle oxygen removal via atomic hydrogen radical cleaning. For this purpose, a custom-made H radical generator is installed in the load lock of our aluminium electron-gun evaporator. It consists of a gas inlet for H_2 molecules connected to a mass-flow controller and a tungsten filament at a temperature of about 1700 °C that dissociates a fraction of the molecules into hydrogen radicals [58].

The cleaning process is assessed via the transport characteristics of InSb/Al nanowire junctions and TEM analysis of the same devices. In particular, we consider as critical indicators of the interface transparency the magnitude of the supercurrents and the amount of interface oxide measured via EDX. During the optimization, we vary the process duration and the hydrogen flow, and keep the substrate temperature constant at 550 K. It has been demonstrated in the literature that this temperature results in an efficient cleaning of InSb allowing for indium- and antimony-based oxides to be removed with similar efficiency [59, 60].

The optimal removal of the native oxide is achieved for a process duration of 30 mins and a hydrogen flow of 2 mln/min. During atomic hydrogen cleaning the H_2 pressure is $6.3 \cdot 10^{-5}$ mbar. This recipe, which is used for all the devices shown in this paper, results in a constant EDX count of oxygen at the interface (i.e. the traces do not show oxygen peaks, see Fig. 8.2d) and yields the highest supercurrents in the Josephson junction devices (~ 90 nA).

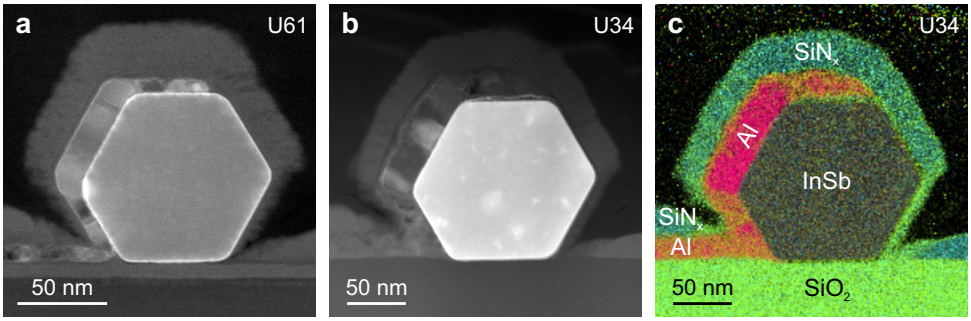

Figure 8.7: Cross-sectional TEM images of InSb nanowires covered by a thin layer of Al. SiN_x was sputter-coated as a protective layer before focused ion beam (FIB) lamella preparation. **a** Annular dark-field (ADF) scanning TEM image of a nanowire cross-section. This sample is identical to the device presented in Figs. 8.2c-e (sample ID: U61). The Al is deposited at an angle of 30° with respect to the substrate plane at $T = 140$ K. **b** ADF scanning TEM image of another nanowire cross-section (sample ID: U34). Here, 30 nm of Al are deposited at an angle of 25° with respect to the substrate plane at $T = 80$ K. **c** EDX elemental composite image of the device in panel (**b**) identifying the individual compounds and the Al thin film.

SUPERCONDUCTOR DEPOSITION

After the semiconducting surface cleaning, the chips are loaded into the evaporator main chamber and cooled down by actively circulating liquid nitrogen through the sample holder. After one hour of thermalization, aluminium is deposited by electron-beam evaporation at a typical rate of 0.2 nm/min.

The optimization of the aluminium growth is performed by studying the quality of thin films deposited on Si substrates – sometimes containing scattered or deposited InSb nanowires – at different evaporation rates, temperatures and angles. It is observed that evaporation angles close to 90° with respect to the substrate plane are favourable for thin-film aluminium growth, whereas for shallower angles the self-shadowing effect of the Al atoms on the surface becomes more apparent, giving rise to columnar growth, possible voids in the film, and a larger roughness [61, 62]. To minimize this angle-dependent self-shadowing effect, the substrate temperature can be slightly increased to give the atoms arriving at the substrate enough momentum to rearrange into a crystal before the next atoms arrive at the substrate. Our results and the work by Dong *et al.* [61] indicate that, for a fixed deposition rate, the temperature optimum depends on the evaporation angle.

In this work, a temperature optimum of around 140 K is found for Al growth at 30° with respect to the substrate plane, allowing for homogeneous 3-facet coverage of the hexagonal nanowires as well as a connection from the nanowires to the substrate. Josephson junctions made at this growth temperature exhibit roughly four times higher supercurrents than similar devices produced when Al was deposited at a substrate temperature of ~ 80 K. Similarly, cross-sectional TEM images of FIB lamellae from nanowires with Al grown at 140 K and 80 K are presented in Fig. 8.7a (as well as Figs. 8.2c,e) and Figs. 8.7b,c, respectively. Comparing these figures, the superior quality of the deposition at 140 K is evident; nanowire facets are better covered and form a continuous film, the crystalline quality of Al is higher and the oxidation of the Al facets is much less prominent than in the case of the deposition at 80 K (in Fig. 8.7b, the abundant oxide formation in the aluminium film at the the top and bottom-left nanowire facets is especially noticeable).

In addition, Fig. 8.8 illustrates a comparison between a higher Al growth temperature (160 K) and Al grown at 140 K. The former leads to both grainy Al covering the middle nanowire facet, which can be better observed in the tilt-view picture Fig. 8.8b, and a film on the substrate where the different grains are clearly distinguishable. Images corresponding to deposition at 140 K instead show a featureless Al film on the middle facet, where roughness is indiscernible at these SEM conditions (Fig. 8.8d), and a grainy but more uniform Al structure on the substrate.

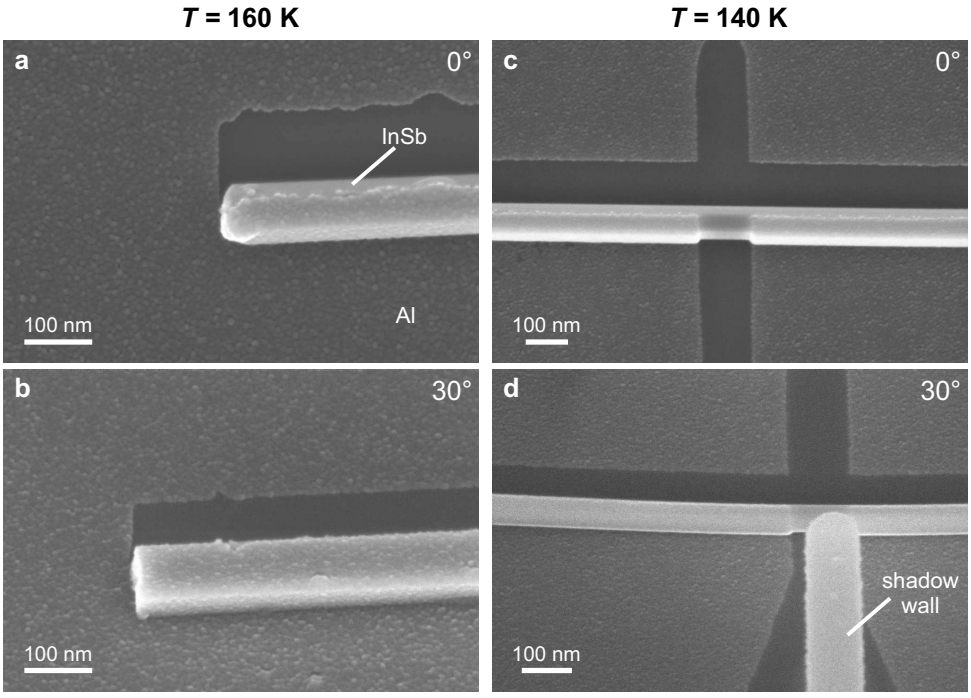

Figure 8.8: SEM images of InSb nanowires with Al thin films deposited at different temperatures. For both samples the evaporation angle is 30° relative to the substrate plane. **a**, **b** Top-view and tilt-view (tilt angle: 30°) SEM images of InSb nanowires covered with an Al thin film deposited at 160 K. The maximum film thickness, which corresponds to the middle nanowire facet, is 20 nm. **c**, **d** Top-view and tilt-view (tilt angle: 30°) SEM images of a nanowire Josephson junction. Here, the Al thin film is deposited at 140 K and the film thickness of the middle nanowire facet is 15 nm. Panel (**d**) exhibits a featureless Al shell on the middle wire facet, whereas grains are visible on the middle facet in the case of Al grown at 160 K (panel (**b**)).

TYPICAL YIELD OF THE NANOWIRE TRANSFER FOR JOSEPHSON JUNCTION DEVICES

Depending on the layout, our pre-patterned chips typically accommodate up to 16 nanowire devices. It is readily viable to have around 10 devices on a single chip to consistently optimize the fabrication parameters. The yield per chip can be affected by the accidental transfer of multiple wires at once or by nanowires breaking during the transfer. In Figs. 8.9 and 8.10, we show scanning electron micrographs taken prior to the cool-down of the Josephson junctions. On the first chip (sample ID: U12) 13 nanowires are transferred and result in 12 working devices, i.e. where the junctions are well-defined. On the second chip (sample ID: U55) 12 nanowires are positioned and yield 9 working devices. Among those, 7 are hexagonal-shaped nanowires and 2 turned out to be narrow nano-flakes [63, 64], which can be indistinguishable from nanowires in optical microscopy.

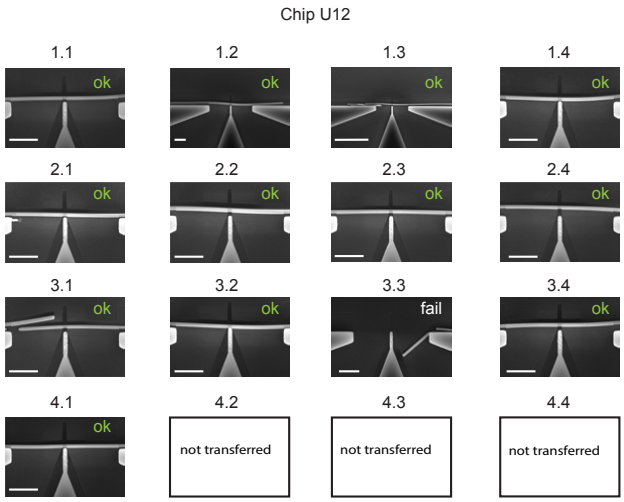

Figure 8.9: Typical yield of the nanowire transfer for Josephson junction devices: Scanning electron micrographs of all Josephson junction devices on a typical chip (sample ID: U12) taken after the Al deposition. Out of 13 nanowire transfer attempts, 12 nanowires are perfectly positioned, and only in one case the transfer failed (device 3.3). The scale bars indicate 1 μm.

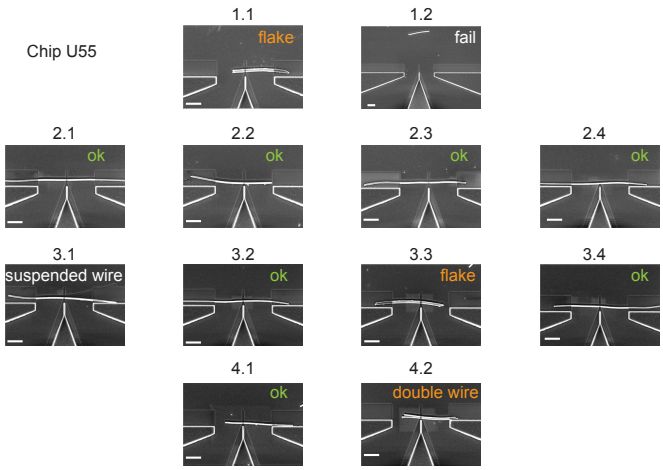

Figure 8.10: Typical yield of the nanowire transfer for Josephson junction devices: Scanning electron micrographs of all Josephson junction devices on a typical chip (sample ID: U55) taken after the Al deposition. Out of 12 nanowire transfer attempts, 7 nanowires are perfectly positioned, 2 of them are not (devices 1.2 and 3.1), 2 narrow flakes – rather than nanowires – are accidentally transferred (devices 1.1 and 3.3), and in one case, two nanowires are transferred in the same location (device 4.2). The scale bars indicate 1 μm.

8.8.2. ADDITIONAL TRANSPORT MEASUREMENTS OF JOSEPHSON JUNCTIONS

In this section, we summarize the characteristics of the Josephson junction devices listed in Tab. 8.1. All devices are fabricated by evaporating an Al thin film at 30° with respect to the substrate plane. Device 3 differs from the other samples in the thickness of the Al shell. We note that despite such a low shell thickness, all nanowire devices on sample U59 are in electrical contact with the Al film on the substrate.

Jos. junct.	Sample ID/ device name	Evap. angle	Channel width (nm)	Maximum Al thickness (nm)	Oxidation
dev. 1	U55/2.3	30°	100	16	in O_2 atm.
dev. 2	U51/1.2	30°	100	16	in O_2 atm.
dev. 3	U59/2.3	30°	100	11	Al_2O_3 cap.
dev. 4	U55/3.3	30°	160	16	in O_2 atm.

Table 8.1: Summary of the Josephson junction devices presented in this study. Devices 1, 2, and 3 are all nominally identical in their geometries with a nanowire diameter of 100 nm and a separation between the Al contacts of 115 nm. Device 3 was made with a thinner Al shell thickness and capped with around 20 nm of Al_2O_3. Device 4 is a Josephson junction formed in an InSb nano-flake. Here, the channel width is 160 nm.

Device 1 The current and differential conductance in the normal state (V_{SD} = 10 mV) display a steplike increase as a function of V_{BG} (Figs. 8.11a,b), a signature of ballistic transport at zero magnetic field in device 1. At lower bias voltage, features of the induced superconductivity appear such as the conductance peaks due to multiple Andreev reflections and the zero-bias supercurrent peak (Figs. 8.11c,d). A line-cut of Fig. 8.11c is presented in Fig. 8.3b, whereas a line-cut of Fig. 8.11d is shown in panel (e). Here, the experimental data (red trace) is fitted with the theoretical model (green trace) to identify the number and the transmissions of the nanowire subbands, which are plotted in Fig. 8.11f. Similarly, in Fig. 8.12a, we illustrate the extracted transmission probabilities of the three lowest subbands in the back-gate voltage range of Fig. 8.11c. The sum of these transmission probabilities extracted from the MAR pattern is compared to the normal-state conductance in Fig. 8.12b.

Device 2 The normal-state current and conductance (V_{SD} = 10 mV) as a function of back-gate voltage are displayed in Figs. 8.13a,b. While conductance plateaus are more difficult to identify than in the case of device 1, the presence of an induced superconducting gap is clear from the MAR conductance peaks and the supercurrent peak (Figs. 8.13c and d). By fitting each line-cut of panel (c) (just like in panel (d)), we can extract the transmissions of the nanowire subbands across the full measurement range (Fig. 8.13e). The closing of the superconducting gap and the suppression of the switching current with the magnetic field aligned along three perpendicular orientations are shown in Fig. 8.14 and Fig. 8.15, respectively.

Device 3 Device 3 differs from the first two samples by having a significantly thinner Al shell. To protect the thin film from oxidation, the device is capped in-situ with a

20 nm Al_2O_3 layer. This results in a large zero-field switching current of more than 50 nA (Fig. 8.16) and a critical magnetic field of ~ 2 T (Fig. 8.17).

Device 4 In this nano-flake device, the normal-state current manifests sharp steps and the differential conductance features quantized plateaus owing to ballistic transport in the junction (Figs. 8.18a,b). The presence of a moderate supercurrent (Fig. 8.18c) demonstrates that our fabrication technique can be used not only to proximitize one-dimensional nanowires, but also other types of nanostructures such as quasi-two-dimensional flakes.

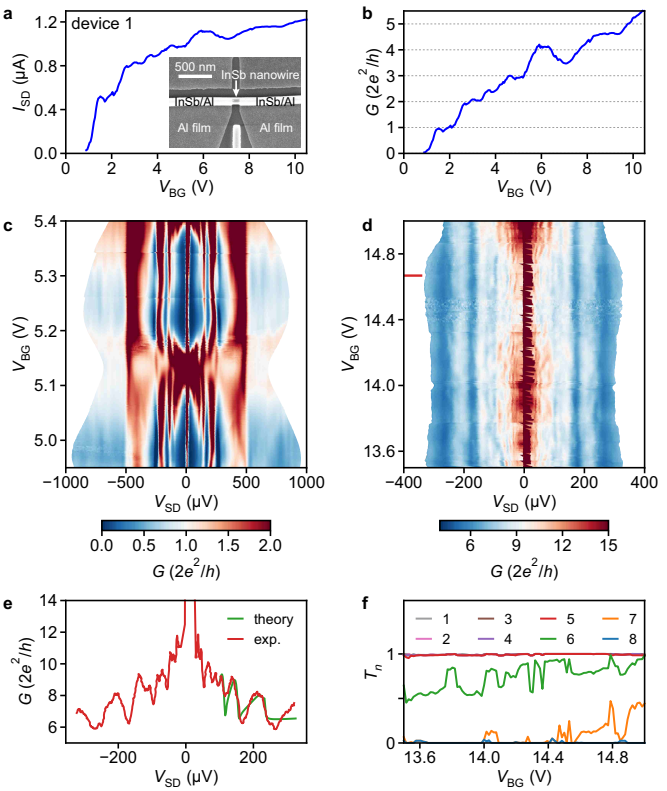

Figure 8.11: Additional transport measurements of the first Josephson junction device. **a** I_{SD} vs. V_{BG} sweep at V_{SD} = 10 mV, showing the field-effect tunability of the junction. Inset: scanning electron micrograph of the device. **b** DC conductance, G, after subtracting the series resistance, as a function of V_{BG} at 10 mV bias voltage. **c**, **d** G vs. V_{SD} and V_{BG} in the few-subbands and many-subbands regime, respectively: vertical features in both scans at constant bias voltages are the characteristic peaks originating from MARs. **e** Line-cut of (**d**) at V_{BG} = 14.67 V in red and best fit of the trace in green according to the coherent scattering model in section 8.8.3. **f** Extracted transmission probabilities, T_n, as a function of V_{BG} in the multi-subbands regime, with $n \in \{1, 2, \ldots, 8\}$. In this back-gate voltage range, the transmission of the first five subbands is already saturated at $T_n = 1$.

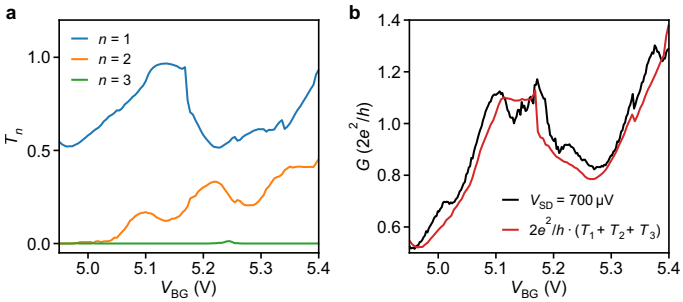

Figure 8.12: Tunability of the subbands of the first Josephson junction device. **a** Transmission probabilities, T_n, of the first three subbands as a function of V_{BG}. The parameters are extracted by fitting the conductance map of Fig. 8.11c with the coherent scattering model described in section 8.8.3. **b** Out-of-gap conductance as a function of V_{BG} in black (i.e. vertical line-cut of Fig. 8.11c at $V_{SD} = 700\,\mu V$) together with the sum of the transmission probabilities in red.

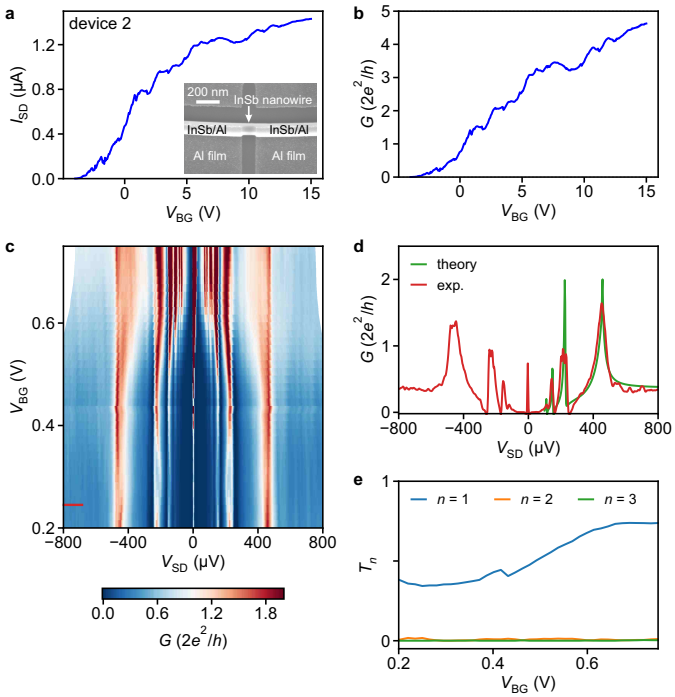

Figure 8.13: Additional transport measurements of the second Josephson junction device. **a** I_{SD} vs. V_{BG} sweep at $V_{SD} = 10\,mV$, showing the field-effect tunability of the junction. Inset: scanning electron micrograph of the device. **b** DC conductance, G, after subtracting the series resistance, as a function of V_{BG} at 10 mV bias voltage. **c** G vs. V_{SD} and V_{BG} in the weak-tunnelling regime: subharmonic gap features correspond to different orders of MARs. **d** Line-cut of (**c**) at $V_{BG} = 0.25\,V$ in red and best fit of the trace in green according to the coherent scattering model in section 8.8.3. **e** Extracted transmission probabilities, T_n, depicted as a function of V_{BG} with $n \in \{1,2,3\}$.

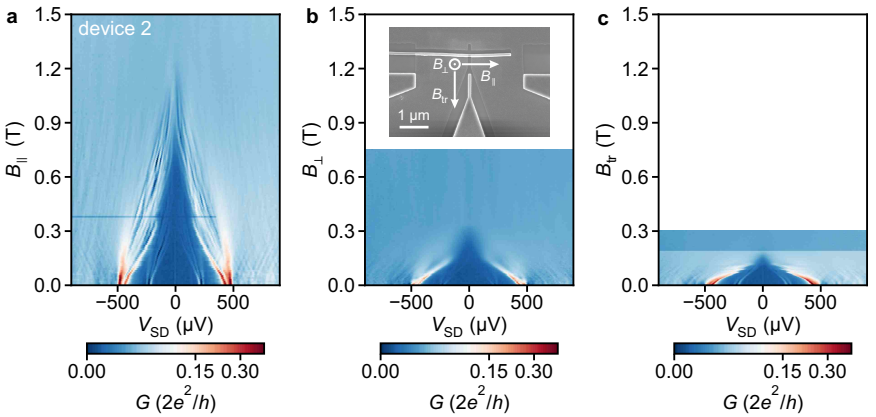

Figure 8.14: Superconducting critical magnetic fields of the second Josephson junction device. Colour maps of G vs. V_{SD} and magnetic field taken at $V_{BG} = 1.45\,V$ for different magnetic field orientations: in **a** the field $B_{\parallel}$ is oriented parallel to the nanowire direction, in **b** $B_{\perp}$ is orthogonal to the plane of the substrate, and in **c** the transversal field B_{tr} is orthogonal to the nanowire direction but in the substrate plane. The inset in panel (**b**) shows a scanning electron micrograph of the device together with the different magnetic field directions.

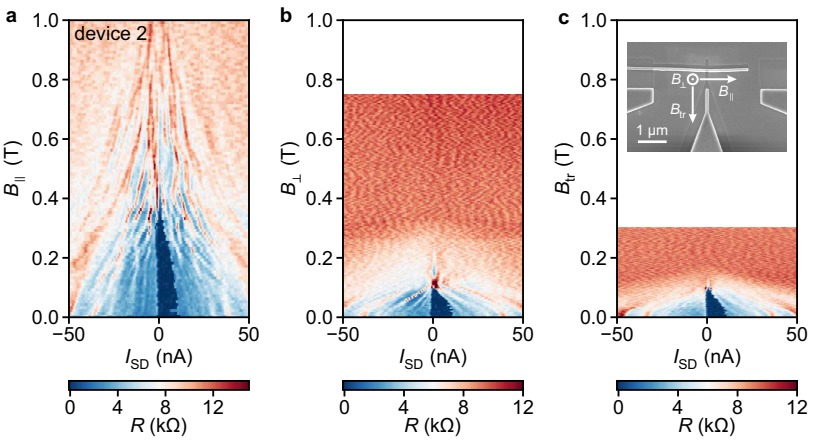

Figure 8.15: Switching current of the second Josephson junction device in the open-channel regime ($V_{BG} = 5.7\,V$). Differential resistance, R, as a function of I_{SD} and magnetic field in three different orientations: **a** Magnetic field, $B_{\parallel}$, aligned parallel to the nanowire, **b** magnetic field, $B_{\perp}$, oriented out-of-plane, and **c** transversal in-plane magnetic field, B_{tr}. The vectors in the inset of panel (**c**) illustrate the three field orientations.

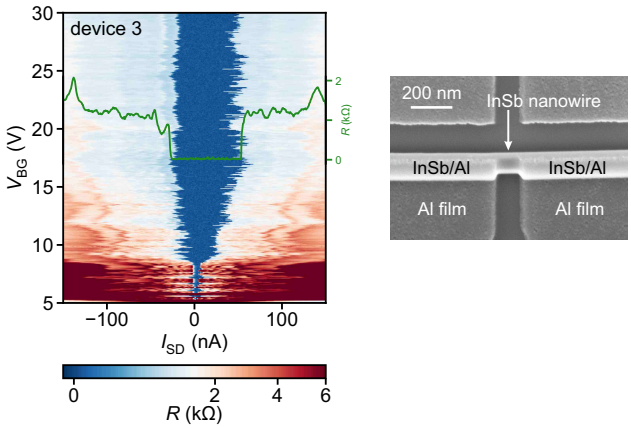

Figure 8.16: Back-gate dependence of the switching current of the third Josephson junction device. Colour map of R as a function of I_{SD} and V_{BG}; the green trace is taken at $V_{BG} = 13.82$ V. The switching current (in dark blue) is suppressed in the low back-gate voltage regime. The inset on the right shows a scanning electron micrograph of the device. The Al segments are capped with a protective layer of Al_2O_3.

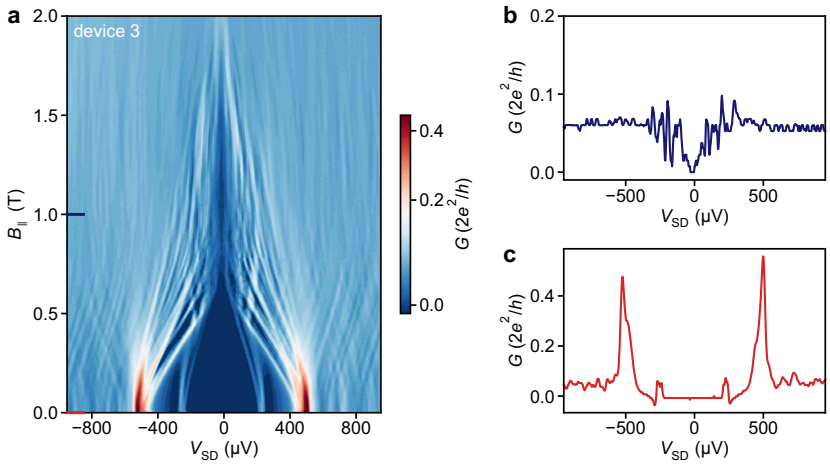

Figure 8.17: Transport measurements of the third Josephson junction device. **a** V_{SD} vs. $B_\parallel$ in the tunnelling regime. Owing to the thinner Al shell, the superconducting critical field is $B_c \sim 2$ T, much larger than for the previous two junctions. The tunnelling conductance peaks at $\pm 2\Delta_{ind}$ split into a manifold of resonances at a finite magnetic field due to the different g factors of the discrete quasiparticle states at the gap edge. **b**, **c** Line-cuts of (**a**) at the positions indicated by the two lines.

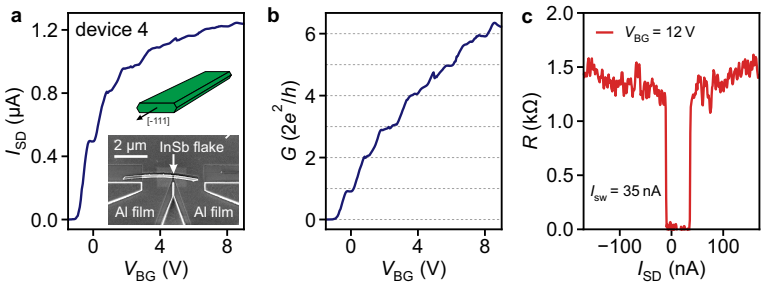

Figure 8.18: Ballistic transport and supercurrent in an InSb flake Josephson Junction (device 4) at zero magnetic field. **a** I_{SD} vs. V_{BG} at $V_{SD} = 10\,\text{mV}$. Bottom inset: scanning electron micrograph of the nano-flake Josephson junction. Top inset: schematic of the cross-section of the nano-flake [64]. **b** G vs. V_{BG} at $V_{SD} = 10\,\text{mV}$. The conductance displays distinct plateaus at multiples of $2e^2/h$, indicating the stepwise population of the one-dimensional subbands in the nanowire. **c** R vs. I_{SD} at $V_{BG} = 12\,\text{V}$. The device exhibits a switching current of $\sim 35\,\text{nA}$ in the open-channel regime.

8.8.3. MODELLING OF ANDREEV TRANSPORT

MODELLING OF THE CONDUCTANCE OF A BIASED JOSEPHSON JUNCTION AND THE FITTING PROCEDURE

We calculate the conductance of a voltage-biased Josephson junction following the approach of ref. [65]. In the model, we account for the electrons and holes propagating through the normal region of the junction with the transparency T. The quasiparticles are accelerated by the voltage V_{SD} applied to the structure and are Andreev reflected at the superconducting leads with the induced superconducting gap Δ_{ind}. The sequential Andreev reflections imprint the conductance with the subgap features appearing at $V_{SD} = 2\Delta_{ind}/Ne$, where N is integer – see Fig. 8.19.

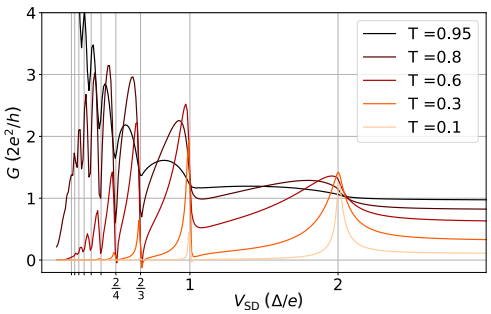

Figure 8.19: Conductance, G, of a single-mode Josephson junction versus bias voltage, V_{SD}, for five transparencies (T) of the normal region.

For the analysis of the experimental conductance traces we estimate the total conductance $G_{theory}(V_{SD})$ of a multimode nanowire Josephson junction as a sum of M single-mode contributions resulting from the presence of M modes of the transverse quantization [66]:

$$G_{theory}(V_{SD}) = \sum_{i=1}^{M} G_i(V_{SD}, T_i, \Delta_{ind}), \tag{8.1}$$

where T_i is the transmission probability for the i'th mode.
We obtain T_i and Δ_{ind} (induced in the nanowire by the presence of the Al shell) by fitting the numerically calculated conductance to the experimental one by minimizing $\chi = \int [G_{\text{exp}}(V_{\text{SD}}) - G_{\text{theory}}(V_{\text{SD}})]^2 dV_{\text{SD}}$. M is a free parameter of the fitting procedure and it is chosen as the smallest number for which at least one of the parameters T_i is zero.

THEORY FOR MULTIPLE ANDREEV REFLECTIONS IN THE PRESENCE OF SUBGAP STATES

The original theory developed in ref. [65] assumes a bulk superconducting density of states in the leads. To account for different properties of the two leads, especially the presence of subgap states in one of the contacts, we extend this theory as follows.
We consider a Josephson junction consisting of two superconducting electrodes connected through a normal scattering region. We assume that the first contact is kept at zero voltage, while the second one is biased at V_{SD}.
In the normal region, adjacent to the L'th lead, the quasiparticle wave function takes the form,

$$\Psi_L = \sum_n \left[\begin{pmatrix} A_n^L \\ B_n^L \end{pmatrix} e^{ikx} + \begin{pmatrix} C_n^L \\ D_n^L \end{pmatrix} e^{-ikx} \right] e^{-i[E+neV_{\text{SD}}]t/\hbar}, \tag{8.2}$$

where A_n^L, C_n^L (B_n^L, D_n^L) correspond to the electron (hole) amplitudes, the time dependence stems from the voltage applied to the leads and x points in the direction opposite to the scattering region.
We describe the scattering properties of the normal region by the scattering matrix:

$$S_0 = \begin{pmatrix} r & t \\ t & -r \end{pmatrix}, \tag{8.3}$$

which sets the transmission probability through the scattering region with the transmission amplitude $t = \sqrt{T}$ and the reflection amplitude $r = \sqrt{1-T}$.
We rely on the short-junction approximation and use the energy-independent S_0 to setup the matching conditions for the wave functions Ψ_L. The electron and hole coefficients are related by:

$$\begin{pmatrix} A_n^{\text{I}} \\ A_{n+1}^{\text{II}} \end{pmatrix} = S_0 \begin{pmatrix} C_n^{\text{I}} \\ C_{n+1}^{\text{II}} \end{pmatrix}, \tag{8.4}$$

and

$$\begin{pmatrix} D_n^{\text{I}} \\ D_{n-1}^{\text{II}} \end{pmatrix} = S_0^* \begin{pmatrix} B_n^{\text{I}} \\ B_{n-1}^{\text{II}} \end{pmatrix}, \tag{8.5}$$

respectively. The shifts of the indexes correspond to the changes of quasiparticle energies due to the bias voltage.
At each superconductor–normal-conductor interface we take into account the Andreev reflection:

$$\begin{pmatrix} C_n^L \\ B_n^L \end{pmatrix} = \begin{pmatrix} a_n & 0 \\ 0 & a_n \end{pmatrix} \begin{pmatrix} D_n^L \\ A_n^L \end{pmatrix}, \tag{8.6}$$

with the amplitude $a_n \equiv a(E + neV_{\text{SD}})$, where,

$$a(E) = \frac{1 - \delta_{L,I}\Gamma(E)}{\Delta_{\text{ind}}} \begin{cases} E - \text{sgn}(E)\sqrt{E^2 - \Delta_{\text{ind}}^2} & |E| > \Delta_{\text{ind}} \\ E - i\sqrt{\Delta_{\text{ind}}^2 - E^2} & |E| \le \Delta_{\text{ind}}. \end{cases} \tag{8.7}$$

The Andreev reflection amplitude is modified by the factor $[1-\delta_{L,I}\Gamma(E)]$ where,

$$\Gamma(E) = \frac{\gamma^2}{(E \pm E_0)^2 + \gamma^2}, \tag{8.8}$$

is the Lorentzian distribution that accounts for absorption of the quasiparticles in the subgap states (with the energy $\pm E_0$) in the first lead. We set $\gamma = 4\,\mu$eV.

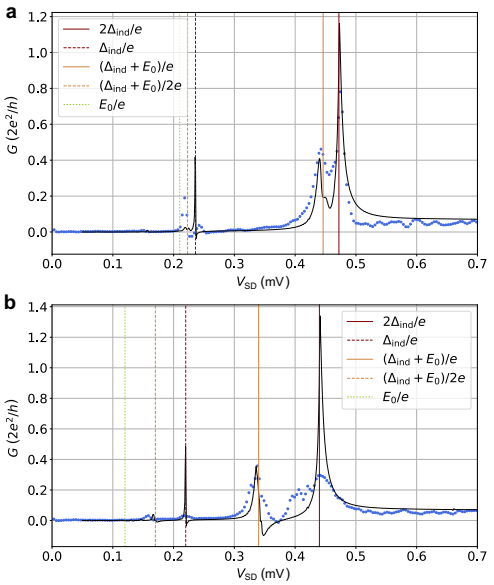

Figure 8.20: Experimental (blue dots) and theoretical (black curves) conductance traces of a Josephson junction with the subgap states in one of the superconducting leads. **a** is for $B_\parallel = 0$ and **b** is for $B_\parallel = 0.2$ T.

The electronic excitations in the normal part of the junction originate from the quasiparticles incoming from the nearby superconducting contacts. We therefore write down equation (8.6) including the quasiparticle source terms [67]:

$$\begin{aligned}\begin{pmatrix} C_n^L \\ B_n^L \end{pmatrix} = &\begin{pmatrix} a_n & 0 \\ 0 & a_n \end{pmatrix}\begin{pmatrix} D_n^L \\ A_n^L \end{pmatrix} \\ &+ \begin{pmatrix} J(E+eV_L) \\ 0 \end{pmatrix}\frac{1}{\sqrt{2}}\delta_{p,e}\delta_{s,L}\kappa_L^+ \\ &+ \begin{pmatrix} 0 \\ J(E-eV_L) \end{pmatrix}\frac{1}{\sqrt{2}}\delta_{p,h}\delta_{s,L}\kappa_L^-,\end{aligned} \tag{8.9}$$

with $J(E) = \sqrt{[1-a(E)^2]F_D(E)}$, where $F_D(E, T = 30\text{ mK})$ is the Fermi distribution. In equation (8.9) p sets the injected quasiparticle type, s determines the lead in which we consider the source term, and $\kappa_1^\pm = \delta_{n,0}$, $\kappa_2^\pm = \delta_{n,\pm1}$ keep track of the quasiparticle energy shifts due to the bias.

We calculate the current I^L in the L'th lead as:

$$I^L = \sum_{\iota=-I_{\max}}^{I_{\max}} I_\iota^L e^{\imath V_{\rm SD} e i t/\hbar}, \tag{8.10}$$

with the Fourier components,

$$I_\iota^L = \frac{e}{\hbar\pi} \sum_{s=1,2} \sum_{p=e,h} \int_{-\infty}^{\infty} dE \sum_{n=-N_{\max}}^{N_{\max}} (\mathbf{U}_{\iota+n}^{L*} \mathbf{U}_n^L - \mathbf{V}_{\iota+n}^{L*} \mathbf{V}_n^L). \tag{8.11}$$

$\mathbf{U}_n^L = \left(A_n^L, B_n^L\right)^T$ and $\mathbf{V}_n^L = \left(C_n^L, D_n^L\right)^T$ are vectors that consist of the electron and hole amplitudes. The DC current is obtained for $\iota = 0$ and subsequently used to calculate the conductance, $G = dI^L/dV_{\rm SD}$. To efficiently sample the non-uniform conductance trace we use the Adaptive package [68].

$\boldsymbol{B}_{\|}$ (T)	$\boldsymbol{\Delta}_{\rm ind}$ (μeV)	$\boldsymbol{T_1}$	$\boldsymbol{E_0}$ (μeV)
0	236	0.065	210
0.2	220	0.065	120

Table 8.2: Parameters used for the calculation of the conductance traces in Fig. 8.20.

In Fig. 8.20, we show the calculated MAR conductance traces (black curves) together with two cross-sections (blue dots) from the experimental map in Fig. 8.3c. We focus here on two cases: $B_\| = 0$ and $B_\| = 0.2\,$T with the parameters used for the calculations given in the first and second row of Table 8.2, respectively. The calculated traces agree qualitatively well with the data: they capture the peak positions and the overall line shape. In particular, we observe two ordinary MAR peaks at $V_{\rm SD} = 2\Delta_{\rm ind}/Ne$ with $N = 1,2$ and two peaks induced by the presence of the subgap state at $V_{\rm SD} = (\Delta_{\rm ind} + E_0)/Ne$ with $N = 1,2$. The increase of the magnetic field significantly alters the energy of the subgap state causing a further splitting between the MAR and the subgap-induced peaks. Nevertheless, the low-energy transport at higher magnetic fields shown in the conductance map in Fig. 8.3c, with multiple states detaching from the gap edge, goes beyond the approximations of our model.

8.8.4. ADDITIONAL TRANSPORT MEASUREMENTS IN NORMAL-METAL–SUPERCONDUCTOR JUNCTIONS

CALIBRATING THE AC CONDUCTANCE

The AC conductance is measured using a standard low-frequency lock-in technique. Some of the employed current-to-voltage amplifiers have been found to suffer from a relatively low bandwidth. This required a recalibration of the measured differential conductance of the N–S devices. The approach shown here is similar to a calibration procedure developed by Jouri Bommer, Guanzhong Wang and Michiel de Moor (see also guidelines on lock-in measurements by the same authors: `http://homepage.tudelft.nl/q40r9/lockin-meas-guide-v20200603.pdf`).

Fig. 8.21 shows the raw conductance data from Fig. 8.4 prior to the subtraction of any

series resistance. For the mapping of the lock-in conductance, G_{LI}, to the numerical DC conductance, G_{num}, the data is binned into a two-dimensional histogram (resolution $0.003 \cdot 2e^2/h$). Since the numerical conductance suffers from noise, we determine the centre of the distribution for each bin of G_{LI} by fitting a Gaussian distribution to the histogram of G_{num} (see right panel of Fig. 8.21). Data points that are more than 5 standard deviations from the centre of the distributions are discarded as outliers. Here, the mapping yields the parametrization $G_{\mathrm{num}} = -0.016 \cdot G_{\mathrm{LI}}^2 + 0.995 \cdot G_{\mathrm{LI}}$.

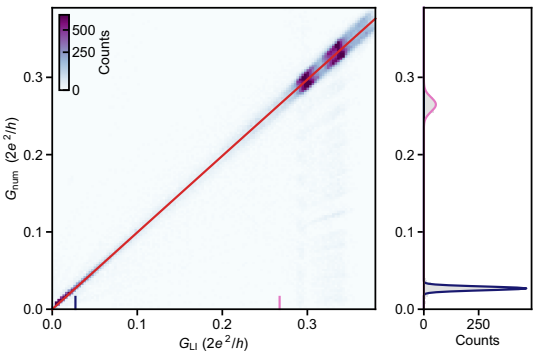

Figure 8.21: Calibration function extracted from the conductance data of the N–S junction presented in Fig. 8.4. Numerical differential conductance, G_{num}, vs. AC differential conductance, G_{LI}. Here, the lock-in frequency is $f = 23\,\mathrm{Hz}$.

Fig. 8.22 shows the calibration for the left junction of the correlation device in Fig. 8.5e. In Fig. 8.23, the calibration is presented for the right junction of the correlation device in Fig. 8.5f. This is the only device that was measured at a relatively large lock-in frequency ($f = 72\,\mathrm{Hz}$). The right panels of Fig. 8.22 and Figs. 8.23a-c show exemplary fits of the histograms using a Gaussian. The red traces represent the fitting by the least-squares method using the polynomial regression function $G_{\mathrm{num}} = A \cdot G_{\mathrm{LI}}^2 + B \cdot G_{\mathrm{LI}} + C$. The mapping in Fig. 8.22 yields the parametrization $G_{\mathrm{num}} = -0.108 \cdot G_{\mathrm{LI}}^2 + 1.043 \cdot G_{\mathrm{LI}} - 0.003$. In Fig. 8.23, the weighted average of the fitting functions yields the mapping function $G_{\mathrm{num}} = 0.023 \cdot G_{\mathrm{LI}}^2 + 1.034 \cdot G_{\mathrm{LI}} - 0.040$, where the residuals of the individual measurements provide the weights. Fig. 8.23d summarizes the parabolic (A) and linear (B) fit parameters from Figs. 8.23a-c. The black data point indicates the weighted average of the fit parameters.

8

N–S JUNCTION SPECTROSCOPY

Deep in the tunnelling regime the subgap conductance is strongly suppressed. As illustrated in Fig. 8.24, the ratio of the above-gap conductance and the subgap conductance is approximately a factor of 100. In Figs. 8.24a,b the differential conductance line-cuts from N–S device 1 (i.e. the same device as in Fig. 8.4) are fitted using the BCS–Dynes term (red) and the BTK model (green). The data in Figs. 8.24c,d show line-cuts from another N–S junction (device 2). The fitting parameters in the BTK model are the induced gap, Δ_{ind}, the normal-state conductance, G_{N}, and the temperature, T. For device 1 it yields an induced gap of $\Delta_{\mathrm{ind}} = 231\,\mu\mathrm{eV}$ and for device 2 the extracted gap is $\Delta_{\mathrm{ind}} = 241\,\mu\mathrm{eV}$. In the BTK model the only effective broadening parameter is the temperature, which for both devices yields $T \approx 95\,\mathrm{mK}$.

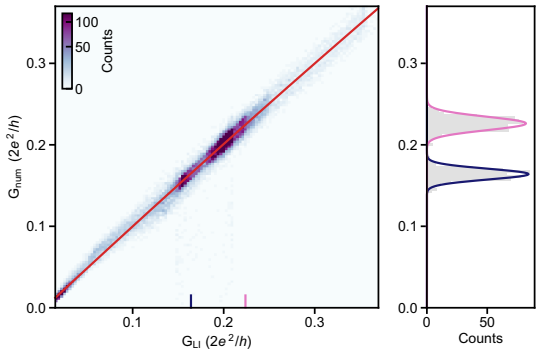

Figure 8.22: Calibration function extracted from the conductance data of the N–S junction presented in Fig. 8.5e . Numerical differential conductance, G_{num}, vs. AC differential conductance, G_{LI}. Here, the lock-in frequency is $f = 23\,\mathrm{Hz}$.

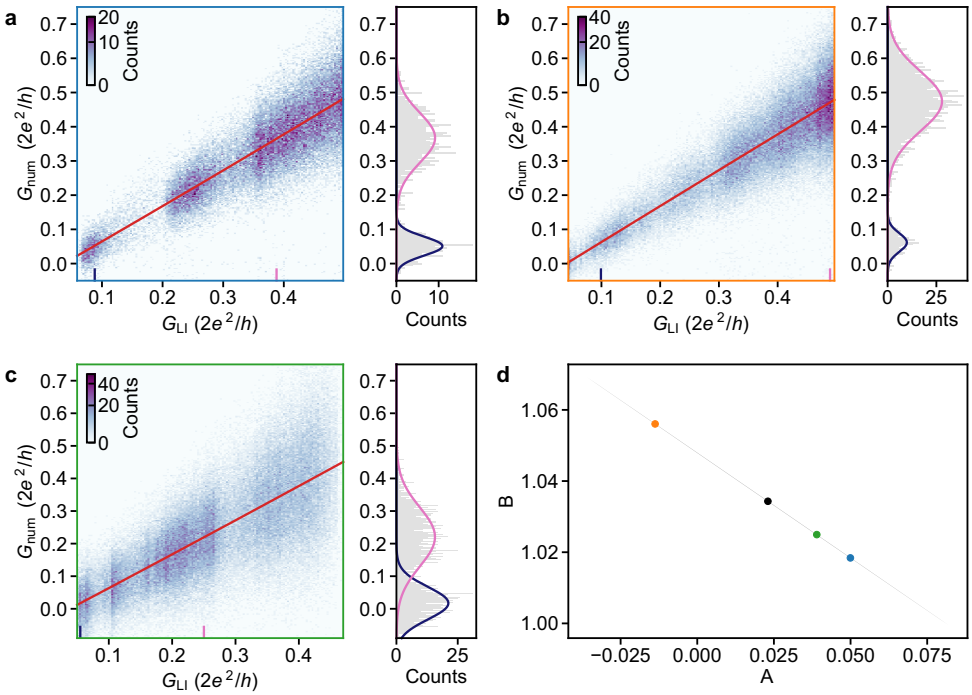

Figure 8.23: Calibration functions extracted for the N–S junction presented in Fig. 8.5f. **a**-**c** Numerical differential conductance, G_{num}, vs. AC differential conductance, G_{LI}. Each of the three panels is from separate data set. Here, the lock-in frequency is $f = 72\,\mathrm{Hz}$. **d** Summary of the parabolic (A) and linear (B) fit parameters in panels (**a**-**c**). The colors of the data points correspond to the axis colors of the respective panels. The black data point denotes the weighted average fit parameters, where the weights are determined by the residuals of the individual fits. The grey area designates the 95% confidence interval.

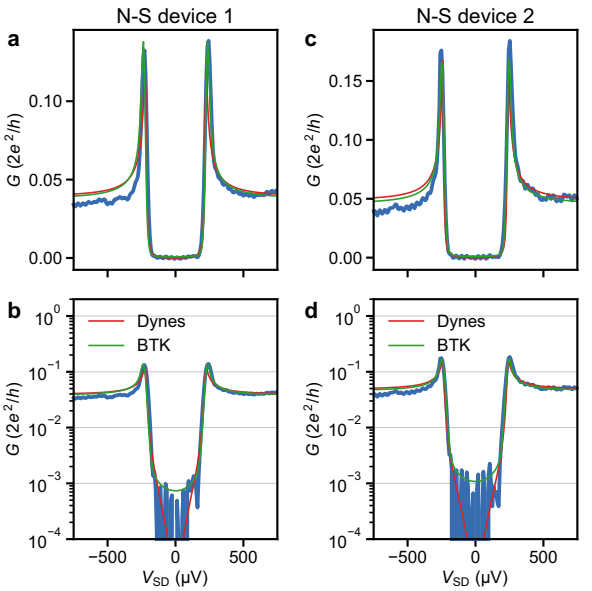

Figure 8.24: **a**, **b** Differential conductance vs. bias-voltage line-cuts from N–S device 1 (same as in Fig. 8.4) on a linear scale in (**a**) and on a logarithmic scale in (**b**). Here, the tunnel-gate voltage is $V_{TG} = 0.530\,V$ and the super-gate voltage is $V_{SG} = 0\,V$. **c**, **d** Differential conductance vs. bias-voltage line-cuts from N–S device 2 on a linear scale in (**c**) and on a logarithmic scale in (**d**). Here, the tunnel-gate voltage is $V_{TG} = 2.004\,V$ and the super-gate voltage is $V_{SG} = 7.0\,V$. The fit of the BCS–Dynes term and of the BTK model are shown in red and green, respectively.

TEMPERATURE DEPENDENCE OF THE INDUCED GAP

In Fig. 8.25, we present the temperature dependence from another device (N–S device 3). In the limit $k_B T \ll \Delta_{ind}$, the subgap conductance, G_S, scales with temperature, T, as [34]

$$G_S\,(V_{SD} = 0) = G_N \sqrt{\frac{2\pi\Delta_{ind}}{k_B T}}\, e^{-\Delta_{ind}/k_B T}, \tag{8.12}$$

where G_N is the normal-state conductance and k_B is the Boltzmann constant. The purple trace in Fig. 8.25a measured at $T = 18\,mK$ is well described by the BTK model with an induced gap of $\Delta_{ind} = 237\,\mu eV$. This is very similar to the magnitude of the induced gap of the other two N–S devices shown in Fig. 8.24, albeit those junctions are formed during a separate Al deposition step. The theoretical model in equation (8.12) can describe the smearing of the density of states with temperature. It yields a fit parameter of $\Delta_{ind} \approx 210\,\mu eV$, which is a bit smaller than the gap directly extracted from the tunnelling spectroscopy.

HARD INDUCED GAP

In Fig. 8.26, we report the fit of the BTK model to the data shown in Fig. 8.4b (N–S device 1). The extracted induced superconducting gap is $\Delta_{ind} \sim 230\,\mu eV$.

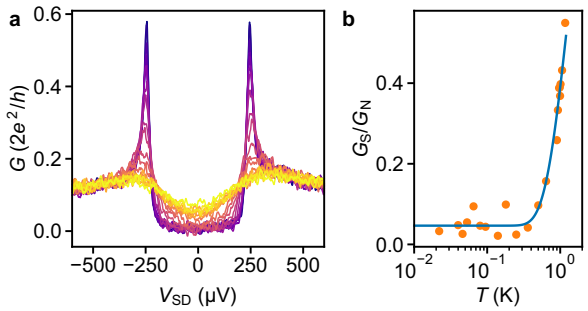

Figure 8.25: Temperature dependence of the induced gap (N–S device 3). **a** Tunnelling conductance vs. bias voltage between $T = 18\,\text{mK}$ (purple) and $T = 1.17\,\text{K}$ (yellow). **b** Subgap conductance averaged between $V_{SD} = \pm 30\,\mu\text{V}$ (G_S) divided by the normal-state conductance (G_N) as a function of T. The blue trace is a fit to equation (8.12).

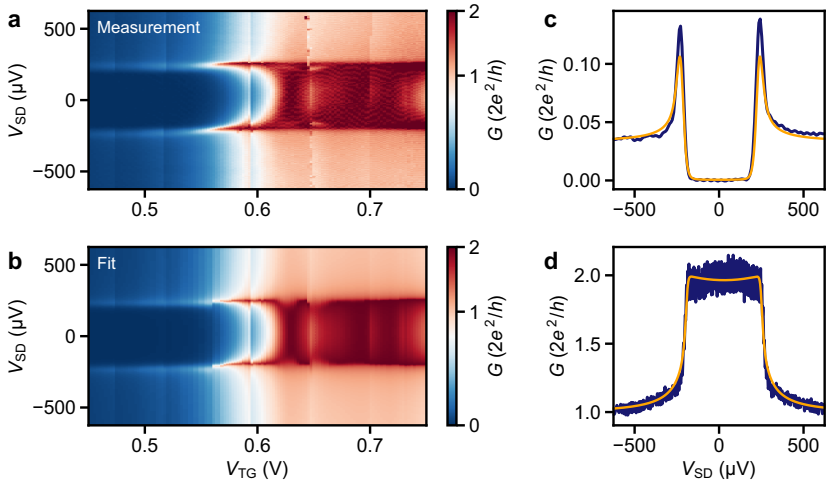

Figure 8.26: N–S junction voltage-bias spectroscopy and the corresponding fit of the BTK model [21] for N–S device 1. **a** Differential conductance, G, as a function of source–drain voltage, V_{SD}, and bottom tunnel-gate voltage, V_{TG}, from Fig. 8.4b. **b** Fit of the BTK model to the data set in panel (**a**). The fit parameters include the induced gap, the temperature, and the barrier strength Z, wich is given by the transmission $(1 + Z^2)^{-1}$. **c**, **d** Line-cut of the data in panel (**a**) (dark blue) at $V_{TG} = 0.53\,\text{V}$ and at $V_{TG} = 0.69\,\text{V}$, respectively. The orange traces show the corresponding fits to the BTK model.

ZERO-BIAS PEAKS IN THE N–S DEVICE

In Fig. 8.27, we present additional data from the first N–S device (cf. Fig. 8.4) in a magnetic field for two different super-gate voltages. In Fig. 8.4, we present ballistic transport and pronounced Andreev enhancement for the same N–S device.

ZERO-BIAS PEAKS AND SUPER-GATE DEPENDENCE

Additional N–S spectroscopy measurements of the left N–S junction of the device presented in Fig. 8.5 are shown in Fig. 8.28. Here, the voltage at the super gate – the bottom gate controlling the electrochemical potential in the hybrid nanowire segment – is larger ($V_{SG} = 0.525\,\text{V}$ vs. $0\,\text{V}$). The differential conductance vs. V_{SD} and $B_\parallel$ is depicted in Fig. 8.28a,

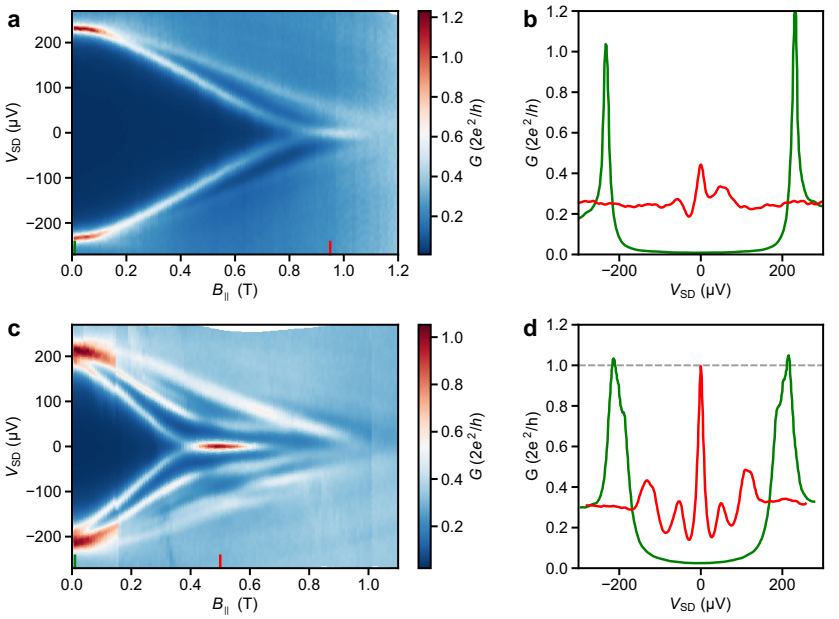

Figure 8.27: Magnetic-field-dependent voltage-bias spectroscopy for N–S device 1 from Fig. 8.4, demonstrating the formation of zero-bias peaks in the differential conductance. **a** G as a function of V_{SD} and $B_{\parallel}$. The super-gate voltage is $V_{SG} = 7.5\,V$ and the tunnel-gate voltage is $V_{TG} = 0.5\,V$. **b** Line-cuts of (**a**) at the positions indicated by the two lines. **c** G as a function of V_{SD} and $B_{\parallel}$. Here, $V_{SG} = 2.97\,V$ and $V_{TG} = 0.417\,V$. **d** Line-cuts of (**c**) at the positions indicated by the two lines.

the bias-voltage line-cut in Fig. 8.28b illustrates the pronounced zero-bias conductance peak at large magnetic fields. However, the magnitude of the ZBP conductance depends on the tuning of the tunnel-gate and super-gate voltages (cf. Fig. 8.28c).

In Fig. 8.29 additional data from the high-field regime are presented (here $B_{\parallel} = 0.85 - 1.15\,T$). For the same bottom-gate settings as in Fig. 8.28 we observe ZBPs that emerge concurrently on both boundaries of the superconductor–semiconductor nanowire segment (cf. Figs. 8.29a,b). By fixing the magnetic field at $B_{\parallel} = 1.0\,T$ we can observe the evolution of the ZBPs at the left and right N–S junctions as a function of the voltage on the super gate underneath the hybrid nanowire segment (see Figs. 8.29c,d). The asymmetry in the conductance of Fig. 8.29d with respect to bias polarity is related to energy-dependent tunnel barrier transmission at the right N–S junction.

The concurrent evolution of the ZBPs on both N–S boundaries of the correlation device as a function of the super-gate voltage is also depicted in Fig. 8.30 for same tunnel-gate settings as in Fig. 8.5.

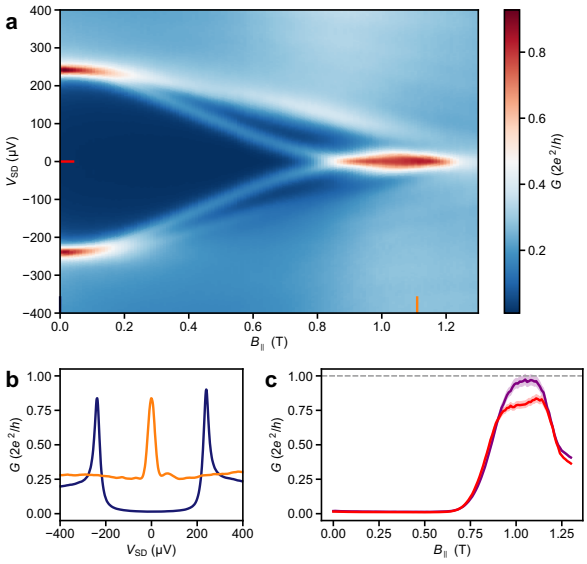

Figure 8.28: Voltage-bias spectroscopy of a subgap state with a large zero-bias peak conductance close to $2e^2/h$ (measured at the left N–S junction of the device presented in Fig. 8.5). Here, the super-gate voltage $V_{SG} = 0.525\,V$. **a** Differential conductance, G, as a function of the bias voltage at the left terminal, V_{SD}, and the magnetic field along the wire axis. **b** Voltage-bias line-cut of the differential conductance at zero field (blue) and at $B_\parallel = 1.11\,T$ (orange). **c** G vs. $B_\parallel$ line-cuts at $V_{SD} = 0\,\mu V$ from panel (**a**) (red, at $V_{SG} = 0.525\,V$) and from Fig. 8.5e (purple, at $V_{SG} = 0\,V$). The shaded areas behind the solid traces correspond to the variation in conductance assuming an uncertainty of $\pm 0.5\,k\Omega$ in estimating the actual series resistance.

8.8.5. REALIZATION OF ADVANCED HYBRID DEVICES

In this section, we present another example of more advanced nanowire devices that can be realized using the shadow-wall technique. In Fig, 8.6, we have introduced the necessary ingredients to realize the basic implementation of a topological qubit using the shadow-wall technique. In Fig. 8.31, we show another application of the shadow-wall concept, which is intended as an experimental implementation of a theoretical proposal by Schrade and Fu [69]. It represents a superconducting quantum interference device (SQUID) formed by two InSb nanowires (green) placed deterministically in close vicinity of shadow walls (blue). Previous realizations of nanowire SQUIDs relied on electron-beam lithography and standard lift-off technique [70]. Here, top gates (yellow) are fabricated to form a single Josephson junction (JJ) on the left side of the device and a superconducting island is defined by two tunnel gates and one plunger gate on the right side of the device. Source and drain electrodes are created by bonding directly to the Al film (grey) at the bottom and at the top of the SQUID loop, respectively. By utilizing shadow-wall substrates with bottom gates, this SQUID sample can be realized without any post-interface fabrication steps.

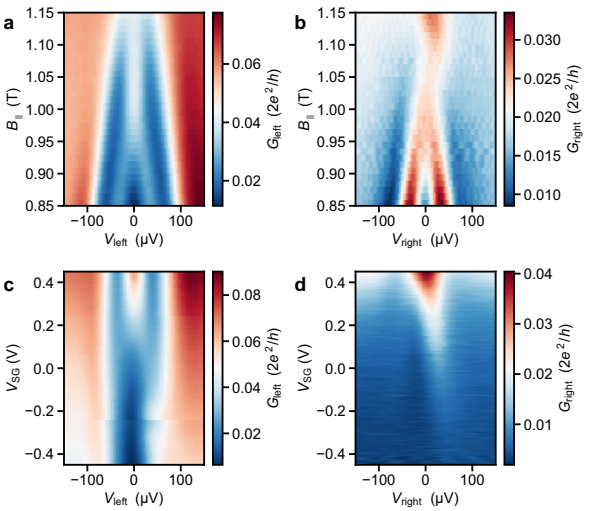

Figure 8.29: Simultaneous appearance of zero-bias peaks on both hybrid boundaries (same device as in Fig. 8.5). The two tunnel gates are set to $V_{TG,left} = 0.47\,V$ and $V_{TG,right} = 0.13\,V$. **a**, **b** Differential conductance, $G_{left/right}$, as a function of magnetic field, $B_\parallel$, and bias voltage at the left and right terminal, respectively. Here, the super-gate voltage $V_{SG} = 0.525\,V$, i.e. identical as for the data in Fig. 8.28a. **c**, **d** Differential conductance, $G_{left/right}$, at $B_\parallel = 1.0\,T$ as a function of V_{SG} and bias voltage at the left and right terminal, respectively.

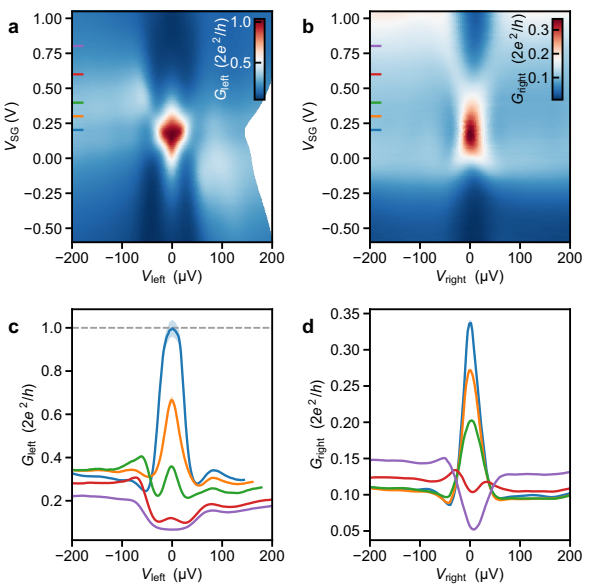

Figure 8.30: Simultaneous appearance of zero-bias peaks on both hybrid boundaries (same device and same tunnel-gate settings as in Fig. 8.5). The two tunnel gates are set to $V_{TG,left} = 0.52\,V$ and $V_{TG,right} = 0.21\,V$. **a**, **b** Differential conductance, $G_{left/right}$, at $B_\parallel = 1.0\,T$ as a function of V_{SG} and bias voltage at the left and right terminal, respectively. **c**, **d** Line-cuts from panels (**a**) and (**b**) at the values of V_{SG} designated by the coloured lines. The shaded areas behind the solid traces correspond to the variation in conductance assuming an uncertainty of $\pm 0.5\,k\Omega$ in estimating the actual series resistance.

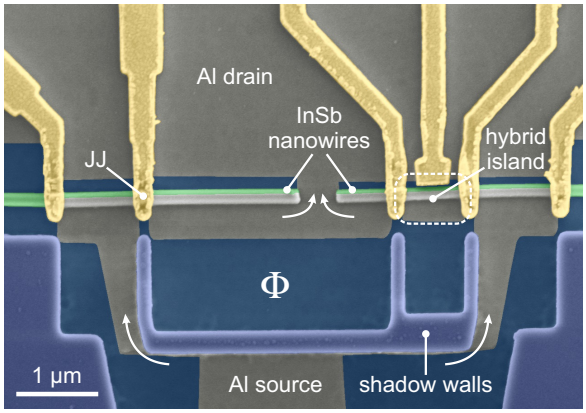

Figure 8.31: SQUID sample formed by placing two InSb nanowires next to each other in the shadow region of the dielectric walls. Electrical current flows from source to drain via the Josephson junction (denoted as JJ) and the hybrid charge island as indicated by the white arrows. The magnetic flux threading through the SQUID loop is denoted as Φ. The bottom of the SQUID loop is partly formed by the Al thin film covering the side of the central shadow wall.

REFERENCES

[1] S. Heedt, M. Quintero-Pérez, F. Borsoi, A. Fursina, N. van Loo, G. P. Mazur, M. P. Nowak, M. Ammerlaan, K. Li, S. Korneychuk, J. Shen, M. A. Y. van de Poll, G. Badawy, S. Gazibegovic, K. van Hoogdalem, E. P. A. M. Bakkers, and L. P. Kouwenhoven, *Shadow-wall lithography of ballistic superconductor-semiconductor quantum devices,* ArXiv e-prints **2007.14383** (2020).

[2] Y. Oreg, G. Refael, and F. von Oppen, *Helical liquids and Majorana bound states in quantum wires,* Phys. Rev. Lett. **105**, 177002 (2010).

[3] R. M. Lutchyn, J. D. Sau, and S. Das Sarma, *Majorana fermions and a topological phase transition in semiconductor-superconductor heterostructures,* Phys. Rev. Lett. **105**, 077001 (2010).

[4] R. M. Lutchyn, E. P. A. M. Bakkers, L. P. Kouwenhoven, P. Krogstrup, C. M. Marcus, and Y. Oreg, *Majorana zero modes in superconductor–semiconductor heterostructures,* Nat. Rev. Mater. **3**, 52 (2018).

[5] A. Y. Kitaev, *Unpaired Majorana fermions in quantum wires,* Phys.-Uspekhi **44**, 131 (2001).

[6] C. Nayak, S. H. Simon, A. Stern, M. Freedman, and S. Das Sarma, *Non-Abelian anyons and topological quantum computation,* Rev. Mod. Phys. **80**, 1083 (2008).

[7] S. Plugge, A. Rasmussen, R. Egger, and K. Flensberg, *Majorana box qubits,* New J. Phys. **19**, 012001 (2017).

[8] T. Karzig, C. Knapp, R. M. Lutchyn, P. Bonderson, M. B. Hastings, C. Nayak, J. Alicea, K. Flensberg, S. Plugge, Y. Oreg, C. M. Marcus, and M. H. Freedman, *Scalable designs for quasiparticle-poisoning-protected topological quantum computation with Majorana zero modes,* Phys. Rev. B **95**, 235305 (2017).

[9] S. Takei, B. M. Fregoso, H.-Y. Hui, A. M. Lobos, and S. Das Sarma, *Soft superconducting gap in semiconductor Majorana nanowires,* Phys. Rev. Lett. **110**, 186803 (2013).

[10] O. Gul, H. Zhang, F. K. de Vries, J. van Veen, K. Zuo, V. Mourik, S. Conesa-Boj, M. P. Nowak, D. J. van Woerkom, M. Quintero-Pérez, M. C. Cassidy, A. Geresdi, S. Koelling, D. Car, S. R. Plissard, E. P. A. M. Bakkers, and L. P. Kouwenhoven, *Hard superconducting gap in InSb nanowires,* Nano Lett. **17**, 2690 (2017).

[11] P. Krogstrup, N. L. B. Ziino, W. Chang, S. M. Albrecht, M. H. Madsen, E. Johnson, J. Nygård, C. M. Marcus, and T. S. Jespersen, *Epitaxy of semiconductor-superconductor nanowires,* Nat. Mater. **14**, 400 (2015).

[12] S. Gazibegovic, D. Car, H. Zhang, S. C. Balk, J. A. Logan, M. W. A. de Moor, M. C. Cassidy, R. Schmits, D. Xu, G. Wang, P. Krogstrup, R. L. M. Op het Veld, K. Zuo, Y. Vos, J. Shen, D. Bouman, B. Shojaei, D. Pennachio, J. S. Lee, P. J. van Veldhoven, S. Koelling, M. A. Verheijen, L. P. Kouwenhoven, C. J. Palmstrøm, and E. P. A. M. Bakkers, *Epitaxy of advanced nanowire quantum devices,* Nature **584**, 434 (2017).

[13] M. W. A. de Moor, J. D. S. Bommer, D. Xu, G. W. Winkler, A. E. Antipov, A. Bargerbos, G. Wang, N. van Loo, R. L. M. O. het Veld, S. Gazibegovic, D. Car, J. A. Logan, M. Pendharkar, J. S. Lee, E. P. A. M. Bakkers, C. J. Palmstrøm, R. M. Lutchyn, L. P. Kouwenhoven, and H. Zhang, *Electric field tunable superconductor-semiconductor coupling in Majorana nanowires,* New J. Phys. **20**, 103049 (2018).

[14] S. A. Khan, C. Lampadaris, A. Cui, L. Stampfer, Y. Liu, S. J. Pauka, M. E. Cachaza, E. M. Fiordaliso, J.-H. Kang, S. Korneychuk, T. Mutas, J. E. Sestoft, F. Krizek, R. Tanta, M. C. Cassidy, T. S. Jespersen, and P. Krogstrup, *Highly transparent gatable superconducting shadow junctions,* ACS Nano (2020).

[15] J. Cao, Q. Wang, and H. Dai, *Electron transport in very clean, as-grown suspended carbon nanotubes,* Nat. Mater. **4**, 745 (2005).

[16] M. Octavio, M. Tinkham, G. E. Blonder, and T. M. Klapwijk, *Subharmonic energy-gap structure in superconducting constrictions,* Phys. Rev. B **27**, 6739 (1983).

[17] H. A. Nilsson, P. Samuelsson, P. Caroff, and H. Q. Xu, *Supercurrent and multiple Andreev reflections in an InSb nanowire Josephson junction,* Nano Lett. **12**, 228 (2012).

[18] S. Li, N. Kang, D. X. Fan, L. B. Wang, Y. Q. Huang, P. Caroff, and H. Q. Xu, *Coherent charge transport in ballistic InSb nanowire Josephson junctions,* Sci. Rep. **6**, 24822 (2016).

[19] V. Mourik, K. Zuo, S. M. Frolov, S. Plissard, E. P. A. M. Bakkers, and L. P. Kouwenhoven, *Signatures of Majorana fermions in hybrid superconductor-semiconductor nanowire devices,* Science **336**, 1003 (2012).

[20] T. O. Rosdahl, A. Vuik, M. Kjaergaard, and A. R. Akhmerov, *Andreev rectifier: A nonlocal conductance signature of topological phase transitions,* Phys. Rev. B **97**, 045421 (2018).

[21] G. E. Blonder, M. Tinkham, and T. M. Klapwijk, *Transition from metallic to tunneling regimes in superconducting microconstrictions: Excess current, charge imbalance, and supercurrent conversion,* Phys. Rev. B **25**, 4515 (1982).

[22] C. W. J. Beenakker, *Quantum transport in semiconductor-superconductor microjunctions,* Phys. Rev. B **46**, 12841 (1992).

[23] S. Vijay and L. Fu, *Teleportation-based quantum information processing with Majorana zero modes,* Phys. Rev. B **94**, 235446 (2016).

[24] B. Béri and N. R. Cooper, *Topological Kondo effect with Majorana fermions,* Phys. Rev. Lett. **109**, 156803 (2012).

[25] M. Bjergfelt, D. J. Carrad, T. Kanne, M. Aagesen, E. M. Fiordaliso, E. Johnson, B. Shojaei, C. J. Palmstrøm, P. Krogstrup, T. S. Jespersen, and J. Nygård, *Superconducting vanadium/indium-arsenide hybrid nanowires,* Nanotechnology **30**, 294005 (2019).

[26] T. Rieger, D. Rosenbach, D. Vakulov, S. Heedt, Th. Schäpers, D. Grützmacher, and M. I. Lepsa, *Crystal phase transformation in self-assembled InAs nanowire junctions on patterned Si substrates,* Nano Lett. **16**, 1933 (2016).

[27] D. J. Carrad, M. Bjergfelt, T. Kanne, M. Aagesen, F. Krizek, E. M. Fiordaliso, E. Johnson, J. Nygård, and T. Sand Jespersen, *Shadow epitaxy for in Situ growth of generic semiconductor/superconductor hybrids,* Adv. Mater. **32**, 1908411 (2020).

[28] F. Boscherini, Y. Shapira, C. Capasso, C. Aldao, M. del Giudice, and J. H. Weaver, *Exchange reaction, clustering, and surface segregation at the Al/InSb(110) interface,* Phys. Rev. B **35**, 9580 (1987).

[29] C. Thomas, R. E. Diaz, J. H. Dycus, M. E. Salmon, R. E. Daniel, T. Wang, G. C. Gardner, and M. J. Manfra, *Toward durable Al-InSb hybrid heterostructures via epitaxy of 2ML interfacial InAs screening layers,* Phys. Rev. Mater. **3**, 124202 (2019).

[30] G. Badawy, S. Gazibegovic, F. Borsoi, S. Heedt, C.-A. Wang, S. Koelling, M. A. Verheijen, L. P. Kouwenhoven, and E. P. A. M. Bakkers, *High mobility stemless InSb nanowires,* Nano Lett. **19**, 3575 (2019).

[31] V. Ambegaokar and A. Baratoff, *Tunneling between superconductors,* Phys. Rev. Lett. **10**, 486 (1963).

[32] Y.-J. Doh, J. A. van Dam, A. L. Roest, E. P. A. M. Bakkers, L. P. Kouwenhoven, and S. De Franceschi, *Tunable supercurrent through semiconductor nanowires,* Science **309**, 272 (2005).

[33] T. A. Fulton and L. N. Dunkleberger, *Lifetime of the zero-voltage state in Josephson tunnel junctions,* Phys. Rev. B **9**, 4760 (1974).

[34] M. Tinkham, *Introduction to superconductivity* (Dover Publications, 1996).

[35] E. Scheer, P. Joyez, D. Esteve, C. Urbina, and M. H. Devoret, *Conduction channel transmissions of atomic-size aluminum contacts,* Phys. Rev. Lett. **78**, 3535 (1997).

[36] B. Nijholt and A. R. Akhmerov, *Orbital effect of magnetic field on the Majorana phase diagram,* Phys. Rev. B **93**, 235434 (2016).

[37] A. E. Antipov, A. Bargerbos, G. W. Winkler, B. Bauer, E. Rossi, and R. M. Lutchyn, *Effects of gate-induced electric fields on semiconductor Majorana nanowires,* Phys. Rev. X **8**, 031041 (2018).

[38] S. Abay, H. Nilsson, F. Wu, H. Q. Xu, C. M. Wilson, and P. Delsing, *High critical-current superconductor-InAs nanowire-superconductor junctions,* Nano Lett. **12**, 5622 (2012).

[39] K. T. Law, P. A. Lee, and T. K. Ng, *Majorana fermion induced resonant Andreev reflection,* Phys. Rev. Lett. **103**, 237001 (2009).

[40] H. Pan and S. Das Sarma, *Physical mechanisms for zero-bias conductance peaks in Majorana nanowires,* Phys. Rev. Research **2**, 013377 (2020).

[41] M. Kjaergaard, F. Nichele, H. J. Suominen, M. P. Nowak, M. Wimmer, A. R. Akhmerov, J. A. Folk, K. Flensberg, J. Shabani, C. J. Palmstrøm, and C. M. Marcus, *Quantized conductance doubling and hard gap in a two-dimensional semiconductor-superconductor heterostructure,* Nat. Commun. **7**, 12841 (2016).

[42] H. Zhang, Ö. Gül, S. Conesa-Boj, M. P. Nowak, M. Wimmer, K. Zuo, V. Mourik, F. K. de Vries, J. van Veen, M. W. A. de Moor, J. D. S. Bommer, D. J. van Woerkom, D. Car, S. R. Plissard, E. P. Bakkers, M. Quintero-Pérez, M. C. Cassidy, S. Koelling, S. Goswami, K. Watanabe, T. Taniguchi, and L. P. Kouwenhoven, *Ballistic superconductivity in semiconductor nanowires,* Nat. Commun. **8**, 16025 (2017).

[43] S. Heedt, A. Manolescu, G. A. Nemnes, W. Prost, J. Schubert, D. Grützmacher, and Th. Schäpers, *Adiabatic edge channel transport in a nanowire quantum point contact register,* Nano Lett. **16**, 4569 (2016).

[44] Y.-H. Lai, J. D. Sau, and S. Das Sarma, *Presence versus absence of end-to-end nonlocal conductance correlations in Majorana nanowires: Majorana bound states versus Andreev bound states,* Phys. Rev. B **100**, 045302 (2019).

[45] F. Nichele, A. C. C. Drachmann, A. M. Whiticar, E. C. T. O'Farrell, H. J. Suominen, A. Fornieri, T. Wang, G. C. Gardner, C. Thomas, A. T. Hatke, P. Krogstrup, M. J. Manfra, K. Flensberg, and C. M. Marcus, *Scaling of Majorana zero-bias conductance peaks,* Phys. Rev. Lett. **119**, 136803 (2017).

[46] O. Gül, H. Zhang, J. D. S. Bommer, M. W. A. de Moor, D. Car, S. R. Plissard, A. Bakkers, E. P. A. M. Geresdi, K. Watanabe, T. Taniguchi, and L. P. Kouwenhoven, *Ballistic Majorana nanowire devices,* Nat. Nanotechnol. **13**, 192 (2018).

[47] A. Grivnin, E. Bor, M. Heiblum, Y. Oreg, and H. Shtrikman, *Concomitant opening of a bulk-gap with an emerging possible Majorana zero mode,* Nat. Commun. **10**, 1940 (2019).

[48] J. Chen, P. Yu, J. Stenger, M. Hocevar, D. Car, S. R. Plissard, E. P. A. M. Bakkers, T. D. Stanescu, and S. M. Frolov, *Experimental phase diagram of zero-bias conductance peaks in superconductor/semiconductor nanowire devices,* Sci. Adv. **3** (2017), 10.1126/sciadv.1701476.

[49] G. L. R. Anselmetti, E. A. Martinez, G. C. Ménard, D. Puglia, F. K. Malinowski, J. S. Lee, S. Choi, M. Pendharkar, C. J. Palmstrøm, C. M. Marcus, L. Casparis, and A. P. Higginbotham, *End-to-end correlated subgap states in hybrid nanowires,* Phys. Rev. B **100**, 205412 (2019).

[50] P. Yu, J. Chen, M. Gomanko, G. Badawy, E. P. A. M. Bakkers, K. Zuo, V. Mourik, and S. M. Frolov, *Non-Majorana states yield nearly quantized conductance in superconductor-semiconductor nanowire devices,* arXiv e-prints **arXiv:2004.08583** (2020), arXiv:2004.08583 .

[51] C. Moore, T. D. Stanescu, and S. Tewari, *Two-terminal charge tunneling: Disentangling Majorana zero modes from partially separated Andreev bound states in semiconductor-superconductor heterostructures,* Phys. Rev. B **97**, 165302 (2018).

[52] A. Vuik, B. Nijholt, A. R. Akhmerov, and M. Wimmer, *Reproducing topological properties with quasi-Majorana states,* SciPost Phys. **7**, 61 (2019).

[53] H. Pan, W. S. Cole, J. D. Sau, and S. Das Sarma, *Generic quantized zero-bias conductance peaks in superconductor-semiconductor hybrid structures,* Phys. Rev. B **101**, 024506 (2020).

[54] D. de Jong, J. van Veen, L. Binci, A. Singh, P. Krogstrup, L. P. Kouwenhoven, W. Pfaff, and J. D. Watson, *Rapid detection of coherent tunneling in an* InAs *nanowire quantum dot through dispersive gate sensing,* Phys. Rev. Appl. **11**, 044061 (2019).

[55] R. C. Dynes, V. Narayanamurti, and J. P. Garno, *Direct measurement of quasiparticle-lifetime broadening in a strong-coupled superconductor,* Phys. Rev. Lett. **41**, 1509 (1978).

[56] C.-X. Liu, F. Setiawan, J. D. Sau, and S. Das Sarma, *Phenomenology of the soft gap, zero-bias peak, and zero-mode splitting in ideal Majorana nanowires,* Phys. Rev. B **96**, 054520 (2017).

[57] K. Flöhr, M. Liebmann, K. Sladek, H. Y. Günel, R. Frielinghaus, F. Haas, C. Meyer, H. Hardtdegen, Th. Schäpers, D. Grützmacher, and M. Morgenstern, *Manipulating InAs nanowires with submicrometer precision,* Rev. Sci. Instrum. **82**, 113705 (2011).

[58] J. L. Webb, J. Knutsson, M. Hjort, S. Gorji Ghalamestani, K. A. Dick, R. Timm, and A. Mikkelsen, *Electrical and surface properties of InAs/InSb nanowires cleaned by atomic hydrogen,* Nano Lett. **15**, 4865 (2015).

[59] L. Haworth, J. Lu, D. I. Westwood, and J. E. MacDonald, *Atomic hydrogen cleaning, nitriding and annealing InSb (100),* Appl. Surf. Sci. **166**, 253 (2000).

[60] R. Tessler, C. Saguy, O. Klin, S. Greenberg, E. Weiss, R. Akhvlediani, R. Edrei, and A. Hoffman, *Oxide-free InSb (100) surfaces by molecular hydrogen cleaning,* Appl. Phys. Lett. **88**, 1918 (2006).

[61] L. Dong, R. W. Smith, and D. J. Srolovitz, *A two-dimensional molecular dynamica simulation of thin film growth by oblique deposition,* J. Appl. Phys. **80**, 5682 (1997).

[62] A. Barranco, A. Borras, A. R. Gonzalez-Elipe, and A. Palmero, *Perspectives on oblique angle deposition of thin films: From fundamentals to devices,* Prog. Mater. Sci. **76**, 59 (2016).

[63] F. K. de Vries, M. L. Sol, S. Gazibegovic, R. L. M. o. h. Veld, S. C. Balk, D. Car, E. P. A. M. Bakkers, L. P. Kouwenhoven, and J. Shen, *Crossed Andreev reflection in InSb flake Josephson junctions,* Phys. Rev. Research **1**, 032031 (2019).

[64] S. Gazibegovic, *Bottom-up grown InSb nanowire quantum devices,* Ph.D. thesis, Department of Applied Physics (2019).

[65] D. Averin and A. Bardas, *ac Josephson effect in a single quantum channel,* Phys. Rev. Lett. **75**, 1831 (1995).

[66] A. Bardas and D. V. Averin, *Electron transport in mesoscopic disordered superconductor-normal-metal-superconductor junctions,* Phys. Rev. B **56**, R8518 (1997).

[67] M. P. Nowak, M. Wimmer, and A. R. Akhmerov, *Supercurrent carried by nonequilibrium quasiparticles in a multiterminal Josephson junction,* Phys. Rev. B **99**, 075416 (2019).

[68] B. Nijholt, J. Weston, J. Hoofwijk, and A. Akhmerov, *Adaptive: parallel active learning of mathematical functions, 10.5281/zenodo.3475095,* (2019).

[69] C. Schrade and L. Fu, *Andreev or Majorana, Cooper finds out,* ArXiv e-prints **1809.06370** (2018).

[70] D. B. Szombati, S. Nadj-Perge, D. Car, S. R. Plissard, E. P. A. M. Bakkers, and L. P. Kouwenhoven, *Josephson φ_0-junction in nanowire quantum dots,* Nat. Phys. **12** (2016).

9

SINGLE-SHOT FABRICATION OF SEMICONDUCTING-SUPERCONDUCTING NANOWIRE DEVICES

Semiconducting-superconducting nanowires attract widespread interest owing to the possible presence of non-abelian Majorana zero modes, which hold promise for topological quantum computation. However, the search for Majorana signatures is challenging because reproducible hybrid devices with desired nanowire lengths and material parameters need to be reliably fabricated to perform systematic explorations in gate voltages and magnetic fields. Here, we exploit a fabrication platform based on shadow walls that enables the in-situ, selective and consecutive depositions of superconductors and normal metals to form normal-superconducting junctions. Crucially, this method allows to realize devices in a single shot, eliminating fabrication steps after the synthesis of the fragile semiconductor/superconductor interface. At the atomic level, all investigated devices reveal a sharp and defect-free semiconducting-superconducting interface and, correspondingly, we measure electrically a hard induced superconducting gap. While our advancement is of crucial importance for enhancing the yield of complex hybrid devices, it also offers a straightforward route to explore new material combinations for hybrid devices.

This chapter has been published as, F. Borsoi, G. P. Mazur, N. van Loo, M. P. Nowak, L. Bourdet, K. Li, S. Korneychuk, A. Fursina, E. Memisevic, G. Badawy S. Gazibegovic, K. van Hoogdalem, E. P. A. M. Bakkers, and L. P. Kouwenhoven, S. Heedt, and M. Quintero-Pérez, *Single-shot fabrication of semiconducting-superconducting nanowire devices*, arXiv:2009.06219 (2020) [1].

9.1. INTRODUCTION

Semiconductor-superconductor nanowires are prime candidates towards topological quantum computation based on the manipulation of Majorana zero modes [2–4]. However, to serve as basic units of complex architectures [5–8], hybrid nanowires require a homogeneous and pristine interface between the semi- and the superconductor. In state-of-the-art methods, a superconducting film is deposited in-situ after the growth of the semiconductor nanowires [9, 10], which are then transferred onto insulating substrates for further fabrication. The superconductor is chemically etched away from certain sections of the wires to realize gate-tunable regions. This approach has a major drawback: the selectivity of the metal etching is often uncontrollable and results in damage to the semiconductor crystal, as well as in chemical contaminations [11, 12]. An alternative method to obtain gate-tunable regions is the shadow evaporation of the superconductor. This can be obtained by engineering complex nanowire growth chips with trenches or horizontal bridges [12–14]. In this case, the nanowire growth needs to be accurately optimized, the variety of possible devices is minimal, and hybrid nanowires still need to be transferred onto a substrate and subsequently processed. Crucially, the semiconductor-superconductor interface is unstable and prone to degradation with time and temperature, a problem that is particularly severe for the case of InSb/Al where the degradation takes place even at room temperature [15–19]. The interface instability poses a limit to the development and systematic exploration of topological circuits.

Here, we establish a fabrication method based on our previously introduced shadow-wall lithography technique [20] that overcomes these problems and enables the synthesis of high-quality hybrid devices in a single shot. The complete elimination of processing after the formation of the delicate semiconductor-superconductor interface is the critical aspect of our approach. To achieve this, we employ chips with pre-patterned bonding pads, bottom gates and shadow walls, next to which we transfer the semiconducting nanowires. The shadow walls and their particular design facilitate the selective deposition of the superconductor as well as contact leads without breaking the vacuum, eliminating the need for extra lithography steps. We demonstrate the versatility of our approach by creating hybrid junctions, which are the primary devices utilized to verify the emergence of Majorana excitations. The high quality of the devices is probed by transmission electron microscopy and by quantum transport measurements. All the investigated devices reveal a sharp and defect-free semiconductor-superconductor interface and, consequently, a hard induced superconducting gap. Our technique is inherently versatile and can have vast applications, from sparking rapid exploration of different combinations of materials to enabling the fabrication of more complex devices.

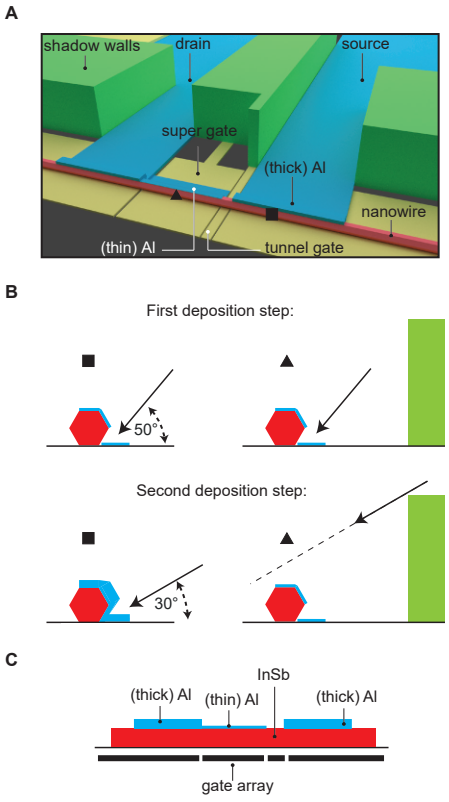

Figure 9.1: **Fabrication of asymmetric Josephson junctions.** (**A**) An illustration of an asymmetric Josephson junction device: the nanowire (in red) is separated from the bottom gates (in yellow) by a dielectric layer and is adjacent to shadow walls (in green). The superconducting film (in blue) covers the wire selectively. The relevant gates are the 'super gate' and the 'tunnel gate' whose actions are discussed later. (**B**) Cross-sections of the device taken at the two positions indicated by the square and triangle after the first (top panel) and the second evaporation step (bottom panel). (**C**) Longitudinal cross-section of the hybrid nanowire after the two steps.

9.2. PREPARATION OF SINGLE-SHOT NANOWIRE DEVICES

In our work, we exploit the properties of InSb nanowires and Al films, a combination of materials that is promising for the study of Majorana physics [13, 20, 21]. Nanowires are typically ~ 10 µm long [22], and the Al thin films can be grown homogeneously with thicknesses as low as 5 nm. The way the two materials are combined in-situ is illustrated in Fig. 9.1A. In brief, nanowires are transferred from the 'growth' to the 'device' substrate under an optical microscope. With accurate nano-manipulation, single nanowires (in red) are placed in the vicinity of dielectric shadow walls (in green) onto a gate oxide, which capacitively couples the wires to bottom gates (in yellow). Thanks to an atomic hydrogen cleaning step, the native oxide of the wires is removed without damaging the semiconductor crystal and introducing contaminations [23, 24]. The superconductor is

then deposited in-situ via e-gun evaporation at a substrate temperature of ~ 140 K.

Critically, the deposition is divided into two steps. First, we evaporate a thin Al layer at 50° with respect to the substrate (top panel of Fig. 9.1B), and then a thick Al layer at 30° (bottom panel of Fig. 9.1B). The two layers have a controlled thickness of 5 – 11 nm and 35 – 45 nm respectively (with ~ 0.1 nm of accuracy). A longitudinal schematic cross-section of the device is illustrated in Fig. 9.1C to emphasize that, due to the shallow angle of the second evaporation and the position of the middle wall, only the two source and drain nanowire sections (Fig. 9.1A) are covered by the thick Al layer. This process enables the formation in a single shot of hybrid asymmetric Josephson junctions with Al leads of different thicknesses, and this controlled variation can be used as a knob to tune the superconducting properties of the junctions [25]. When a normal metal (*e.g.*, Pt) is deposited in the second step onto the thin Al layer, the source and drain nanowire sections act as normal leads due to the inverse proximity effect forming a single-shot NS device (see Fig. 9.5). Differently from ref. [20], the combination of such shadow wall design and double-angle deposition enables to engineer in situ multiple layer depositions providing a route to eliminate or minimize further the fabrication. In particular, our method enables the direct formation of short tunnelling junctions which are favourable to minimize the emergence of non-topological subgap states [26]. As a result, our chips can be mounted in a dilution refrigerator within a few hours after the evaporation, preventing the formation of chemical intermixing at the fragile InSb/Al interface. The total elimination of detrimental processes such as heating steps, metal etching, lithography and electron microscopy makes our flow advantageous with respect to other state-of-the-art methods, and similar principles have been applied successfully in the context of carbon nanotube devices [27].

9.3. MATERIAL ANALYSIS

We evaluate the quality of the hybrid nanowires with transmission electron microscopy (TEM), and energy-dispersive x-ray analysis (EDX) performed on cross-sectional lamellas prepared via focused ion beam (FIB). The lamellas corresponding to Figs. 9.2A and D have been taken from cross-sections of nanowires with thin and thick Al coverage, respectively. Figs. 9.2B and E present typical bright-field scanning transmission electron microscopy images (BF STEM) of the thin- and thick-Al nanowire sections.

The EDX micrograph of Fig. 9.2A shows that, with the first deposition, the Al coating forms a continuous polycrystalline layer on two of the wire facets and on the substrate with a thickness of 6.5 nm on the top and 8.5 nm on the top-side facet. There is no connection between the thin Al shell on the wire and the thin Al on the substrate. Similarly, Fig. 9.2D illustrates that the thick-Al coverage is 26 nm and 49 nm depending on the facet. The wire exhibits three-facet coverage with a continuous metallic connection to the substrate, which allows for the creation of electrical contacts to the wire.

Importantly, the interface between Al and InSb is sharp and clean, demonstrating a good connection between the two materials and no damage from hydrogen cleaning on the semiconductor. The EDX elemental mapping manifests an oxygen peak at the InSb/Al interface that is much weaker compared to the native oxide on the surface of the nanowire visible in the EDX line scan, highlighting the successful hydrogen cleaning treatment (Figs. 9.2C and F).

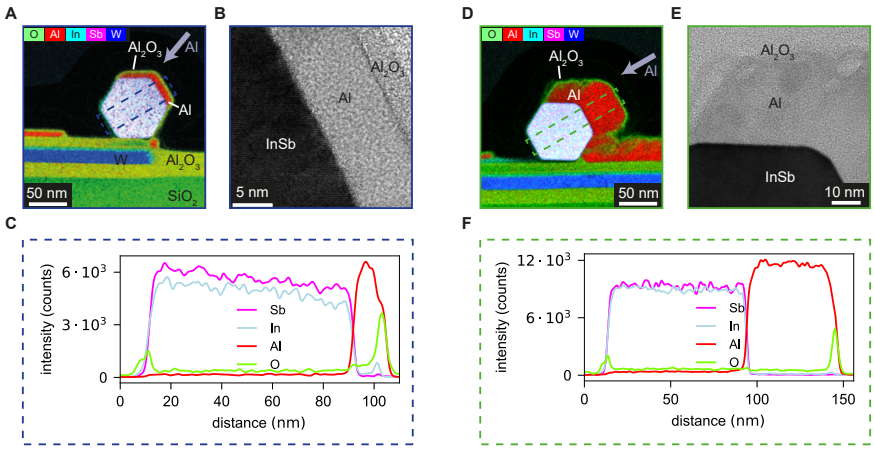

Figure 9.2: **Material analysis.** (**A**) Composite image of EDX elemental maps of the InSb nanowire covered with a thin layer of aluminum deposited at 50° (cf. grey arrow). (**B**) Bright field (BF) STEM image of the InSb/Al interface. (**C**) Elemental line scan extracted from (**A**) perpendicular to the top-side facet of the nanowire. (**D**) Composite image of EDX elemental maps of the InSb nanowire covered with a thick layer of aluminum evaporated at 30° (cf. grey arrow). (**E**) Annular dark-field (ADF) STEM image focusing on the aluminum layer on the top facet of the nanowire. (**F**) Elemental line scan extracted from (**D**) perpendicular to the top-side facet of the nanowire.

9.4. MULTIPLE ANDREEV REFLECTIONS IN ASYMMETRIC JOSEPHSON JUNCTIONS

We validate our nanowire devices via low-temperature electrical transport. We consider first an asymmetric Josephson junction device (scanning electron micrograph in Fig. 9.3A). A DC bias voltage with a small AC excitation, $V_{SD} + \delta V_{AC}$, is applied between source and drain, yielding a current $I + \delta I_{AC}$. Both the DC current and the differential conductance $G = \delta I_{AC}/\delta V_{AC}$ are measured. The gate voltage V_{TG} applied at the 'tunnel gate' tunes the transmission of the junction, whereas the voltage V_{SG} at the 'super gate' controls the chemical potential of the proximitized wire.

The conductance through the device displays prominent peaks due to multiple Andreev reflections and a zero-bias peak due to Josephson supercurrent (Fig. 9.3B). Notably, these observations are found across all the measured devices, proving the strong and reproducible hybridization between the semi- and the superconductor (Fig. 9.12). The observation of different orders of multiple Andreev reflections demonstrates that transport is phase-coherent across a length scale of multiple times the 100 nm-junction.

In widely studied symmetric junctions, multiple Andreev reflection peaks arise at subharmonic values of the superconducting gap [28, 29]. In asymmetric junctions, transport mechanisms such as the ones presented in Fig. 9.3C favour multiple Andreev processes at energies that relate to both gaps in a particular way. Odd orders manifest as conductance peaks at subharmonic values of the sum of the two gaps [30, 31]:

$$V_{SD} = \frac{\Delta_1 + \Delta_2}{Ne} \quad \text{with } N = 1, 3, 5, \ldots \tag{9.1}$$

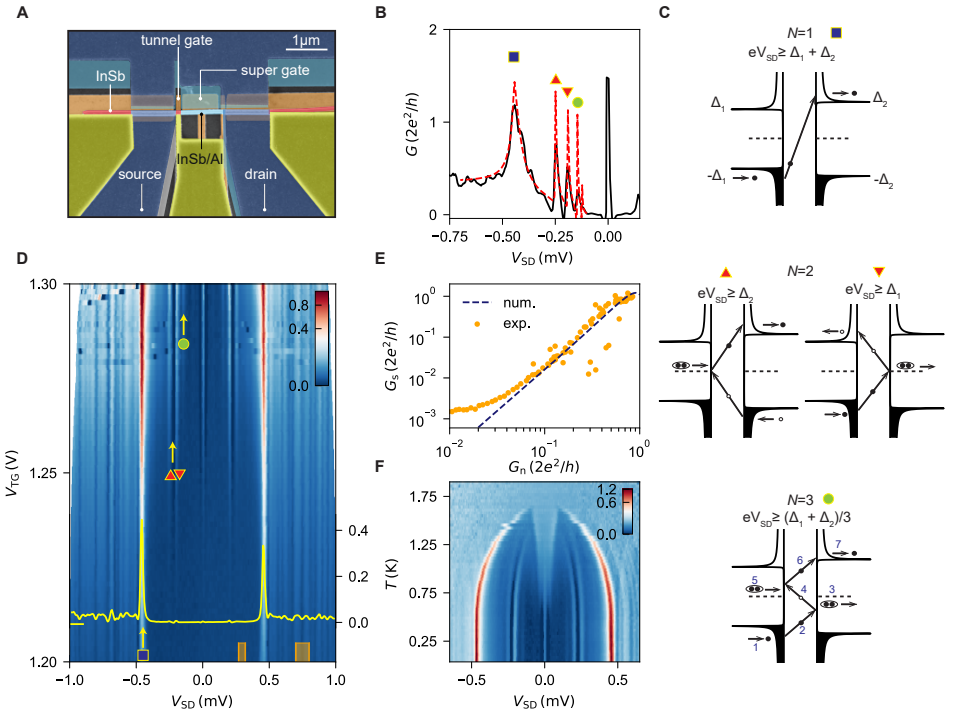

Figure 9.3: **Multiple Andreev reflections in asymmetric junctions.** (**A**) False-colour scanning electron micrograph of the first device. (**B**) G in units of $2e^2/h$ vs. V_{SD} at $V_{TG} = 1.38\,V$ (black trace) and theoretical fit (dashed red trace). The blue square, red triangles and yellow circle indicate respectively multiple Andreev reflection peaks of the first, second and third order. (**C**) Schematic of the multiple Andreev reflections processes. Top, middle and bottom panels describe first, second and third orders, respectively. Electrons (holes) are shown as black (white) circles, and pairs of two electrons identify Cooper pairs. (**D**) Color map of G in units of $2e^2/h$ vs. V_{TG} and V_{SD} displaying tunnelling conductance peaks at constant bias voltages. The square, the triangles and the circle correlate these peaks to the processes depicted in (**C**). The yellow trace is a line-cut at $V_{TG} = 1.21\,V$, as indicated by the yellow tick. Values on the right y-axis are in units of $2e^2/h$. (**E**) In orange, G_s *versus* G_n (average conductances in the bias ranges $[0.27, 0.32]$ mV and $[0.70, 0.80]$ mV respectively), and in black, the result of the numerical calculations. (**F**) Color map of G in $2e^2/h$ *vs.* V_{SD} and temperature T of the second device.

where Δ_1 and Δ_2 are the small and the large gaps, respectively, N is the order, and e is the electronic charge. Differently, even orders give rise to doublets of peaks at subharmonic energies of both gaps Δ_i with $i = 1, 2$:

$$V_{SD} = \frac{2\Delta_i}{Ne} \quad \text{with } N = 2, 4, 6, \ldots \tag{9.2}$$

While the positions of the peaks depend on the magnitude of the two induced gaps, their intensity is related to the number and the transmission of the confined nanowire modes. To extract these parameters, we develop a theoretical model that accounts for different superconducting gaps in the two leads. In Fig. 9.3B we plot the result of the numerical calculation (red dashed trace) together with the experimental conductance

(black trace). Here, the junction is found in the single-subband regime with transmission probability of 0.35 and the gap values are $\Delta_1 = 192\,\mu$eV, $\Delta_2 = 250\,\mu$eV. The peaks at $eV_{SD} = -(\Delta_1 + \Delta_2)$ (blue square), along with the doublet at $eV_{SD} = -\Delta_{1,2}$ (red triangles) and the one at $eV_{SD} = -(\Delta_1 + \Delta_2)/3$ (green circle), obey eqs. 9.1 and 9.2 for $N = 1, 2, 3$ perfectly. Subharmonic structures where different gaps are involved were reported only in early investigations in planar Pb/InSb/Sn junctions [30, 31]. In Fig. 9.3D, we show the activation of these peaks upon varying V_{TG}. While orders above $N = 3$ are better resolved at higher junction transparency (Fig. 9.6), the hard induced gap found in the tunnelling regime (see yellow trace) corroborates the high quality of the InSb/Al interface presented above.To demonstrate the hardness of the gap, we have calculated the conductance of the system assuming hard gaps in both leads as a function of junction transmission probability. In Fig. 9.3E, we illustrate the agreement between the simulation and the experimental data. Here, G_s is obtained by averaging theoretical and experimental conductance traces in the bias range $[0.27, 0.32]$ mV. The theoretical normal-state conductance G_n equals to $T_p \cdot 2e^2/h$, with T_p the transmission probability, and the experimental one is the average in the bias window $[0.70, 0.80]$ mV. The experimental trace only deviates from the theoretical calculation for values of G_s approaching $\sim 10^{-3} \cdot 2e^2/h$, that is the noise floor of our electronics. With this method, we have proposed Josephson junctions as alternative, and simpler devices to widely adopted normal-superconductor junctions for inferring the hardness of the gap. The difference in film thickness results also in two disparate superconducting critical temperatures: $T_{c1} \sim 1.66$ K and $T_{c2} \sim 1.74$ K, values that reflect the well-known enhancement in thin Al films with respect to the bulk value of 1.2 K [25, 32]. We illustrate the difference of the two junction sides in Fig. 9.3F with the conductance map *versus* bias voltage and temperature taken on a second asymmetric junction device. The sub-harmonic conductance peaks with $N = 2$, corresponding to $\pm\Delta_1$ and $\pm\Delta_2$, gradually shift to zero energy. The peak close to zero bias emerging at $T > 0.5$ K can be explained in term of thermally-activated quasiparticle current, which we illustrate further in Fig. 9.11. We note that the second device is conceptually similar to the first one, and exhibits comparable induced superconducting properties ($\Delta_1 = 203\,\mu$eV and $\Delta_2 = 253\,\mu$eV at base temperature). However, in the second device, the nanowire section coupled to the thin Al film is longer than the first (1.5 μm vs. 1.0 μm). We emphasize that the ability to tune this parameter with ease (*i.e.*, by shadow-wall design) is an innovative result of our architecture, and it is relevant in topological circuits because it sets the maximum separation between emerging Majorana modes.

9.5. TUNNELLING SPECTROSCOPY IN ASYMMETRIC JOSEPHSON JUNCTIONS

The well controllable thickness of each shell deposited in our method allows for the creation of devices that can be tuned to realize different superconducting or normal elements. Such a transition is presented in Fig. 9.4, where we display results obtained on the second device. Upon increasing the magnetic field along the wire ($B_\parallel$), the device transits from a Josephson junction (SS) into a normal-semiconductor-superconductor structure (NS), and eventually becomes a normal junction (NN) (Fig. 9.4A). The first transition is accompanied by the coalescence of the $\pm(\Delta_1 + \Delta_2)/e$ peaks into the $\pm\Delta_2/e$

peaks at ~ 0.40 T, and the second occurs when Δ_2 vanishes at ~ 2 T. These two field boundaries allow for tunnelling-spectroscopy measurements in the NS configuration in a large magnetic field range relevant for topological superconductivity [33]. A similar result was demonstrated in planar junctions on two-dimensional electron gases where the asymmetry of the critical fields was introduced by patterning one of the two leads much smaller than the superconducting coherence length [34, 35].

The versatility of our device preparation is also accompanied by the capability of tuning the device properties via the electric fields of the bottom gates. By varying the super-gate voltage, for instance, it is possible to both change the number of bands in the wire and shift the electron density close to or far from the Al interface, renormalizing properties such as the hardness of the induced gap, the effective g-factor and the spin-orbit coupling [21, 36, 37].

At $V_{SG} = -1.75$ V, when the electron density is confined at the interface, bias spectroscopy reveals an Al-like hard-gap up to ~ 1.8 T (Fig. 9.4B). When increasing super-gate voltage to $V_{SG} = 0.2$ V, we observe the first state (with an effective g-factor of ~ 5.5) coalescing with its own electron-hole symmetric partner in a zero-bias peak with conductance height of ~ $2e^2/h$ (Fig. 9.4C). Although a $2e^2/h$-high peak is a hallmark of a resonant Andreev reflection into a Majorana state, the energy and peak height are tunable by both the super- and the tunnel-gate voltages (Fig. 9.14). This tunability suggests that this state might be a localized (i.e., non-topological) Andreev bound state located near the junction [38].

At $V_{SG} = 0.5$ V and $V_{SG} = 0.7$ V, when the positive gate voltage allows the occupation of a greater number of nanowire bands, we observe that, upon increasing the magnetic field, a low-energy state oscillates around zero energy (Figs. 9.4D and E). Additional subgap states shift down in energy (with an effective g-factor of $6-12$ in the first case, and 22 at maximum in the second) and are repelled via the spin-orbit interaction, which in finite-length systems can couple states with different orbitals and spins [21, 39]. These states are tunable in energy by the super gate, but they are insensitive to variations in the tunnel gate (Fig. 9.13). While this robustness in barrier transparency has been used in the past to substantiate the presence of Majorana modes, we stress that the population of multiple nanowire subbands (see simulations in Fig. 9.16), together with orbital effects, result in a complex topological-phase diagram, making it arduous to assess the physical origin of the peaks in a normal-superconductor junction [33].

Because of this difficulty and of the presence of Andreev states at normal-superconductor junctions [40], future work will focus on three-terminal devices that enable probing both end-to-end subgap states correlations and, possibly, the presence of a topological gap [41]. It is striking to note that the presented method, by allowing an accurate design and realization of standardized Majorana devices, will undoubtedly accelerate the progress in this direction.

9.6. DISCUSSION

One of the most significant challenges in the search for topological excitations in condensed matter is alleviating the complexity of the devices. This is a key aspect when it comes to reproducible measurements, high fabrication yield and eventually scalability. To this purpose, we introduce here an innovative technology to obtain hybrid nanowire

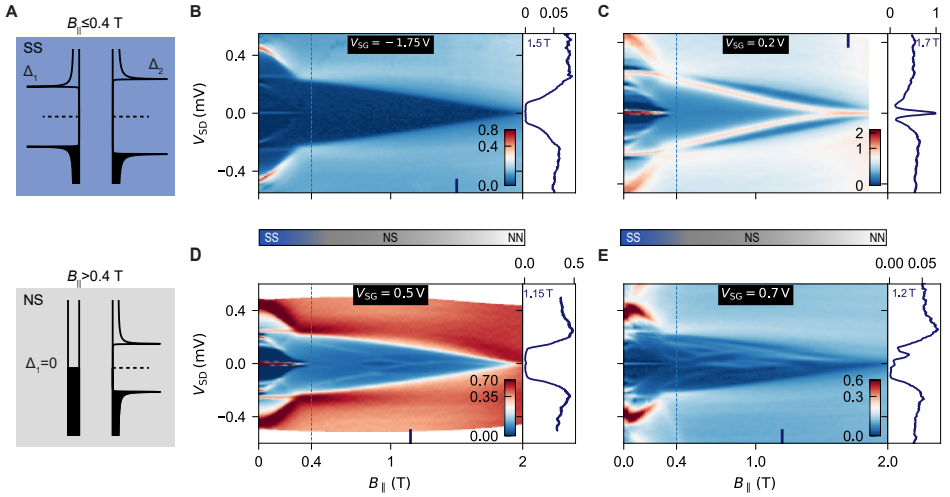

Figure 9.4: **Tunnelling spectroscopy in asymmetric Josephson junctions.** (**A**) Top and bottom panels illustrate two schematics of the density of states at $B_\parallel \leq 0.4$ T, and $B_\parallel > 0.4$ in the asymmetric SS and NS junction regimes. The transition between the two regimes is marked with a vertical dashed line in the other panels. There, we display color maps of G in units of $2e^2/h$ vs. V_{SD} and $B_\parallel$. The data sets differ in the value of V_{SG}, which increases from (**B**) to (**E**): in (**B**) V_{SG} equals −1.75 V, in (**C**) 0.2 V, in (**D**) 0.5 V and in (**E**) 0.7 V. Side panels show vertical line-cuts at the positions indicated by the blue lines and labels. The two horizontal bars illustrate the junction regimes as a function of magnetic field.

junctions. By combining a double-angle evaporation with shadow walls, we demonstrate the possibility of completely eliminating the need for fabrication processing after the delicate semiconductor-superconductor interface is created. This method not only drastically reduces possible chemical contaminations and the deterioration of the interface but also results in reproducible and adjustable devices, with fast fabrication turnaround. Moreover, differently from previous shadowing methods without shadow walls [13, 14], all the dimensions of the proximitized nanowire sections are accurately tunable.
While this study could not corroborate the presence of a topological state in hybrid nanowires, it lays the groundwork for future investigation of extremely long Majorana wires and for the fabrication of advanced devices such as hybrid two-path interferometers for the read-out of Majorana qubits [42–44]. Crucially, the versatility of the platform can spark rapid explorations of different material combinations toward a topological qubit, such as different semiconductors and superconductors, but also metals and ferromagnets. It also enables the direct synthesis of artificial Kitaev chains [45–47], facilitates advancement in Andreev qubits [48], and the engineering of quasiparticle traps in devices such as superconducting qubits [49–51].

AUTHOR CONTRIBUTIONS

F.B., M.Q.P., S.H. and L.P.K. conceived the experiment. F.B. carried on the electrical transport measurements. F.B., A.F., M.Q.P, N.v.L, S.H. and E.M. designed and fabricated

the substrates. M.Q.P. and G.P.M. performed the atomic hydrogen cleaning and the metal deposition steps. M.P.N. performed numerical simulations of the multiple Andreev reflections processes. L.B. and K.v.H. carried on simulations on the hybrid nanowire devices. G.B., S.G. and E.P.A.M.B. grew the nanowires. K.L. prepared the FIB lamellae. S.K. performed the TEM analysis. F.B., M.Q.P. and S.H. wrote the manuscript. All authors provided critical feedback. L.P.K., M. Q. P. and S.H. supervised the project.

DATA AVAILABILITY

The data and the codes that create the figures in this chapter are available at `https://data.4tu.nl/articles/dataset/Data_underlying_the_manuscript_Single-shot_synthesis_of_semiconducting-superconducting_nanowires/12764870`.

9.7. METHODS

SUBSTRATES FABRICATION

Bottom gates are fabricated by reactive-ion etching a ~ 17 nm thick W film with SF_6 gas, and are then covered by a ~ 18 nm layer of Al_2O_3 deposited via Atomic Layer Deposition. Shadow walls are created in the same top-down approach: a ~ 700 nm thick layer of PECVD Si_xN_y is reactive-ion etched by CHF_3. Shadow walls of the device presented in Fig. 9.5 are made by patterning and developing a ~ 1 µm-thick layer of HSQ that is subsequently baked at 300 °C. The substrates are then cleaned thoroughly for one hour with oxygen plasma to remove resist residues.

NANOWIRE GROWTH AND TRANSFER

Stemless InSb nanowires are grown with the method described in ref. [22]. They are then deterministically transferred from the growth-substrate to the device-substrate and pushed in the vicinity of shadow walls using an optical microscope and a micro-manipulator.

SEMICONDUCTOR SURFACE TREATMENT AND METAL DEPOSITION

After the nanowire transfer, the chip is loaded into the load-lock of the metal evaporator. Here, the semiconductor oxide is gently removed with an atomic hydrogen cleaning treatment similar to ref. [20]. A tungsten filament at ~ 1700 °C dissociates H_2 molecules into H^* radicals which react with the oxygen at the nanowire surface and remove it. Typical parameters for this process are: a hydrogen flow of 2.2 ml/min, a process pressure of $6.3 \cdot 10^{-5}$ mbar and a process time of ~ 1 hour. The holder onto which the chip is clamped is kept at 277 °C for ~ 3 hours to ensure thermalization, and hydrogen cleaning is performed at this temperature.
The chip is then loaded from the load-lock into the main chamber of the evaporator. Here, it is cooled down and thermalized for an hour at ~ 140 K. Thin Al is evaporated first at 50° with respect to the substrate plane (5 – 11 nm, measured by the evaporator crystal). Subsequently, Al (or Pt, depending on the device type) is deposited at 30° (35 – 45 nm, measured by the evaporator crystal). The deposition rate is maintained at ~ 0.2 nm/min. The chip is brought back into the load-lock, where it is oxidized for 5 minutes in an

oxygen pressure of 200 mTorr while still actively cooling the chip holder to maintain a temperature of ~ 140 K. The load-lock is vented only when the chip has reached room temperature.

TRANSPORT MEASUREMENTS

Electrical transport measurements were carried out in dilution refrigerators at a base temperature of approximately 15 – 20 mK and an electron temperature of approximately 35 mK. Lock-in conductance measurements were conducted at low frequency of 12 – 15 Hz, and the lock-in data was calibrated according to the measured DC conductance as demonstrated in ref. [20]. The data presented so far was taken from two representative devices. Additional data of these two devices is shown in Figs. 9.6, 9.7, 9.8, 9.9, 9.10, 9.11, 9.13 and 9.14. In total, we fabricated and cooled down three chips with respectively 3, 4 and 6 nanowire devices that all manifested similar induced superconducting properties. Exemplary transport characteristics of additional asymmetric junction devices are shown in Fig. 9.12, while data from a normal-superconducting junction is displayed in Fig. 9.5.

DETERMINATION OF THE EFFECTIVE g-FACTOR

We estimate the effective g-factor of the subgap states in Fig. 9.4 by considering their average slope vs. the magnetic field as:

$$g = \frac{2\Delta E}{\mu_B \Delta B_{\parallel}} \tag{9.3}$$

where ΔE is the variation in energy in a magnetic field range ΔB, and μ_B is the Bohr magneton.

TEM ANALYSIS

TEM investigation was carried out at 200 keV with Thermo Fisher Talos transmission electron microscope equipped with Super-X EDX detector. TEM samples were prepared with focused-ion beam technique making use of Thermo Fisher Helios dual beam scanning electron microscope. Additional TEM analysis is shown in Fig. 9.15.

9.8. SUPPLEMENTARY INFORMATION

9.8.1. SINGLE-SHOT NORMAL-SUPERCONDUCTOR JUNCTIONS

A second application of our technique is highlighted in the device presented in Fig. 9.5A. It represents a normal metal-superconductor junction realized in a very similar manner as the device in Fig. 9.3A. The substantial difference is that the leads are now made by a normal metal rather than a superconductor, enabling bias spectroscopy at zero magnetic field. For its realisation, after the deposition of a thin Al layer (~ 7 nm) at 50°, we evaporate in-situ a film of Pt (~ 30 nm) at 30° that creates the two leads.

Basic characterization of the device as a function of parallel magnetic field is shown in Fig. 9.5B. The measurement is taken with the super-gate voltage at 1 V, and with the junction strongly depleted by the tunnel gate. The red trace taken at zero field illustrates the quasiparticle density of states in the hybrid nanowire, which shows a hard induced gap of ~ 275 μeV. Upon increasing the parallel magnetic field, the in-gap conductance remains strongly suppressed up to ~ 3 T, while the induced superconducting gap vanishes completely at ~ 3.5 T (Fig. 9.5B). The increment of the critical field and of superconducting gap of this device with respect to the two asymmetric junction devices is due to the different Al thickness (here 7 nm versus 11.5 and 12.5 nm of the first and second device respectively). We emphasize that the ability to form a nanowire-based junction in-situ involving different materials and with properties tunable by design has not been reported before. In the future, it is important to assess whether the combination of different metals induces strain in the nanowire system.

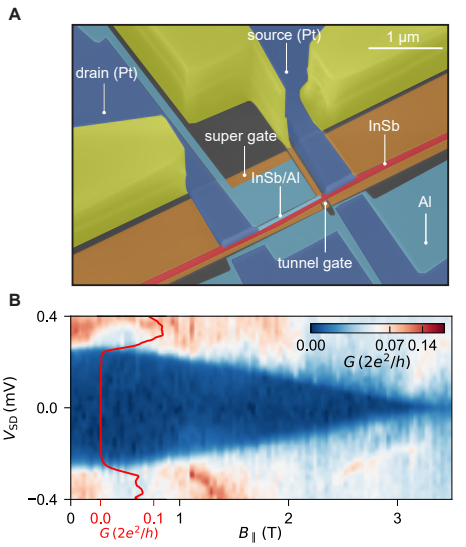

Figure 9.5: **Single-shot normal-superconductor junctions.** (**A**) False-color scanning electron micrograph of a representative device based on Pt source and drain, an InSb nanowire, and Al as superconductor. (**B**) Bias spectroscopy as a function of parallel magnetic field at $V_{SG} = 1$ V. The red trace is taken at zero magnetic field. The noise in the measurement is due to the gate instability.

9.8.2. MULTIPLE ANDREEV REFLECTIONS IN THE OPEN REGIME

Here, we display additional data related to the multiple Andreev processes occurring in asymmetric Al junctions. In Fig. 9.6A, we show a conductance map as a function of V_{SD} and V_{TG} in the open regime. Differently from the data-set presented in Fig. 9.3B and C where the out-of-gap conductance is $0.01 - 0.35 \cdot 2e^2/h$, here the out-of-gap conductance is $\sim 2 \cdot 2e^2/h$. In Fig. 9.6B, a conductance line-cut (black trace) is fitted with the coherent scattering model to evaluate the transmission though the one-dimensional channels (dashed red trace). Vertical line-cuts indicate the bias voltages at which the sub-harmonic features appear according to eqs. 4.2 and 4.3. The fit parameters reveal the two induced gaps ($\Delta_1 = 201\,\mu$eV and $\Delta_2 = 244\,\mu$eV) and indicate that three nanowire bands transmit with probabilities of 1, 0.82 and 0.33.

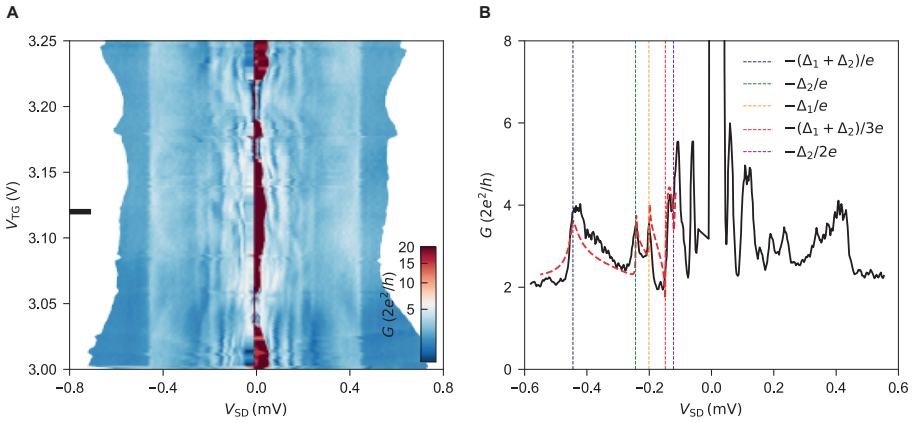

Figure 9.6: **Multiple Andreev Reflections in the open regime.** (**A**) G vs V_{SD} and V_{TG} in the open regime. (**B**) The black trace is a line-cut of (**A**) taken at gate value indicated by the horizontal line, the red dashed trace is the best fit using the coherent-scattering model.

9.8.3. MODELLING MULTIPLE ANDREEV REFLECTIONS IN AN ASYMMETRIC JUNCTION

Below we introduce the model used to calculate conductance of a Josephson junction in which the two superconducting leads are characterized by different gap parameters: Δ_1 and Δ_2. In our model we consider a Josephson junction composed of two superconducting electrodes which are connected by a normal scattering region and are biased by V_{SD} voltage.

We adopt the quasiparticle wave-function adjacent to the L'th lead in the form [52]:

$$\Psi_L = \sum_n \left[\begin{pmatrix} A_n^L \\ B_n^L \end{pmatrix} e^{ikx} + \begin{pmatrix} C_n^L \\ D_n^L \end{pmatrix} e^{-ikx} \right] e^{-i[E+neV_{SD}]t/\hbar}. \tag{9.4}$$

A_n^L, C_n^L correspond to the electron and B_n^L, D_n^L to the hole amplitudes.

The scattering properties of the normal part of the junction are characterized by the

scattering matrix:

$$S_0 = \begin{pmatrix} r & t \\ t & -r \end{pmatrix}, \tag{9.5}$$

with the amplitudes for the transmission $t = \sqrt{T}$ and reflection $r = \sqrt{1-T}$.

We assume that the junction is in short-junction regime and hence we take S_0 as energy independent. We match the wave-functions Eq. (9.4) using S_0 obtaining the relations for electron and hole coefficients:

$$\begin{pmatrix} A_n^{\mathrm{I}} \\ A_{n+1}^{\mathrm{II}} \end{pmatrix} = S_0 \begin{pmatrix} C_n^{\mathrm{I}} \\ C_{n+1}^{\mathrm{II}} \end{pmatrix}, \tag{9.6}$$

and

$$\begin{pmatrix} D_n^{\mathrm{I}} \\ D_{n-1}^{\mathrm{II}} \end{pmatrix} = S_0^* \begin{pmatrix} B_n^{\mathrm{I}} \\ B_{n-1}^{\mathrm{II}} \end{pmatrix}, \tag{9.7}$$

respectively. The shifts of the indexes correspond to the changes of quasiparticle energies due to the bias voltage.

At each superconductor-normal interface we take into account Andreev reflections:

$$\begin{aligned} \begin{pmatrix} C_n^L \\ B_n^L \end{pmatrix} = & \begin{pmatrix} a_n^L & 0 \\ 0 & a_n^L \end{pmatrix} \begin{pmatrix} D_n^L \\ A_n^L \end{pmatrix} \\ & + \begin{pmatrix} J_L(E+eV_L) \\ 0 \end{pmatrix} \frac{1}{\sqrt{2}} \delta_{p,e} \delta_{s,L} \kappa_L^+ \\ & + \begin{pmatrix} 0 \\ J_L(E-eV_L) \end{pmatrix} \frac{1}{\sqrt{2}} \delta_{p,h} \delta_{s,L} \kappa_L^-, \end{aligned} \tag{9.8}$$

with the amplitude $a_n^L \equiv a^L(E + neV_{\mathrm{SD}})$, where,

$$a^L(E) = \frac{1}{\Delta_L} \begin{cases} E - \mathrm{sgn}(E)\sqrt{E^2 - \Delta_L^2} & |E| > \Delta_L \\ E - i\sqrt{\Delta_L^2 - E^2} & |E| \le \Delta_L \end{cases}. \tag{9.9}$$

The last two terms in Eq. (9.8) correspond to the source terms due to the quasiparticles incoming from the nearby superconducting electrodes [53], with the amplitude $J_L(E) = \sqrt{(1 - a_L(E)^2) F_D(E)}$, where $F_D(E, T = 30\,\mathrm{mK})$ is the Fermi distribution and where $V_{L=1} = 0$, $V_{L=2} = V_{\mathrm{SD}}$, $\kappa_1^{\pm} = \delta_{n,0}$, $\kappa_2^{\pm} = \delta_{n,\pm 1}$.

We calculate the DC current I^L in the L'th lead as:

$$I^L = \frac{e}{\hbar\pi} \sum_{s=1,2} \sum_{p=e,h} \int_{-\infty}^{\infty} dE \sum_{n=-N_{\max}}^{N_{\max}} (\mathbf{U}_n^{L*} \mathbf{U}_n^L - \mathbf{V}_n^{L*} \mathbf{V}_n^L). \tag{9.10}$$

$\mathbf{U}_n^L = \left(A_n^L, B_n^L\right)^T$ and $\mathbf{V}_n^L = \left(C_n^L, D_n^L\right)^T$ are vectors that consist of the electron and hole amplitudes. The summation is carried over the position of the source term s and p, the injected quasiparticle type. The DC current is subsequently used to calculate the conductance $G = dI^L/dV_{\mathrm{SD}}$.

9.8.4. FITTING PROCEDURE

To extract the induced gaps and the transmission probability of the normal part of the junctions studied in the experiment, we first calculate conductance of a multimode wire as a sum of contributions corresponding to M modes of the transverse quantization as [54]:

$$G_{\text{theory}}(V_{\text{SD}}) = \sum_{i}^{M} G_i(V_{\text{SD}}, \Delta_1, \Delta_2, T_i). \tag{9.11}$$

T_i determines the transmission probability for the i'th mode. Next, we fit the conductance obtained in theory to the experimental traces by minimizing $\chi = \int [G_{\text{exp}}(V_{\text{SD}}) - G_{\text{theory}}(V_{\text{SD}})]^2 dV_{\text{SD}}$ over Δ_1, Δ_2, T_i. The comparison between the experimental conductance and the fitted theoretical traces are displayed in Fig. 9.3B (single-band regime) and in Fig. 9.6B (multi-band regime). In both scans, we see a single peak corresponding to the sum of the induced gaps for $eV_{\text{SD}} = \pm|\Delta_1 + \Delta_2|$. Higher-order subgap features are reflected by peaks at $eV_{\text{SD}} = \pm\Delta_1$ and $eV_{\text{SD}} = \pm\Delta_2$ and as a third-order process with the peak at $eV_{\text{SD}} = \pm|(\Delta_1 + \Delta_2)/3|$.

9.8.5. HARD GAP AND MAGNETIC FIELD DEPENDENCE IN THE FIRST DEVICE

In Fig. 9.7A, we display a color map of G vs. V_{SD} and $B_\parallel$ of the first device. Upon increasing magnetic field, the two-gap edges at symmetric bias values of $(\Delta_1 + \Delta_2)/e$ shift down in energy owing to the rapid dependence of Δ_1 on the magnetic field (i.e., Δ_1 is the superconducting gap of the thick-Al section). When Δ_1 reaches zero at ~ 0.34 T, the device transitions from a Josephson to a normal-superconductor junction. Tunnelling spectroscopy reveals a hard gap up to ~ 1.6 T. Exemplary line-cuts are shown in Fig. 9.7C, while the line-cut in Fig. 9.7B at zero magnetic field manifests Andreev reflections conductance peaks of the first order (blue square) and second order (red triangles). The small difference between the critical fields of the first and second device (~ 1.8 T vs. ~ 2.0 T) is due to the slight difference between the two evaporation runs (12.5 nm vs. 11.5 nm nominally at 50° with respect to the substrate). When the device is tuned in the NS regime by the magnetic field at 0.5 T, and upon increasing the voltage on the gate beneath the junction, we observe the enhancement of the subgap conductance due to Andreev processes in the junction. The plot of the subgap (G_{s}) and normal-state (G_{n}) conductances agrees well with the Beenakker formula [55] without fitting parameters suggesting low-disorder in the junction and a hard induced superconducting gap (Fig. 9.8)

9.8.6. EFFECT OF MAGNETIC FIELD ORIENTATIONS: SUPERCONDUCTING GAP AND SUPERCURRENT

We perform tunnelling-spectroscopy measurements in the second device for three different magnetic field orientations. The super-gate voltage is at -1.75 V and the tunnel gate is at 1.3 V. In Fig. 9.9A, the field $B_\parallel$ points along the wire direction, in panel B the field $B_{\parallel,\perp}$ is perpendicular to the wire and in-plane, and in panel C the field $B_\perp$ is oriented orthogonally to the substrate. The critical fields of the thin-Al hybrid nanowire are respectively ~ 2 T, ~ 0.37 T and ~ 0.3 T. This observation is consistent with the geometry of the 2-facet Al shell. In the same device, we studied the behaviour of the gate-tunable Josephson supercurrent in a magnetic field (Fig. 9.10). The zero-field supercurrent ranges typically

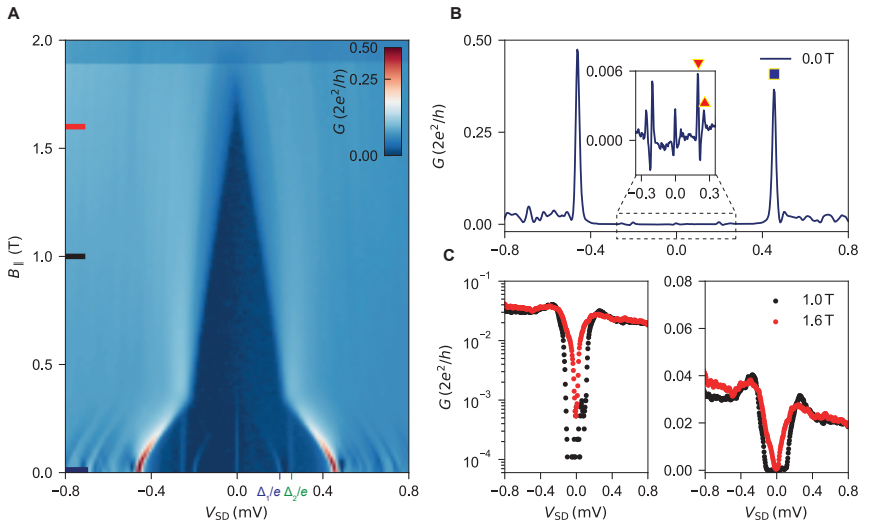

Figure 9.7: **Hard gap and magnetic field dependence in the first device.** (**A**) Color-map of G *vs.* V_{SD} and $B_\parallel$. (**B**) Line-cut at zero field of measurement in (**A**). The inset in (**B**) shows a zoom-in of the multiple Andreev reflection peaks at bias voltage around zero. Peaks marked with the blue square and the red triangles correspond to the first and second orders, respectively. (**C**) Log-scale (left panel) and linear (right panel) plots of conductance traces at 1.0 and 1.6 T manifesting a subgap conductance that is suppressed with respect to the normal-state conductance by a factor of ~ 100 similar to what reported in 9, 13.

from 0 to ~ 20 nA depending on the gates configuration. At a super-gate voltage of 1.95 V and tunnel-gate voltage of 1.8 V, the supercurrent of ~ 10 nA is suppressed at $B_\parallel = 0.33$ T, that is close to the critical magnetic field of the thick-Al lead. Upon changing the magnetic field orientation, we observe the same behaviour consistent with what reported in Fig. 9.9.

9.9. THERMALLY-ACTIVATED QUASIPARTICLE TRANSPORT

In this section, we present an explanation for the conductance peak at low bias voltage and high-temperature reported in Fig. reffig:Figure 3 chap9F of the main text. In a finite temperature, the bands above the superconducting gap in both superconducting leads become populated by quasiparticles as the non-vanishing tails of the Fermi distribution overlap with the superconducting density of states. Non-zero bias introduces misalignment between the bands and as a result induces non-zero, ohmic-like current flowing between the superconductors. This current does not involve Andreev reflections; hence it is considerable even in tunnelling regime where the MARs current is strongly suppressed at low bias. However, when the gaps are unequal, only a share of the thermally activated quasiparticles – with the energies exceeding the gap difference – can enter the opposite superconductor. As voltage increases, the gap edges move to each other and as a result, also the number of quasiparticles that can enter the opposite lead increases, further adding to the growth of the current. The latter process stops when the bias voltage aligns the top of

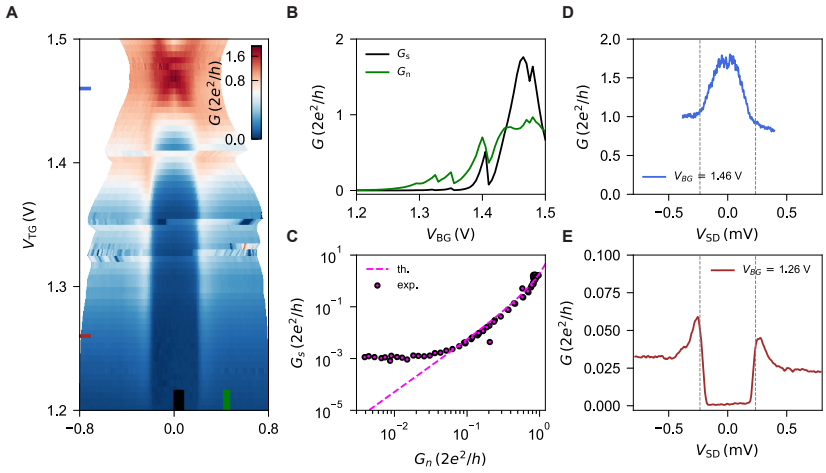

Figure 9.8: **Andreev enhancement in the first device.** (**A**) Color-map of G *vs.* V_{SD} and V_{TG} at $B_{\parallel} = 0.5$ T in the NS regime. (**B**) Line-cuts of the measurement in (**A**) averaged in the ranges indicated by the two vertical ticks. The two traces are plotted *versus* each other in (**C**), together with the Beenakker expected trend (dashed line). (**D**), (**E**) Horizontal line-cuts of (**A**) at values indicated by the two horizontal ticks. Vertical dashed lines identify bias voltages of $\pm\Delta/e$, with $\Delta = 235\,\mu$eV.

the two superconducting gaps at the same level, *i.e.* when $V_{SD} = \pm|\Delta_1 - \Delta_2|/e$. This results in a decrease of the current growth and a pronounced shoulder in $G(V_{SD})$ dependence, with a conductance drop at $V_{SD} = |\Delta_1 - \Delta_2|/e$ as can be observed in Fig. reffig:Figure 3 chap9F and in the line-cuts in Figs. 9.11B and C.

9.9.1. ZERO-MAGNETIC FIELD TRANSPORT IN ADDITIONAL DEVICES

Here, we display basic transport characteristics of a third, a fourth and a fifth device respectively in Figs. 9.12A, B, and C. In all three cases, the conductance in the tunnelling regime manifests strong suppression at low bias voltage and additional peaks due to multiple Andreev reflections. In Figs. 9.12A, and C, the zero-bias supercurrent peak is also visible. These results, together with the data presented in the first and second devices, support the reproducibility of our fabrication process.

9.9.2. SUBGAP STATES: GATE DEPENDENCE

In Figs. 9.13A and C we show the tunnel- and super- gate dependences of the low-energy spectrum when $V_{SG} = 0.5$ V. The measurements are taken at $B_{\parallel} = 1.2$ T, and enable to expand what is presented in Fig. 9.4D. The range of the two sweeps is similar (30 and 25 mV respectively) to better illustrate the action of the two gates on the subgap states. The low-energy spectrum is not affected by the variation of the transmission of the junction, which changes by a factor of two with the voltage V_{TG} (see line-cuts in Fig. 9.13B). Differently, the low-energy spectrum does depend on the super gate along which oscillations take place, probably due to level repulsion between the subgap states. The same considerations

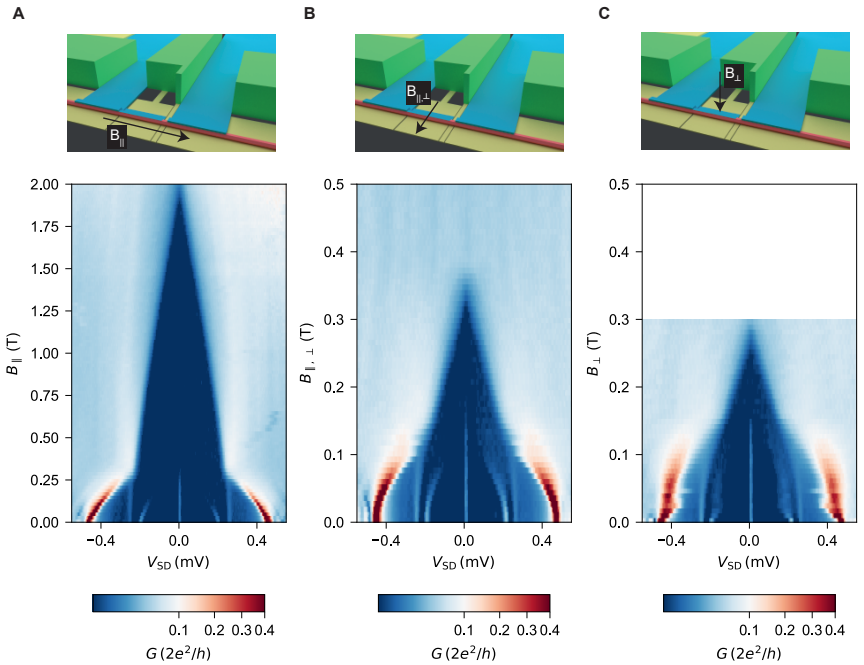

Figure 9.9: **Effect of magnetic field orientations.** Bias-spectroscopy measurements for three different magnetic field orientations. In (**A**) the field is parallel to the wire, in (**B**) is perpendicular to it and in-plane, in (**C**) it is orthogonal to the substrate.

are valid for the data-set shown in Figs. 9.13D, E and F taken for $V_{SG} = 0.7\,V$ at $B_{\parallel} = 0.9\,T$. The tunnel-gate dependence in panel D manifests few resonances due to an accidental quantum dot located at the junction, but the low-energy states seem unaffected.

9

9.9.3. ADDITIONAL MATERIAL ANALYSIS

The quality of the InSb nanowire was evaluated with TEM by preparing a longitudinal FIB cut along the wire. Extensive STEM imaging with high-angle annular dark field (HAADF), annular dark field (ADF) and bright field (BF) detectors has not revealed any extended crystallographic defects in the wire, such as stacking faults or dislocations (Figs. 9.15A and B as examples). The thickness of Al clearly changes at the junction region from thicker layer on the left side of the junction to the thinner one on the right (Fig. 9.15A). High-resolution annular bright field (ABF) STEM image shows clean InSb/Al interface and good crystallinity of both materials. The roughness of the interface in Fig. 9.15C is attributed to its tilt in the viewing direction caused by the difficulty in the sample preparation of the hexagonal nanowire along the main axis.

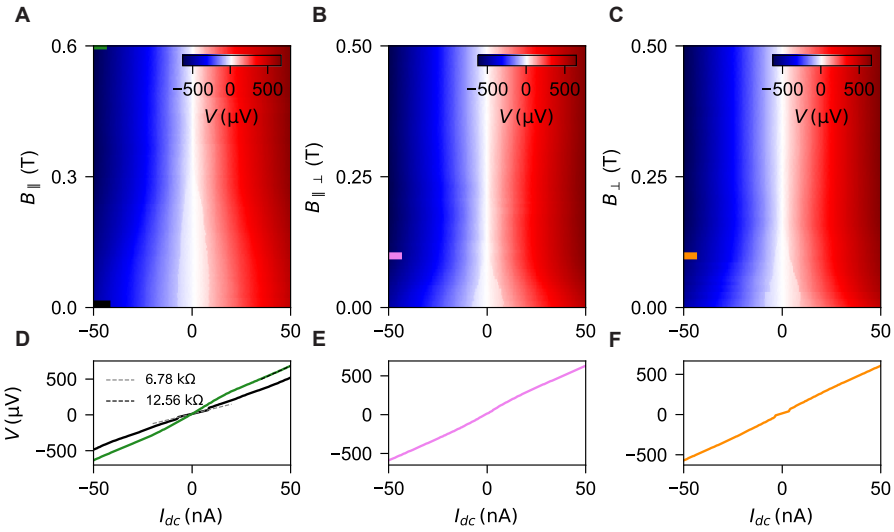

Figure 9.10: **Effect of magnetic field orientations on the supercurrent** Current (I_{dc}) *vs.* voltage (V) traces as a function of magnetic field for three different orientations. The data are taken in the two-probe configuration, therefore, from the supercurrent regime, we can fit the setup resistance (grey dashed fit). The sum of the normal state resistance of the junction and of the circuit is measured from the slope of the data at 0.6 T, at a high current bias (dark green fit). The normal state resistance (R_n) is found 5.78 kΩ. Considering a switching current (I_{sw}) of 12 nA, we estimate the $I_{sw}R_n$ product of ~ 70 μV at zero magnetic field. This value is similar to what reported in shadowed symmetric junctions [20].

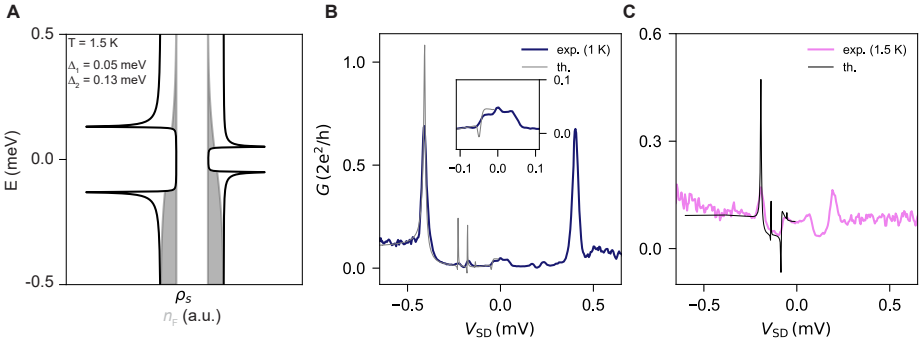

Figure 9.11: **Thermally-activated quasiparticle transport** (**A**) Schematic of the single-particle density of states of the two leads (ρ_s) with decreased gaps of $\Delta_1 = 0.05$ and $\Delta_2 = 0.13$ meV, together with the Fermi-Dirac distributions n_F (in grey) calculated at 1.5 K. (**B**), (**C**) Two exemplary line-cuts of Fig. 3F of the main text at 1 K and 1.5 K, respectively. The inset in panel (**B**) is a zoom-in of the low-bias regime. Thick (thin) traces are experimental (theoretical) conductances.

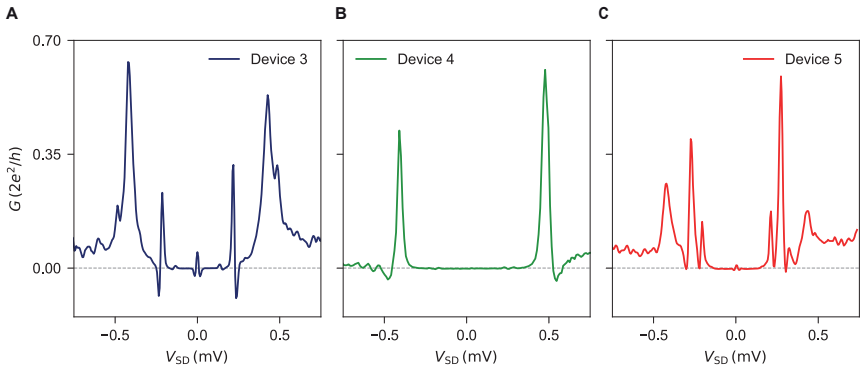

Figure 9.12: **Zero-magnetic field transport in additional devices.** G versus V_{SD} for three additional devices. Devices 4 and 5 differ in evaporation run with respect to device 3. Each device has a different thin-Al section length, namely 2.0, 2.5 and 1.0 µm for panels **A**, **B** and **C** respectively.

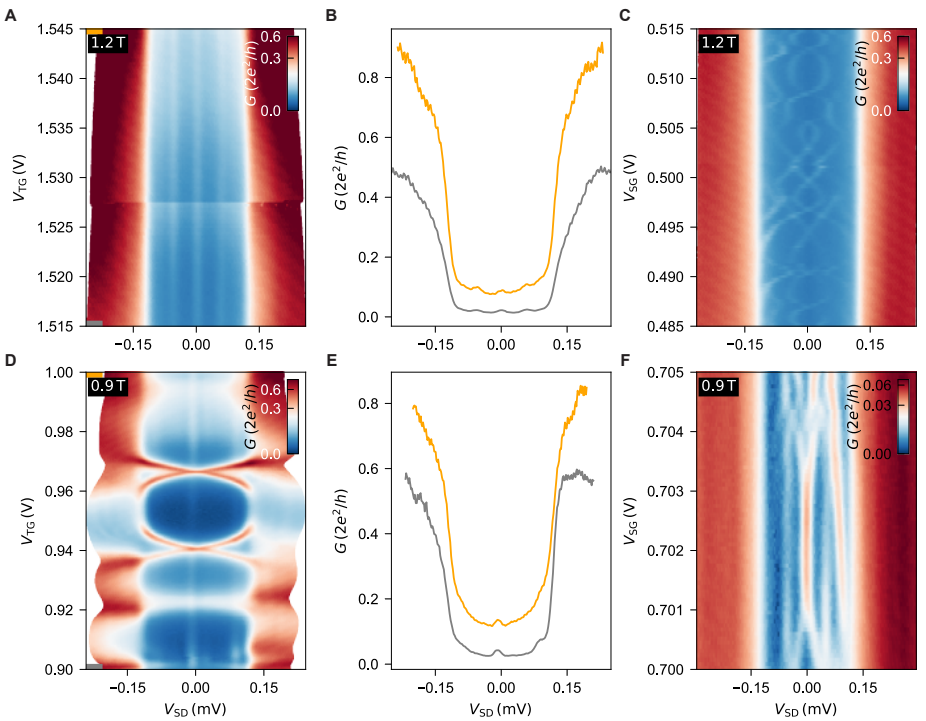

Figure 9.13: **Subgap states: gate dependence.** (**A**), (**B**) G vs. V_{TG} and V_{SD} and line-cuts taken at the positions indicated by the horizontal lines at $B_{\parallel} = 1.2$ T. (**C**) G vs. V_{SG} and V_{SD} at the same magnetic field. (**D**), (**E**) G vs. V_{TG} and V_{SD} and line-cuts at the positions indicated by the horizontal lines at $B_{\parallel} = 0.9$ T. (**F**) G vs. V_{SG} and V_{SD} at the same magnetic field. Faint and periodic diagonal features appearing in panels A, C and F are originated from low-frequency noise in our setup.

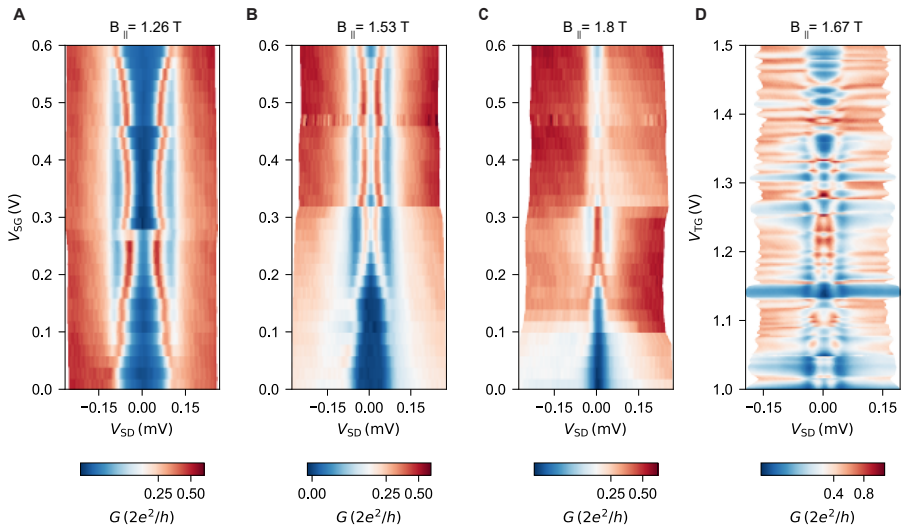

Figure 9.14: **Zero-bias peak gate dependence.** (**A**), (**B**) and (**C**) G versus V_{SD} and V_{SG} taken with $B_{\parallel}$ at 1.26 T, 1.53 T and 1.8 T, respectively. (**D**) G versus V_{SD} and V_{TG} at $B_{\parallel}$ = 1.67 T.

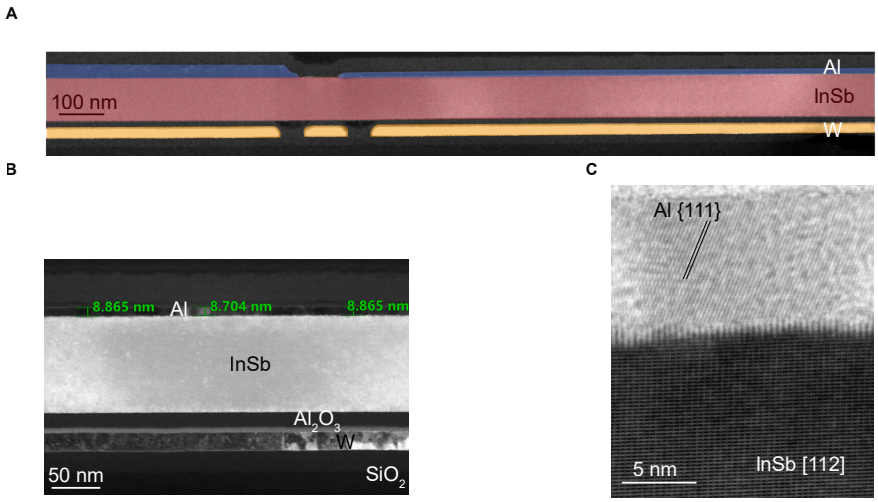

Figure 9.15: **Additional material analysis.** (**A**) False-colour HAADF STEM image along the longitudinal FIB cut of the InSb nanowire showing the junction with the thin Al layer on the right size on top of the wire and the thick one on the left side. The nanowire is shown in red, the gates in orange and the Al in blue. (**B**) Magnified ADF STEM image of the InSb nanowire with the thin Al coating. (**C**) High-resolution ABF STEM image of the InSb/Al interface in the region with thin Al coating.

9.9.4. SIMULATIONS OF PROXIMITIZED WIRE

In Fig. 9.4, we illustrate the behaviour of the spectrum of the wire as a function of magnetic field and super-gate voltage. The latter influences the number of subgap states and their effective g-factor, and consequently it would effect the onset of a potential transition to the topological regime. In order to study this phenomenon and the oscillatory states observed in Fig. 9.4D and E, we perform two types of simulations. The first one is phase-diagram calculation of the topological gap as a function of super-gate potential and magnetic field. We proceed along the line of [56]: the electrostatic potential is solved within the Thomas-Fermi approximation, which is used in a Bogoliubov-de Gennes equation discretized on a finite-difference grid. The superconductor properties are integrated into self-energy boundary conditions, as discussed in [56], which allow to calculate the gap (E_{gap}) and topological invariant (Q). We include orbital effects of the magnetic field through Peierl's substitution, and the closing of the superconducting gap as:

$$\Delta(B) = \Delta_0 \sqrt{1 - \frac{B^2}{B_c^2}} \tag{9.12}$$

with $B_c = 2$ T, $\Delta_0 = 0.25$ meV. The band offset between Al and InSb is set at 50 meV, and the Rashba SOC is $\alpha_R = 0.1$ eV nm. We also compute ξ_M, the length of the Majorana wavefunction, from the eigenvalue decomposition of the translation operator (see ref. [33]). The geometry of our model is shown in Fig. 9.16A. In Fig. 9.16B, the product of the gap and the topological invariant as a function of magnetic field and supergate V_{SG} is plotted. We see the appearance of topological phases starting at $V_{\text{SG}} \simeq -0.25$ V, and a maximum topological gap of 50 μeV. We emphasize that this simulation cannot predict the exact position of the topological phases in parameter space, because the band offset and the density of interface charges at the interface are unknown. In Fig. 9.16C, the associated Majorana length is shown for the same parameters: the smallest length of 150 nm is observed in the first band, but it quickly increases with magnetic field to up to more than 1 μm. Given that the length of Al in the experimental device is 1.5 μm, it is expected that the two Majorana wave-functions should be strongly hybridized. The second type of simulations performed aims to make a more detailed analysis of the oscillations of the lowest energy state when entering a regime of hybridized Majoranas. To that end, we apply the same methodology as in the previous simulation, but in the cross-section of a finite wire in the XZ plane. We then solve for the states with energies below the gap in this 2D system. The geometry is shown in Fig 9.17A. It is important to highlight here that this simulation reproduces the coupling to the superconductor and the electrostatic profile less accurately than the previous one. Because the superconductor appears only on the top, there is less hybridization in this case, and the Rashba spin-orbit coupling is renormalized less strongly. Therefore, in order to see Majorana lengths comparable to the one in the first band of Fig. 9.16C we need to reduce effectively the Rashba coefficient (at least by a factor 10). We use again $B_c = 2$ T, $\Delta_0 = 0.25$ meV, and a band offset of 50 meV, but this time we sweep over several values of α_R. The results are shown in Fig. 9.17B for the first topological phase, at $V_{\text{SG}} = 0.016$ V.

For the two values of expected Rashba coefficient in InSb wires (0.05 and 0.1 eV·nm) we do not find any oscillation. For a Rashba coefficient ten times smaller, oscillations appear, with an amplitude of a few μeV increasing with magnetic field. This is much smaller than

the amplitude of the measured oscillations. From these simulations we can conclude that without any disorder or inhomogeneity in the system, it is unlikely that states in the topological regime show oscillations decaying with magnetic field.

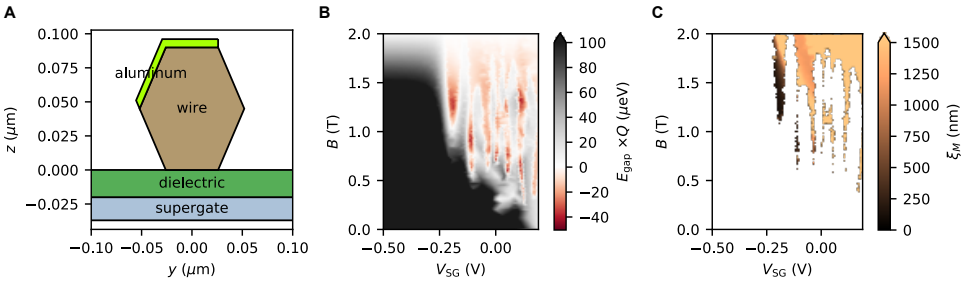

Figure 9.16: **Phase-diagram simulation of topological gap and Majorana length.** (**A**) Geometry used in the simulation; the wire is infinite in the x direction. (**B**) Product of gap and topological invariant; positive indicates a trivial phase and negative a topological phase. (**C**) Majorana length.

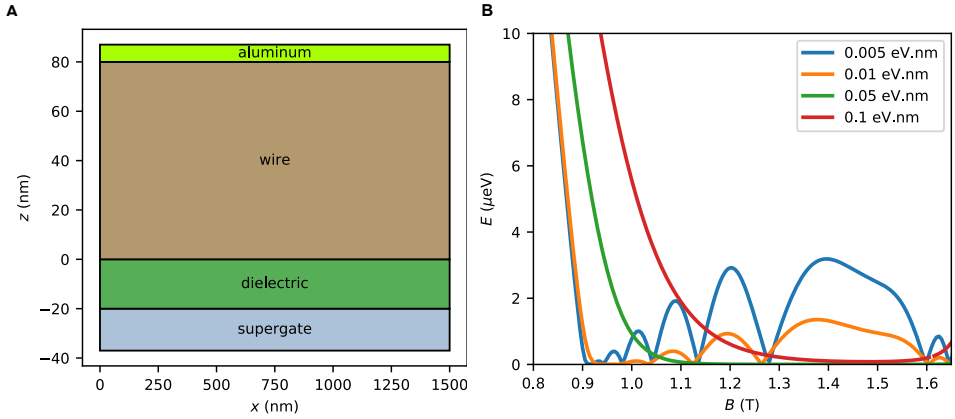

Figure 9.17: **2D simulation of finite nanowire.** (**A**) Geometry used in simulation. (**B**) Dependence of the energy of the lowest state in a magnetic field. The curves are the results of different simulations with varying α_R.

REFERENCES

[1] F. Borsoi, G. P. Mazur, N. van Loo, M. P. Nowak, L. Bourdet, K. Li, S. Korneychuk, A. Fursina, E. Memisevic, G. Badawy, S. Gazibegovic, K. van Hoogdalem, E. P. A. M. Bakkers, L. P. Kouwenhoven, S. Heedt, and M. Quintero-Pérez, *Single-shot fabrication of semiconducting-superconducting nanowire devices,* ArXiv e-prints **2009.06219** (2020).

[2] Y. Oreg, G. Refael, and F. von Oppen, *Helical liquids and Majorana bound states in quantum wires,* Phys. Rev. Lett. **105**, 177002 (2010).

[3] R. M. Lutchyn, J. D. Sau, and S. Das Sarma, *Majorana fermions and a topological phase transition in semiconductor-superconductor heterostructures,* Phys. Rev. Lett. **105**, 077001 (2010).

[4] J. Alicea, *New directions in the pursuit of Majorana fermions in solid state systems,* Rep. Prog. Phys. **75**, 076501 (2012).

[5] T. Hyart, B. van Heck, I. C. Fulga, M. Burrello, A. R. Akhmerov, and C. W. J. Beenakker, *Flux-controlled quantum computation with Majorana fermions,* Phys. Rev. B **88**, 035121 (2013).

[6] S. Plugge, A. Rasmussen, R. Egger, and K. Flensberg, *Majorana box qubits,* New J. Phys. **19**, 012001 (2017).

[7] T. Karzig, C. Knapp, R. M. Lutchyn, P. Bonderson, M. B. Hastings, C. Nayak, J. Alicea, K. Flensberg, S. Plugge, Y. Oreg, C. M. Marcus, and M. H. Freedman, *Scalable designs for quasiparticle-poisoning-protected topological quantum computation with Majorana zero modes,* Phys. Rev. B **95**, 235305 (2017).

[8] S. Vijay and L. Fu, *Teleportation-based quantum information processing with Majorana zero modes,* Phys. Rev. B **94**, 235446 (2016).

[9] P. Krogstrup, N. L. B. Ziino, W. Chang, S. M. Albrecht, M. H. Madsen, E. Johnson, J. Nygård, C. M. Marcus, and T. S. Jespersen, *Epitaxy of semiconductor-superconductor nanowires,* Nat. Mater. **14**, 400 (2015).

[10] M. Bjergfelt, D. J. Carrad, T. Kanne, M. Aagesen, E. M. Fiordaliso, E. Johnson, B. Shojaei, C. J. Palmstrøm, P. Krogstrup, T. S. Jespersen, and J. Nygård, *Superconducting vanadium/indium-arsenide hybrid nanowires,* Nanotechnology **30**, 294005 (2019).

[11] M. W. A. de Moor, *Quantum transport in nanowire networks*, Ph.D. thesis, Delft University of Technology (2019).

[12] S. A. Khan, C. Lampadaris, A. Cui, L. Stampfer, Y. Liu, S. J. Pauka, M. E. Cachaza, E. M. Fiordaliso, J.-H. Kang, S. Korneychuk, T. Mutas, J. E. Sestoft, F. Krizek, R. Tanta, M. C. Cassidy, T. S. Jespersen, and P. Krogstrup, *Highly transparent gatable superconducting shadow junctions,* ACS Nano (2020).

[13] S. Gazibegovic, D. Car, H. Zhang, S. C. Balk, J. A. Logan, M. W. A. de Moor, M. C. Cassidy, R. Schmits, D. Xu, G. Wang, P. Krogstrup, R. L. M. Op het Veld, K. Zuo, Y. Vos, J. Shen, D. Bouman, B. Shojaei, D. Pennachio, J. S. Lee, P. J. van Veldhoven, S. Koelling, M. A. Verheijen, L. P. Kouwenhoven, C. J. Palmstrøm, and E. P. A. M. Bakkers, *Epitaxy of advanced nanowire quantum devices,* Nature **584**, 434 (2017).

[14] D. J. Carrad, M. Bjergfelt, T. Kanne, M. Aagesen, F. Krizek, E. M. Fiordaliso, E. Johnson, J. Nygård, and T. Sand Jespersen, *Shadow epitaxy for in Situ growth of generic semiconductor/superconductor hybrids,* Adv. Mater. **32**, 1908411 (2020).

[15] J. H. Pei, R. Manzke, and C. G. Olson, *Exchange reaction at the Al-InSb (110) interface,* Chin. J. Phys. **26** (1988).

[16] F. Boscherini, Y. Shapira, C. Capasso, C. Aldao, M. del Giudice, and J. H. Weaver, *Exchange reaction, clustering, and surface segregation at the Al/InSb(110) interface,* Phys. Rev. B **35**, 9580 (1987).

[17] R. Sporken, P. Xhonneux, R. Caudano, and J. Delrue, *The formation of the Al-InSb(110) interface,* Surf. Sci. **193**, 47 (1988).

[18] C. Thomas, R. E. Diaz, J. H. Dycus, M. E. Salmon, R. E. Daniel, T. Wang, G. C. Gardner, and M. J. Manfra, *Toward durable Al-InSb hybrid heterostructures via epitaxy of 2ML interfacial InAs screening layers,* Phys. Rev. Mater. **3**, 124202 (2019).

[19] S. Gazibegovic, *Bottom-up grown InSb nanowire quantum devices,* Ph.D. thesis, Department of Applied Physics (2019).

[20] S. Heedt, M. Quintero-Pérez, F. Borsoi, A. Fursina, N. van Loo, G. P. Mazur, M. P. Nowak, M. Ammerlaan, K. Li, S. Korneychuk, J. Shen, M. A. Y. van de Poll, G. Badawy, S. Gazibegovic, K. van Hoogdalem, E. P. A. M. Bakkers, and L. P. Kouwenhoven, *Shadow-wall lithography of ballistic superconductor-semiconductor quantum devices,* ArXiv e-prints **2007.14383** (2020).

[21] M. W. A. de Moor, J. D. S. Bommer, D. Xu, G. W. Winkler, A. E. Antipov, A. Bargerbos, G. Wang, N. van Loo, R. L. M. O. het Veld, S. Gazibegovic, D. Car, J. A. Logan, M. Pendharkar, J. S. Lee, E. P. A. M. Bakkers, C. J. Palmstrøm, R. M. Lutchyn, L. P. Kouwenhoven, and H. Zhang, *Electric field tunable superconductor-semiconductor coupling in Majorana nanowires,* New J. Phys. **20**, 103049 (2018).

[22] G. Badawy, S. Gazibegovic, F. Borsoi, S. Heedt, C.-A. Wang, S. Koelling, M. A. Verheijen, L. P. Kouwenhoven, and E. P. A. M. Bakkers, *High mobility stemless InSb nanowires,* Nano Lett. **19**, 3575 (2019).

[23] L. Haworth, J. Lu, D. I. Westwood, and J. E. MacDonald, *Atomic hydrogen cleaning, nitriding and annealing InSb (100),* Appl. Surf. Sci. **166**, 253 (2000).

[24] R. Tessler, C. Saguy, O. Klin, S. Greenberg, E. Weiss, R. Akhvlediani, R. Edrei, and A. Hoffman, *Oxide-free InSb (100) surfaces by molecular hydrogen cleaning,* Appl. Phys. Lett. **88**, 1918 (2006).

[25] R. Meservey and P. M. Tedrow, *Properties of very thin aluminum films,* J. Appl. Phys. **42**, 51 (1971), https://doi.org/10.1063/1.1659648 .

[26] M. Valentini, F. Peñaranda, A. Hofmann, M. Brauns, R. Hauschild, P. Krogstrup, P. San-Jose, E. Prada, R. Aguado, and G. Katsaros, *Non-topological zero bias peaks in full-shell nanowires induced by flux tunable andreev states,* ArXiv e-prints **2008.02348** (2020), https://arxiv.org/abs/2008.02348.

[27] J. Cao, Q. Wang, and H. Dai, *Electron transport in very clean, as-grown suspended carbon nanotubes,* Nat. Mater. **4**, 745 (2005).

[28] G. E. Blonder, M. Tinkham, and T. M. Klapwijk, *Transition from metallic to tunneling regimes in superconducting microconstrictions: Excess current, charge imbalance, and supercurrent conversion,* Phys. Rev. B **25**, 4515 (1982).

[29] M. Octavio, M. Tinkham, G. E. Blonder, and T. M. Klapwijk, *Subharmonic energy-gap structure in superconducting constrictions,* Phys. Rev. B **27**, 6739 (1983).

[30] M. Kuhlmann, U. Zimmermann, D. Dikin, S. Abens, K. Keck, and V. M. Dmitriev, *Andreev-reflection in semiconductor-coupled superconducting weak-links,* Z. Phys. B **96**, 13 (1994).

[31] U. Zimmermann, S. Abens, D. Dikin, K. Keck, and V. M. Dmitriev, *Multiple Andreev-reflection in asymmetric superconducting weak-links,* Z. Phys. B **97**, 59 (1995).

[32] J. F. Cochran and D. E. Mapother, *Superconducting transition in aluminum,* Phys. Rev. **111**, 132 (1958).

[33] B. Nijholt and A. R. Akhmerov, *Orbital effect of magnetic field on the Majorana phase diagram,* Phys. Rev. B **93**, 235434 (2016).

[34] H. J. Suominen, M. Kjaergaard, A. R. Hamilton, J. Shabani, C. J. Palmstrøm, C. M. Marcus, and F. Nichele, *Zero-energy modes from coalescing Andreev states in a two-dimensional semiconductor-superconductor hybrid platform,* Phys. Rev. Lett. **119**, 176805 (2017).

[35] F. Nichele, A. C. C. Drachmann, A. M. Whiticar, E. C. T. O'Farrell, H. J. Suominen, A. Fornieri, T. Wang, G. C. Gardner, C. Thomas, A. T. Hatke, P. Krogstrup, M. J. Manfra, K. Flensberg, and C. M. Marcus, *Scaling of Majorana zero-bias conductance peaks,* Phys. Rev. Lett. **119**, 136803 (2017).

[36] A. E. Antipov, A. Bargerbos, G. W. Winkler, B. Bauer, E. Rossi, and R. M. Lutchyn, *Effects of gate-induced electric fields on semiconductor Majorana nanowires,* Phys. Rev. X **8**, 031041 (2018).

[37] G. W. Winkler, A. E. Antipov, B. Van Heck, A. A. Soluyanov, L. I. Glazman, M. Wimmer, and R. M. Lutchyn, *Unified numerical approach to topological semiconductor-superconductor heterostructures,* Phys. Rev. B **99**, 245408 (2019).

[38] H. Pan, W. S. Cole, J. D. Sau, and S. Das Sarma, *Generic quantized zero-bias conductance peaks in superconductor-semiconductor hybrid structures,* Phys. Rev. B **101**, 024506 (2020).

[39] T. D. Stanescu, R. M. Lutchyn, and S. Das Sarma, *Dimensional crossover in spin-orbit-coupled semiconductor nanowires with induced superconducting pairing,* Phys. Rev. B **87**, 094518 (2013).

[40] E. Prada, P. San-Jose, M. W. A. de Moor, A. Geresdi, E. J. H. Lee, J. Klinovaja, D. Loss, J. Nygård, R. Aguado, and L. P. Kouwenhoven, *From Andreev to Majorana bound states in hybrid superconductor–semiconductor nanowires,* Nature Reviews Physics **2**, 575 (2020).

[41] T. O. Rosdahl, A. Vuik, M. Kjaergaard, and A. R. Akhmerov, *Andreev rectifier: A nonlocal conductance signature of topological phase transitions,* Phys. Rev. B **97**, 045421 (2018).

[42] L. Fu, *Electron teleportation via Majorana bound states in a mesoscopic superconductor,* Phys. Rev. Lett. **104**, 056402 (2010).

[43] A. M. Whiticar, A. Fornieri, E. C. T. O'Farrell, A. C. C. Drachmann, T. Wang, C. Thomas, S. Gronin, R. Kallaher, G. C. Gardner, M. J. Manfra, C. M. Marcus, and F. Nichele, *Coherent transport through a Majorana island in an Aharonov–Bohm interferometer,* Nat. Commun. **11**, 3212 (2020).

[44] F. Borsoi, K. Zuo, S. Gazibegovic, R. L. M. Op het Veld, E. P. A. M. Bakkers, L. P. Kouwenhoven, and S. Heedt, *Transmission phase read-out of a large quantum dot in a nanowire interferometer,* Nat. Commun. **11**, 3666 (2020).

[45] A. Y. Kitaev, *Unpaired Majorana fermions in quantum wires,* Phys.-Uspekhi **44**, 131 (2001).

[46] J. D. Sau and S. D. Sarma, *Realizing a robust practical Majorana chain in a quantum-dot-superconductor linear array,* Nat. Comm. **3**, 964 (2012).

[47] I. C. Fulga, A. Haim, A. R. Akhmerov, and Y. Oreg, *Adaptive tuning of Majorana fermions in a quantum dot chain,* New J. Phys. **15**, 045020 (2013).

[48] M. Hays, G. de Lange, K. Serniak, D. J. van Woerkom, D. Bouman, P. Krogstrup, J. Nygård, A. Geresdi, and M. H. Devoret, *Direct microwave measurement of Andreev-bound-state dynamics in a semiconductor-nanowire Josephson junction,* Phys. Rev. Lett. **121**, 047001 (2018).

[49] L. Sun, L. DiCarlo, M. D. Reed, G. Catelani, L. S. Bishop, D. I. Schuster, B. R. Johnson, G. A. Yang, L. Frunzio, L. Glazman, M. H. Devoret, and R. J. Schoelkopf, *Measurements of quasiparticle tunneling dynamics in a band-gap-engineered transmon qubit,* Phys. Rev. Lett. **108**, 230509 (2012).

[50] J. Aumentado, M. W. Keller, J. M. Martinis, and M. H. Devoret, *Nonequilibrium quasiparticles and 2e periodicity in single-Cooper-pair transistors,* Phys. Rev. Lett. **92**, 066802 (2004).

[51] J. van Veen, A. Proutski, T. Karzig, D. I. Pikulin, R. M. Lutchyn, J. Nygård, P. Krogstrup, A. Geresdi, L. P. Kouwenhoven, and J. D. Watson, *Magnetic-field-dependent quasiparticle dynamics of nanowire single-Cooper-pair transistors,* Phys. Rev. B **98**, 174502 (2018).

[52] D. Averin and A. Bardas, *ac Josephson effect in a single quantum channel,* Phys. Rev. Lett. **75**, 1831 (1995).

[53] M. P. Nowak, M. Wimmer, and A. R. Akhmerov, *Supercurrent carried by nonequilibrium quasiparticles in a multiterminal Josephson junction,* Phys. Rev. B **99**, 075416 (2019).

[54] A. Bardas and D. V. Averin, *Electron transport in mesoscopic disordered superconductor-normal-metal-superconductor junctions,* Phys. Rev. B **56**, R8518 (1997).

[55] C. W. J. Beenakker, *Quantum transport in semiconductor-superconductor microjunctions,* Phys. Rev. B **46**, 12841 (1992).

[56] S. Vaitiekėnas, G. W. Winkler, B. van Heck, T. Karzig, M.-T. Deng, K. Flensberg, L. I. Glazman, C. Nayak, P. Krogstrup, R. M. Lutchyn, and C. M. Marcus, *Flux-induced topological superconductivity in full-shell nanowires,* Science **367** (2020).

10

Conclusion and outlook

10.1. MATERIALS AND FABRICATION ROUTES

Materials and fabrication methods are undoubtedly two of the core pillars of this thesis. To recap, chapter 7 presents the growth as well as the transport characterisation of stemless InSb nanowires, and chapter 8 unveils a technique to realise high-quality InSb/Al nanowire devices. In the latter, we use on-chip dielectric walls to cast shadows onto individual nanowire sections during the deposition of the superconductor. Notably, the shadow-wall technique allows simplifying the realisation of semiconducting-superconducting devices to previous approaches. Unreproducible fabrication steps – such as metal etching – are avoided altogether, electrostatic gates are self-aligned with the junctions, and the device dimensions are targeted with lithographic precision. The cleanliness of this method results in devices manifesting ballistic superconductivity and Majorana signatures. In chapter 9, we take a step further and demonstrate the single-shot fabrication of normal-superconductor junctions. With this technique, the normal (or superconducting) ohmic leads are integrated with the evaporation of the superconducting shell without breaking the vacuum. In the near future, developments of this approach will allow extending this idea to the realisation of single-shot three-terminal devices to facilitate the study of end-to-end correlations and the evolution of the gap in the bulk [1].

A milestone towards the device scalability will be the combination of the **shadow-wall technique with the selective-area growth (SAG) platform**. The latter enables the growth of high-quality InAs, and InSb nanowires networks [2–5] and will alleviate the need to transfer single nanowires next to shadow-walls. In the future, we shall aim at developing a technology based on pre-fabricated smart chips (i.e., with bondpads and shadow walls) and on an in-situ sequence of the kind:

1. growth of SAG nanowires next to shadow walls,
2. deposition of one (or two) superconductor(s) and/or metal(s) at one (or two) angle(s),
3. deposition of a capping layer.

Eventually, multiple chips should be ready for systematic low-temperature electrical characterisation. For this purpose, it would be beneficial to perform **multiplex transport measurements** to maximise the number of chips to test in a single cool-down [6].

Altough in the future this technique can also serve to fabricate qubit architectures, we can already use this technology for testing new materials. At the moment, the shadow-wall method combined with stemless nanowires can be already used as a playground for novel combinations. The first goal should be to find a superconductor which maintains **a sizeable gap at the high magnetic fields** required to enter the topological regime. In Al-based devices, the gap is only $\sim 200\,\mu$eV at zero magnetic field and, upon approaching the critical field ($2-3$ T at maximum), is substantially reduced. But nature offers alternatives to Al. Several possibilities have already been considered: NbTiN [7], V [8, 9], Sn [10, 11], Ta, Nb [12], Pb [13]. Indium is also promising, and being investigated at the moment in our group in collaboration with E. Bakkers group. For the ultimate goal of topological quantum computing, some of the aforementioned materials should be discarded. In fact,

despite Nb and NbTiN have high critical temperatures (respectively 9 and 15 K), they are not parity-preserving superconductors. This stems from the fact that niobium is prone to the formation of metallic NbO_x compounds that lead to localised metallic states [14]. It is unclear whether a capping layer that prevents oxidation can solve this issue, but it is an option worth considering. In contrast with Nb-based superconductors, Al, β-Sn and Pb are indeed parity-preserving. In the work of Carrad *et al.* [12], tunnelling spectroscopy in Ta-devices revealed a hard induced superconducting gap, suggesting Ta as a promising candidate too. To validate this observation, one should demonstrate the Cooper-pair charging effect in Ta-islands. Vanadium can also be an interesting alternative, but the same validation is required.

It is important to remark that the growth and the stability of these superconducting films are not trivial aspects and should be carefully considered. While the technology of Al-based quantum devices is rather mature, this is not the case for other superconductors. To give just a few examples of complications that arise in different materials, thin films of Sn and In are vulnerable to dewetting, and Pb can be etched by water. Therefore, careful optimisation of their growth parameters and the storage technique is required before their systematic use. A complete series of considerations on these materials is discussed in Kanne *et al.* [13].

A way to circumvent these technical issues relies on using aluminum films coated with a submonolayer of a heavy metal with intrinsic spin-orbit coupling [15, 16]. To validate this approach in nanowire devices, we realised a single-shot normal-superconductor junction where we deposited ~ 0.2 nm of platinum onto the 8 nm-shell of aluminum. The non-superconducting layer of platinum is too thin to have an appreciable effect on the Al superconducting gap. Still, it results in a substantial enhancement of the critical parallel field due to interfacial spin-mixing interaction (Fig. 10.1). While further experiments are required to optimise the thickness of Pt on Al to maximise the critical magnetic field, this materials combination remains a promising path forward.

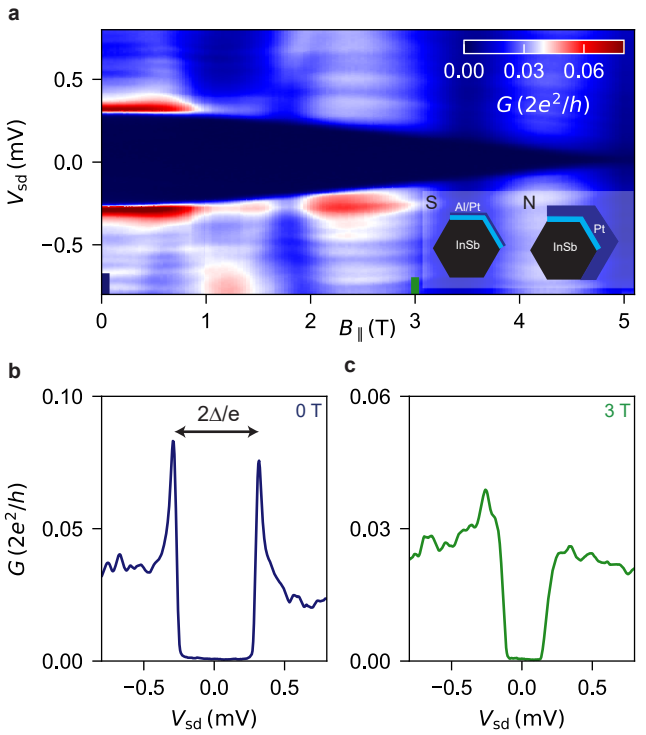

Figure 10.1: **Transport in single-shot InSb/Al/Pt normal-superconductor junctions. a** Differential conductance (G) versus bias voltage (V_{sd}) and magnetic field oriented along the nanowire direction ($B_{\parallel}$). The 8 nm-thick Al shell on the superconducting side (S) of the junction is covered with a layer of ~ 0.2 Pt that enhances the superconducting critical magnetic field up to 5 T. The normal side (N) is composed by this same layer covered with ~ 20 nm of Pt that anti-proximitizes the nanowire (bottom inset). **b** and **c** depict linecuts at the magnetic field values indicated. The induced gap at zero magnetic field is $\Delta = 0.3$ meV.

When the semiconducting-superconducting interface is highly transparent, the induced gap becomes close to the parent gap, and the properties of the semiconductors are strongly renormalised: the effective mass increases, while the effective g-factor and spin-orbit energy decrease [17–21]. Such renormalisation poses challenges for entering the topological regime. For this reason, efforts should be put in **creating a controllable barrier** between the two materials. In two-dimensional systems, this is achieved by forming quantum wells coupled to a superconductor. An example is the heterostructure InGaAs/InAs/InGaAs/Al studied in refs. [22, 23]. In one-dimensional systems, one strategy can be to encapsulate the semiconductor, say InAs or InSb, with another semiconductor with higher bandgap energy. InSb has the same lattice constant of CdTe; therefore, the formation of epitaxial core-shell InSb-CdTe nanowires is favourable (Fig. 10.2). The function of the CdTe layer can be twofold: beyond decreasing the coupling to the superconductor, it is expected to reduce surface scattering, leading to a possible increase in the electron mobility of the nanowires. In the future, we shall validate this hypothesis and study the dependence of the induced superconducting gap with respect to the CdTe shell thickness.

Thanks to the shadow-wall technique, this experiment should be rather straightforward.

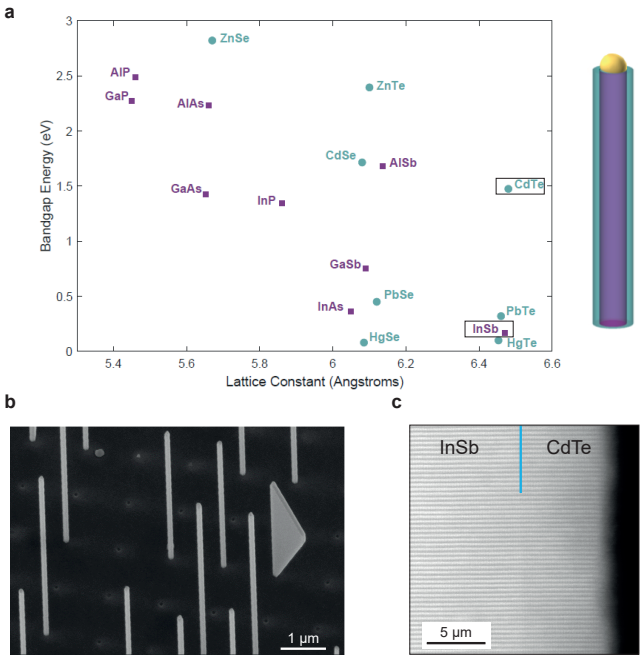

Figure 10.2: **Core-shell InSb-CdTe nanowires. a** III-V (in purple) and II-VI (in turquoise) compounds versus lattice constant and semiconducting bandgap energy. InSb and CdTe are in evidence, they have approximately the same lattice constant, but different bandgap. The figure is adapted from [24]. **b** Microscopy of stemless InSb-CdTe wires grown in E. Bakkers lab. **c** TEM study showing the epitaxial relation at the interface.

10.2. FUTURE EXPERIMENTAL DIRECTIONS

The rapid progress in the realization of high-quality hybrid devices has led to cleaner data and additional Majorana signatures. Despite the large experimental efforts, it is still not possible to conclude that delocalized Majorana modes have been observed in hybrid wires. A critical missing piece of the puzzle is the observation of **the closing and re-opening of the bulk gap** followed by the emergence of two correlated zero-bias peaks at nanowire ends. The measurements of the local and non-local conductance in a three-terminal device have been suggested as a tool to investigate these complex effects [1]. Experiments and detailed simulations have revealed that the non-local conductance – which provides a measurement of the bulk gap – is typically relatively small, sensitive to disorder and difficult to interpret [25–27]. Therefore, despite being a critical experiment in the search for a topological phase, it is expected that it will take the community a few years to reconcile experimental observations and theoretical predictions.

One of the complications in these experiments stems from the ubiquitous presence of non-topological zero-energy states due to non-uniform electrostatic potentials. These states are known in the literature as either quasi-Majoranas, local Majoranas or partially separated Andreev bound states [28–35]. Local Majoranas form typically in the vicinity of the junctions, and, despite being spatially partially or fully overlapping, they have approximately orthogonal spins. When a magnetic field is applied, their different polarisations lead to two couplings to the leads, which can be exponentially different. If one of the two local Majoranas is completely decoupled from the lead, tunnelling spectroscopy measurements will provide a false-positive Majorana signature (i.e., a robust zero-bias peak). To distinguish local vs non-local Majorana states in normal-superconductor junctions, we shall consider **the transmission of a ballistic normal-superconductor junction far away from the tunnelling regime**. In brief, when the barrier enables the transmission of a single-spin channel ($G \leq e^2/h$), a quantized zero-bias peak is expected in both cases. Upon activating the transmission of the second spin channel ($G \leq 2e^2/h$), the Majorana zero-bias peak remains quantized and broadens to a plateau inside the gap due to Andreev reflections. Eventually, with the activation of a third spin channel ($G \leq 3e^2/h$), the Majorana peak will exceed $2e^2/h$. Differently, two quasi-Majoranas can accommodate transport of both spin channels resulting in a peak which can reach $G \leq 4e^2/h$ when the out-of-gap conductance is $2e^2/h$. Therefore, while local Majoranas result in a zero-bias peak, separated Majoranas would display a zero-bias dip [31, 36] (Fig. 10.3). This experiment is conceptually simple and should be performed in long nanowire devices where emerging Majoranas are truly decoupled. Moreover, it can be promptly implemented in three-terminal devices, where the information of the non-local conductance can be integrated with the possible peak-to-dip evolution.

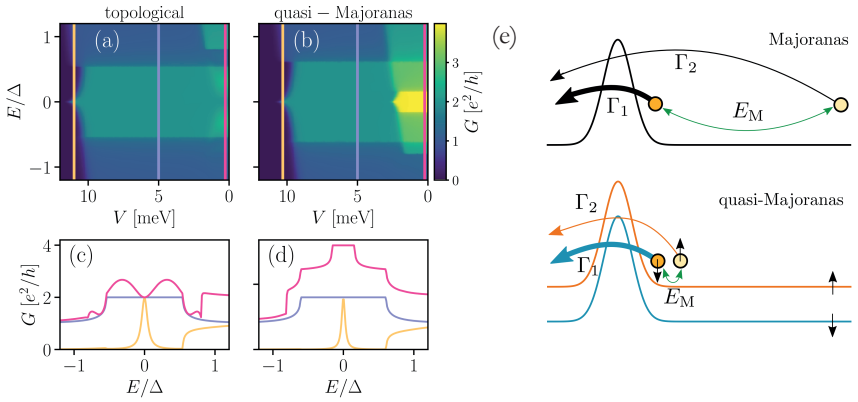

Figure 10.3: **Differentiating Majoranas from quasi-Majoranas in an NS junction.** (a), (b) Conductance versus bias energy (E) and height of the barrier (V) for topological Majoranas and quasi-Majoranas, respectively. (c), (d) Conductance linecuts of (a) (b). In (e), we show a schematic of the couplings of Majoranas and quasi-Majoranas to an external lead via a tunnel barrier. In long wires, spinless and far-away topological Majoranas with coupling E_M have typically $\Gamma_1 \gg \Gamma_2$ (top panel). The same can occur for spinful and overlapping local Majoranas that experience two effective barriers in a magnetic field (bottom panel). The figure is taken from ref [31].

An alternative approach to infer the Majorana non-locality relies on studying phase-coherent transport in two-path interferometers [37]. Our experiment discussed in chapter 4 and the preliminary observations in ref. [38] signal a good start in this direction. Moreover, recent developments in the growth of nanowire networks are opening the possibilities of more investigations in the near future [2–4]. We expect that the rich physics in hybrid interferometers will attract the same sizeable scientific interest that semiconducting interferometers had in the past. To investigate topological effects, we shall first consider **a Coulomb semiconducting-superconducting island embedded in a semiconducting interferometer** (Fig. 10.4a). When the island is much longer than the superconducting coherence length, incoherent tunnelling processes mediated by local Andreev states are suppressed. In contrast, electron teleportation via Majorana modes – if present – remains active and phase-coherent. To investigate this effect, we suggest studying the amplitude of the Aharonov-Bohm oscillations as a function of the parallel magnetic field and chemical potential for different device lengths. Regions in such parameter space with the highest coherent signal – and characterised by 1e-periodic Coulomb oscillations – might serve to map the topological phase diagram [39]. Here, as a second step, the dependence of the transmission phase on the island parity should be carefully studied. Because the electron transmission via two Majoranas scales as $i\gamma_1\gamma_2$ (chapter 2), a π-shift at resonance accompanied by a phase plateau in the Coulomb valleys are the two predicted fingerprints of delocalised Majorana modes. Observing these signatures represents a milestone to demonstrate the Majorana non-locality and toward the interferometric read-out of topological qubits [37, 40, 41].

Eventually, superconducting interferometers (SQUIDs) can also be used to differentiate Majorana and localised Andreev states (Fig. 10.4b). When **a long superconducting island is embedded in an asymmetric DC SQUID**, the current-phase relation can be

read-out [42]. If the island hosts two pairs of Andreev states, the sign of the 1e-periodic supercurrent inverts upon changing the electron parity. In contrast, the supercurrent sign is parity-independent when Majorana modes are present [43, 44]. The transfer of a Cooper pair across the island is in the first case mediated by the two overlapping Majoranas on the left side (say γ_1, γ_2) and then by the second pair of overlapping Majoranas on the right side (say γ_3, γ_4). The overall tunnelling coefficient will then scale as $\gamma_1, \gamma_2\gamma_3\gamma_4$ which is a parity-dependent term. Delocalized Majoranas would, in contrast, result in the term $(\gamma_1\gamma_2)^2$, which equals 1. Studying this effect is challenging because it requires measurable supercurrents in the ~ 1 T regime, however, we expect it to be feasible in the near future thanks to the advancements brought by the shadow-wall technique.

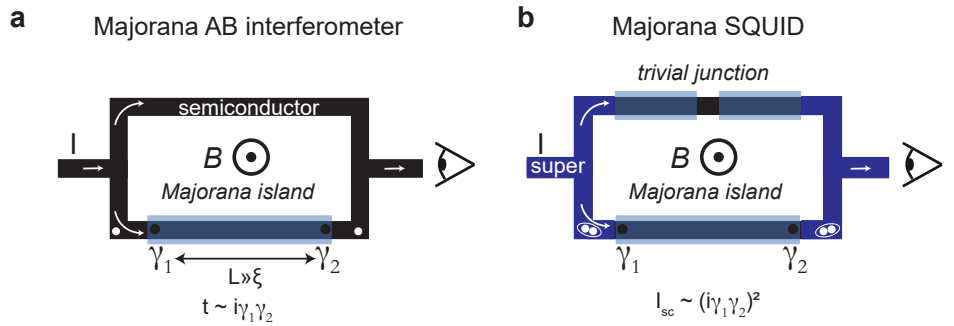

Figure 10.4: **Majorana interferometers a** A two-path Aharonov-Bohm interferometer hosting a Coulomb-blockaded Majorana island. Single-electron transfer via separated Majorana states remains phase-coherent independently from their distance. **b** A Majorana SQUID: an s-wave superconductor (in blue) is in contact with two hybrid semiconducting nanowires. A Majorana island is defined in one path, and a trivial junction in the other. The full current-phase relation enables to distinguish the presence of two Majoranas from four local Majoranas.

The advancements reported in this thesis lay the ground for future investigations of **other types of topological phases of matter**. Majorana zero modes obey Ising-type non-Abelian statistics (Z_2) and therefore are computationally limited in the sense that are not sufficient for universal quantum computation. This is in stark contrast with Fibonacci anyons (Z_n, with $n > 2$ and prime), which are fractional Majoranas, or parafermions, that emerge at the interface between different phases of matter [45, 46]. Parafermions are proposed to emerge in fractional quantum Hall systems with induced superconductivity, but their realization is still hindered by the decline of hard induced superconductivity at the required magnetic fields ($5-10$ T) [47].

Progress in nanowires with spin-orbit interaction, large electron tunability and hard superconducting induced gap calls for the possible implementation of other parafermions: **Kramers pairs** of Majorana modes (Z_4) [48–51]. Kramers pairs are incredibly intriguing because they can sustain a topological phase at zero magnetic field and, upon braiding sequences, enable a larger number of protected operations such as $\pi/4$ rotations in the Bloch sphere (whereas Majorana modes provide only $\pi/2$ rotations). The minimal setup

required to create Kramers pairs consists of **two parallel Rashba nanowires** with different spin-orbit interactions (NW1 and NW2) coupled to an s-wave superconductor (S). Cooper pairs in S can tunnel via direct Andreev reflection in NW1 and NW2 inducing intrawire superconducting pairing correlations. Moreover, if the two wires are close to each other, Cooper pairs split and propagate in NW1 and NW2 via crossed Andreev reflection giving rise to interwire correlations. When the interwire coupling dominates over the intrawire coupling (i.e., which requires strong electron-electron interactions), and under certain conditions on the chemical potential, the double-wire system hosts zero-energy Kramers pairs at the edges at zero magnetic field, which can be investigated by tunnelling spectroscopy [49, 51].

Experiments in this thesis together with the works of refs. [19, 20] have demonstrated that properties such as the spin-orbit interaction in hybrid nanowires can be controlled by gate voltages fulfilling a requirement of this proposal. Moreover, the work of Ueda *et al.* [52] demonstrated that the condition of interwire coupling pairing bigger than the intrawire coupling is satisfied in pairs of ballistic InAs/Al nanowires due to electron-electron interaction naturally occurring in such confined nanostructures. This alleviates the need for using quantum dots in double-wire architectures and enables the direct investigations of Kramers pairs by tunnelling spectroscopy.

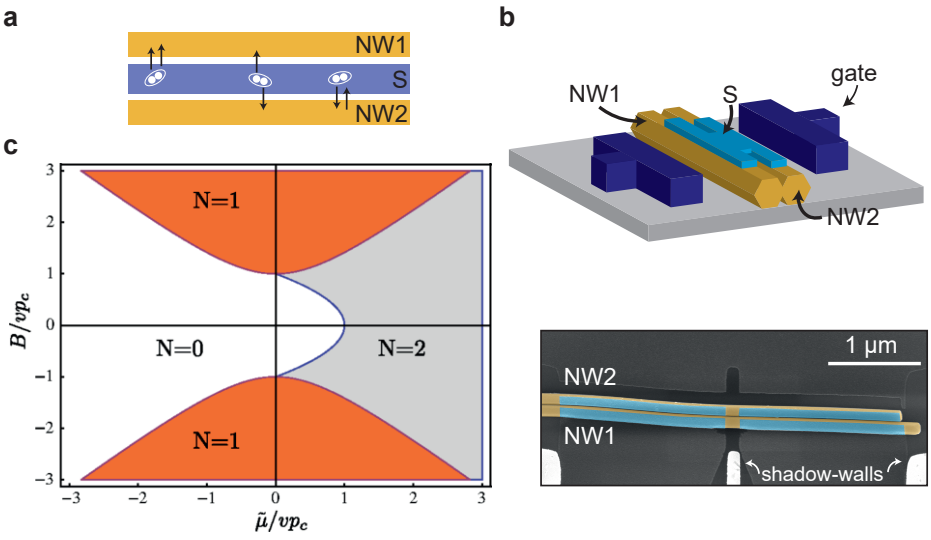

Figure 10.5: **Majoranas and Kramers pairs a** Schematic of two Rashba nanowires (in ochre) with intrawire and interwire superconducting couplings mediated by direct and crossed Andreev reflections via an s-wave superconductor (in light blue). **b** A three-dimensional illustration together with an implementation of the scheme with shadow-wall InSb/Al nanowires. Because Kramers pairs can arise at zero magnetic field, a thick Al film evaporated at angle α that is $60° < \alpha < 90°$ with respect to the substrate can be used to form a continuous layer that covers both nanowires. Additional gates (in blue) are added in the illustration to tune the spin-orbit energy differently in the two wires. **c** Calculated topological phase diagram versus effective magnetic field (y-axis) and chemical potential (x-axis) imported from ref. [48]. In the grey region with $N = 2$, the double-wire system hosts Kramers pairs, in the orange one with $N = 1$ it hosts Majorana modes, and in the white one is set in the trivial regime.

REFERENCES

[1] T. O. Rosdahl, A. Vuik, M. Kjaergaard, and A. R. Akhmerov, *Andreev rectifier: A nonlocal conductance signature of topological phase transitions,* Phys. Rev. B **97**, 045421 (2018).

[2] F. Krizek, J. E. Sestoft, P. Aseev, S. Marti-Sanchez, S. Vaitiekėnas, L. Casparis, S. A. Khan, Y. Liu, T. Stankevič, A. M. Whiticar, A. Fursina, F. Boekhout, R. Koops, E. Uccelli, L. P. Kouwenhoven, C. M. Marcus, J. Arbiol, and P. Krogstrup, *Field effect enhancement in buffered quantum nanowire networks,* Phys. Rev. Mater. **2**, 093401 (2018).

[3] S. Vaitiekenas, A. M. Whiticar, M.-T. Deng, F. Krizek, J. E. Sestoft, C. J. Palmstrøm, S. Marti-Sanchez, J. Arbiol, P. Krogstrup, L. Casparis, and C. M. Marcus, *Selective-area-grown semiconductor-superconductor hybrids: A basis for topological networks,* Phys. Rev. Lett. **121**, 147701 (2018).

[4] P. Aseev, A. Fursina, F. Boekhout, F. Krizek, J. E. Sestoft, F. Borsoi, S. Heedt, G. Wang, L. Binci, S. Martí-Sánchez, T. Swoboda, R. Koops, E. Uccelli, J. Arbiol, P. Krogstrup, L. P. Kouwenhoven, and P. Caroff, *Selectivity map for molecular beam epitaxy of advanced III-V quantum nanowire networks,* Nano Lett. **19**, 218 (2019).

[5] P. Aseev, G. Wang, L. Binci, A. Singh, S. Martí-Sánchez, M. Botifoll, L. J. Stek, A. Bordin, J. D. Watson, F. Boekhout, D. Abel, J. Gamble, K. Van Hoogdalem, J. Arbiol, L. P. Kouwenhoven, G. de Lange, and P. Caroff, *Ballistic InSb nanowires and networks via metal-sown selective area growth,* Nano Lett. **19**, 9102 (2019).

[6] B. Paquelet Wuetz, P. L. Bavdaz, L. A. Yeoh, R. Schouten, H. van der Does, M. Tiggelman, D. Sabbagh, A. Sammak, C. G. Almudever, F. Sebastiano, J. S. Clarke, M. Veldhorst, and G. Scappucci, *Multiplexed quantum transport using commercial off-the-shelf CMOS at sub-kelvin temperatures,* npj Quantum Inf. **6**, 43 (2020).

[7] O. Gül, H. Zhang, J. D. S. Bommer, M. W. A. de Moor, D. Car, S. R. Plissard, A. Bakkers, E. P. A. M. Geresdi, K. Watanabe, T. Taniguchi, and L. P. Kouwenhoven, *Ballistic Majorana nanowire devices,* Nat. Nanotechnol. **13**, 192 (2018).

[8] E. J. H. Lee, X. Jiang, M. Houzet, R. Aguado, C. M. Lieber, and S. De Franceschi, *Spin-resolved Andreev levels and parity crossings in hybrid superconductor–semiconductor nanostructures,* Nat. Nanotechnol. **9**, 79 (2014).

[9] M. Bjergfelt, D. J. Carrad, T. Kanne, M. Aagesen, E. M. Fiordaliso, E. Johnson, B. Shojaei, C. J. Palmstrøm, P. Krogstrup, T. S. Jespersen, and J. Nygård, *Superconducting vanadium/indium-arsenide hybrid nanowires,* Nanotechnology **30**, 294005 (2019).

[10] M. Pendharkar, B. Zhang, H. Wu, A. Zarassi, P. Zhang, C. P. Dempsey, J. S. Lee, S. D. Harrington, G. Badawy, S. Gazibegovic, J. Jung, A. H. Chen, M. A. Verheijen, M. Hocevar, E. P. A. M. Bakkers, C. J. Palmstrøm, and S. M. Frolov, *Parity-preserving and magnetic field resilient superconductivity in indium antimonide nanowires with tin shells,* arXiv e-prints **1912.06071** (2019).

[11] S. A. Khan, C. Lampadaris, A. Cui, L. Stampfer, Y. Liu, S. J. Pauka, M. E. Cachaza, E. M. Fiordaliso, J.-H. Kang, S. Korneychuk, T. Mutas, J. E. Sestoft, F. Krizek, R. Tanta, M. C. Cassidy, T. S. Jespersen, and P. Krogstrup, *Highly transparent gatable superconducting shadow junctions,* ACS Nano (2020).

[12] D. J. Carrad, M. Bjergfelt, T. Kanne, M. Aagesen, F. Krizek, E. M. Fiordaliso, E. Johnson, J. Nygård, and T. Sand Jespersen, *Shadow epitaxy for in situ growth of generic semiconductor/superconductor hybrids,* Adv. Mater. **32**, 1908411 (2020).

[13] T. Kanne, M. Marnauza, D. Olsteins, D. J. Carrad, J. E. Sestoft, J. de Bruijckere, L. Zeng, E. Johnson, E. Olsson, K. Grove-Rasmussen, and J. Nygård, *Epitaxial Pb on InAs nanowires,* ArXiv e-prints **2002.11641** (2020).

[14] A. Darlinski and J. Halbritter, *Angle-resolved xps studies of oxides at nbn, nbc, and nb surfaces,* Surf. Interface Anal. **10**, 223 (1987).

[15] P. M. Tedrow and R. Meservey, *Critical magnetic field of very thin superconducting aluminum films,* Phys. Rev. B **25**, 171 (1982).

[16] X. S. Wu, P. W. Adams, Y. Yang, and R. L. McCarley, *Spin proximity effect in ultrathin superconducting Be-Au bilayers,* Phys. Rev. Lett. **96**, 127002 (2006).

[17] C. Reeg, D. Loss, and J. Klinovaja, *Metallization of a rashba wire by a superconducting layer in the strong-proximity regime,* Phys. Rev. B **97**, 165425 (2018).

[18] A. E. Antipov, A. Bargerbos, G. W. Winkler, B. Bauer, E. Rossi, and R. M. Lutchyn, *Effects of gate-induced electric fields on semiconductor Majorana nanowires,* Phys. Rev. X **8**, 031041 (2018).

[19] M. W. A. de Moor, J. D. S. Bommer, D. Xu, G. W. Winkler, A. E. Antipov, A. Bargerbos, G. Wang, N. van Loo, R. L. M. O. het Veld, S. Gazibegovic, D. Car, J. A. Logan, M. Pendharkar, J. S. Lee, E. P. A. M. Bakkers, C. J. Palmstrøm, R. M. Lutchyn, L. P. Kouwenhoven, and H. Zhang, *Electric field tunable superconductor-semiconductor coupling in Majorana nanowires,* New J. Phys. **20**, 103049 (2018).

[20] S. Vaitiekėnas, M.-T. Deng, J. Nygård, P. Krogstrup, and C. M. Marcus, *Effective g factor of subgap states in hybrid nanowires,* Phys. Rev. Lett. **121**, 037703 (2018).

[21] J. Shen, S. Heedt, F. Borsoi, B. van Heck, S. Gazibegovic, R. L. M. Op het Veld, D. Car, J. A. Logan, M. Pendharkar, S. J. J. Ramakers, G. Wang, D. Xu, D. Bouman, A. Geresdi, C. J. Palmstrøm, E. P. A. M. Bakkers, and L. P. Kouwenhoven, *Parity transitions in the superconducting ground state of hybrid InSb-Al Coulomb islands,* Nat. Commun. **9**, 4801 (2018).

[22] M. Kjaergaard, F. Nichele, H. J. Suominen, M. P. Nowak, M. Wimmer, A. R. Akhmerov, J. A. Folk, K. Flensberg, J. Shabani, C. J. Palmstrøm, and C. M. Marcus, *Quantized conductance doubling and hard gap in a two-dimensional semiconductor-superconductor heterostructure,* Nat. Commun. **7**, 12841 (2016).

[23] J. Shabani, M. Kjaergaard, H. J. Suominen, Y. Kim, F. Nichele, K. Pakrouski, T. Stankevic, R. M. Lutchyn, P. Krogstrup, R. Feidenhans'l, S. Kraemer, C. Nayak, M. Troyer, C. M. Marcus, and C. J. Palmstrøm, *Two-dimensional epitaxial superconductor-semiconductor heterostructures: A platform for topological superconducting networks,* Phys. Rev. B **93**, 155402 (2016).

[24] T. Wang, N. Moll, K. Cho, and J. D. Joannopoulos, *Deliberately designed materials for optoelectronics applications,* Phys. Rev. Lett. **82**, 3304 (1999).

[25] G. L. R. Anselmetti, E. A. Martinez, G. C. Ménard, D. Puglia, F. K. Malinowski, J. S. Lee, S. Choi, M. Pendharkar, C. J. Palmstrøm, C. M. Marcus, L. Casparis, and A. P. Higginbotham, *End-to-end correlated subgap states in hybrid nanowires,* Phys. Rev. B **100**, 205412 (2019).

[26] D. Puglia, E. A. Martinez, G. C. Ménard, A. Pöschl, S. Gronin, G. C. Gardner, R. Kallaher, M. J. Manfra, C. M. Marcus, A. P. Higginbotham, and L. Casparis, *Closing of the induced gap in a hybrid superconductor-semiconductor nanowire,* ArXiv e-prints **2006.01275** (2020).

[27] H. Pan, J. D. Sau, and S. D. Sarma, *Three-terminal nonlocal conductance in Majorana nanowires: distinguishing topological and trivial in realistic systems with disorder and inhomogeneous potential,* ArXiv e-prints **2009.11809** (2020).

[28] G. Kells, D. Meidan, and P. W. Brouwer, *Near-zero-energy end states in topologically trivial spin-orbit coupled superconducting nanowires with a smooth confinement,* Phys. Rev. B **86**, 100503 (2012).

[29] E. Prada, P. San-Jose, and R. Aguado, *Transport spectroscopy of n s nanowire junctions with Majorana fermions,* Phys. Rev. B **86**, 180503 (2012).

[30] C. Moore, T. D. Stanescu, and S. Tewari, *Two-terminal charge tunneling: Disentangling Majorana zero modes from partially separated Andreev bound states in semiconductor-superconductor heterostructures,* Phys. Rev. B **97**, 165302 (2018).

[31] A. Vuik, B. Nijholt, A. R. Akhmerov, and M. Wimmer, *Reproducing topological properties with quasi-Majorana states,* SciPost Phys. **7**, 61 (2019).

[32] E. Prada, P. San-Jose, M. W. A. de Moor, A. Geresdi, E. J. H. Lee, J. Klinovaja, D. Loss, J. Nygård, R. Aguado, and L. P. Kouwenhoven, *From Andreev to Majorana bound states in hybrid superconductor–semiconductor nanowires,* Nature Reviews Physics **2**, 575 (2020).

[33] H. Pan and S. D. Sarma, *Zero-bias conductance peaks in Majorana nanowires: the good, the bad, and the ugly,* ArXiv e-prints **1910.11413** (2019).

[34] H. Pan, W. S. Cole, J. D. Sau, and S. Das Sarma, *Generic quantized zero-bias conductance peaks in superconductor-semiconductor hybrid structures,* Phys. Rev. B **101**, 024506 (2020).

[35] H. Pan and S. Das Sarma, *Physical mechanisms for zero-bias conductance peaks in Majorana nanowires,* Phys. Rev. Research **2**, 013377 (2020).

[36] H. Zhang, D. E. Liu, M. Wimmer, and L. P. Kouwenhoven, *Next steps of quantum transport in Majorana nanowire devices,* Nat. Commun. **10**, 5128 (2019).

[37] L. Fu, *Electron teleportation via Majorana bound states in a mesoscopic superconductor,* Phys. Rev. Lett. **104**, 056402 (2010).

[38] A. M. Whiticar, A. Fornieri, E. C. T. O'Farrell, A. C. C. Drachmann, T. Wang, C. Thomas, S. Gronin, R. Kallaher, G. C. Gardner, M. J. Manfra, C. M. Marcus, and F. Nichele, *Coherent transport through a Majorana island in an Aharonov–Bohm interferometer,* Nat. Commun. **11**, 3212 (2020).

[39] M. Thamm and B. Rosenow, *Transmission amplitude through a Coulomb blockaded Majorana wire,* ArXiv e-prints **2010.15092** (2020).

[40] C. Drukier, H.-G. Zirnstein, B. Rosenow, A. Stern, and Y. Oreg, *Evolution of the transmission phase through a Coulomb-blockaded Majorana wire,* Phys. Rev. B **98**, 161401 (2018).

[41] M. Hell, K. Flensberg, and M. Leijnse, *Distinguishing Majorana bound states from localized Andreev bound states by interferometry,* Phys. Rev. B **97**, 161401 (2018).

[42] J. van Veen, A. Proutski, T. Karzig, D. I. Pikulin, R. M. Lutchyn, J. Nygård, P. Krogstrup, A. Geresdi, L. P. Kouwenhoven, and J. D. Watson, *Magnetic-field-dependent quasiparticle dynamics of nanowire single-Cooper-pair transistors,* Phys. Rev. B **98**, 174502 (2018).

[43] C. Schrade and L. Fu, *Andreev or Majorana, Cooper finds out,* ArXiv e-prints **1809.06370** (2018).

[44] C. Schrade and L. Fu, *Majorana superconducting qubit,* Phys. Rev. Lett. **121**, 267002 (2018).

[45] J. K. Pachos, *Introduction to Topological Quantum Computation*, 1st ed. (Cambridge University Press, USA, 2012).

[46] S. Trebst, M. Troyer, Z. Wang, and A. W. W. Ludwig, *A short introduction to Fibonacci anyon models,* Progress of Theoretical Physics Supplement **176**, 384 (2008).

[47] R. S. K. Mong, D. J. Clarke, J. Alicea, N. H. Lindner, P. Fendley, C. Nayak, Y. Oreg, A. Stern, E. Berg, K. Shtengel, and M. P. A. Fisher, *Universal topological quantum computation from a superconductor-abelian quantum Hall heterostructure,* Phys. Rev. X **4**, 011036 (2014).

[48] E. Gaidamauskas, J. Paaske, and K. Flensberg, *Majorana bound states in two-channel time-reversal-symmetric nanowire systems,* Phys. Rev. Lett. **112**, 126402 (2014).

[49] J. Klinovaja and D. Loss, *Time-reversal invariant parafermions in interacting Rashba nanowires,* Phys. Rev. B **90**, 045118 (2014).

[50] J. Klinovaja and D. Loss, *Parafermions in an interacting nanowire bundle,* Phys. Rev. Lett. **112**, 246403 (2014).

[51] C. Schrade, M. Thakurathi, C. Reeg, S. Hoffman, J. Klinovaja, and D. Loss, *Low-field topological threshold in Majorana double nanowires,* Phys. Rev. B **96**, 035306 (2017).

[52] K. Ueda, S. Matsuo, H. Kamata, S. Baba, Y. Sato, Y. Takeshige, K. Li, S. Jeppesen, L. Samuelson, H. Xu, and S. Tarucha, *Dominant nonlocal superconducting proximity effect due to electron-electron interaction in a ballistic double nanowire,* Sci. Adv. **5** (2019).

ACKNOWLEDGEMENTS

The work at hand could not be conceived and carried out without many precious people orbiting around me in these years. Like in a story tale, each of them played a role: someone from the beginning teaching me the art of science, others somewhere in the middle joining for a venture, and others toward the end, ensuring the happy ending of the story. But my long trajectory to Delft started much earlier than this PhD, from an office in Pisa in the faraway 2014, and will continue after this defense. But will come back to this later.

The first person I met when entering the B-wing of the TNW building in September 2015 was **Leo**. I was joining this group for a few months exchange program, and, of course, at that time, I was not aware that my destiny would bring me here for another four and half years of PhD. I also did not know the meaning of 'topological' in front of 'superconductivity', which together formed the name and the direction of the research group. Leo, thanks for showing me what it means, but more importantly for passing along to your students your attitude toward science: an intricate blend between being concrete and playful, without giving up the chance of dreaming big. Thanks to your wisdom, you have attracted and let interact incredible minds, which have laid the groundwork for the next generations of scientists in the house. I am confident that this will continue. Thanks for letting me stay in the group until the end. I enjoyed every moment (yes, even when nothing had worked for about 2 out of 4 years), every advice, every discussion, your promptness when needed, and, above others, your gentle pushes. They were crucial to building up my self-confidence and strengthen my passion.
Sebastian, you have been the calm and scrupulous person that I so much needed in these years. Our interaction resulted eventually into valuable works. If I look back to one of your project-tree which you used to start some of the crucial meetings, I am happy than many branches have been ticked off in green. With a bit of nostalgia, I can now remember all the things we also failed: from bombarding the wires with a bit too much hydrogen to measuring horrible stuff in the fridge. I am fulfilled that, after a lot of frustration (which maybe caused some of our white hair), everything worked out beautifully. I wish you and Anna good luck in life, and, of course, I hope you can marry soon.
Marina, you have been the one carrying the magic wand which we, starting off the Loop Qubit team with only the three of us, so much were seeking for. When science was not going well, you felt it deeply, when science was excellent, you were filled with joy. There is so much passion in you that I am confident you will choose the right track every time life asks. The UTS project was often frustrating, but you and I were dreamers, and would not leave our determination to go. While it happened rarely, we were lucky enough that one of us stayed in good spirit to keep the other going. Crucial was when we saw the TEM images of our first successful sample; it took me some time to convince you that, with two fully grown Al facet, this was the 'one'. Thanks for your determination in so many other things, from taking me on five years ago in the cleanroom, but also for unstoppably

searching for the right Al deposition temperature. If there was one, that was the turning point. Wish you and Thjis the best with little Jimi.
Nick, and **Greg**, I love the enthusiasm you spark together. I am so grateful to you for all the work you are still carrying out with curiosity, ambition and determination, and for all we accomplished together. While it was sometimes exhausting, the search for the perfect device seems accomplished. Thanks to all the chat, the coffees together, the uncountable meetings. You were real friends to me along the way. With you, the Loop Qubit team is absolutely in great hands. **Vukan**, and **Jiyin**, same for you. You are another perfectly working couple. I am so happy you both found your way of carrying on meaningful experiments. Thanks to your persistence, you are in a promising and extremely intriguing direction, I wish you all the best. **Alexandra**, thanks for transmitting to me invaluable lessons in the cleanroom, your strength will bring you anywhere you aim to. **Kevin**, thanks for letting me into your simulation's world, and for triggering meaningful discussions, often centred around the complicate matter of topological qubit read-out. I wish you all the best to this team I am leaving. Thanks to the new joiners **Filip**, **Lin**, **Mathilde**, and **Cristina**. The future seems prosperous with you on board.

Guan, our friendship is already more than five years old, when we both were fresh Master students. I loved chatting with you, and it has always been entertaining independently on the topic. Good luck with finishing your PhD, you are almost there. In the meantime, we will, for sure, continue with our walks and tennis games. **Jie**, and **Kun**, you were both crucial at the beginning of my PhD. You made me a better researcher with your own and different characters in the cleanroom and the lab. I will remember your passion and persistence with joy. All the best for your career. **Bernard**, at certain phases you were our hero. In the early days of our collaboration, we started skyping at absurd times in the evening, till you decided that it was better to simply move to Delft. Thanks for sharing your insights, but above all for having kept patience across our two island papers. I am sure this quality will be of crucial importance now that you are a father. Thanks for also being an advisor in the latest period. **James**, my favourite Scottish man. Upon arriving in Delft, it took me a month to understand your English, but then we blended it up nicely. I had such a good time with you, and, of course, thanks for all the early teaching of microwaves 101 (and for letting me discover Kek). **Willemijn** and **Damaz**, you too played an essential role in the real beginning. I am very thankful to you for creating an enjoyable atmosphere all around. It sparks both funny and deep conversations. I acknowledge that this would not have been the same without unreplaceable characters in Topo (or QuRe?) such as **Michiel**, **Fokko**, **Jouri**, **Jasper**, **Alex**, **Arno**, **Daniel**, **Nicolo'**, **Nikolai**, **Di**, **Christian**, **Ting**, **Ivan** and **Christine**. Thanks for the help on the go, for the uncountable Champions league matches together, for the pre-Covid parties, and for maintaining each other in good spirit (especially with darts). I am confident that the fresher generation of PhD students will keep these traditions going with success. Good luck to you all **Lin**, **Jaap**, **David**, **Marta**, **Christian**, **Lukas**, and **Alberto**. You form a group of such brilliant people that you will nail your PhD down. Overall Topo has also gained experience in many other people such as **Kongyi**, **Léo**, **Svetlana**, **Elvedin**, and **Daan**. Thanks to all of you because you have been of tremendous help in different stages of my research: from priceless calculation to cleanroom help and material analysis. Léo, in particular, I remember with

joy our trip to California with Guan. I think I have never eaten so much Mexican and avocados like in those days. That trip will remain unforgettable, also because it was our last real trip before Covid interrupted these getaways conferences.

Along these years, I owe my gratitude to several members of the Microsoft Quantum Lab. While I have already mentioned some of them, thanks to **David**, **Wolfgang**, **Pavel**, **John**, **Angela**, **Georg W.**, **CK**, **Gijs**, **Emrah**, **Morteza**, **Andrey A.** and **Peter K.** for sharing your knowledge and capabilities with great humility and transparency.
But, speaking frankly, how could our lab run without the techs? I am so grateful to have had on my side people like **Olaf**, **Mark**, **Jason**, **Remco**, **Jelle**, **Roy** and **Siebe**. I have no words to stress your importance for our group. Thanks for making sense of fridges, wirings, and, Mark, without you, the UTS would be in danger. The upgrade and the continuous maintenance of the system have highlighted your problem-solving capabilities above all. **Raymond S.** and **Raymond V.**, we appreciate the fact that we can bombard you with stupid questions on electronics, and you can still answer to us with politeness. Thanks to the incredible Kavli cleanroom staff: minimizing evacuations, acid spills, and keeping the machines running is daunting. Thank **Marc Z.**, **Charles**, **Ewan**, **Marco B.**, **Marco**, **Anja**, **Hozanna**, **Arnold**, **Pauline**, **Eugene**: you make such a fantastic team.
Everybody doing a PhD wants that things go smoothly. While nobody can promise you that science works, I had the luck of interacting very often with **Simone** and **Jenny**. With the highest capacity, you managed to run things in such a smooth way. Simone, thanks for your first welcome in QuTech, you have been so kind to me that you even picked me up from a hospital. Jenny, you have been for me and all the group members an invaluable reference point. **Csilla**, you blended in our group with grace. I owe you so much for continuously running things smoothly and always bring joy around us. **Avradeep**, thanks for your friendship. Our overlap was short, but you made an impact on us. Thanks for teaching me all your cleanroom tricks, for elevating my language in my MSc thesis, for passing along unforgettable Indian recipes, and hosting king-size dinners together. I feel very nostalgic of the old days with you and Arijita. **Maja**, thinking outside the box is your art. Thanks for hosting me as a student in the old days and being patient in front of all my questions regarding the microwave setups. Thanks also for keeping a door open in Sydney, I would love to pass by! **Nick de Jong**, in the early days of the Loop Qubit, you brought in incredible ideas and fabrication inputs, such as the trick of contacting the wire from the side. **Michal N.**, I sincerely appreciate our collaboration, and I hope it can continue in the future. Thanks for the uncountable discussions, and for always adding the right words and fits into our articles. **Chris Palmstrom** and all your team of brilliant students, if my PhD could start, it was thanks to your cluster in Santa Barbara, and your idea of using hydrogen radicals to clean off oxides from the nanowires gently. Thanks for your transparency and wisdom in passing along relevant information for our projects in Delft. **Erik Bakkers**, without the growth of such high-quality nanowires, the thesis at hand would not be written. Thanks for the valuable interaction along the way. **Ghada**, **Sasa**, and **Roy**: the truth is that you were the one growing the nanowires! Thanks for your dedication, the continuous development, and for giving birth to endless fresh ideas. Good luck with your next steps in your careers. During these four years, we had the privilege of taking onboard several gifted Master students, such as **Chien-An**, **Senja**, and **May-An**.

Thanks for sharing your enthusiasm, I learned a lot from each of you.

Giordano, we met on our first week in the Netherlands at the rainiest uitje of QuTech history in 2015. Since then, you have been alongside as a senior advisor (sorry for the 'senior'). Thanks for your endless advices, and for keeping me updated on your remarkable process. Eventually, a joke after the other, you even convinced me to stay and join the germanium team. I am delighted to kick in a closer collaboration with you and continue our joyful visits with Clelia, Gabriel and Maya. **Menno**, I am really looking forward to starting my postdoc in your team. Thanks for taking me on board and for also being in my PhD committee. Next to the physics of a growing number of interacting dots, I am eager to learn from the charismatic scientist you are.
Michael W. thanks for being my co-promotor, and for leading Topo in a fantastic way in the recent years. I wish you and **Srijit** good luck with continuing at the same level. You represented for me two solid presences in which I could count on. Thanks to all the other PIs in QuTech for putting the bar higher every day (this does not make things simple for us, by the way), to the board of directors, to the various engineers, and to all the other managers in QuTech for maintaining the excellence of the environment and for the remarkable efforts in dealing with the pandemic.

I owe my gratitude to all committee members for accepting my invitation and the burden alongside. Next to Leo, Michael W., Marina, and Menno, I am delighted of your presence **Yuval Oreg**, **Gary Steele**, **Yuli Nazarov**, and **Alessandro Tredicucci**. In particular, thank you Alessandro T. for that meeting in your office in Pisa in 2014, it opened big opportunities for my future to be. With your presence at my defence, we close an adventurous circle of six years.
In-person and online conferences and interviews were able to trigger meetings with extremely knowledgeable scientists such as **Floris Zwanenburg**, **Alexander Brinkman**, **Wilfred van der Wiel**, **Klaus Ensslin**, **Thomas Ihn**, **Ramon Aguado**, **Elsa Prada**, and **Mihir Pendharkar**. Everyone taught me something precious, which I will keep with me along the way.

Time to zoom out a bit. **Luca B**. and **Roberta M.**, thanks for two beautiful years together and cheering us up all the time. Thanks to your friendship and all your initiatives to lift up our spirit in the grey Dutch days. I wish you all the best for your life together, and I hope that one day we can live in the same city to restore our daily and crazy interaction.
Agnese and **Alessandro**, I am thrilled that staying in Delft means continuing our almost daily interplay and friendship made of long cycles, chatty walks, and endless dinners. Your cheerfulness has been contagious, and made our life so much nicer and sportier.
Mario, and **Luca**, the damned virus shifted our periodical coffees and dinners from the tables of various restaurants to Delftse Hout. More walking and less eating. I know, unfortunate, but was great to set such a habit to confess all our sins. I wish you two the best for your lives. **Matteo** and **Monica**, our first meeting in Indonesia, sunrise at the temple Borobudur, was exciting. What followed in the other 25 days, including escaping earthquakes at the tip of the volcano, was the result of a newly born friendship. Thanks for all the special time together, from scootering in frightful Indonesian streets to your

cheerful visits in Delft. Best wishes for your upcoming parenthood! Thanks to all the other friends we made in our time in Delft, from our lovely neighbors **Yolanda** and **José**, to the other legendary Kavli Warriors: **Gustavo**, **Maarten**, **Thjis**, **Jorge**, **Stefano**, **Tim**, **Mohsen**, **Sébastian**, **Nikos**, **Kaushik**, **Antariksha**. I am looking forward to playing with you again. I owe my deepest gratitude to our beloved friends in Ireland. **Nicola** and **Holger**, you have been for us our adopted aunt and uncle for ten years, being the reference points for so many essential things. The long, and unforgettable summers with you, **Shawn**, **Maddy**, **Connor**, and **Junah**, have become an actual tradition we would like to continue. We are looking forward to the moment to finally tell you all, sitting on the long table in your kitchen.

Grazie a tutti coloro che fin da molto prima sono stati vicini a me, dai miei grandiosi vicini di casa, **Mariangela**, **Luciano**, **Barbara**, **Luca** e prole, ai miei padrini adottati **Renzo** e **Anna**. Grazie agli amici romani **Roberto**, **Donatella**, **Luigi** e **Alberto** per tutto l'incoraggiamento, la stima reciproca, ma soprattutto per quanto ci siamo divertiti assieme. Grazie agli amici di sempre: **Davide C.** e **Chiara**, **Simone**, **Matteo**, **Mattia** e **Sara**, **Davide M.** e **Desy**, **Riccardo D. B.**. Ad ogni rientro in Italia, ci avete sempre fatto sentire vicini a voi. Le nostre chiacchierate in pasticceria (spesso diventate confessionali per qualcuno), le passeggiate insieme, e le lunghissime giornate al mare, ma soprattutto la vostra pura amicizia sono pilastri per la mia felicità. Grazie per tutto quello che siete stati negli ultimi vent'anni. **Maurizio**, **Carmen**, **Matteo** e **Simone**, sono grato per la vostra preziosa presenza lungo questi anni. Grazie per le innumerevoli chiacchierate, il sostegno continuo, le vacanze assieme e per tutto il tempo con voi, mi avete sempre fatto sentire come a casa.
Grazie ai nonni **Maria**, **Luigi**, zii **Valerio** e **Giuseppe** per avermi insegnato ad amare la natura ed i suoi prodotti, ma anche a zia **Rita** e zio **Piero** per essere sempre stati affianco a noi, soprattutto quando si trattava di scuola e libri. Grazie ai nonni **Dosolina**, **Gildo** per essermi sempre stati accanto; grazie agli zii **Vilma**, **Roberto**, **Aurora**, **Nino**, **Olindo**, **Lequien**, **Aliette**, ai cugini **Leonardo**, **Jacopo**, **Son** e **Alberto** per i nostri gioiosi ritrovi. Che memorie!

Ed infine grazie di cuore alla mia famiglia: **mamma Lucia**, **papà Gino**, **Miriam** e **Marta** per il massimo supporto, per aver sempre creduto in me, ma soprattutto per tutto l'amore. Mi avete insegnato fin dall'inizio ad avere fame, cuore, e coraggio, perché sapevate che il resto veniva da sé. Questa tesi è molto vostra.

Se c'è sempre stato un noi, è perché ci sei tu con me, **Grazia**. Il tuo essere solare e ambiziosa, insieme al tuo coraggio e pensiero divergente, mi hanno accompagnato con forza e dolcezza fino a qui. In questi anni, Delft è stata la nostra casa, e non vedo l'ora di scoprire cosa ha in serbo per noi adesso. Grazie davvero, amore mio.

CURRICULUM VITÆ

Francesco BORSOI

26-03-1992 Born in Pordenone, Italy.

EDUCATION

2006–2011 Scientific High School
Liceo M. Grigoletti, Pordenone, Italy.

2011–2014 BSc Physics
University of Trieste, Italy.

2014–2016 MSc Physics
University of Pisa, Italy.

Thesis:	Magnetic field resilient superconducting circuit elements for Majorana parity detection
Internal Supervisor:	prof. A. Tredicucci
External Supervisor:	prof. dr. ir. L. P. Kouwenhoven

2016–2020 PhD research
Delft University of Technology, The Netherlands.

Thesis:	Advances in semiconducting-superconducting nanowire devices
Promotor:	prof. dr. ir. L. P. Kouwenhoven
Co-promotor:	dr. M. Wimmer

List of Publications

10. *Engineering of spin-mixing proximity effect in semi-super hybrids*
G. P. Mazur, N. van Loo, M. Quintero-Pérez, J. Wang, P. Vinke, R. Dekker, **F. Borsoi**, M. Andrzejczuk, G. Badawy, S. Gazibegovic, E. P.A.M. Bakkers, S. Heedt, and L. P. Kouwenhoven
In preparation

9. *Nonlocal correlations in the subgap spectrum of hybrid nanowires*
S. Heedt, **F. Borsoi**, M. Quintero-Pérez, N. van Loo, A. Fursina, G. Badawy, S. Gazibegovic, K. van Hoogdalem, E. P. A. M. Bakkers, G. de Lange, and L. P. Kouwenhoven
In preparation

8. *A full parity phase diagram of a Majorana island*
J. Shen, G. W. Winkler, **F. Borsoi**, S. Heedt, V. Levajac, J. Wang, D. van Driel, D. Bouman, S. Gazibegovic, R. L. M. Op het Veld, D. Car, J. A. Logan, M. Pendharkar, C. J. Palmstrøm, E. P. A. M. Bakkers, L. P. Kouwenhoven, B. van Heck
arXiv:2012.10118 (2020)

7. *Single-shot fabrication of semiconductor-superconductor nanowire devices*
F. Borsoi, G. P. Mazur, N. van Loo, M. P. Nowak, L. Bourdet, K. Li, A. Fursina, E. Memisevic, G. H. A. Badawy, S. Gazibegovic, K. van Hoogdalem, E. P. A. M. Bakkers, L. P. Kouwenhoven, S. Heedt, M. Quintero-Pérez
arXiv:2009.06219 (2020)

6. *Shadow-wall lithography of ballistic superconductor-semiconductor quantum devices*
S. Heedt*, M. Quintero-Pérez*, **F. Borsoi***, A. Fursina, M. Ammerlaan, N. van Loo, K. Li, G. P. Mazur, M. P. Nowak, J. Shen, M.-A. van de Poll, G. H. A. Badawy, S. Gazibegovic, K. van Hoogdalem, E. Yucelen, E. P. A. M. Bakkers, and L. P. Kouwenhoven
arXiv:2007.14383 (2020)

5. *Transmission phase read-out of a large quantum dot in a nanowire interferometer*
F. Borsoi, K. Zuo, S. Gazibegovic, R. L. M. Op het Veld, E. P. A. M. Bakkers, L. P. Kouwenhoven, and S. Heedt
Nature Communications 11, 3666 (2020)

4. *High Mobility Stemless InSb Nanowires*
G. Badawy, S. Gazibegovic, **F. Borsoi**, S. Heedt, C. Wang, S. Koelling, M. A. Verheijen, L. P. Kouwenhoven, and E. P. A. M. Bakkers
Nano Letters 19, 3575-3582 (2019)

3. *Selectivity Map for Molecular Beam Epitaxy of Advanced III-V Quantum Nanowire Networks*
   P. Aseev, A. Fursina, F. Boekhout, F. Krizek, J. E. Sestoft, **F. Borsoi**, S. Heedt, G. Wang, L. Binci, S. Martí-Sánchez, T. Swoboda, R. Koops, E. Uccelli, J. Arbiol, L. P. Kouwenhoven, and P. Caroff
   Nano Letters 19, 218-227 (2019)

2. *Magnetic-Field-Resilient Superconducting Coplanar-Waveguide Resonators for Hybrid Circuit Quantum Electrodynamics Experiments*
   J.G. Kroll, **F. Borsoi**, K.L. van der Enden, W. Uilhoorn, D. de Jong, M. Quintero-Pérez, D.J. van Woerkom, A. Bruno, S.R. Plissard, D. Car, E.P.A.M. Bakkers, M.C. Cassidy, and L.P. Kouwenhoven
   Physical Review Applied 11, 064053 (2019)

1. *Parity transitions in the superconducting ground state of hybrid InSb–Al Coulomb islands*
   J. Shen*, S. Heedt*, **F. Borsoi***, B. van Heck, S. Gazibegovic, R. L. M. Op het Veld, D. Car, J. A. Logan, M. Pendharkar, S. J. J. Ramakers, G. Wang, D. Xu, D. Bouman, A. Geresdi, C. J. Palmstrøm, E. P. A. M. Bakkers, L. P. Kouwenhoven
   Nature Communications **9**, 4801 (2018)

* equal contribution